

**DEEP PROBE: INVESTIGATING THE LITHOSPHERE OF WESTERN NORTH
AMERICA WITH REFRACTION SEISMOLOGY**

by

ANDREW ROBERT GORMAN

B.Sc., University of Calgary, 1987

A THESIS SUBMITTED IN PARTIAL FULFILLMENT OF
THE REQUIREMENTS FOR THE DEGREE OF
DOCTOR OF PHILOSOPHY

in

THE FACULTY OF GRADUATE STUDIES
(Department of Earth and Ocean Sciences)

We accept this thesis as conforming
to the required standard

THE UNIVERSITY OF BRITISH COLUMBIA

October 2000

© Andrew Robert Gorman, 2000

In presenting this thesis in partial fulfilment of the requirements for an advanced degree at the University of British Columbia, I agree that the Library shall make it freely available for reference and study. I further agree that permission for extensive copying for scholarly purposes may be granted by the head of my department or by his or her representatives. It is understood that copying or publication of this thesis for financial gain shall not be allowed without my written permission.

Department of Earth and Ocean Sciences

The University of British Columbia

2219 Main Mall

Vancouver, BC, Canada

V6T 1Z4

Date:

3 November 2000

Abstract

The Laurentian Craton, composed of the exposed Canadian Shield ringed by sediment-covered platforms, is the Precambrian heart of North America. The craton can be divided into several provinces representing ancient Archean blocks and the suture regions which stitched them together. In western Canada, Montana and Wyoming, the general distribution of Precambrian cratonic elements has been established by previous potential field studies combined with the analysis of basement rocks extracted from a small number of exploration drill holes that penetrated the overlying sedimentary basin, and from limited outcrops in southern Montana and Wyoming. The major blocks identified in this region include the Archean Hearne (mostly beneath Alberta) and Wyoming (beneath Montana and Wyoming) Provinces. A third block, the Medicine Hat Block, often interpreted to be the southernmost part of the Hearne Province, is considered independent in this study.

The objectives of this thesis are to determine the velocity structure and characteristics of the crust and sub-crustal lithospheric mantle beneath the three Archean domains and the relationships among them to further understanding of the tectonic development of cratonic western North America. These objectives are met through interpretation of data from the Deep Probe / SAREX seismic refraction experiment of 1995, the largest of its type ever undertaken on the continent. Twenty large chemical explosions were detonated along a 3000-km-long profile running from Great Slave Lake to southern New Mexico and recorded at ~ 2000 closely spaced seismograph stations between central Alberta and northern New Mexico. Interpretations, of increasing complexity, are based on: (1) the tau-p downward continuation of individual shot records, (2) a ray-theoretical travel-time inversion with Earth curvature considerations, and (3) detailed modelling of specific features with a finite difference wave propagation method.

Interpretations of velocities and structures are made to depths as great as 150 km. From features of the crustal structure and their correspondence with two north-dipping relict subduction zones in the upper mantle, the boundaries between the three major Archean blocks are delineated and associated with the Vulcan Structure and Great Falls Tectonic Zone, two poorly understood tectonic features in the region. A prominent 10-to-30 km thick high velocity layer at the base of the Wyoming Province and Medicine Hat Block is interpreted to represent Proterozoic crustal underplating and alteration. The composition and physical properties of the crust-mantle boundary, the relict subduction zones and a heterogeneous upper mantle layer lying between depths of 100 km and 140 km are investigated to further understand lithospheric development in this region. The seismic interpretation is combined with previous work to develop a revised scenario for the tectonic assembly of western Laurentia.

Table of Contents

Abstract	ii
List of Tables	viii
List of Figures	ix
Acknowledgements	xvi
Dedication	xviii
1 INTRODUCTION	1
1.1 Rationale	5
1.2 Regional Tectonic Setting	6
1.3 The Seismic Method	14
1.4 Previous Studies	17
1.4.1 Southern Alberta and Montana - Crustal Studies	17
1.4.2 Upper Mantle Studies	18
2 THE DEEP PROBE SEISMIC REFRACTION EXPERIMENT	28
2.1 Preliminary Field Procedures	29
2.1.1 Initial Source and Receiver Site Selection	30
2.1.2 Final Source and Receiver Site Selection / Permitting of Private Lands	30
2.1.3 Environmental Permitting	31

<i>Table of Contents</i>	iv
2.1.4 GPS Surveying of Source and Receiver Locations	32
2.1.5 Drilling and Loading of Source Locations	33
2.2 Data Acquisition	36
2.2.1 Seismometer Deployment	36
2.2.2 Timing Corrections	38
2.2.3 Field Instrumentation	39
2.2.4 Instrument Deployments	42
2.2.5 Clean-up	44
2.3 Post-Experiment Procedures	44
2.3.1 Finalisation of Geographical Survey Information	44
2.3.2 Merging of Seismic Data Sets	45
2.3.3 PLOTSEC	45
2.3.4 Gain	46
2.3.5 Updating SEG-Y Headers	48
2.3.6 Merging and Archiving Data	48
2.4 Introduction to the Deep Probe Data Set	49
3 PRELIMINARY 2-D VELOCITY MODEL FROM TAU-P ANALYSIS	57
3.1 Application to Deep Probe	58
3.2 Procedure	59
3.2.1 Tau- p transform	59
3.2.2 Downward continuation of τ - p transformed data into z - p space	60

<i>Table of Contents</i>	v
3.2.3 Forward modelling	62
3.2.4 Synthesis for a 2-D velocity model	63
3.3 Discussion	64
4 CONSIDERING EARTH CURVATURE: MODIFICATION OF THE RAY- THEORETICAL TRAVEL TIME INVERSION ROUTINE	67
4.1 Ray tracing	69
4.1.1 Ray tracing through a 'flat' Earth	69
4.1.2 Ray tracing through a cylindrical Earth	71
4.1.3 Application of the cylindrical parameterisation	72
4.2 Modelling results	74
4.2.1 Synthetic example: 1-D comparison of RAYINVR and WKBJ algorithms	74
4.2.2 Experimental example: the Deep Probe experiment	78
4.3 Discussion	80
5 IMAGING THE LITHOSPHERE OF WESTERN LAURENTIA	81
5.1 Data	82
5.1.1 Acquisition Details	82
5.1.2 Seismic Observations	83
5.1.3 Preliminary Interpretations	86
5.2 Radial Earth Ray-Theoretical Travel-Time Inversion	89
5.2.1 Method	89
5.2.2 Data Analysis	91

<i>Table of Contents</i>	vi
5.2.3 A Cross-Section of Platformal Western Laurentia	97
5.2.4 Resolution	108
5.3 Implications for the History of Lithospheric Assemblage in Western Laurentia	111
5.3.1 Three Crustal Blocks Develop Independently	112
5.3.2 Hearne - Medicine Hat Block - Wyoming Assemblage	113
5.3.3 Proterozoic vs. Archean lithosphere development	116
5.3.4 Lower Crustal Layer Emplacement	117
5.4 Summary	120
6 BEYOND RAY THEORY	123
6.1 Preliminary Modelling Concerns	124
6.1.1 A Word or Two on Scales of Observation	124
6.1.2 Finite Difference Theory	128
6.1.3 Selection of Finite Difference Parameters	130
6.1.4 Procedural Details	132
6.1.4.1 Input Model Set-up	133
6.1.4.2 Creation of the Acoustic Model	135
6.1.4.3 Creation of the Visco-elastic Model	137
6.1.4.4 Execution of the finite difference code	137
6.1.4.5 Output	140
6.1.5 Model Parameter Testing Issues	142
6.2 The Nature of the Moho	146

<i>Table of Contents</i>	vii
6.2.1 Investigations of a Moho Transition Zone	147
6.2.2 Structures on Moho: Distinct vs. smooth change	158
6.3 Dipping Reflectors in the Upper Mantle	168
6.4 P_n Coda and Teleseismic P_n Considerations	175
6.5 Summary	188
7 DISCUSSION, CONCLUSIONS AND RECOMMENDATIONS	192
7.1 Summary of Results	193
7.2 North American Ramifications of the Experiment	196
7.3 Recommendations	197
References	200
Appendices	210
A Deep Probe Summary Data Plots	210
B Summary of Modifications to the RAYINVR Code	224
B.1 General Modifications	224
B.2 Ordinary Differential Equations for a Radial Earth	225
B.3 Supplementary Routines	226
B.4 Plotting Routines	227

List of Tables

2.1	Summary of shot point information.	31
2.2	Summary of instruments deployed.	37
2.3	Summary of gains applied to Deep Probe data.	47
2.4	General information about the data	49
4.1	Corresponding flat Earth and cylindrical Earth quantities	71
4.2	r , Δ and l , ζ parameterisation equivalents for a cylindrical Earth	73
5.1	The number of picks made for each phase followed by the average uncertainty (ms) in parentheses.	92
5.2	Statistical modelling results.	96
6.1	Frequency vs. wavelength of various seismic waves.	125
6.2	Utility routines used to modify and plot the finite-difference models.	134
6.3	Viscoelastic parameter relationships.	138
6.4	Finite difference input parameters.	139

List of Figures

1.1	Deep Probe location map.	2
1.2	Potential field data of northern portion of Deep Probe profile	8
1.3	Basement domains interpreted from figure 2.	10
1.4	Introductory ray diagram and time-distance plot.	16
1.5	Geothermal and solidus curves for the lithosphere as related to a simplified model of the lower lithosphere beneath the Baltic Shield.	27
2.1	Deep Probe and SAREX data merging flowchart.	46
2.2	Data examples: (a) Deep Probe 149 and SAREX 1 (Shot point location at Canada - USA Border). (b) Deep Probe 155 and SAREX 11.	51
2.3	Three-component broad-band seismograph recordings from the Canadian National Seismograph Network (CNSN).	52
2.4	Normalised amplitude spectra for shot profiles 49 and 55.	53
2.5	Peaceful Nuclear Explosion seismic profile Quartz, central Russia.	54
2.6	Comparison of Deep Probe Profile 55 and Quartz Profile 323.	55
3.1	Summary flow chart for τ - p analysis and derivation of $v(z)$	59
3.2	τ - p transform of the data in Fig. 2.2.	61
3.3	Downward continuations of the τ - p -transformed data into z - p space.	61

3.4	WKB-calculated travel times for P_g , P_mP and P_n phases (1, in green) overlaid on the input data.	63
3.5	2-D model derived from merging the results of all analysed profiles from the data set.	65
4.1	Schematic illustration summarising change from Cartesian to cylindrical co-ordinates.	68
4.2	Ray traced in Cartesian co-ordinates.	70
4.3	Ray traced in cylindrical co-ordinates.	71
4.4	Ray traced in cylindrical co-ordinates which are parameterised in terms of l and ζ	72
4.5	1-D input model.	74
4.6	Flat Earth RAYINVSR modelling of 1-D input model.	75
4.7	Comparison of flat-Earth transformed velocity profile to original cylindrical-Earth velocity profile (Fig. 4.5).	76
4.8	Flat Earth RAYINVSR modelling of flat-Earth transformed input model.	76
4.9	Cylindrical Earth RAYINVSR modelling of 1-D input model.	77
4.10	Flat Earth RAYINVSR model of Shot 55.	78
4.11	Cylindrical Earth RAYINVSR model of Shot 55.	79
5.1	Merged data set: offsets between 0 and 282 km from SAREX 11, offsets beyond 282 km from Deep Probe 55.	84
5.2	P_n phase extracted from SAREX 9.	85
5.3	Initial 2-D interpretation of Deep Probe	86

5.4	Model node distribution (squares and triangles) superimposed on a skeleton of the Deep Probe model.	93
5.5	Summary of ray tracing results by phase: P_1P , P_i , P_mP , and P_n	95
5.6	Data examples: dipping reflectors	98
5.7	Interpreted Deep Probe velocity model.	100
5.8	Schematic structural interpretation of the Deep Probe velocity model.	101
5.9	Merged data set: Deep Probe 49 and SAREX 1 (Shot point location at Canada - USA Border	103
5.10	Data examples: lower crustal layer of the Wyoming Province and Medicine Hat Block.	105
5.11	Cartoon summarising the tectonic assemblage of western Laurentia.	112
5.12	Cartoon summarising Sweet Grass Hills xenolith ages and source depths (adapted from Ross and Davis 2000).	118
6.1	Length-scales of heterogeneity in the physical properties of the Earth, L , as compared to the wavelength of the investigating seismic wave, λ	124
6.2	Finite-difference grid about a point (x_0, z_0, t_0) . The pressure field, $P(x, z, t)$, is advanced from the t_0 to $t_0 + \Delta t$ level using values from the t_0 and $t_0 - \Delta t$ levels.	128
6.3	Model 4 - RAYINVR model for the SAREX deployment with the Earth flattening transform applied and a discretisation of 120 m.	136
6.4	Amplitude considerations: (a) SAREX Shot 9 (b) Finite difference synthetic seismogram of SAREX Shot 9.	141
6.5	Grid size comparison. Grid dimensions of 100, 120 and 150 m.	143

6.6	Model depth comparison: (a) 125 km vs. (b) 150 km.	144
6.7	Model 5 - Transitional Moho.	148
6.8	1-D profile through Model 5 at model position 274 km.	149
6.9	SAREX 9 finite difference synthetics. Comparison of (a) Model 4: a discrete Moho discontinuity to (b) Model 5: a layered transitional Moho boundary zone. Enlargements of real data are included for comparison.	150
6.10	Model 11 - Transitional Moho created by addition of elliptical structures in the uppermost mantle.	151
6.11	1-D profile through Model 11 at model position 274 km.	152
6.12	SAREX 9: Model 11 finite-difference synthetic. Moho boundary zone defined by elliptical bodies.	153
6.13	Model 10 - Sharp Moho discontinuity overlying a 10-km thick lid in upper mantle with no velocity gradient.	154
6.14	SAREX 9. Comparison of (a) real data to (b) Model 10: a Moho boundary zone defined by a 10-km thick layer of zero velocity gradient.	155
6.15	Model 12 - 2-D transitional Moho (as in Model 10) within a 10-km thick lid in upper mantle with zero velocity gradient.	156
6.16	SAREX 9: Model 12 finite-difference synthetic. Moho boundary zone defined by elliptical bodies within a 10-km-thick lid in the upper mantle with zero velocity gradient.	157
6.17	Model 6 - Sharp Moho break.	159
6.18	Comparison of SAREX shots 4 (a) and 9 (b) to highlight features in the data resulting from the steep structure in the Moho beneath the Medicine Hat Block. . . .	160

6.19 SAREX 4 finite difference synthetics. Comparison of (a) Model 4: a smooth step in the Moho beneath the MHB to (b) Model 6: a sharp step.	163
6.20 SAREX 5 finite difference synthetics. Comparison of (a) Model 4: a smooth step in the Moho beneath the MHB to (b) Model 6: a sharp step.	164
6.21 SAREX 6 finite difference synthetics. Comparison of (a) Model 4: a smooth step in the Moho beneath the MHB to (b) Model 6: a sharp step.	165
6.22 SAREX 8 finite difference synthetics. Comparison of (a) Model 4: a smooth step in the Moho beneath the MHB to (b) Model 6: a sharp step.	166
6.23 SAREX 9 finite difference synthetics. Comparison of (a) Model 4: a smooth step in the Moho beneath the MHB to (b) Model 6: a sharp step.	167
6.24 Model 4a - RAYINVR model for SAREX deployment with Earth flattening transform and 120 m discretisation.	172
6.25 SAREX 9 finite difference synthetics. Comparison of (a) Model 4a: positive velocity anomaly slabs to (b) Model 4: negative velocity anomaly slabs. Central frequency = 1.75 Hz.	173
6.26 SAREX 9: Model 4b finite difference synthetic. Subducted slabs defined by a -1.0 km/s velocity anomaly. Central frequency = 1.75 Hz.	174
6.27 SAREX 9 with teleseismic P_n and P_n coda features highlighted	177
6.28 Model 7 - Elliptical velocity anomalies inserted between depths of 100 and 140 km.	179
6.29 SAREX 9 finite difference synthetics. Comparison of (a) Model 4: a transparent upper mantle to (b) Model 7: a mantle with coarse elliptical anomalies added between 100 and 140 km depth. Central frequency = 1.75 Hz.	180

- 6.30 SAREX 9 finite difference synthetics. Comparison of (a) Model 4: a transparent upper mantle to (b) Model 7: a mantle with coarse elliptical anomalies added between 100 and 140 km depth. Central frequency = 3.25 Hz. 181
- 6.31 (a) Model 8 - Elliptical velocity anomalies inserted between depths of 100 and 140 km. (b) SAREX 9 finite difference synthetic for Model 8. Central frequency = 3.25 Hz. 183
- 6.32 (a) Model 9 - Elliptical velocity anomalies inserted between depths of 100 and 140 km. (b) SAREX 9 finite difference synthetic for Model 9. Central frequency = 3.25 Hz. 184
- 6.33 Model 9a: modified for the dimensions of Deep Probe 55 - Elliptical velocity anomalies inserted between depths of 100 and 140 km. 185
- 6.34 Deep Probe 55 / SAREX 11. Comparison of (a) real data to (b) finite difference synthetic. Model 9: a mantle with coarse elliptical anomalies added between 100 and 140 km depth. Central frequency = 3.25 Hz. 187
- A.1 Deep Probe 143: (a) Colour variable density plot with picks overlaid in green. (b) RAYINVR ray-trace diagram. (c) RAYINVR travel-time calculations overlaid on picks. 212
- A.2 Deep Probe 149 and SAREX 1: (a) Colour variable density plot with picks overlaid in green. (b) RAYINVR ray-trace diagram. (c) RAYINVR travel-time calculations overlaid on picks. 213
- A.3 SAREX 2: (a) Colour variable density plot with picks overlaid in green. (b) RAYINVR ray-trace diagram. (c) RAYINVR travel-time calculations overlaid on picks. 214

- A.4 SAREX 3: (a) Colour variable density plot with picks overlaid in green. (b) RAY-INVR ray-trace diagram. (c)RAYINVR travel-time calculations overlaid on picks. 215
- A.5 SAREX 4: (a) Colour variable density plot with picks overlaid in green. (b) RAY-INVR ray-trace diagram. (c)RAYINVR travel-time calculations overlaid on picks. 216
- A.6 SAREX 5: (a) Colour variable density plot with picks overlaid in green. (b) RAY-INVR ray-trace diagram. (c)RAYINVR travel-time calculations overlaid on picks. 217
- A.7 SAREX 6: (a) Colour variable density plot with picks overlaid in green. (b) RAY-INVR ray-trace diagram. (c)RAYINVR travel-time calculations overlaid on picks. 218
- A.8 SAREX 8: (a) Colour variable density plot with picks overlaid in green. (b) RAY-INVR ray-trace diagram. (c)RAYINVR travel-time calculations overlaid on picks. 219
- A.9 SAREX 9: (a) Colour variable density plot with picks overlaid in green. (b) RAY-INVR ray-trace diagram. (c)RAYINVR travel-time calculations overlaid on picks. 220
- A.10 SAREX 10: (a) Colour variable density plot with picks overlaid in green. (b) RAYINVR ray-trace diagram. (c)RAYINVR travel-time calculations overlaid on picks. 221
- A.11 SAREX 11: (a) Colour variable density plot with picks overlaid in green. (b) RAYINVR ray-trace diagram. (c)RAYINVR travel-time calculations overlaid on picks. 222
- A.12 Deep Probe 155: (a) Colour variable density plot with picks overlaid in green. (b) RAYINVR ray-trace diagram. (c)RAYINVR travel-time calculations overlaid on picks. 223

Acknowledgements

As I pause to reflect back over the last six years, a multitude of names and faces streams through my mind. Many of these people had a direct influence on the course of my research, others influenced my academic development and still others provided friendship and support in my life within and outside the university.

First and foremost, I sincerely thank my advisor, Prof. Ron Clowes, who has been a constant source of encouragement and advice. He has given me plenty of room to assert independence in my research while helping me to maintain perspective and focus. In particular, I thank Ron for countless conversations which set me off on new paths of investigation and productivity.

I also thank the members of my supervisory committee, Profs. Bob Ellis, Jim Mortensen and Michael Bostock for their insight at various times during my research and for their helpful reviews of my thesis.

As a graduate student in geophysics within the Department of Earth and Ocean Sciences, I have benefitted from the close proximity to the world-class academic minds of our faculty and a first-rate graduate student body. Through course-work, teaching assistantships, seminars, coffee room debates and hallway chats, my skills as a researcher, educator, speaker and debater have been honed. Countless members of the UBC community deserve thanks, but in particular I would like to acknowledge three people. John Amor, without whom I never would have navigated a sea of computer programming and system administrating problems, is an invaluable pillar upon which the seismology group at UBC rests. Dr. Phil Hammer, who at times likely wished that his office were farther from mine, has been a fountain of ideas and technical help. Charly Bank, my friend and office mate, has always been a sounding board for my ideas, complaints and chat.

Central to my thesis was the acquisition of the Deep Probe Experiment during the summer of 1995. Instrumentation and instrument support personnel for this experiment were provided by the

Geological Survey of Canada (GSC) Instrumentation Group (which achieved an almost perfect data collection record), the IRIS/PASSCAL Instrument Center, the United States Geological Survey (USGS) and the GeoForschungsZentrum Potsdam in Germany. Special thanks are due Tim Cartwright and Peter Carroll of *LITHOPROBE* and Ed Criley, Grey Jensen, and Tom Burdette of the USGS, for assistance with shot points. Numerous private landowners, as well as provincial, state and federal agencies in Canada and the USA permitted the use of land in their care to access and position shot and receiver points. Financial support for Deep Probe came from *LITHOPROBE* [funded by a research network grant from the Natural Sciences and Engineering Research Council (NSERC) and the GSC], the National Science Foundation and the United States Air Force. And of course, this experiment could not have been undertaken without the willing assistance of approximately 100 volunteers from various academic institutions in North America and Europe who deployed instruments in the field during the experiment. On a personal note, I thank my field assistant, Shawn Rastad, for his help in the field with surveying and members of my family in Alberta, John and Jacquie Gorman of Spruce Grove, Michael and Jackie Gorman of Calgary, and Jane and Richard Galway of Calgary for numerous free meals and beds during the field season.

Additional financial support for this research was provided by an NSERC individual research grant to Ron Clowes and a MacKay Graduate Scholarship.

I consider myself very fortunate to have family and friends who have been encouraging and supportive in this endeavour. I thank my parents – John and Eileen Gorman, brothers – John and Michael, and aunt and uncle – Jane and Richard Galway, for being a steady source of goodwill and for encouraging me to follow my dreams. I thank my friends and fellow students, particularly Derek Scherger, Karl Butler, Kevin Jarvis, Rob Luzitano, Mark McCaskill and Kim Welford for their camaraderie and willingness to listen to my joys and sorrows. Finally, and most importantly, I thank my wife Sandy for standing by me through this part of my life. Her enthusiasm for life, compassion for others and innate goodness have given my life perspective and meaning.

*For Sandy,
my inspiration,*

*and Clare,
our inspiration.*

Chapter 1

Introduction

For Once, Then, Something

*OTHERS taunt me with having knelt at well-curbs
Always wrong to the light, so never seeing
Deeper down in the well than where the water
Gives me back in a shining surface picture
My myself in the summer heaven, godlike
Looking out of a wreath of fern and cloud puffs.
Once, when trying with chin against a well-curb,
I discerned, as I thought, beyond the picture,
Through the picture, a something white, uncertain,
Something more of the depths-and then I lost it.
Water came to rebuke the too clear water.
One drop fell from a fern, and lo, a ripple
Shook whatever it was lay there at bottom,
Blurred it, blotted it out. What was that whiteness?
Truth? A pebble of quartz? For once, then, something.*

– Robert Frost (from Harper's Magazine, July 1920).

Deep Probe was a bold seismic experiment that set out to peer into the depths of the lithosphere of western North America with higher resolution than ever before. It remains unique among refraction studies due to the size of sources used (1000 - 25,000 kg), total length of receiver array (~2000 km), spacing of receivers (1 - 2 km) and depths investigated (as deep as 660 km). While not achieving all of its ambitious goals, the experiment has made a significant contribution to the understanding of the tectonic history of western North America by investigating the deepest reaches of the lithosphere with a detail never before achieved in this region.

The study corridor approximately follows the 110th meridian, spanning almost 3000 km (28°

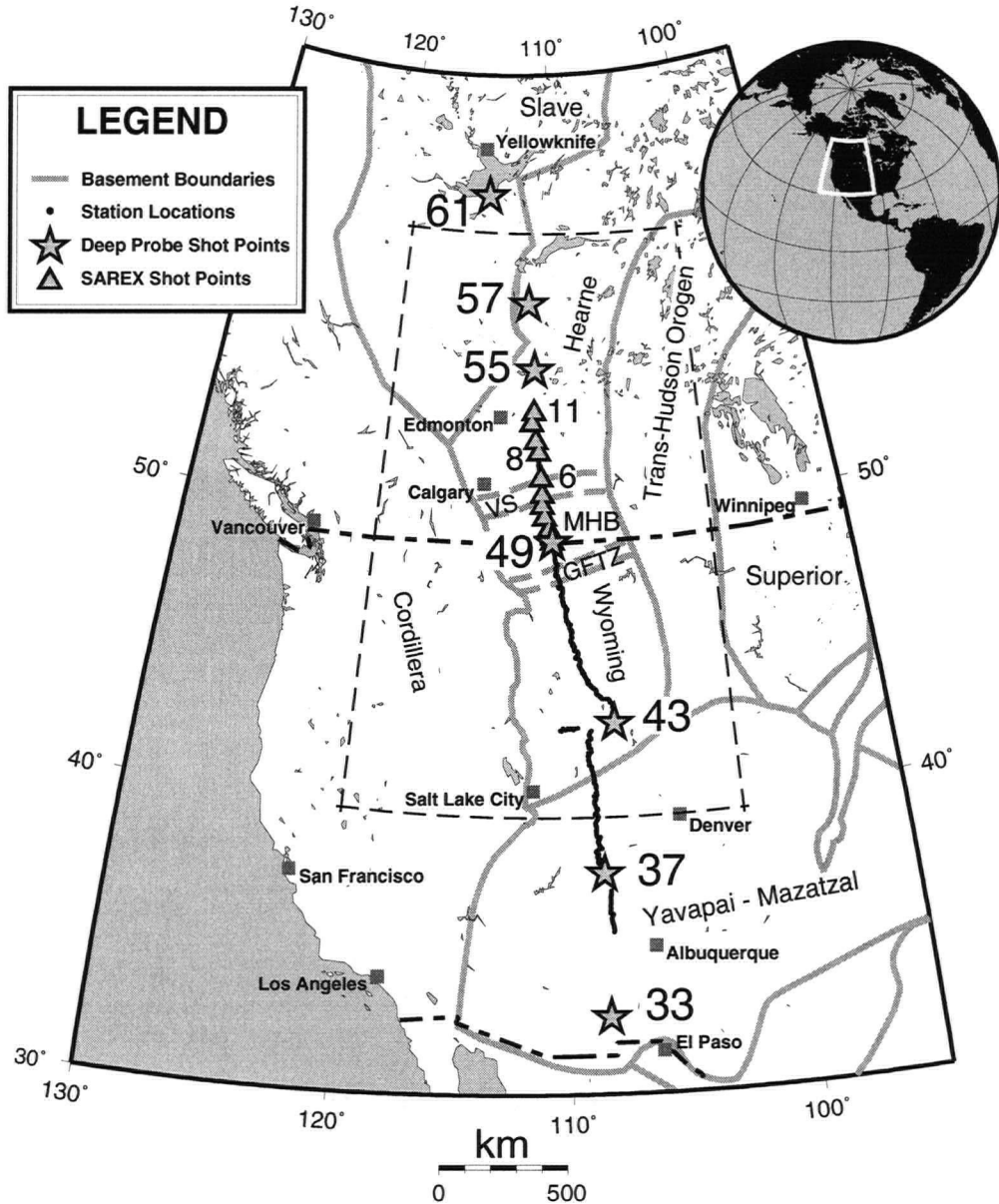


Figure 1.1: Location map showing the Deep Probe corridor in western North America. Small circles (overlapping to form a line) are seismograph stations occupied for the 1995 active source experiment. Deep Probe shot points (stars) are numbered by their approximate latitude; SAREX shot points (triangles) are numbered 1 - 11 from south to north. Grey lines denote borders of major crustal provinces [Hoffman 1989]. The Medicine Hat Block (MHB), previously considered part of the Hearne Province, lies between the Hearne and Wyoming provinces and is shown with its bounding features: the Vulcan Structure (VS) and Great Falls Tectonic Zone (GFTZ). Dashed boundary denotes map coverage in Figs. 1.2 and 1.3.

of latitude or almost 8% of the Earth's circumference) from the northernmost shot point in the Northwest Territories to the southernmost shot point in New Mexico (Fig. 1.1). Ten shots, up to 10 times larger than those used in conventional crustal studies, were recorded by seismographs every 1-2 km to maximum source-receiver offsets of about 2500 km. The Deep Probe field study was preceded by a conventional study, the Southern Alberta Refraction Experiment (SAREX), to provide additional information on the crustal velocity structure of southern Alberta as part of the *LITHOPROBE* Alberta Basement Transect (Fig. 1.1) [Clowes *et al.* 2000]. SAREX involved 10 source locations with a 55-km spacing in southern Alberta recorded every 1-1.25 km from southern Montana to central Alberta. Unless specifically stated, this thesis regards the SAREX data as being part of the Deep Probe data set. The interpretation of this combined data set has resulted in the development of a model for the velocity structure of the Earth from the lower crust to depths as great as 150 km into the mantle.

The Deep Probe experiment was originally planned to target the mantle lithosphere of the Archean Hearne craton underlying southern Alberta [Ross and Kanasewich 1992]. However, the scope of the study was greatly expanded when colleagues from the United States joined the original *LITHOPROBE* program, bringing more instruments and, most critically, providing a number of shot points within the U.S. The enhanced Deep Probe experiment expanded coverage to the Archean Wyoming craton and the Proterozoic terranes of the southern Rocky Mountains and Colorado Plateau. Together, Deep Probe and SAREX encompassed a number of scientific objectives.

1. The development of a well-constrained two-dimensional (2-D) velocity section of the crust and upper mantle extending from central Alberta to central New Mexico.
2. The interpretation and evaluation of this section in terms of geological structure and tectonic history.

3. The identification and characterisation of anticipated heterogeneous bodies and rheological fabrics within the sub-crustal lithosphere of this section.
4. Recording arrivals from the mantle transition zone in order to gather new information on the nature and characteristics of the 410-km and 660-km discontinuities.

This thesis details the investigations undertaken to satisfy the first three objectives. Evaluation of the last of the objectives has proven to be elusive. In the northern half of the profile, possible arrivals with very low signal-to-noise ratios have travel-time characteristics consistent with expected reflections from the 410-km discontinuity; in the south, other very weak arrivals appear to have travel-time characteristics associated with the 660-km discontinuity. Unfortunately, enhancement techniques applied (*e.g.*, eigenimage analysis [Ulrych *et al.* 1999] and coherency filtering [Milkereit and Spencer 1989]) have not been successful at clarifying these tantalising observations.

In Chapter 1, I introduce the rationale for the Deep Probe experiment, discuss the tectonic setting in western North America in the context of features identifiable by the experiment, and review the seismic refraction method applied for Deep Probe in relation to seismic experiments of similar scale conducted around the world. Chapter 2 is a summary of the field procedure followed to acquire the Deep Probe data set and the data processing steps which followed. Previously published as a *LITHOPROBE* report [Gorman *et al.* 1997], these topics deserve attention in this thesis because the quality of the recorded data was strongly dependent on the methods used to gather and process it. A catalogue of the recovered data is provided. The next four chapters detail the interpretation of the Deep Probe data. Three interpretive techniques, of increasing complexity, are used. In Chapter 3, a preliminary 2-D model for the Deep Probe profile is developed by combining numerous 1-D velocity profiles obtained by a downward continuation of tau-p transformed

waveform data. The technique and the result of its application to the Deep Probe data set are discussed. The strength of this technique is its ability to rapidly determine a preliminary velocity model which can then be used as input for more detailed analyses. This chapter is based on a previously published paper [Gorman and Clowes 1999]. Chapter 4 details required modifications to the ray-theoretical travel-time inversion routine [Zelt and Smith 1992] that were necessary to account for the effects of Earth curvature over the length scales observed by the Deep Probe experiment. The detailed 2-D interpretation of the data set, derived by the methods of Chapter 4, are discussed in Chapter 5. This detailed interpretation includes the development of a modified history of accretion for the lithosphere of western North America. This chapter is based on a paper currently in review [Gorman *et al.* 2000]. Chapter 6 examines some of the specific lithospheric structures identified in Chapter 5 using the technique of finite difference forward modelling; this is in order to gain a better understanding of features which cannot be completely described using ray theoretical approaches alone. Finally, additional discussion, conclusions and recommendations for future research are given in Chapter 7.

1.1 Rationale

An unanswered question in continental geodynamics is the role played by the subcrustal lithosphere in vertical motions that intermittently influence the interiors of continents. One such region is the Archean Medicine Hat Block (MHB), a "crustal platform unit" generally assumed to be part of the Hearne Province of the North American craton. This region is now overlain by sedimentary rocks, deposited intermittently from the Mesoproterozoic to the Oligocene, which provide an opportunity to evaluate the long-term history of the MHB over the last 1.5 billion years [Ross and Kanasewich 1992]. The region of the MHB at present is tectonically quiet, but evidence suggests that this has not always been so. Extensive petroleum exploration has revealed that the sedimentary section above the MHB contains persistent differences from those deposited on the adjacent

domains of the Hearne and Wyoming provinces, indicating that the lithospheric mantle may have played an important role in the tectonic history of the region.

The nature of the lithospheric mantle below the Medicine Hat Block and its role in the tectonic history of the area are enigmatic. Prior geophysical observations in the area, essential in providing the depth dimension of geological studies, have not had sufficient resolution to form any conclusions about crust-mantle interactions. Geophysical techniques, such as the analysis of potential field and magnetotelluric data, have provided information on particular physical properties of the crust in this region but have not been useful for extracting information on the upper mantle. Seismic reflection and earlier seismic refraction techniques have detailed the structures seen in the crust but have not been particularly good for the mantle.

The Deep Probe refraction seismic data set provides an excellent opportunity to study this region in detail. As one of the largest refraction surveys ever undertaken, it provides new information about the deepest regions of the crust and upper mantle in the vicinity of the study area. Interpretation of these data adds to a new understanding of the tectonic history of the various crustal elements of this part of North America and also their historical and current relationship to the underlying lithospheric mantle.

1.2 Regional Tectonic Setting

The primary geological focus of this thesis is the Precambrian platform of western Laurentia and the upper mantle underlying it. Platforms are defined as the subsurface analogues of shields; together they constitute the relatively stable cratonic heart of a continent. In this region, the platform is composed of predominantly Archean-aged crustal blocks which lie buried beneath the Phanerozoic sedimentary rocks of the Western Canada Sedimentary Basin and the American Great Plains. The two largest blocks, the Hearne and Wyoming provinces, are two of the seven major Archean

provinces that coalesced in the Precambrian to form Laurentia, the North American craton [Hoffman 1988, 1989]. Where it is exposed in the Canadian Shield, the Hearne Province has been extensively studied and analysed, but where it lies under the Western Canada Sedimentary Basin, it has only been sampled directly by cores taken from wells drilled by the petroleum industry [Ross *et al.* 1991]. The Wyoming Province crops out in several locations in the central parts of Late Mesozoic to Early Tertiary Laramide uplifts [Frost and Frost 1993]. However, the extent of these outcrops amounts to less than a tenth of the total area underlain by the province [Houston *et al.* 1993].

In Alberta and northern Montana, the hydrocarbon-rich Phanerozoic Western Canada Sedimentary Basin overlies Archean basement. The platform has been divided into distinct crustal domains based on U-Pb geochronological data obtained from basement drill cores recovered during petroleum exploration coupled with regional patterns observed in potential field (gravity and magnetics) data and in the geology of the overlying sedimentary basin (Figs. 1.2 and 1.3) [Ross *et al.* 1991, Villeneuve *et al.* 1993]. As early as 1941, a basement domain termed Montania was identified in southern Alberta and northern Montana based on well data from the fledgling petroleum industry [Deiss 1941]. The sedimentary record for Montania, spanning ~ 1.5 Ga, shows evidence for a stable basement topographic high. This suggests a different Proterozoic and Phanerozoic tectonic history for the underlying basement from regions to the north and south. The region identified as Montania correlates remarkably well with the Medicine Hat Block (MHB), defined by distinctive potential field characteristics and bounded by prominent potential field anomalies: the Vulcan Structure to the north and the Great Falls Tectonic Zone (GFTZ) to the south (Figs. 1.2 and 1.3) [Pilkington *et al.* 1992].

Sparsely distributed isotopic ages of core samples give some control on the timing of the assembly of the basement beneath the Western Canada Sedimentary Basin (Fig. 1.3) [Ross *et al.* 1991]. North of the Medicine Hat Block, various rock samples suggest that the Hearne Province

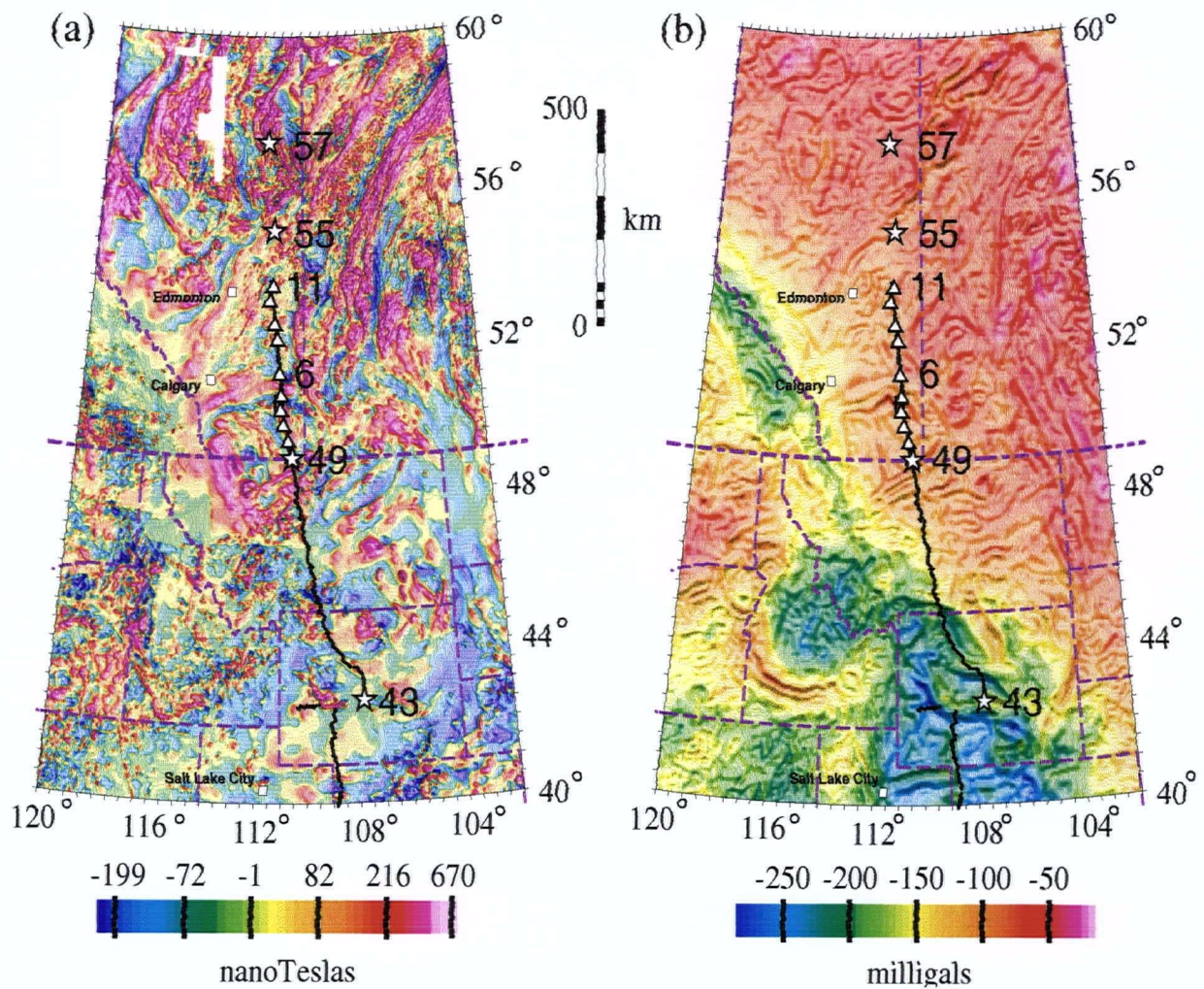


Figure 1.2: Potential field data of northern portion of Deep Probe profile (west-central North America). Locations of Deep Probe (stars) and SAREX (triangles) shot points are indicated. (a) Aeromagnetic (residual total field) anomaly map. (b) Bouguer gravity with shaded relief of the horizontal gradient magnitude (sun inclination = 60° , declination = 355°). Canadian gravity anomaly data are from the Canadian Gravity Anomaly Database of the Canadian Geodetic Information System maintained by the Geodetic Survey Division, Geomatics Canada. Canadian magnetic data are from the National Aeromagnetic Data Base maintained by the Regional Geophysics Section, Continental Geoscience Division of the Geological Survey of Canada. American data are from the DNAG 6 km gravity compilation and 2 km magnetic compilation available from the National Geophysical Data Centre, USGS, Boulder, CO. Data courtesy of Warner Miles, Regional Geophysics Section, Continental Geoscience Division, Geological Survey of Canada.

was assembled and modified between 2.71 and 1.78 Ga. Within the Vulcan Structure, a single sample of metabasite in the western part of the structure gives an age of 2.62 Ga, and a sample of hornblende monzonite from the eastern part of the structure shows a similar age of 2.58 Ga.

However, these rock ages do not provide any additional information on the actual age of a possible suture associated with the structure. The Medicine Hat Block appears to be an older section of crust as several metaplutonic gneiss units within it have been dated at 3.27 - 2.65 Ga.

The Wyoming Province can be studied directly in numerous locations due to Sevier and Laramide aged up-thrusts [*e.g.*, Dutch and Nielsen 1990, Frost and Frost 1993] (Fig. 1.3). A broadly similar history has been interpreted for the Archean rocks present in such diverse regions as the Cheyenne Belt in southern Wyoming (interpreted as the suture zone between the Archean Wyoming Province and the Proterozoic Colorado Block to the south) and the Ruby, Madison, Tobacco Root and Little Belt Mountains of southern Montana. Although instrumental in exposing Archean rock at the surface, the tectonic history of the Wyoming Province also has made indirect geophysical observations of the Wyoming crust difficult due to the effects of deep basins interspersed with dramatic uplifts in the upper 10 km of the crust. Zircons recovered from several gneiss units show that at 3.8 Ga the Wyoming Province contains fragments of some of the oldest crust on earth. It is interpreted to be composed predominantly of small micro-continental fragments that were intruded by Late Archean crustally-derived granites and granodiorites and was largely stabilised by 2.7-2.6 Ga [Frost and Frost 1993]. Unlike other Archean provinces such as the Superior Province of east-central Canada, the Wyoming Province does not contain significant amounts of metavolcanic rocks (greenstone belts of possible island arc origin) and there is no evidence of closed ocean basins between various units internal to the province.

Due to the Phanerozoic sedimentary cover, the relationship between the Hearne and Wyoming provinces is enigmatic, and as such is one of the major foci of this thesis. In view of the Archean ages of basement core samples recovered in this region, the Wyoming - Hearne system could have been established prior to the construction of Laurentia [Hoffman 1988]. However, the two significant east-west-oriented potential-field features, the Vulcan Structure and the Great

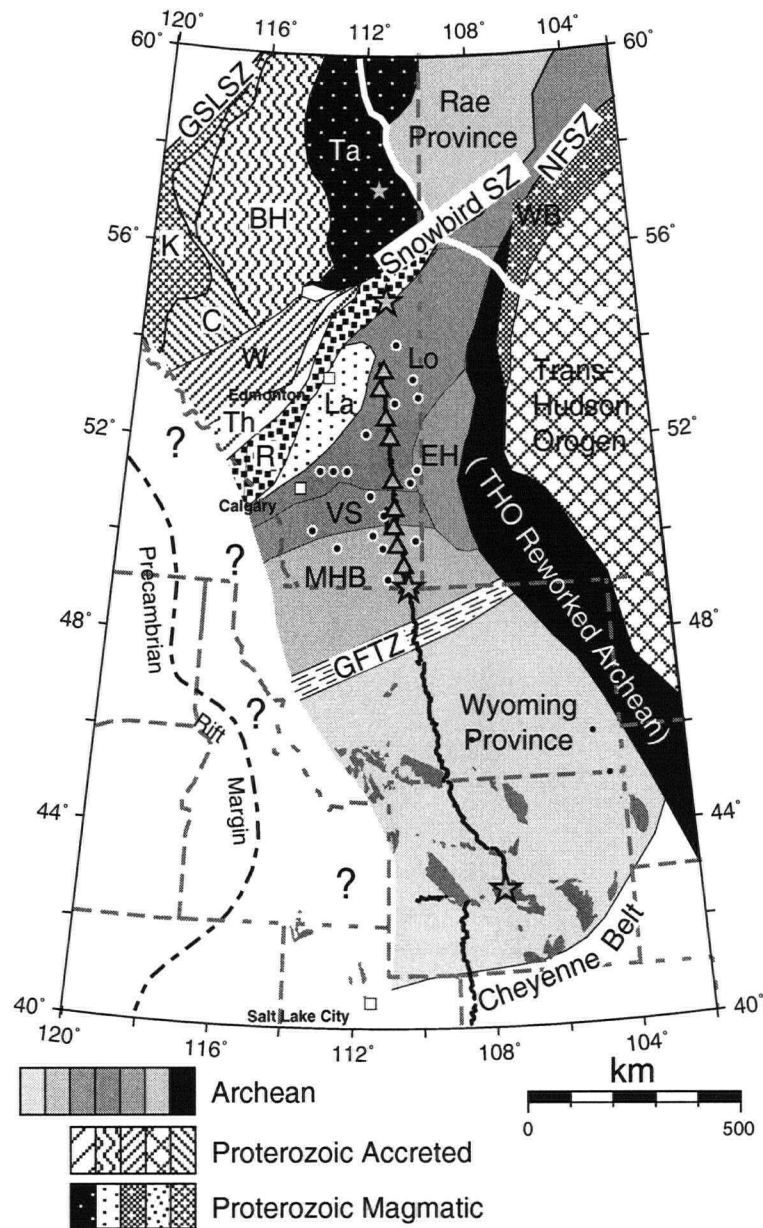


Figure 1.3: Basement domains interpreted from figure 2 [after Ross *et al.* 1999 and Baird *et al.* 1996]. Black dots overlapping to form a line denote positions of seismograph stations occupied for Deep Probe and SAREX. Deep Probe (stars) and SAREX (triangles) shot points are indicated. Labelled domains: BH - Buffalo Head, C - Chinchaga Magnetic Low, EH - Eye Hill High, GFTZ - Great Falls Tectonic Zone, GSLSZ - Great Slave Lake Shear Zone, K - Ksituan Arc, La - Lacombe Domain, Lo - Loverna Block, MHB - Medicine Hat Block, NFSZ - Needle Falls Shear Zone, R - Rimbey Arc, Ta - Taltson Magnetic Low, Th - Thorsby Magnet Low, W - Wabamun Domain, WB - Wathaman Batholith. Hearne Province is composed (in part) of domains labelled Lo, EH, VS and MHB. Archean core sample locations (Alberta only) shown as white circles [Ross *et al.* 1991]. Wyoming Province Archean outcrop shown in dark grey [Houston *et al.* 1993]. Approximate location of Precambrian rift margin dashed on west side of region [Burchfiel and Davis 1975]. Southwestern edge of Canadian Shield indicated by white line in north east.

Falls Tectonic Zone, combined with geochronological dating of the various basement blocks, suggest somewhat different histories for the Hearne and Wyoming provinces for most, if not all, of the Archean. Important in the context of this thesis, geological evidence does not preclude the Medicine Hat Block being a small independent Archean cratonic fragment of its own. Regardless of the location of possible sutures, the Wyoming - Hearne system must have been established by the Paleoproterozoic, prior to subsequent tectonism to the east and west. As an added complication, analyses of xenoliths recovered in the MHB suggest a Paleoproterozoic age (1.78-1.69 Ga) for the lower crust (crystallisation depths between 35 and 40 km). This implies that the deepest parts of these Archean blocks have been either thickened in some way by the addition of younger crustal material or modified by Paleoproterozoic processes. A combination of reworking of older material and addition of new material is also possible [Ross and Davis 2000].

The Vulcan Structure [Eaton *et al.* 1999], named for an Albertan town lying above it, is a WSW – ENE trending crustal feature evident on Bouguer gravity maps as two parallel gravity anomalies: a southern low anomaly, previously referred to as the Vulcan Low and a northern high anomaly, the Matsewin High [Ross *et al.* 1989]. In the past, the feature had been interpreted as a Precambrian ‘rift’ based on seismic reflection, refraction and gravity data [Kanasewich *et al.* 1969]. However, southward dipping reflections on seismic refraction and reflection data more appropriately may indicate northward thrusting of the Medicine Hat Block onto the Hearne Province [Hoffman 1988]. High-resolution seismic reflection data from the Southern Alberta Lithospheric Transect (SALT) experiment in 1995 [Eaton *et al.* 1999, Lemieux *et al.* 2000] are adding to our knowledge of the complexities of the crust in the vicinity of the Vulcan Low and Medicine Hat Block. Movement in the vicinity of the Vulcan Structure appears to have occurred as recently as the Paleocene, and its relationship to features in the North American Cordillera also has been postulated [Price 1996]. For example, the Mesozoic - Cenozoic-aged Crowsnest Pass cross-strike discontinuity, a major tectonic feature in the Eastern Cordillera in the vicinity of the Canada - US

border, is on strike with, and appears to be related to the Vulcan Structure.

The Great Falls Tectonic Zone, lying along the southern edge of the MHB, has commonly been interpreted to be a Proterozoic suture zone between the Hearne and Wyoming provinces. Recent magnetotelluric work has suggested that this is not the case, because Proterozoic (and younger) continental suture zones should preserve conductivity anomalies in the upper crust indicative of continental shelf deposits after the development of an oxygen-rich atmosphere on Earth [Boerner *et al.* 1998]. Such a conductor, representing the top of a planar slab of subducted metasedimentary rock, is not present in the upper crust of this region. There is, however, a deep conductor lying at a depth of about 20 km in the GFTZ. The preferred interpretation by Boerner *et al.* [1996] is that the GFTZ is an Archean suture zone (which would not require a shallow conductivity anomaly) and the deep conductivity feature is indicative of an intracratonic shear zone which has been recurrently active through the Proterozoic and Phanerozoic.

Numerous Phanerozoic plutons are present in the mountains of central Montana and deep crustal and upper mantle xenoliths are relatively abundant in them. Studies of these xenoliths, most of which are found in Eocene minette dykes, show a long and episodic history of crustal scale tectonics in the region of the GFTZ [Carlson and Irving 1994]. Plutonic rocks in the southwestern part of the GFTZ have been examined in detail where they are seen in outcrop in the eastern Cordillera in Montana and Idaho [O'Neill and Lopez 1985]. However, the regional interpretation of the continuation of these features to the northeast into Saskatchewan has not been confirmed by more recent interpretations of the western margin of the Trans-Hudson Orogen [Baird *et al.* 1996].

To the east of the Archean provinces lies the 500-km-wide Paleoproterozoic Trans-Hudson Orogen which separates them from the Superior Province. The Trans-Hudson Orogen is the remnant of a closed global-scale ocean and is the best exposed and preserved suture of the various Paleoproterozoic orogens that stitched together the Precambrian craton of North America [Hoffman

1989]. Recent co-ordinated investigations across the northern extent of the Trans-Hudson Orogen in Saskatchewan and Manitoba by Canada's National Geoscience Mapping Program (NATMAP) [Lucas *et al.* 1999] and seismic work by *LITHOPROBE* [*e.g.*, Lucas *et al.* 1994, Hajnal *et al.* 1997] combined with seismic investigations by the Consortium for Continental Reflection Profiling (COCORP) to the south across Montana and the Dakotas [*e.g.*, Baird *et al.* 1996] have shed light on the nature of the orogen and its relationship with the Hearne and Wyoming cratons. Along the western side of the orogen, it appears that the Trans-Hudson region has underthrust the Hearne and Wyoming provinces to the west. This is evidenced by the continental arc-related rocks along the eastern edge of the Hearne Province in the Canadian Shield and also by seismic reflection and refraction images from *LITHOPROBE* and COCORP data [Baird *et al.* 1996]. The boundary between the Medicine Hat Block and the Trans-Hudson Orogen is not delineated clearly by either seismic or potential field data.

To the south of the Archean Wyoming Province lie the Paleoproterozoic Yavapai and Mazatzal provinces of the southwestern U.S. During the Paleoproterozoic, a rift margin formed along the southern margin of the Wyoming Province, roughly parallel to and coincident with the present location of the Cheyenne belt. The margin subsequently collapsed and the Proterozoic terranes of southwestern North America were accreted to the continent from 2.0-1.3 Ga as a series of island arc collisions with the southwestern edge of Laurentia [Karlstrom and Houston 1984].

To the west, the Archean and Proterozoic basement abuts the accreted terranes of the North American Cordillera. The interpretation of the basement in this region is complicated by the overlying Cordillera and numerous episodes of tectonism related to the accretion of terranes, but the prevailing theory is that the western edge of Laurentia was rifted over an extended period of time in the Proterozoic [O'Neill and Lopez 1985]. This rifting established a passive continental margin and enabled the deposition of the Paleo- to Mesoproterozoic Belt Purcell and Neoproterozoic Windemere metasediments, with thicknesses up to 20 km [Burchfiel and Davis 1975, Ross 1991].

During the formation of the North American Cordillera, the western margin of North America was exposed to four major periods of orogenic activity during the Phanerozoic: Antler (Devonian - Mississippian), Sonoma (Permian - early Triassic), Sevier (Jurassic - Cretaceous) and Laramide (Late Cretaceous - mid Eocene) orogenies [Burchfiel *et al.* 1992]. However, only Laramide tectonism extended far enough east to affect the crust along the Deep Probe corridor. The Laramide event has surface expression along the profile from northern New Mexico to southern Montana, where it is characterised by deeply rooted basement uplifts and sedimentary basins as thick as 10 km throughout the Proterozoic terranes and the southern Wyoming Province. Later in the Tertiary, the southernmost part of the Deep Probe profile and regions to the east were deformed by extension associated with the formation of Basin and Range province and the Rio Grande Rift.

1.3 The Seismic Method

Seismology is the study of seismic waves and how they travel through the Earth. The discipline can be generally divided into two fields categorised by the type of energy source. Earthquake seismology is the study of seismic waves emanating from naturally occurring earthquakes; controlled-source seismology utilises seismic waves created by man at the surface of the Earth (*e.g.*, chemical explosions or mechanical devices). The Deep Probe experiment is a controlled source refraction / wide-angle reflection experiment. As will become clear shortly, it has several characteristics which make it comparable to earthquake-sourced studies including the large size of its sources, the distances to which energy was recorded and the techniques that were used to interpret the data.

The manner in which seismic waves radiate outward from a source location is governed by the wave equation (1.1), the fundamental mathematical concept in seismology which relates the

spatial and time dependence of a disturbance propagating as a wave.

$$\nabla^2\psi = \frac{1}{V^2} \frac{\partial^2\psi}{\partial t^2} \quad (1.1)$$

ψ represents some measure proportional to the displacement of the wave as a function of position and time. V represents the wave's velocity as a function of position (and sometimes time).

As a wave propagates away from the source position, its velocity is affected by the media through which it travels. Changes in velocity will cause the wave to refract and reflect. In studies of the crust and upper mantle using the refraction / wide-angle reflection method (in contrast to the near-vertical incidence multichannel reflection method), specific combinations of refractions and reflections which return to the surface and are recorded by seismographs are referred to as *phases*. Some of the more significant phases include: (i) waves which propagate by refraction through the crust (P_g); (ii) waves which refract through the crust, reflect off the crust-mantle boundary, and refract back through the crust to the Earth's surface ($P_m P$); and (iii) waves which refract through the crust, the uppermost mantle and back through the crust (P_n) (Fig. 1.4a). For analysis and display, waves are often reparameterised as rays, which represent points on an advancing wavefront.

The arrival of seismic energy at the Earth surface is displayed on a graph with distance from the source (offset distance) on the horizontal axis and time after the seismic event on the vertical axis. Instead of actual time, data are often displayed as a function of "reduced time", t_r ,

$$t_r = t - \frac{x}{v_r} \quad (1.2)$$

where time, t , is reduced by the ratio of offset distance, x , to some convenient reduction velocity, v_r . What this does is to place phases that have a slope nearly equal to the reciprocal of v_r as nearly horizontal on the time-distance plot (Fig. 1.4b). This procedure reduces the size of plots necessary for displaying the data and assists in interpretation.

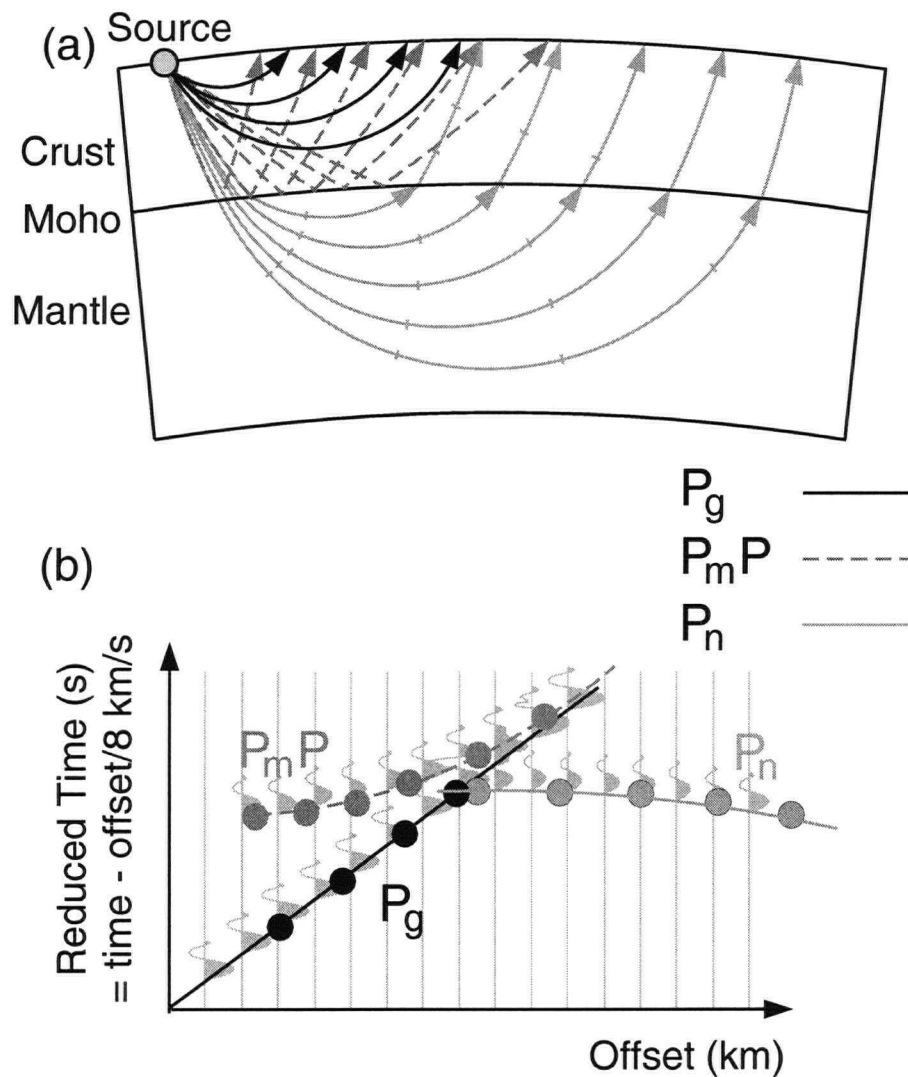


Figure 1.4: Introductory ray diagram and time-distance plot. (a) Ray diagram. Three major phases are traced: P_g - crustal refractions (black), P_mP - Moho reflections (dashed dark grey), P_n - upper mantle refractions (light grey). Wave fronts are indicated by ticks on the P_n rays. (b) Time-distance plot overlaid on stylised synthetic seismogram. Arrival times for each ray in (a) are indicated by dots.

Modern crustal refraction studies make use of such tools as multiple shots, dense receiver arrays and reciprocal ray paths in order to produce 2-D (and in some cases 3-D) interpretations of velocity structure.

1.4 Previous Studies

1.4.1 Southern Alberta and Montana - Crustal Studies

Regional refraction studies in Montana, Wyoming and the Dakotas [McCamy and Meyer 1964], and southern British Columbia, Alberta and Saskatchewan [Chandra and Cumming 1972], were among the first in North America to use the seismic refraction method to evaluate the structure of the crust. Both experiments were characterised by shot spacings of several hundred kilometres and sparse receiver coverage, but nevertheless were successful in determining average crustal velocity profiles for the regions in which they were acquired. In southern Alberta, a series of refraction and reflection studies by University of Alberta researchers [*e.g.*, Kanasewich and Cumming 1965, Clowes *et al.* 1968, Kanasewich 1968, Kanasewich *et al.* 1969] made the first detailed observations of deep crustal and Moho structure in the region of the Medicine Hat Block. This work led to the currently refuted hypothesis of Precambrian rifting as a mechanism for the interpreted structure.

More recently, regional crustal scale seismic studies have been carried out by both COCORP and *LITHOPROBE* in the vicinity of the MHB. However, many questions about the nature of the crust remain unanswered. COCORP's seismic reflection profiles across northern Montana and North Dakota, recorded in 1990, contributed much to the interpretation of the suture zone between the Wyoming Province and Trans-Hudson Orogen [Baird *et al.* 1996], but they run obliquely to the edge of the MHB and do not contribute significantly to our understanding of the relationship between the orogen and the MHB. *LITHOPROBE* has undertaken several exploration efforts in recent years, including the Southern Alberta Lithosphere Transect (SALT) [Eaton and Ross 1996], an extensive near-vertical incidence seismic reflection experiment, and the Southern Alberta Refraction Experiment (SAREX) [Gorman *et al.* 1996], which coincided with the acquisition of Deep Probe. These studies are especially useful in providing detailed crustal information which

can be used in initial velocity structural models for the Deep Probe data.

1.4.2 Upper Mantle Studies

Three general techniques have predominated in recent studies of the upper mantle: petrological studies, quantitative numerical modelling of mantle dynamics, and seismology. Many of these studies have focussed on the mantle transition zone, a seismically identifiable region in the mantle bounded above by the so-called '410-km discontinuity' and below by the '660-km discontinuity', boundaries which correspond petrophysically to depths expected for phase changes of olivine brought about by increasing pressures and temperatures with depth. However, the Deep Probe experiment was unsuccessful in obtaining clearly interpretable data from these depths, so the discussion of upper mantle studies in this section will be limited to those with significance for the upper 150 to 200 km of the mantle.

Petrology

Petrological studies of the uppermost mantle can be divided into two groups: the study of xenoliths brought up from mantle depths by igneous processes and petrophysical laboratory modelling. The latter method has been used extensively to investigate the effects of petrophysical phase changes of mantle constituent minerals brought about by increases in pressure. On a global scale, the uppermost mantle can be considered to have a relatively consistent peridotitic chemical composition [Ita and Stixrude 1992], in which the dominant minerals are olivine (~60%), clinopyroxene (~16%), garnet (~14%) and orthopyroxene (~8%). For pressures corresponding to the upper 200 km of the mantle, olivine is predicted to be stable, but at these depths some garnets, pyroxenes and other trace minerals may undergo various phase changes which will have an effect on elastic properties. If these changes occur over short intervals of temperature and pressure,

then they can be expected to result in velocity contrasts which will be observable to the seismic method.

Contrasting the peridotite generalization for the mineralogy of the uppermost mantle are xenolith studies [*e.g.*, Kopylova *et al.* 1998] which show evidence for a variety of rock assemblages in the sub-crustal lithosphere. For example, in the Slave Province of the Northwest Territories and Nunavut, approximately one quarter of the upper-mantle xenoliths brought to the surface from depths as great as 190 km are eclogite, which suggests that the deep lithospheric peridotites have been invaded by lenses of metamorphosed rock which originated as oceanic-crust [Kopylova *et al.* 1999]. In this case, depending on the size and distribution of eclogitic bodies within the peridotitic host, the seismic method may be able to observe such a bi-modal assemblage of rock types. This is supported by studies of eclogite facies shear zones in outcrop. Analysis of such rocks in the Norwegian Bergen arcs identify the P-wave velocity of the eclogites to be 0.8 to 1.0 km/s greater than their host granulite-facies protoliths.

While not directly observable in the Deep Probe data, the petrophysical characteristics of the previously mentioned 410- and 660-km discontinuities of the upper mantle transition zone are important for how they relate to the overlying uppermost mantle. Although the transition zone has at times been modelled as the chemical boundary between an upper peridotitic mantle and a lower chondritic mantle [*e.g.*, Anderson and Bass 1986], many now consider the entire mantle to be peridotitic with the transition zone caused by petrophysical phase changes in the dominant mineral, olivine [Ita and Stixrude 1992]. Laboratory measurements show that olivine should pass through three phase changes in the temperature-pressure regimes present in the mantle. The 410-km discontinuity corresponds to the depth-pressure regime where α -phase olivine converts to its β - or spinel-phase; the 660-km discontinuity corresponds to the regime where the γ -phase olivine converts to magnesiowüstite and perovskite. These two phase changes are predicted to occur over relatively limited depth intervals and the nature of the transitions is currently the subject of much

petrophysical work [e.g., Wood *et al.* 1996]. The β - to γ -phase change is predicted to occur over a wider interval and with less change in density and velocity, which explains why it is not generally inferred from seismological studies. Although the nature and characteristics of the mantle transition zone are dominated by the properties of olivine, other minerals, the presence of water, or partial melts could significantly affect observed geophysical properties.

Numerical Modelling

Quantitative analysis of fluid dynamics or material flow in the mantle has been undertaken primarily to investigate the question of whether the mantle convects within layers (e.g., above and below the mantle transition zone) or within the entire mantle. If it convects in layers, are there any mechanisms for material to be transported from one layer to another [Peltier and Solheim 1992]? For the uppermost mantle, understanding these mechanisms is vital for interpreting the structures observed there. For example, does the material from a subducting slab remain in the uppermost mantle or can it pass through the mantle transition zone? Do processes exist which would permit upwelling mantle material to be added to the bottom of existing continental crustal blocks?

One significant factor in the quantitative analysis of the mantle is the effect of the temperature-pressure relationship, or Clapeyron slope, on the 410- and 660-km discontinuities [Bina and Helffrich 1994]. The α - to β -phase change for olivine, which is associated with the 410-km discontinuity, is exothermic; the Clapeyron slope is positive. This means that in a cooler temperature regime, the pressure required for the phase change to occur is not as great. As a result, in a cool upper mantle, the 410-km discontinuity will be shallower. The reverse is the case at the 660-km discontinuity for the γ -phase olivine phase change to magnesiowüstite and perovskite. In this case the change is endothermic and the Clapeyron slope is correspondingly negative. In a

cooler temperature regime, the pressure needed for the phase change to occur is greater. Therefore, in a cool upper mantle, the 660-km discontinuity will be deeper than normal. These properties have added significance when considering the motion of material (*e.g.*, cool subducting slabs) across the discontinuities. For example, how does the required phase change affect flow?

The nature of material flow in the uppermost mantle has been characterised by recent numerical modelling analyses including: the development of subduction during the collision of oceanic and continental plates [*e.g.*, Beaumont *et al.* 1994]; the subsidence of continental interiors as a result of mantle flow [*e.g.*, Pysklywec and Mitrovica 1998, Pysklywec and Quintas 2000]; and deep lithospheric deformation brought on by the development of a gravitationally unstable lithosphere during orogenic events [Pysklywec *et al.* 2000]. One of the most interesting results of these models is the effect that the mantle transition zone has on material flow. At the 410-km discontinuity, flow velocity can increase while the reverse is true at the 660-km discontinuity. Ponding of material at the lower discontinuity provides a likely target for the seismic method to investigate.

Earthquake Seismology

Several types of earthquake studies have been used to study and map the upper mantle. These techniques are able to resolve bulk contrasts in elastic properties (*e.g.*, the Moho, 410- and 660-km discontinuities) but they are often limited in their ability to image subtle velocity structures in the uppermost mantle. This section outlines some of the earthquake studies that have been undertaken to: (i) examine the distribution and physical properties of specific features within the upper mantle, such as the upper mantle discontinuities and subducting slabs, (ii) map the velocity structure and discontinuities of the upper mantle on a global scale, and (iii) study the velocity structure of specific tectonic regions of the upper mantle.

Earthquake seismograms record the presence of the upper mantle discontinuities in a variety of ways. Mid-distance earthquake seismograms show distinct $P_{410}P$ and $P_{660}P$ reflections preceding the P_n phase at offset distances beyond 18° . These reflections can also be identified as arrivals within the coda of seismograms with nearer offsets [e.g., Neele 1996]. However, teleseismic receiver-function studies (which will be discussed in more detail later in this section) provide the most widely used and best-resolving means for studying the upper-mantle discontinuities as the 410- and 660-km discontinuities are globally seen to cause a Ps conversion [e.g., Vinnik 1977, Gurrola *et al.* 1994]. Other, more indirect, phases can also be used to examine the mantle transition zone. For example, the transition zone can be clearly identified by precursors to PKPPKP (P'P') [Benz and Vidale 1993]. In these observations, the 660-km discontinuity seems to be a global one, while the 410-km discontinuity appears to be regional. However, this may be the result of a frequency dependence in the observation of the 410-km discontinuity because the P'P' precursor studies have only utilised seismograms recorded by long period instruments.

The seismogenic nature of active subduction zones has enabled the development of unique methods to interpret their sub-crustal extent. Earthquakes from the Wadati-Benioff zones (the region of earthquake hypocentres within a subduction zone) of numerous subduction zones have been recorded and evaluated; the seismogenic region has been shown to extend to depths as great as the 660-km discontinuity. In addition to seismic studies conducted in the vicinity of a subduction zone, the structure of the subducting slab and how it traverses the mantle transition zone can be evaluated by teleseismic studies. For example, secondary phases recorded from deep events within a Wadati-Benioff zone which travel up from the source, reflect off boundaries in the uppermost mantle and then travel a very similar path to the primary phase (e.g., pP or $p_{410}P$) [Vidale and Benz 1992] can be utilised to interpret the velocity structure of the lithosphere overlying the subduction zone.

The velocity structure of the mantle has been mapped on a global scale using a variety of

teleseismic inversion schemes. For example, Su *et al.* [1994] developed a global S-wave velocity structure for the mantle by inverting travel time and waveform information from several mantle phases (*e.g.*, S, SS, ScS) and their residuals (SS-S and ScS-S). Others have used different combinations of phases, with both shear and compressional components, to invert for velocity structure [*e.g.*, Zhou 1996, Grand *et al.* 1997]. Continental-scale tomographic models have been developed using denser arrays [*e.g.*, Grand 1994, van der Lee and Nolet 1997].

Mapping the depths of the 410- and 660-km discontinuities has also been the subject of much attention. On a global scale, precursors to the teleseismic SS phase have been used to map the 660-km discontinuity [Shearer and Masters 1992]. On a regional scale, numerous studies using a variety of methods (as discussed earlier) have been conducted to map both the 410- and 660-km discontinuities. These are often combined with investigations of the nature of the phase boundaries. The results are not always conclusive. For example, a sharp 410-km discontinuity is predicted under the southwestern USA by Neele [1996] while a similar study in the same area [Melbourne *et al.* 1995] predicts a transitional layer instead of a discrete discontinuity. In local studies, the effects of the phase changes of other minerals such as garnet, the introduction of non-peridotitic rocks, the presence of water or occurrences of partial melts all can affect the seismic observations.

Teleseismic receiver function studies have made significant contributions to the study of the upper mantle. Ps converted phases observed in these analyses are the result of steeply propagating P-waves which convert to S at a discontinuity in shear velocity. As discussed earlier, these phases are instrumental in mapping the depths of the upper mantle discontinuities, but the receiver functions also are successfully used to map the velocity structure of the mantle above the 410-km discontinuity. Most of these lithospheric mantle studies have been located in the vicinity of active subduction zones such as Cascadia [*e.g.*, Crosson and Owens 1987, Cassidy and Ellis 1993,

Cassidy *et al.* 1998]. Other studies have looked at the velocity structure beneath permanent seismograph stations distributed over very large areas, such as the Canadian National Seismograph Network [Cassidy 1995]. Recent work has expanded on the traditional teleseismic receiver function analysis by utilising transverse component seismograms to reveal a well-developed anisotropic stratification in the uppermost mantle beneath the Slave Province of northwestern Canada [Bostock 1997, 1998]. The depths at which this layering is observed correspond to depths that should be imaged well by the Deep Probe experiment. In fact, the comparison of these teleseismic results with recent seismic reflection [Cook *et al.* 1998, 1999] and R/WAR [Fernandez Viejo *et al.* 1999] analyses in the same region show remarkable agreement.

Regional inversions of teleseismic data using relatively dense seismograph networks have also been the subject of recent work. For example, the inversion code of VanDecar [1991] has been used to develop regional interpretations of the upper mantle velocity structure in the Yukon Territory [Frederiksen *et al.* 1998] and central Saskatchewan [Bank *et al.* 1998]. Similar studies are currently underway which are targeting the lithosphere beneath the Slave Province [Bank, pers. comm. 2000], southern Alberta [Shragge, pers. comm. 2000] and the Cheyenne Belt in southern Wyoming [Dueker, pers. comm. 2000], the last two of which will be complementary to the results of this thesis.

Controlled-source Seismology

The large-scale Project Early Rise [Iyer *et al.* 1969] was one of the first civilian attempts to examine the velocity structure of the upper mantle using controlled sources. The experiment mimicked the source-receiver geometries of teleseismic studies by detonating large charges in Lake Superior and recording them continent-wide along profiles radiating from the source point. The results included numerous 1-D interpretations of velocity structure from most of the geological regions of North America.

From 1971 to 1990, Russian scientists carried out a series of lithospheric-scale seismic studies in northern Eurasia using both Peaceful Nuclear Explosions (PNEs) and large chemical explosives as sources [e.g., Egorkin and Pavlenkova 1981, Egorkin and Chernyshov 1983, Pavlenkova and Egorkin 1983, Egorkin *et al.* 1987]. Due to the release of the analogue data from these experiments by the Russians and the subsequent application of modern digitisation and analysis techniques, data and results from the experiments are currently being published in the western literature [e.g., Ryberg *et al.* 1995, Pavlenkova *et al.* 1996, Nielsen *et al.* 1999]. These experiments clearly record the upper mantle refracted phase (P_n), the 'teleseismic P_n ' phase and their associated codas to beyond 2500 km. In addition, PNE experiments such as Quartz [Tittgemeyer *et al.* 1996] successfully recorded reflected and refracted energy from the mantle transition zone. Similar results were not forthcoming from Deep Probe; however, the experiment did successfully record information on the upper mantle that matches or surpasses the PNE data in quality due to the close spacing of receivers.

Several hypotheses as to the cause of the teleseismic P_n phase and the P_n coda have been proposed [e.g., Tittgemeyer *et al.* 1996, Morozov *et al.* 1998] and will be discussed in Chapter 6. Most conclude that for the P_n to be such an efficient guided wave, it must involve some form of scattering from heterogeneities in the uppermost mantle [e.g., Perchuć and Thybo 1996]. One-dimensional forward modelling using reflectivity and ray theoretical seismograms has been used to successfully reproduce some of the characteristics of the coda and teleseismic P_n .

Numerous lithosphere-scale R/WAR surveys utilising conventional explosive sources have been undertaken in the last two decades. These include several experiments in Scandinavia which targeted the Baltic Shield and its margins: FENNOLORA [Guggisberg and Berthelsen 1987], EUGENO-S [EUGENO-S Working Group 1988] and BABEL [BABEL Working Group 1990,

1993], and several in Canada associated with *LITHOPROBE*: THORE in the Trans-Hudson Orogen Transect [Hajnal *et al.* 1997], and SNORE in the Slave and Northern Cordilleran Lithospheric Evolution Transect [Fernandez Viejo *et al.* 1999]. All of the aforementioned experiments recorded the teleseismic P_n phase and its associated coda which confirms that these features are generated beneath at least three very different cratonic regions of the Earth. Other experiments have interpreted similar features beneath the southwestern European margin and the south Atlantic Ocean [Pavlenkova 1996] suggesting that the phenomenon is not restricted to continents. Interpretations of older R/WAR data sets are limited by the surface sampling interval (often 10's of km), but the more recent *LITHOPROBE* surveys, Deep Probe, and currently unpublished European lithospheric studies benefit from a station spacing in the order of kilometres. This enables the more subtle waveform characteristics of the upper-mantle phases to be utilised in the interpretation.

Widespread evidence of inhomogeneity in the uppermost mantle (defined in this thesis to be the region of the mantle above the mantle transition zone) adds complexity to the classical lithosphere-asthenosphere model. Two extreme models for the structure of the uppermost mantle are developing. One proposes stratification with alternating weak and rigid layers [*e.g.*, Tittgemeyer *et al.* 1996]. The other proposes patchy inhomogeneity, perhaps caused by partial melting or by inclusions of contrasting rocks [*e.g.*, Ryberg *et al.* 1996]. A more likely scenario is to consider a combination of these two end-member models [Fig. 1.5; Perchuc and Thybo 1996, Pavlenkova 1996]. These hybrid interpretations lend credence to the interpretation of additional discontinuities in the uppermost mantle. For example, evidence is growing for the so-called 8° discontinuity (at a depth of approximately 100 km) and Lehmann discontinuity (at a depth of approximately 150 km) as representing bounds of a globally-present layer of heterogeneity within the upper mantle [Thybo and Perchuc 1997]. The Deep Probe data set enables the development of interpretive models which further evaluate structures within this region of the upper mantle.

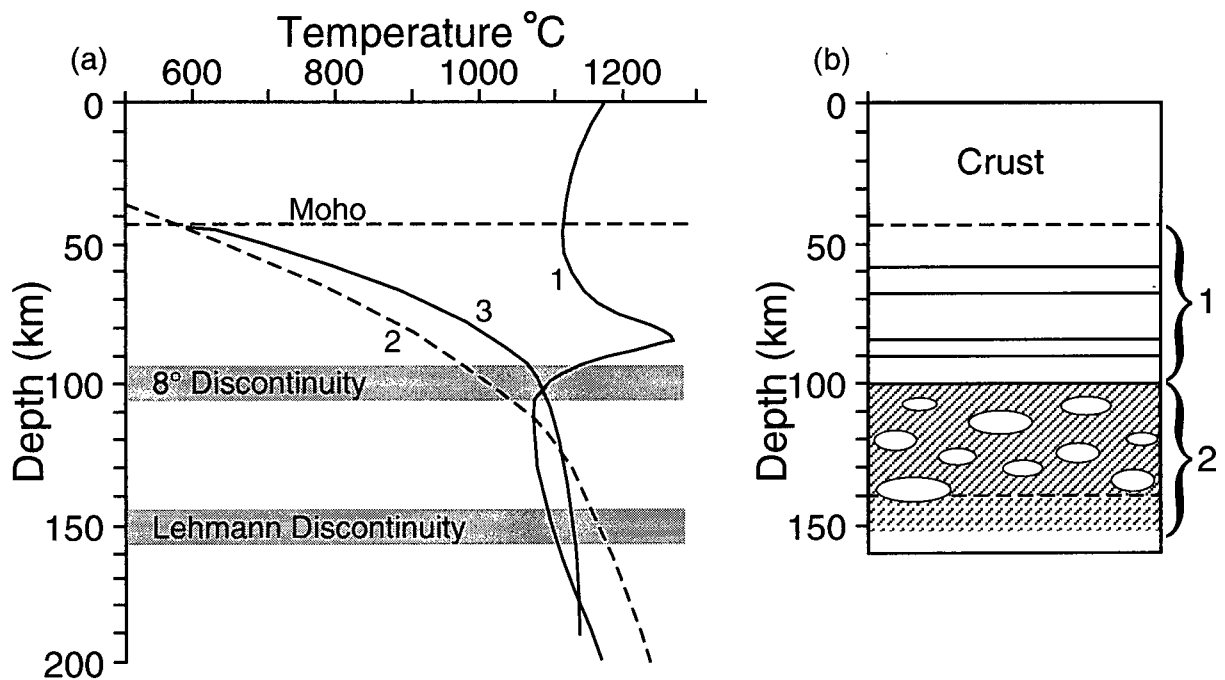


Figure 1.5: Geothermal and solidus curves for the lithosphere as related to a simplified model of the lower lithosphere beneath the Baltic Shield. (a) Geothermal and solidus curves: (1) solidus curve for carbonatitic and kimberlitic magmas, (2) expected average shield geotherm, (3) proposed geotherm for the Baltic Shield which explains the low velocity, strong reflectivity and strong attenuation of the lower interval by separate bodies with kimberlitic or carbonatitic partial melt. (b) A simplified cartoon of the lower lithosphere beneath the Baltic Shield. (1) Layered uppermost mantle. (2) Partial melt in layer between 100 and 150 km [after Perchuc and Thybo 1996].

Chapter 2

The Deep Probe Seismic Refraction Experiment

Energy rightly applied and directed can accomplish anything.

– Nellie Bly (1922).

In July and August 1995, *LITHOPROBE*, in conjunction with other university and governmental institutions carried out the complementary SAREX and Deep Probe seismic refraction / wide-angle reflection (R/WAR) experiments to gather information on the structure of the crust and upper mantle of western North America.

SAREX was a crustal-scale R/WAR survey centred on the Medicine Hat Block in southern Alberta. Ten source points ranging in size from 800 to 2400 kg of explosives (see Table 2.1, page 31) were positioned evenly along a north-south line from 49°N to ~53°30' N. The shots were recorded by 661 portable seismographs deployed along the line at a 1 km station spacing in Canada and 1.25 km in the United States. The recording line extended 320 km into the USA but no shot points were located there. Some of the data from SAREX are used in this study, but SAREX data are also being interpreted as a project separate from Deep Probe [Clowes *et al.* 2000].

Deep Probe, which is a collaborative effort between scientists and institutions in Canada and the USA, aimed to gather information on the sub-crustal lithosphere from two geographical and tectonic foci: the Archean Medicine Hat Block of southern Alberta and northern Montana and the Proterozoic Colorado Plateau / Southern Rocky Mountains of Wyoming, Colorado and New Mexico. The acquisition and interpretation of data, using similar procedures and containing consistent data quality, provides a unique opportunity to evaluate and compare these very different

regions below the North American continent. Deep Probe involved two deployments of 756 portable seismographs. Five shots ranging in size from 3000 to 25,000 kg and located from 33°N to 61°N were shot into each of the deployments (Table 2.1). The seismographs were deployed along a north-south line from central Alberta to northwestern New Mexico with a station spacing of 1.25 km in the US and 2 km in Canada. This provided source-receiver offsets of up to 3000 km, and focussed the bottoming points of seismic rays at increasing depths beneath the zones of interest.

While earlier refraction studies have covered larger areas [Iyer *et al.* 1969], the SAREX and Deep Probe experiments, taken together, are arguably the largest refraction study ever undertaken in North America. They involved more personnel (>100) and more instruments (756 field seismometers) than any other survey in the past. A total of approximately 126 tonnes of explosives were detonated at 20 shot points that spread out over 3100 km (8% of the Earth's circumference). A location map for the experiments is shown in Figure 1.1 (p. 2).

2.1 Preliminary Field Procedures

In the months preceding the acquisition of the Deep Probe and SAREX refraction data, an immense amount of preliminary work was required. The principal investigators and other necessary personnel met twice, once in Calgary, Alberta (12 April 1995) and again in Salt Lake City, Utah (20 and 21 June 1995) to establish operational and technical plans. The nature and scale of this international experiment required that much of the preparatory and post-experiment work be done separately in Canada and the United States. A report detailing this work has been prepared [Gorman *et al.* 1997]. The pertinent details are included in this chapter.

2.1.1 Initial Source and Receiver Site Selection

The trajectory of Deep Probe and SAREX was initially laid out to cover the main blocks of the Archean Hearne and Wyoming Provinces which underlie the Western Canada Sedimentary Basin and the equivalent sedimentary deposits in the western United States. When the support of the American partners in Deep Probe was established, the trajectory was shifted slightly to the east to avoid the Yellowstone Hot Spot. In addition, the length of the profile was extended to cover more of the southern United States.

The final plan called for three deployments of seismographs, including SAREX, running along a line from Great Slave Lake, Northwest Territories to southwestern New Mexico. The northern half of the Deep Probe line investigates the Archean part of the North American craton, while the southern half examines Proterozoic and younger crust tectonically active in the Phanerozoic.

2.1.2 Final Source and Receiver Site Selection / Permitting of Private Lands

In the autumn of 1994, after a proposed trajectory was established for the Deep Probe line, source point locations were scouted for appropriateness and feasibility. In Canada, most of the scouted locations were located on private land with the exception of three located on military bases (Canadian Forces Bases Suffield and Cold Lake) and one on a federal Ministry of Agriculture research ranch; shots at all locations were detonated in drill holes. In the USA, the three shot point locations consisted of one privately-held active open pit mine where the source was detonated in a pond at the bottom of the mine, one mine on public lands where the source was detonated below water at the base of an abandoned mine shaft, and a small area within a National Forest where the source was detonated in drill holes in a manner similar to the Canadian shots. In the spring of 1995, the final selections of seven shot point locations for Deep Probe and eleven shot point

locations for SAREX were made. The ten Deep Probe shots (three of the seven locations were used for both deployments) are designated by their deployment number (1 or 2) followed by their approximate latitude; SAREX shots are numbered sequentially from south to north (Table 2.1). Landowners of the selected shot points were contacted directly and formal permits were drawn up. Permission for SAREX shot 7 was later rescinded by the landowner due to his fear of damage to the aquifer near the shot point. The permitted sites were surveyed using the same GPS procedure that was used for positioning seismometer stations along the line.

Table 2.1: Summary of shot point information.

Shot Point	Location	Latitude	Longitude	Elevation (m)	Julian Day	Shot Time	Charge Size (kg)
2 August 1995							
SAREX 001	Canada/US Border	49°01'34.20"N	110°25'36.48"W	884	214	6:50:00	2400
SAREX 002	Manyberries	49°26'08.52"N	110°35'17.36"W	1028	214	6:30:00	1000
SAREX 003	Medicine Hat	49°51'31.00"N	110°48'42.88"W	759	214	10:30:00	1600
SAREX 004	CFB Suffield	50°15'00.16"N	110°55'42.24"W	695	214	6:40:00	1000
SAREX 005	CFB Suffield	50°37'14.88"N	110°54'01.84"W	779	214	8:20:00	1000
SAREX 006	Helmsdale	51°11'21.52"N	110°58'04.32"W	778	214	6:20:00	800
SAREX 008	Nose Hill	52°05'01.64"N	111°04'26.80"W	785	214	8:10:00	1000
SAREX 009	Hughenden	52°28'49.44"N	111°13'18.24"W	710	214	10:10:00	1600
SAREX 010	Jarrow	53°05'19.84"N	111°26'33.12"W	680	214	10:00:00	2000
SAREX 011	Chailey	53°28'16.32"N	111°18'33.12"W	571	214	8:00:00	2400
9 August 1995							
DP 133	Tyrone, NM	32°37'56.57"N	108°23'16.1"W	1850	221	11:00:00	16329
DP 143	Riverton, WY	42°43'50.81"N	107°40'02.85"W	1931	221	11:30:00	6804
DP 149	Canada/US Border	49°01'03.84"N	110°25'38.48"W	855	221	7:00:00	2400
DP 155	CFB Cold Lake, AB	54°54'54.91"N	111°14'12.66"W	740	221	7:40:00	5000
DP 157	Fort McKay, AB	57°11'18.65"N	111°33'49.45"W	276	221	7:20:00	10000
17 August 1995							
DP 233	Tyrone, NM	32°37'56.57"N	108°23'16.10"W	1850	229	11:00:00	17237
DP 237	Delores, CO	37°34'36.11"N	108°26'39.31"W	2309	229	7:00:00	3629
DP 243	Riverton, WY	42°43'47.60"N	107°39'55.76"W	1932	229	11:30:00	6804
DP 257	Fort McKay, AB	57°11'32.27"N	111°33'10.30"W	279	229	7:30:00	18000*
DP 261	Pine Point, NT	60°52'53.49"N	114°14'07.94"W	207	229	9:00:00	25000**

(*Actual size of source ~14,000 kg; **actual size of source ~16,000 kg.)

2.1.3 Environmental Permitting

A substantial amount of time was required to obtain all the necessary environment approvals needed for the experiment. Once shot locations were finalised, these positions were submitted for approval to the governments of Alberta, the Northwest Territories and Canada, and to the appropriate agencies in the USA, as required by the laws of both countries. Obtaining approval in

Alberta was especially convoluted due, in part, to the bureaucracy which is entrenched there to deal with petroleum industry exploration. For any future experiments, this procedure should be started more than a year in advance of going to the field. For safety and environmental reasons, numerous restrictions are routinely placed on drilling shot holes. In particular, in southern Alberta a zoologist, Dawn Dickinson, had to be hired to search for endangered prairie species such as the burrowing owl and swift fox in the vicinity of proposed locations. None was found.

In the USA, there were two specific environmental concerns. First, during the selection of shot point 237 in the San Juan National Forest in southwestern Colorado, an archaeological survey was required to ensure that any indigenous American archaeological sites were left untouched. Second, at the Day Loma open pit mine site in Wyoming, it was noted that raptors nested in high walls of nearby abandoned mines. However, no nests were found in the high walls of the pit.

2.1.4 GPS Surveying of Source and Receiver Locations

Starting at the end of May 1995, source and receiver locations were positioned using the Global Positioning System (GPS). The GPS hardware and software package used by both Canadian and American surveyors was the Trimble Pathfinder system. The Canadian system was provided by the Geological Survey of Canada and the American system by IRIS / PASSCAL. Stakes were set up at each receiver location and annotated with the station number. Road logs were constructed so that instrument deploying teams could locate the stations easily from their deployment vehicles.

Using the Trimble Pathfinder system, approximately 40 to 50 stations could be positioned by a single survey team each day. Four to five minutes of GPS readings were recorded at each location (about the time it took to hammer in the stake and update the road log on the field PC). The field GPS unit was a six-channel system running in 3-D mode which means that it required information from four GPS satellites at all times. Readings were recorded every 5 seconds. Each

evening, the measurements were downloaded from the field computer to a PC and backed up on disk. A separate GPS base station provided survey information at known geographic locations so that differential processing could be applied to the data to improve the accuracy of the measurements (see Section 2.3.1). Differential processing resulted in a nominal accuracy for the recorded positions of 5 m horizontally and 10 m vertically. Receiver locations in the 1000 - 2999 range were surveyed by personnel from the University of British Columbia (UBC), 3000 - 4999 by personnel from the University of Texas at El Paso (UTEP) and 5000 - 5999 by personnel from Rice University. The positions of 9000 series stations, used in Deep Probe Deployment 1, correspond to the like-numbered 1000 series stations, used in the SAREX deployment, but lie along the west side of Canadian Forces Base Suffield instead of through the middle of the base (*e.g.*, Station 9382 lies on the west boundary of CFB Suffield where it is projected perpendicular to the Deep Probe profile from station 1382.) The deviation from the profile was required due to active military exercises on the base during Deep Probe Deployment 1. They were also surveyed by personnel from UBC.

2.1.5 Drilling and Loading of Source Locations

Canada - All Shots

The drilling and loading of source positions started well in advance of the arrival of deployment crews in the field. In most cases, holes were drilled to a maximum of 50 m by conventional drill trucks, similar to those that would be used for drilling water wells. Depth depended in part on the amount of explosive that would be inserted into the hole and also on the diameter of the drill used. In most cases 10-inch bits were feasible. PVC piping was used at many locations to case the upper part of the hole to prevent collapse. The low density (1.3 g/cm^3) explosive, Blastex, produced by Dyno-Nobel of Salt Lake City, Utah, was delivered to the site in 20-kg sausage-shaped bags.

These were lowered one by one into the hole until the required charge size was reached. Under optimal conditions, these bags of explosives should all be in contact with each other. They are all linked using Cordtex (40 grains/foot) explosive cord with four or five 1-lb booster charges (Trojan Cast Booster) attached along the length of the explosive. This method for loading the holes was not as successful as it should have been. At several shot points (notably Deep Probe shots 257 and 261) it was determined that there was not complete detonation of all the explosives (see Table 2.1).

Shot Location 33

In the USA, at shot points 133 and 233 in southern New Mexico, ground conditions in the vicinity of the shot point were extremely variable due to differences in fractures and weathering. The ground surface was saturated with water flowing from some of the fractures, and from a number of test wells drilled by the mine. Shot holes were drilled with a diameter of 8 inches to a nominal depth of 150 ft, but locations and final depths were determined by the local conditions. Water was encountered in a number of the wells at inconsistent depths; wells were cased using PVC as required. Shot 133 consisted of 33,000 lbs in 15 holes, and 233 of 38,000 lbs in 17 holes. Following the detonation of the shots, the holes were backfilled for safety.

Shot Location 37

At shot point 237, three 8 inch holes were drilled to a nominal depth of 150 ft. Water was encountered at approximately 30 ft and the upper 20 ft of each hole were cased with steel casing. Holes were drilled in a line perpendicular to the Deep Probe trajectory with a 60 ft spacing. The holes were each loaded with 2700 lbs of emulsion, a slurry of ammonium nitrate and fuel oil. After the shot was detonated, the holes were back filled with drill cuttings and plugged with bentonite.

Shot Location 43

Near Riverton, Montana, a shot was attempted to coincide with the SAREX deployment in Canada and Montana. Although this shot failed to detonate, it was instrumental in the success of shots 143 and 243. For the failed SAREX shot, 50-lb bags of explosive emulsion were packed into larger bags along with explosive boosters and detonating cord. A total of 60 450-lb bags (27,000 lbs total) of explosive were prepared in this way. Each bag was carried by helicopter from the edge of the pit and dropped into the water in a closely-spaced array. The bags sank to the bottom of the pond and detonating cord deployed from each bag to be connected to the trigger on a raft in the pond. Two problems were identified with this method: the expense of the helicopter and the fact that the detonating cord did not deploy properly from all bags. Both of these problems were rectified for shots 143 and 243 in Wyoming. Disappointingly, this first batch of explosive emulsion turned out to be insensitive to the explosive boosters and could not be detonated.

For shot points 143 and 243 a second batch of emulsion was ordered. This time it was delivered in bulk and was pumped directly into the larger bags in which boosters and detonating cord were placed. The bags, containing up to 2500 lbs of emulsion each, were suspended from a large inner tube and loaded in the water. The inner tube and bag were towed to the desired location, the bag was released from the inner tube and the detonating cord was played out from the tow boat. This method was less expensive and faster than the helicopter method. Both shot charges of 15,000 lbs each were loaded in this way. Clean up at the pit consisted of skimming the water for plastic remains of emulsion bags and buoys.

2.2 Data Acquisition

2.2.1 Seismometer Deployment

Six different field instrument systems were used to record SAREX and Deep Probe. They came from a variety of sources and each type had its own idiosyncrasies (these are discussed in section 2.2.3). Each of the deployments of SAREX and Deep Probe required two support locations (headquarters) due to the distances that deployers needed to travel.

In the morning of deployment day, the programmed seismographs were picked up at the headquarters and driven in vans or trucks to their preassigned locations. The procedure for setting up a temporary seismograph station in the field differs depending on the instrument type, but the main steps were:

- locate the survey stake corresponding to the desired station number.
- select a position within a few metres of the stake where the seismograph instrument box can be positioned free from natural and man-made hazards.
- record identification numbers of all instruments left at each station in a field log.
- dig a hole or holes to bury the geophone(s). A depth of at least 50 cm or a location on bedrock is optimal.
- position and level the geophones in the holes and attach them to the instrument box.
- carefully bury the geophones to ensure good coupling with the ground.
- tidy up the site to ensure that it will not be disturbed by animals or people during the period of data collection.

Table 2.2 summarises the deployment of instruments for SAREX and Deep Probe.

Table 2.2: Summary of instruments deployed. (1* - Deployed from Medicine Hat, AB; 2* - Deployed from Montana; 3* - South of the Missouri - even stations only; 4* - skip 5084-5087 and 5113-5115; 5* - skip 5239, 5240, 5276, 5277, 5423, and all even stations above 5405.)

Instrument Type	Number of Instruments	Site # (first)	Site # (last)	Trace # (first)	Trace # (last)	Comments
SAREX						
SGR	186	1030	1215	1	186	
PRS-1	181	1216	1396	187	367	
PRS-4	34	1397	1430	368	401	
RefTek (Can)	120	1431	1550	402	521	1*
RefTek (US)	91	1551	1637	522	612	2*
RefTek (US)	49	1650	1754	613	661	3*
Sum: 661						
Deep Probe Deployment 1						
PRS-1	182	1120	1482	1	182	
PRS-4	34	1484	1550	183	216	
SGR	186	1551	1736	217	402	
RefTek	259	1737	1995	403	661	
PDA's	20	1996	2015	662	681	
SCR	75	2016	2090	682	756	
Sum: 756						
Deep Probe Deployment 2						
SGR	185	1911	2095	1	185	
SCR	16	2096	2111	186	201	
SCR	54	3000	3077	202	255	
RefTek	21	3078	3098	256	276	
SCR	5	3099	3103	277	281	
RefTek	104	3105	3208	282	385	
RefTek	128	5000	5134	386	506	4*
PRS-4	34	5135	5168	507	540	
PRS-1	182	5169	5527	541	722	5*
Sum: 729						

The instruments were deployed either by single deployers or by teams of two people. The number of people required depended on the instrumentation type being used and safety considerations. Most of the stations were located on public rights-of-way or ditches along secondary roads. Between 20 and 40 stations were deployed by each deploying team during the day. All shots were fired during the night in order to minimise cultural noise (cars, trucks, trains, other

human activity). The following morning, the deployers returned to the field to pick up the instruments and return them to the headquarters where the data were collected.

2.2.2 Timing Corrections

Chronometers are an integral part of the field instrumentation used for refraction seismology. Both the seismometers and the shooter boxes contain very accurate clocks that are set using satellite information before they are deployed in the field. However, in the hours that these clocks remain in the field, even small inaccuracies can affect the recorded time. This inaccuracy often is in the order of several milliseconds per day. It is therefore vital that the instruments be returned to the headquarters as quickly as possible to determine drift in the instrument clock and estimate the error that is present in the recordings. This is generally done by assuming a linear drift in the degradation of the timing.

Both shot time corrections and seismograph clock drift must be accounted for in order to have accurate timing information for the data. Both the shot time corrections and the seismograph clock drifts are applied in the SEG-Y headers of the data. In the case of the seismograph clock drifts, this can be done:

- by modifying the start time of the trace to reflect the clock drift.
- by including the clock drift as a defined header word which can be utilised later.

For this experiment, all seismograph clock drifts have been incorporated into the trace start time shown in the headers. The drift time used for each instrument is stored in trace header word *cor* (bytes 217-218). This is for informational purposes only and no further processing is required.

2.2.3 Field Instrumentation

Six different types of seismographs and several types of geophones were used during these experiments. The seismographs, together with the geophones to which they were attached, are briefly described below .

- **PRS-1**

Number Used: 182 Owner: GSC

The Geological Survey of Canada (GSC) in consultation with *LITHOPROBE* seismologists developed these Portable Recording System instruments specifically for use in large-scale refraction surveys. The field unit is programmed by one of several PC's running LithoSEIS software (developed at the GSC) in the field headquarters and then attached to a geophone at the deployment site. For these experiments, L-4 geophones with a natural frequency of 1 Hz from Mark Products were used. The PRS-1 instruments record only one channel (the vertical component) of data in solid state memory. The recorded information is uploaded to the same field PC that programmed it once it is returned to the field instrument centre. The data for all the PRS instruments are then compiled in SEG-Y format and archived on exabyte tapes.

- **PRS-4**

Number Used: 34 Owner: GSC

These instruments extend the abilities of the PRS-1 instruments by including the ability to record three components. For these experiments, one vertical and two horizontal L-4 geophones were used. They also have a triggering ability which enables them to be used in earthquake seismology experiments.

- **RefTek**

Number Used: 260 Owner: IRIS-PASSCAL

These instruments are manufactured by Refraction Technology Inc. (hence the name) and were provided by the Program for Array Seismic Studies of the Continental Lithosphere (PASSCAL) of the Incorporated Research Institutions for Seismology (IRIS). The field units are programmed by a palmtop computer at the HQ and then attached to a three-component geophone at the deployment site. Some of the RefTek units contain GPS receivers and are therefore capable of avoiding clock drift problems. (At the time of the experiment, the software was not yet available which would let the unit calculate an accurate geographic position.) L-28 (with a natural frequency of 4.5 Hz), L-22 and Sprengnether S6000 (both with natural frequencies of 2 Hz) geophones were used. The RefTeks record their data on disk, which enables long recording times. When the instruments were returned to the field headquarters, the information was uploaded to a Sun Sparcstation for compilation processing. Data were archived to exabyte tapes.

- **SGR**

Number Used: 185 Owner: USGS

These Seismic Group Recorders were provided by the United States Geological Survey (USGS). The SGRs were developed by Amoco and built by Globe Universal Sciences, Inc. for regional refraction studies in the Middle East in the 1980's. They have an overall frequency response of 2 to 200 Hz and a theoretical dynamic range of 156 dB. The deployment process is similar to that of the PRS instruments. L-4 (1 Hz) and L-28 (4.5 Hz) geophones from Mark Products were used with these instruments. Data are recorded in digital format on specially designed tape cassettes that are removed from the instrument and read into an Everex System 1800 microcomputer upon return to the field headquarters. The compiled data are archived on 9-track tapes.

- **SCR**

Number Used: 75 Owner: USGS

The United States Geologic Survey also provided the Seismic Cassette Recorder instruments. These were developed in the 1970's for regional exploration work in Siberia. Again, the deployment process is similar to that for the PRS instruments, although more manual work is required in selecting settings on the boxes. The SCR system passes the output from the geophone through three parallel amplifiers, each with a separate manually adjustable attenuation setting. L-4 (1 Hz) and L-28 (4.5 Hz) geophones from Mark Products were also used with these instruments. The data are recorded in FM analogue format on conventional audio cassette tapes. After the experiment, the data were digitised and compiled at the USGS office in Menlo Park, California for further display and processing. They were archived and distributed on exabyte tapes.

- **PDAS**

Number Used: 20 Owner: GFZ-Potsdam

These Portable Data Acquisition System instruments were provided by GeoForschungs-Zentrum (GFZ) Potsdam, Germany. They are manufactured by Teledyne Brown Engineering (formerly Teledyne Geotech) and record in solid state memory and an on additional hard disk. The geophones used by the PDAS instruments were Mark Products L-4C-3D (1 Hz). The clocks in the instruments are TCXO temperature compensated crystal clocks which were synchronised by GPS every four hours. These data were compiled at GFZ-Potsdam and made available via the internet.

2.2.4 Instrument Deployments

SAREX Deployment

The Southern Alberta Refraction Experiment (SAREX) had headquarters in Medicine Hat, Alberta and Billings, Montana. To simplify the procedures involved with crossing the international boundary, deploying teams did not cross the border, (*i.e.*, deploying teams in northern Montana were based in Billings even though they were geographically much closer to Medicine Hat).

Early in the morning of 2 August 1995, the ten SAREX shot points were detonated in southern Alberta (Table 2.1, page 31). These were located at approximately 50 km intervals along the line from the Canada - USA border (49°N) to the North Saskatchewan River ($\sim 53^{\circ}30'N$). All of the shots were successful electronically initiated, chronometer-controlled detonations. Weather conditions on the night of the shot were good, although isolated thunder storms did occur. Personnel from the University of Texas at El Paso (UTEP) attempted three times to detonate a charge at a mine site near Riverton, Montana for recording by the SAREX array. These attempts were unsuccessful due to an insensitive batch of explosives, as mentioned previously.

For the SAREX deployment, instruments were deployed from north of Chailey, Alberta (station 1030) to near Red Lodge, Montana (station 1650). Of the 661 stations deployed, 622 stations were successful in recording data, representing a success rate of 94.1%.

Deep Probe Deployment 1

This first deployment of the Deep Probe experiment used the same headquarters locations as SAREX. However, some of the personnel who had been stationed in Medicine Hat for SAREX moved to Billings for Deployment 1. Only the PRS instruments were deployed north of the Canada - USA border during Deployment 1.

Early in the morning of 9 August 1995, the five Deployment 1 shot points (100 series shots) were detonated (Table 2.1, page 31). Weather conditions in southern Alberta and northern Montana on the night of the shots were quite poor. Wind speeds were very high along several hundred kilometres of the line. The decision to go ahead was made in the hope that the winds would die. Communication with shot point 155 was not possible due to its remote location, so once committed, the decision could not be changed. The increase in wind generated noise is noticeable when compared to the SAREX data.

For Deep Probe Deployment 1, instruments were deployed from near Jarrow, Alberta (station 1120) to just south of the Wind River Indian Reservation in Wyoming (station 2016). Of the 756 stations deployed, 706 stations were successful in recording data, representing a success rate of 93.4%.

Deep Probe Deployment 2

For the second deployment of Deep Probe, the headquarters locations were moved south to Rock Springs, Wyoming and Grand Junction, Colorado. Ground conditions in Wyoming, Colorado and New Mexico in general were much rockier; digging holes to bury geophones was an arduous task. To compensate, two days were set aside for preparing site locations prior to the actual deployment day.

Early in the morning of 17 August 1995, the five Deployment 2 shot points (200 series shots) were detonated (Table 2.1, page 31). Weather conditions along the line for this deployment were generally good. Unfortunately, the two most northerly shot points (257 and 261) had incomplete detonations. Estimates of the quantity of undetonated explosive emulsion were determined at these two shots and this resulted in downgrading shot 257 from 18,000 kg to 14,000 kg and shot 261 from 25,000 kg to 16,000 kg.

For Deep Probe Deployment 2, instruments were deployed from northern Wyoming (station 1911) to northern New Mexico (station 5169). Of the 733 stations deployed, 699 stations were successful in recording data, representing a success rate of 95.4%.

2.2.5 Clean-up

Post survey clean-up was undertaken wherever our activities affected the surrounding countryside. At all shot point locations, except those located in active mines and on military bases, it was a condition of the permit that clean-up be done. This involved filling any resulting holes or craters and removing any debris (such as PVC piping) ejected from the shot hole. In some cases, contractors were hired to perform this reclamation work. At seismograph station locations, geophone holes were refilled and any visible signs of the experiment (*e.g.*, stakes and flagging) were removed.

2.3 Post-Experiment Procedures

2.3.1 Finalisation of Geographical Survey Information

The first step undertaken after returning from the field was to finalise the geographical survey information for all the source and receiver locations used. In most cases, Global Positioning System (GPS) information was used to position field locations (see section 2.1.4). In order to increase the accuracy of the GPS measurements, base stations were recorded at known geographical locations so that differential calculations could be conducted. This resulted in reduced values for the geographical locations that are deemed to be accurate to within 5 m horizontally and 10 m vertically. The data were reduced using the standard North American Datum of 1983 (NAD '83). The reduced data were archived in SEG-P1 format (Appendix 9 of Gorman *et al.*, 1997).

2.3.2 Merging of Seismic Data Sets

Figure 2.1 outlines the major steps that were required to merge data from the five different types of field instruments. This lengthy process is described in detail below.

The major steps in the process were to:

- read the various field tapes into the PLOTSEC environment (see section 2.3.3).
- update and correct the file header information for each instrument type.
- update and correct the trace header information for each trace.
- merge various time windows created due to limitations in the various field instruments and recording formats.
- select an appropriate time window for archiving the data.
- merge the data from each instrument type into a single SEG-Y file.

2.3.3 PLOTSEC

Six different types of seismographs were used in the field, with five slightly different data formats based on the Society of Exploration Geophysicists standard known as SEG-Y. In order to merge the various data sets, John Amor at UBC developed the PLOTSEC suite of FORTRAN programs based on earlier work by Barry Zelt of UBC. This robust set of programs facilitates reading, modifying and merging various input data sets into a single, standardised SEG-Y format data set for each shot point.

The data are read into the system using a routine called `plotsec_rseg.y`. One of the features of this routine is the ability to resample the input data using a cubic spline algorithm. A common sample interval of 8 ms was selected. This affected the data from the following instruments.

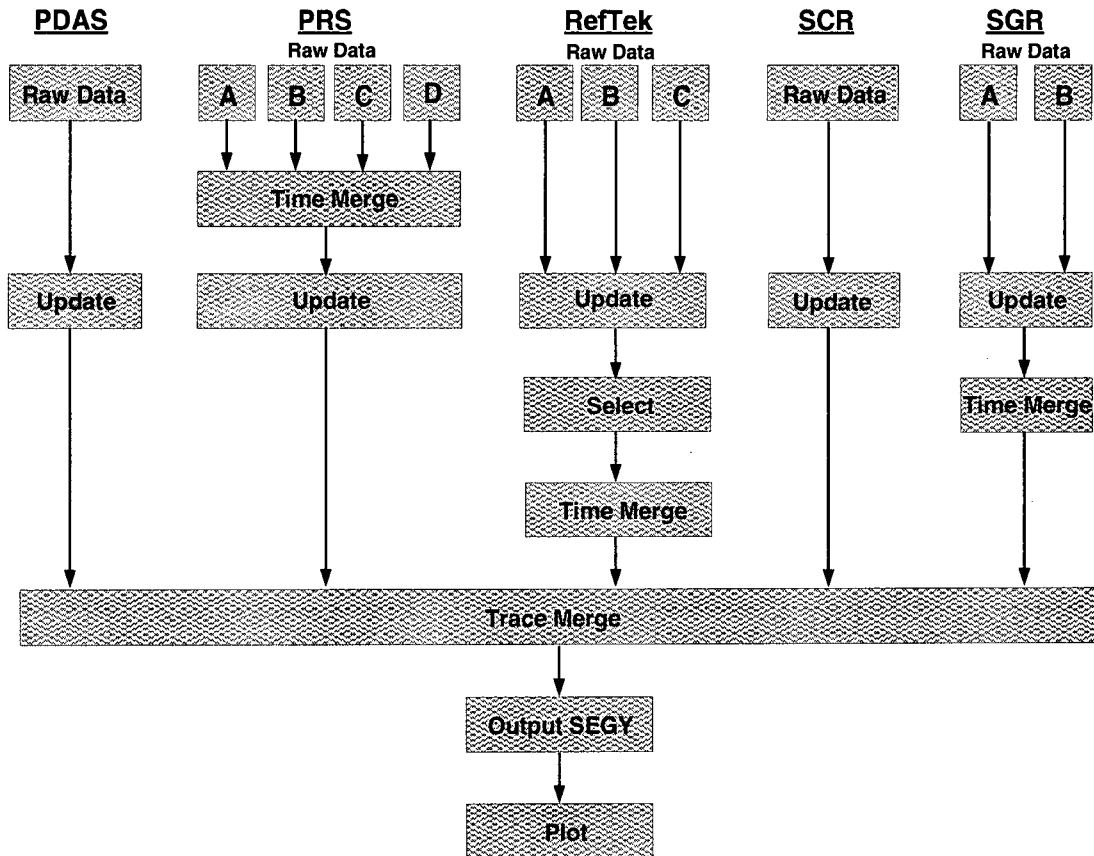


Figure 2.1: Deep Probe and SAREX data merging flowchart.

- PRS: originally recorded at 120 samples per second (approx. 8.3333 s).
- SCR: digitised from analogue field tapes at a 5 ms sample interval.
- PDAS: originally recorded at a 10 ms sample interval.

If necessary, `plotsec_win` could be used at this time to select or exclude specific traces.

2.3.4 Gain

Gain is also a subject that was dealt with in `plotsec_rseg`. The unique mechanical and electrical properties of each seismograph and geophone result in a different amplitude being recorded for

each instrument - geophone combination. In an attempt to approximate 'true relative amplitudes' between the data of various instrument types, the gain was set as shown in Table 2.3 for each data type as it was read in.

Table 2.3: Summary of gains applied to Deep Probe data.

Instrument Type	Geophone Type	Gain Applied
PRS	L-4	1
RefTek	L-22	1.136×10^7
RefTek	L-28	3.289×10^7
RefTek	S6000	1.136×10^7
SGR	L-4	1.90464×10^7
SGR	L-28	1.90464×10^7
SCR	L-4	1
SCR	L-28	1
PDAS	L-4C-3D	1

However, in some limited cases, gain concerns remain in the data and will be evident if they are not plotted with trace-to-trace amplitude corrections. For example, the specific locations of L-4 and L-28 geophones within the SGR deployments for Deep Probe are not known. Assisted by the fact that most (>90%) were L-4 geophones, an attempt was made to determine the distribution of geophone types based on amplitude differences observed in the data. However, amplitudes for these traces varied by a factor of 4 to 10 from shot to shot resulting in an inability to sort of the traces by this technique. In the end, the same gain was applied to traces with either geophone type and for this reason, true amplitude plots should be treated with suspicion for many of the SGR traces. A similar problem seems to affect the 20 PDAS instruments. Although the data should have a similar amplitude to those from neighbouring instrument types, they seem to be approximately one order of magnitude greater than what is expected. Again, the reason for this has not been ascertained, but observations suggest that they are all scaled by approximately the same

amount. If true amplitude plots are required in the future, then these traces could be empirically scaled by a single factor to approximately match neighbouring traces; this would not be a feasible procedure with the SGR instruments as the scaling amplitudes vary from shot to shot.

2.3.5 Updating SEG-Y Headers

The final data are all saved using the SEG-Y version 3.00 (IASPEI) format. The major updates that were required globally were:

- shot and receiver survey information. These data were compiled in SEG-P1 format files that could be accessed by the `plotsec_update` routine. The program was then able to calculate such parameters as the distance between the shot and the receiver. (This was done using a Seismic Analysis Code (SAC) subroutine [Tapley and Tull 1992] based upon the reference spheroid of 1968 and defined by a major radius of 6378.160 km and a flattening factor of 0.00335293.)
- shot information such as time of the shot and charge size. This information was obtained from simple input files that could be accessed by `plotsec_update`.

The Deep Probe Field Report [Gorman *et al.* 1997] provides a full documentation of the updating of SEG-Y headers for each seismometer group.

2.3.6 Merging and Archiving Data

Once all the headers from the various instrument types were updated, the data were merged into a single file (shot point gather) using `plotsec_merge`. At this point the data are still in the PLOTSEC format and contain all the data recorded for a specific shot point. SEG-Y files were created from these final data sets using the `plotsec_wseggy` routine. In this routine, such things as window size

and reduction velocity could be selected so that the SEG-Y file was more manageable in size. All merged data are archived at the *LITHOPROBE* Seismic Processing Facility at the University of Calgary.

Table 2.4: General information about the data

Number of traces per shot	~700
Length of trace (after merging of field data)	55 to 90 s
Sample interval	8 ms
Total number of samples per trace	6876 to 11251
Total number of samples per shot	~4.8 to 8.5 million
Estimated frequency content of data	0.25 - 12 Hz
Estimated signal to noise ratio of 'good' data zones	1.5
Estimated signal to noise ratio of 'poor' data zones	0.5

2.4 Introduction to the Deep Probe Data Set

The data recorded during Deep Probe and SAREX varied greatly in quality depending on the source-receiver offset, near-surface conditions at the receivers, near-surface conditions at the sources and variable weather conditions along the lengthy profile. In general, the SAREX data set is of a more consistent quality than the Deep Probe data set since the source and receiver conditions were similar for all shots. For Deep Probe, high signal-to-noise data were recovered to offsets of about 700 km, fair data quality was seen in some cases as far as 1400 km, and poor data quality was observed beyond that. Pre-analysis processing was limited to band pass filtering. Coherency filtering was performed, but did not significantly improve the ability to interpret the main phases and in some cases appeared to degrade subtle features with low signal-to-noise ratios.

Representative sets of data from the experiment are presented in Fig. 2.2, and summary data plots of all shots are included in Appendix A. The primary seismic phases are labelled P_g - energy refracting within the crust, P_mP - energy reflecting off the Moho, P_n - energy refracting in the uppermost mantle and P - the extension of P_n as the P body wave propagates deeper in the upper

mantle. The scale of plots that can be presented in this thesis do not always enable all phases that were identified and picked to be visible. Analysis of the data was performed on both large-format plots containing all the data and using computer screen plots at a variety of scales.

The 20 shots detonated during this experiment were at 16 distinct source locations. Three of the shot locations were recorded by both the first and second Deep Probe deployment of instruments (shots 133/233, 143/243 and 157/257) and one was recorded by the first Deep Probe deployment and the SAREX deployment (Deep Probe 149 and SAREX 1; see Table 2.1). From this point on in this thesis, unless referring to specific shots, the Deep Probe shot points will be denoted by their two digit approximate latitude (*e.g.*, 43, and 49). For data recorded by two deployments, it can be assumed unless specified otherwise, that the data from both have been merged into a single shot record.

Poor data were recorded from shot points 57 and 61 (nearest receivers at offset distances of 490 km and 1800 km respectively) partly because of the far offsets but also due to unforeseen near-source effects which impeded the propagation of seismic energy to the south. Disappointingly, data from these large source points (a detonation yield of 25 tonnes was planned for shot 261 while shot 257 was planned to be 18 tonnes, see Table 2.1) were unable to contribute significant information for the interpretation. Recordings of these two shots by broadband seismographs of the Canadian National Seismograph Network (CNSN) show that energy did propagate well to the north and east. This is evidenced by strong recordings at Inuvik and Yellowknife, Northwest Territories north of the shots, and at Churchill, Manitoba, east of the shots [Fig. 2.3 (a), (b), (d) and (e)], and relatively poorer recordings at the relatively near-by station to the south in Edmonton, Alberta [Fig. 2.3 (c) and (f)]. Shot 157 (5 tonnes) had poor energy propagation in all directions. While recorded at nearby CNSN stations (*e.g.*, Edmonton), and on the nearest offset Deep Probe seismographs, the response was very weak which made accurate interpretations of P_n first arrivals impossible.

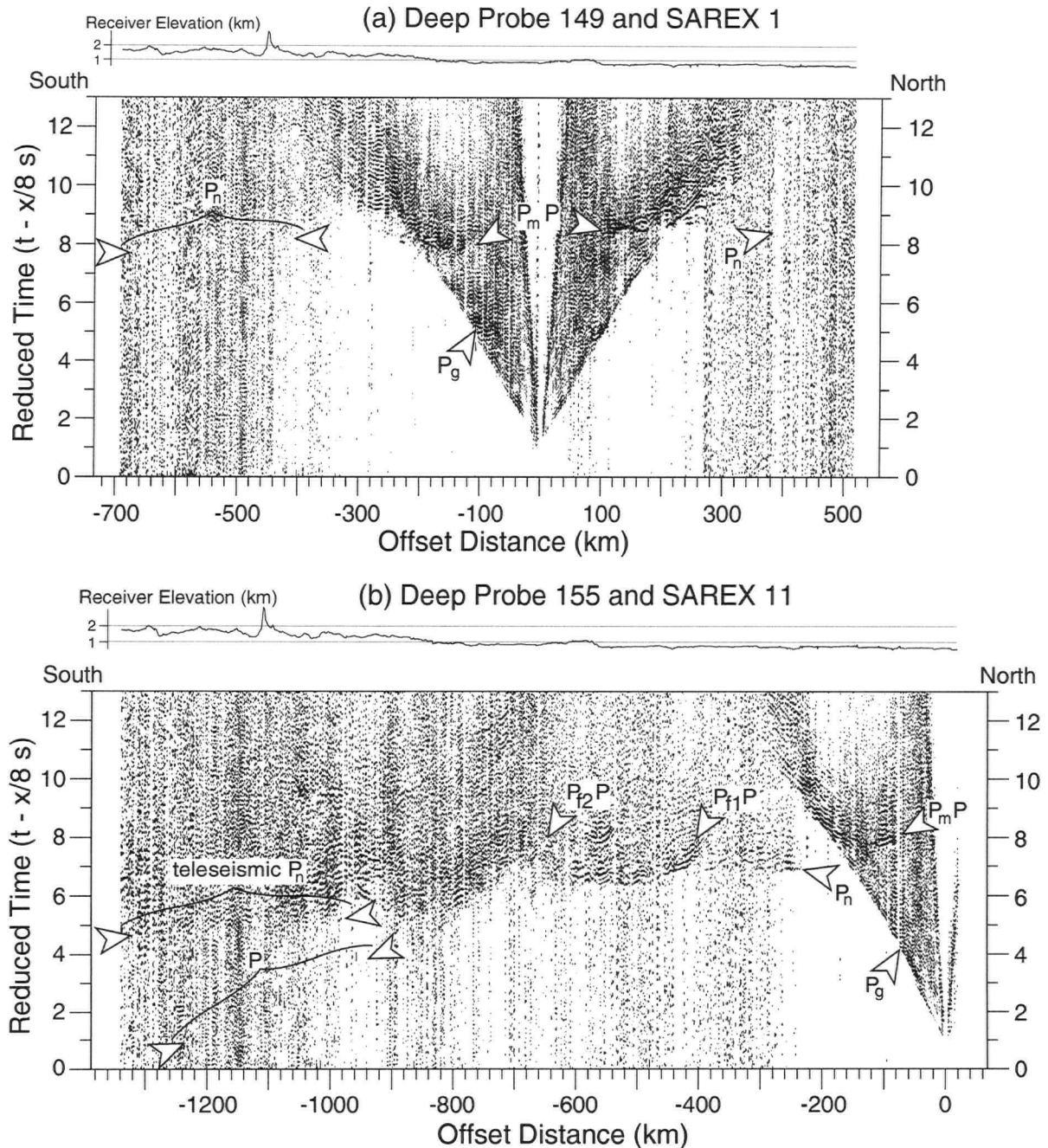


Figure 2.2: Data examples: (a) Deep Probe 149 and SAREX 1 (Shot point location at Canada - USA Border). Labelled phases: P_g - crustal refractions, P_mP - Moho reflections, and P_n - upper mantle refractions. (b) Deep Probe 155 (offsets beyond 232 km) and SAREX 11 (offsets between 0 and 232 km, plotted relative to the position of shot 155). Labelled phases: P_g , P_mP , P_n , P - body wave P, teleseismic P_n - hypothesised to be the result of upper mantle scattering, $P_{f1}P$ and $P_{f2}P$ - upper mantle dipping reflections (see text). Data are merged, bandpass filtered from 0.5 to 8.0 Hz, and plotted in trace-normalised variable area; positive offsets only; 15% bias to remove low amplitudes. Weak phases such as P are observed more clearly on large-scale plots of these data. Elevation profile along the recording line is shown above each plot.

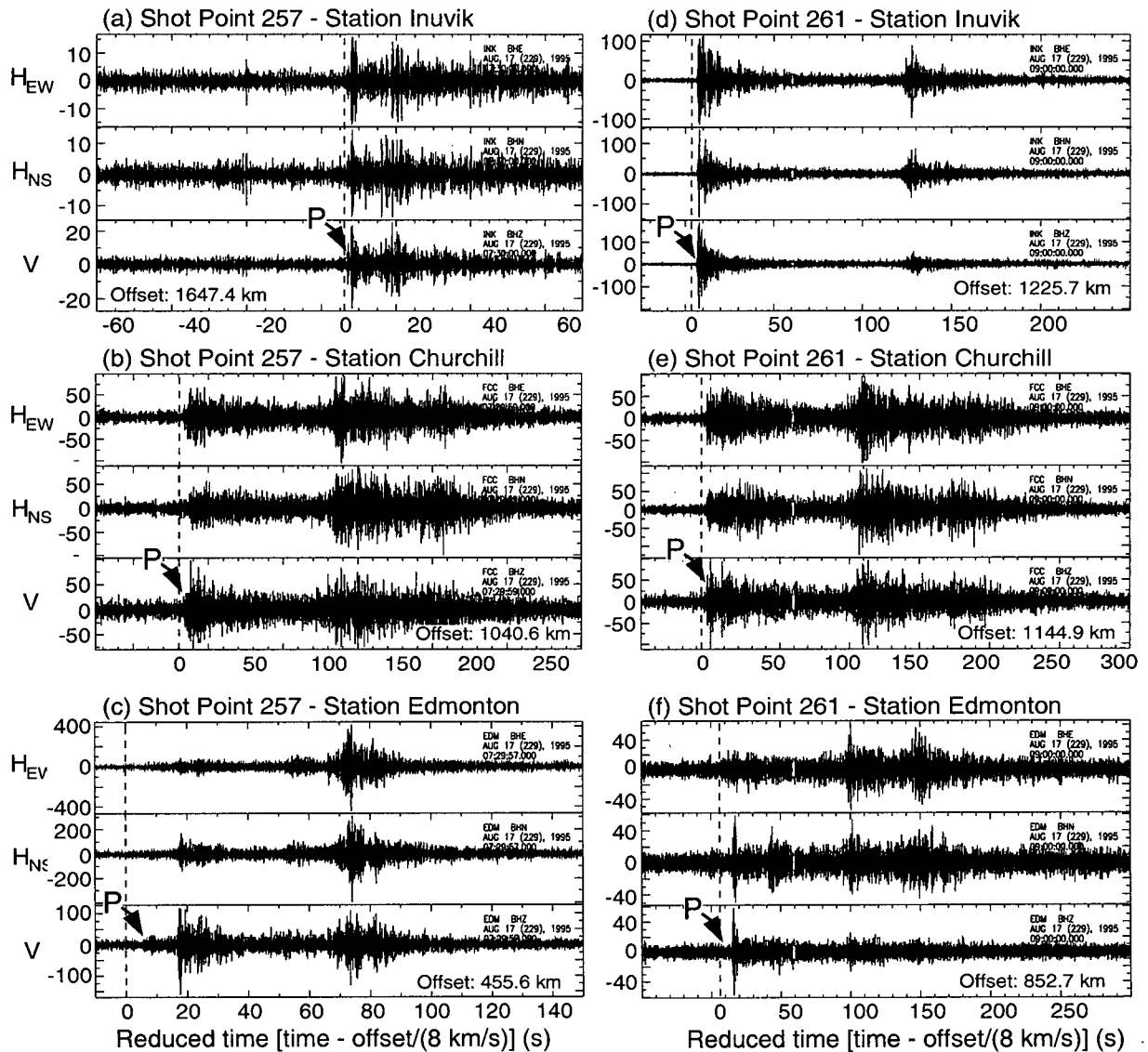


Figure 2.3: Three-component broad-band seismograph recordings from the Canadian National Seismograph Network (CNSN). 2 - 8 Hz Bandpass filter applied. H_{EW} - horizontal (east-west) response, H_{NS} - horizontal (north-south) response, V - vertical response; relative amplitude scale. Dashed line indicates zero reduced time (reduction velocity = 8 km/s). P phase (first arrival) as indicated by arrows on vertical response recordings. (a) Shot 257; Station: Inuvik, NWT. (b) Shot 257; Station: Churchill, MB. (c) Shot 257; Station: Edmonton, AB. (d) Shot 261; Station: Inuvik, NWT. (e) Shot 261; Station: Churchill, MB. (f) Shot 261; Station: Edmonton, AB.

Frequency content in the data varies, as expected, with offset. In general, significant energy is recorded within a bandwidth of 0.25 to 12 Hz. This has been evaluated for most shots by calculating amplitude spectra for various windows of data. Fig. 2.4 shows amplitude content for the

two datasets in Fig. 2.2. These have been produced by calculating the amplitude of the Fourier transform of each windowed trace. The spectra are trace-normalised. This routine was written to be used as a module of PLOTSEC [Amor 1996]. Amplitude spectra plots have been used in conjunction with narrow-bandpass filtered plots of the data to determine suitable parameters for filtering the data prior to interpretation. Data plots in this thesis have been filtered with a band-pass of 0.5 to 8.0 Hz. This frequency window preserves as much of the low frequency signal as possible and removes a significant portion of the higher frequency noise.

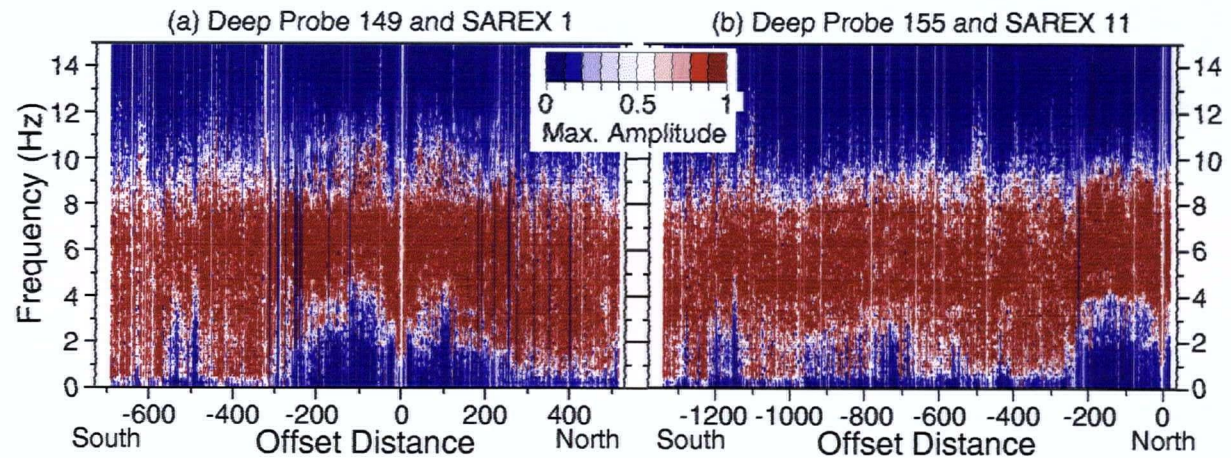


Figure 2.4: Normalised amplitude spectra (in colour) plotted as a function of offset for shot profiles 49 and 55. Analysis window: all traces, 4 to 10 seconds (reduced time; 8 km/s reduction velocity).

Two significant features of the Deep Probe data set are apparent in Fig. 2.2(b) and warrant introduction here. First, two strong upper mantle reflections labelled $P_{f1}P$ and $P_{f2}P$ in the image are observed. These are also recorded on several of the shot profiles from southern Alberta and play a large part in constraining the upper mantle model developed in this thesis. Second, teleseismic P_n arrivals (so-called because they appear to propagate at uppermost-mantle velocities to great distances) are recorded at offset distances between 700 and 1350 km. These events display a shingled character similar to that seen on other upper-mantle-scale data sets collected both within the North American craton [Hajnal *et al.* 1997] and on other Archean cratons around the

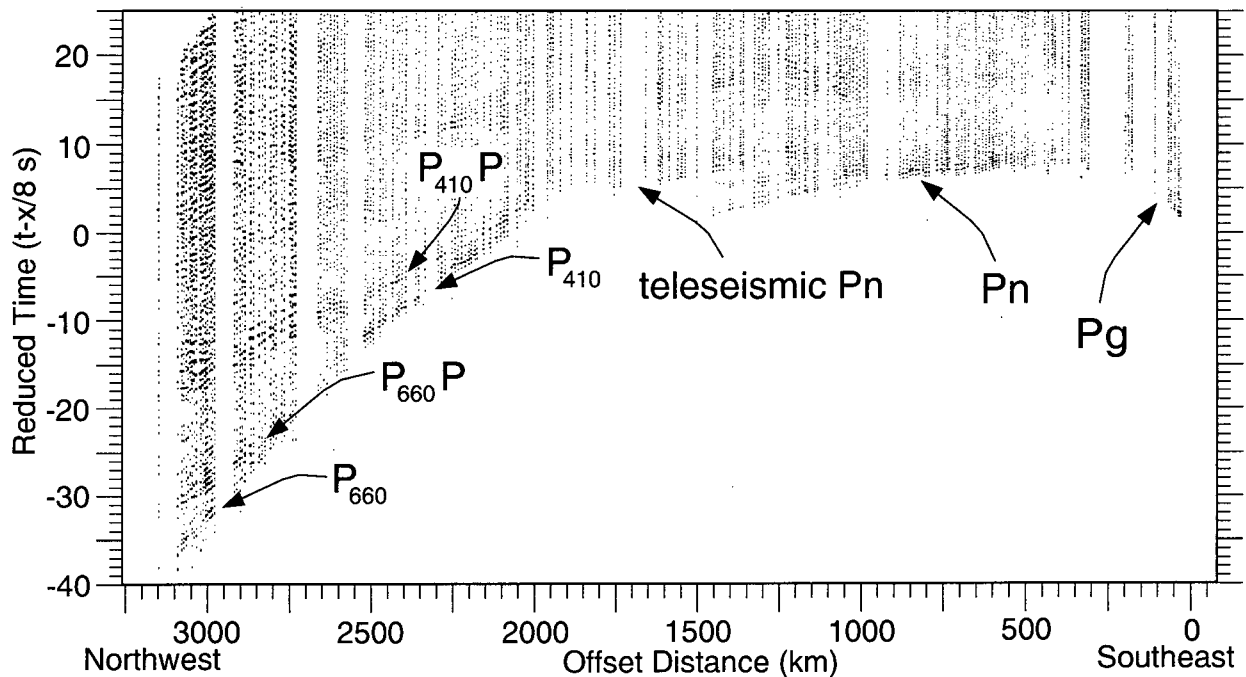
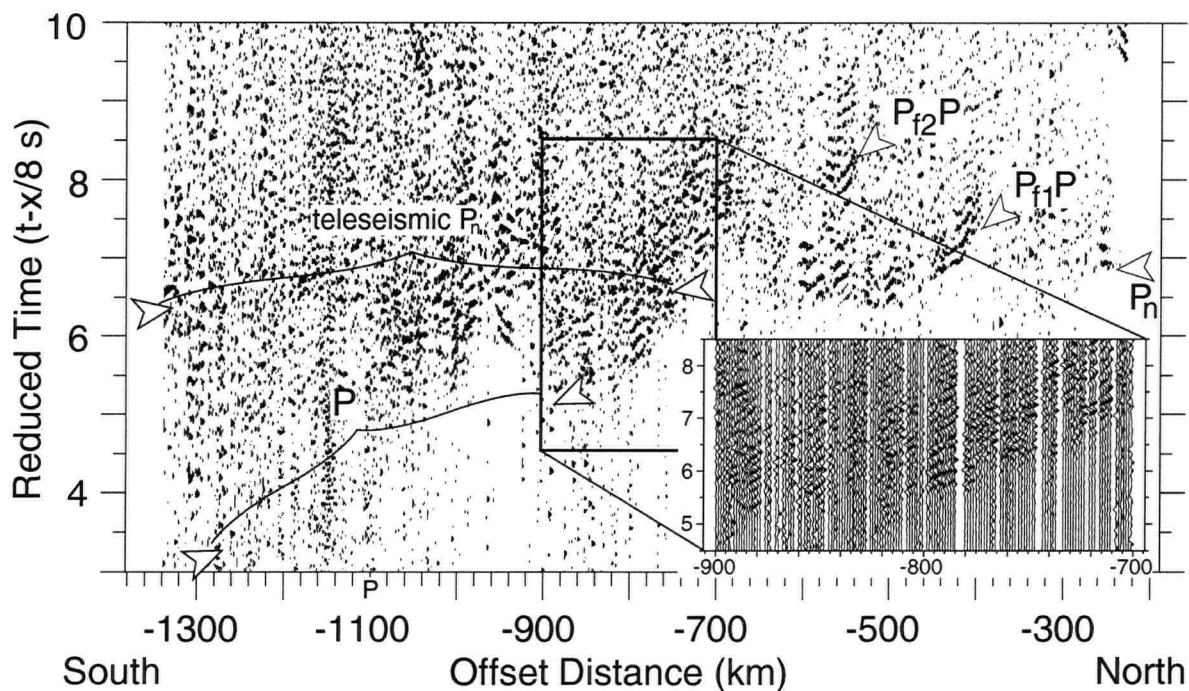


Figure 2.5: Peaceful Nuclear Explosion seismic profile Quartz, central Russia. Labelled phases: P_g - crustal refractions, P_n - upper mantle refractions, teleseismic P_n , $P_{410}P$ and $P_{660}P$ - reflections from the upper mantle discontinuities, and P_{410} and P_{660} - refractions from beneath the 410- and 660-km discontinuities. Bandpass filter: 0.5 - 8 Hz applied. All traces plotted. Variable area, positive offsets only, 15% bias.

world such as the Baltic Shield [Perchuc and Thybo 1996] and northern Eurasia [Ryberg *et al.* 1995, Tittgemeyer *et al.* 1996]. For example, Quartz profile 323 (Fig. 2.5), a Russian Peaceful Nuclear Explosion data set, shows teleseismic P_n arrivals at offset distances as great as 2000 km. Closer comparison of the Quartz and Deep Probe data is enlightening. Fig. 2.6 shows identical time-offset windows of data from Quartz 323 and Deep Probe 55 scaled to similar amplitudes. This comparison emphasises the difference in the sampling interval of the two data sets (~ 10 km for Quartz and ~ 1.25 km for Deep Probe). Even so, remarkable similarities can be seen in the recordings. First, note that P_n arrival times are similar for both data sets, suggesting a similarity in crustal velocity structures. Of major significance, though, is that while trace-to-trace coherency in the coda of the P_n is only suggested in the Quartz data, it is obvious over several kilometres

(a) Deep Probe 155



(b) Quartz 323

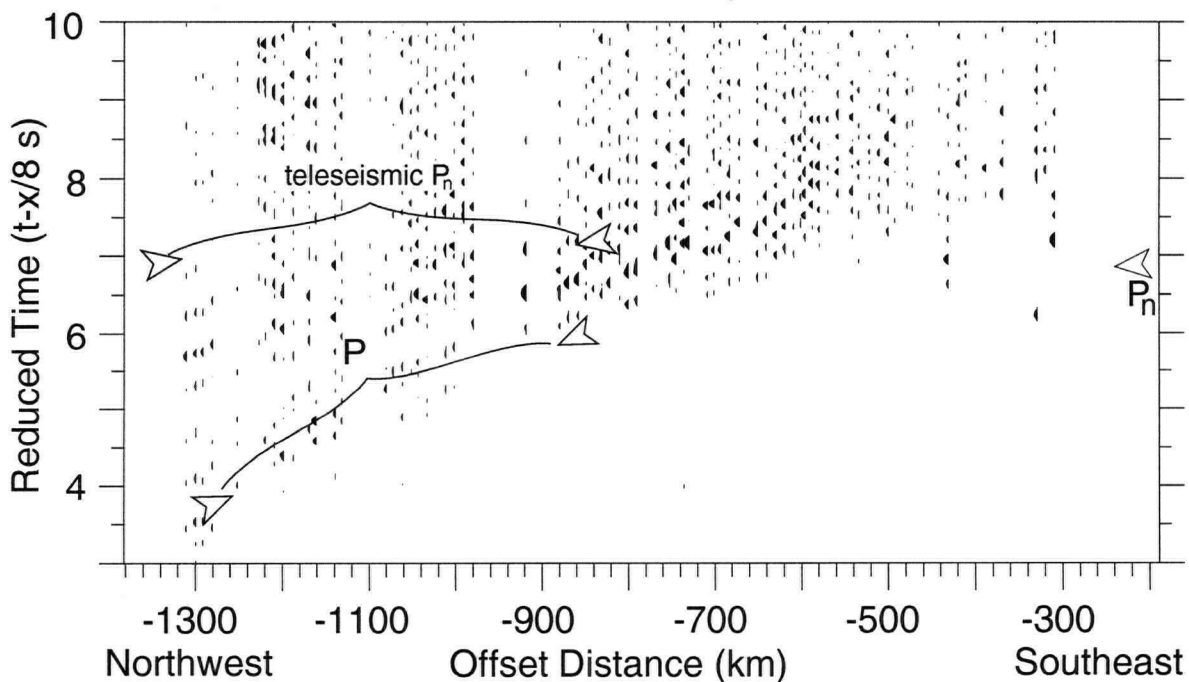


Figure 2.6: Comparison of Deep Probe Profile 55 and Quartz Profile 323. (a) Deep Probe Profile 55 highlighting the P_n phase, upper mantle reflections, the teleseismic P_n phase and its associated coda. An enlargement of a part of teleseismic P_n phase is shown (wiggle-trace, variable area, no bias). (b) Quartz Profile 323 shows P_n and teleseismic P_n . Bandpass filter: 0.5 - 8 Hz applied to both data sets. All traces plotted. Trace-normalised variable area, positive offsets only, 15% bias.

(tens of traces) in the Deep Probe data (enlargement in Fig. 2.6a). The enhanced spatial resolution of the Deep Probe data set enables the testing of more detailed models for the velocity structure of the uppermost mantle. This will be discussed further in Chapter 6.

Quartz profile 323 (Fig. 2.5) also contains strong reflections from the 410- and 660-km discontinuities ($P_{410}P$ and $P_{660}P$) and refractions from beneath the discontinuities (P_{410} and P_{660}) at offset distances beyond 2000 km. The Deep Probe data has shown hints of such arrivals on profiles 33, 37, 55, 57 and 61. While signal-to-noise ratios are less than one, it is tempting to interpret apparently coherent arrivals over tens of kilometres with time-distance characteristics close to those expected for reflections from the 410- and 660-km discontinuities as such reflections. Unfortunately, attempts at special processing to enhance the signal of these enticing events in the Deep Probe data were unsuccessful.

A major part of the Deep Probe field experiment, that has as yet received only cursory evaluation, is the horizontal component data. About half of the stations deployed in the field recorded three components of ground motion. Even though the linear nature of the Deep Probe profile limits the possible analysis of anisotropic effects in this region, the data do afford an opportunity for future research to evaluate certain aspects of anisotropy and lateral inhomogeneities.

Chapter 3

Preliminary 2-D Velocity Model from Tau-P Analysis

Plain question and plain answer make the shortest road out of most perplexities.

– Mark Twain (Life on the Mississippi, 1883).

The tau- p transform or ‘slant stack’ (τ - p , where τ is the intercept travel time and p is slowness, the reciprocal of velocity, v) is used for a variety of applications in seismic data analysis [Yilmaz 1987]. As a tool for extracting 1-D velocity interpretations from seismic refraction data, the downward-continuation of wave-field τ - p transformed shot profiles has proven to be an efficient and effective method which does not involve having to pick arrivals on a seismic section [Clayton and McMechan 1981]. The procedure involves two major steps. First, the entire data set is transformed from the recorded x - t domain into the τ - p domain through a τ - p transform. Second, the τ - p data are downward continued into z - p space using an appropriate input velocity function. The determination of this velocity function is an interpretive process. The downward continuation process results in a depth-slowness function being imaged in the z - p wave field data. By iteratively varying the input velocity function and repeating the downward continuation, this imaged slowness function is forced by the interpreter to converge to the inverse of the input velocity function. The 1-D accuracy of the τ - p velocity analysis can be checked by calculating the time-distance curves resulting from the velocity function and overlaying these on the input refraction data set.

The technique has been used successfully to produce 1-D [McMechan *et al.* 1982, Pike 1986]

and 2-D [Reiter *et al.* 1993] velocity models of the crust from controlled-source seismic experiments, and the uppermost mantle from data sourced by earthquakes [Walck and Clayton 1984]. In this study, the downward-continued wave-field τ - p method has been regularised to facilitate its rapid application to each shot record in a given refraction survey. Furthermore, a simple scheme has been developed to convert individual 1-D $v(z)$ functions for each shot to 2-D $v(x, z)$ curves where x corresponds to the offset of the bottoming location of a ray turning at a depth of z . These 2-D curves are then combined to produce a pseudo-2-D interpretation. This procedure has been applied to develop a preliminary 2-D velocity model for the crust and lithospheric mantle along the length of the Deep Probe profile which can be used as a well-constrained starting model for more rigorous interpretation methods. This chapter is based on a published paper [Gorman and Clowes 1999].

3.1 Application to Deep Probe

The downward-continued wave-field τ - p method was applied to the Deep Probe data set in order to produce a preliminary 2-D interpretation of the velocity structure of the lithosphere of western North America. This model was later the basis of the input model used for the ray-theoretical travel-time inversion scheme. The procedure was applied to five Deep Probe shot records: 37 North, 43 North and South, 49 South and 55 South, and six of the SAREX shots: 1 North and 6, 8, 9, 10, and 11 South. The examples shown in this chapter are from the composite record section of data from S11 (<232 km offsets) and SP55 (232 - 1350 km offsets) (Fig. 2.2(b), page 51) as it best illustrates good data quality at both near and far offsets.

3.2 Procedure

A summary of the τ - p downward continuation procedure to derive a velocity-depth function is presented in the flowchart shown in Fig. 3.1.

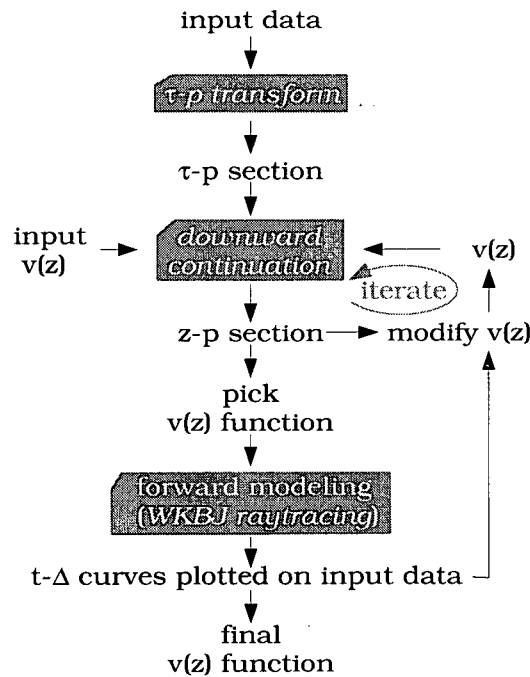


Figure 3.1: Summary flow chart for τ - p analysis and derivation of $v(z)$.

3.2.1 Tau- p transform

The wave-field τ - p transform, or slant stack, $S(\tau, p)$, transforms a conventional seismic record section $P(t, x)$ from the time - offset (t, x) domain to the intercept time - slowness (τ, p) domain.

$$S(\tau, p) = \int_{-\infty}^{\infty} P(\tau + px, x) dx \quad (3.1)$$

The input data set, P , is the observed seismogram wave field. In S , the transformed wave field, τ is the intercept time at zero offset for a given slowness, p . A simple way to look at the

transform is to think of each point in the resulting τ - p plane being the sum of all the points in the input t - x plane lying along a straight line with a slope of p and a time-axis intercept of τ . The seismogram is thus decomposed into plane-wave elements [McMechan *et al.* 1982]. A significant attribute of the τ - p transform routine in handling input digital data is that the trace spacing does not have to be uniform, a feature well suited to lithospheric-scale refraction surveys. Fig. 3.2 shows the τ - p transform of the data in Fig. 2.2(b).

3.2.2 Downward continuation of τ - p transformed data into z - p space

The downward-continuation procedure makes use of the fact that each trace in the input τ - p section represents plane waves with a common velocity. Using an input velocity function, $v(z)$, a new trace, s , is created for each input τ - p trace, S . This procedure is very similar to migration in that all points on the input time trace are mapped to points on the output depth trace by the criteria imposed by the transform. In effect, the input trace is stretched and squeezed to form the output trace. Maximum 'stretching' occurs at the depth, z , where the particular slowness of the input trace, p , is equal to the inverse of the input velocity function, $v(z)$. No energy is transferred between traces; this is a simple trace-by-trace operation.

The downward continuation is represented by:

$$s(p, z) = S[\tau - \Psi(p, z), p] \quad (3.2)$$

where

$$\Psi(p, z) = 2 \int_0^z \sqrt{|v^{-2}(z) - p^2|} dz \quad (3.3)$$

An input velocity function, $v(z)$, is required. If the function is correct, the maximum-amplitude, lowest-frequency portion of the output will coincide with the input function. A good model is achieved through iteration.

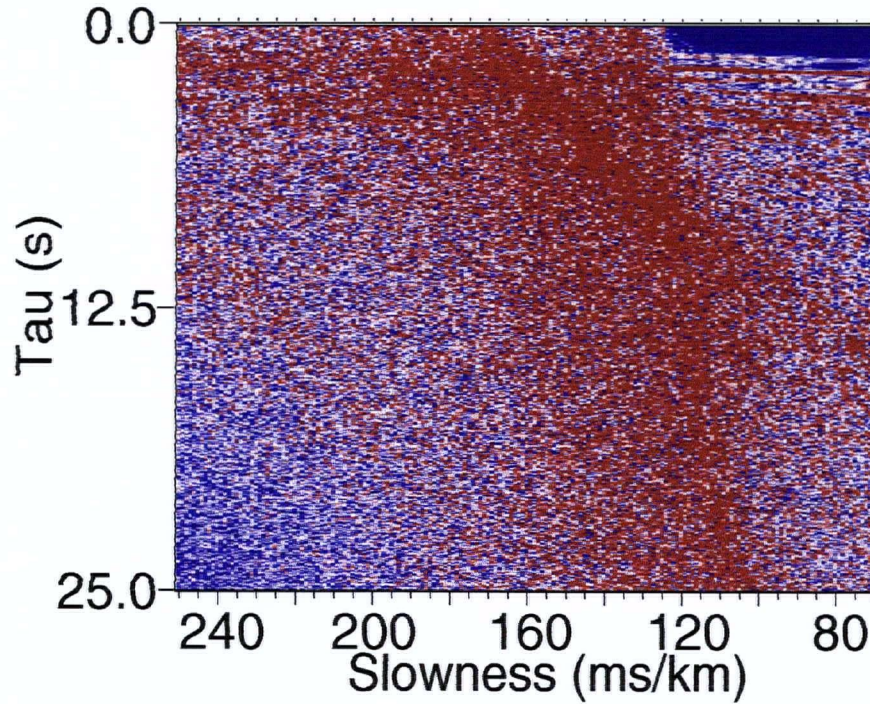


Figure 3.2: τ - p transform of the data in Fig. 2.2(b). Plot shows true absolute value of amplitude scaled from 0 amplitude (blue) to maximum amplitude (red).

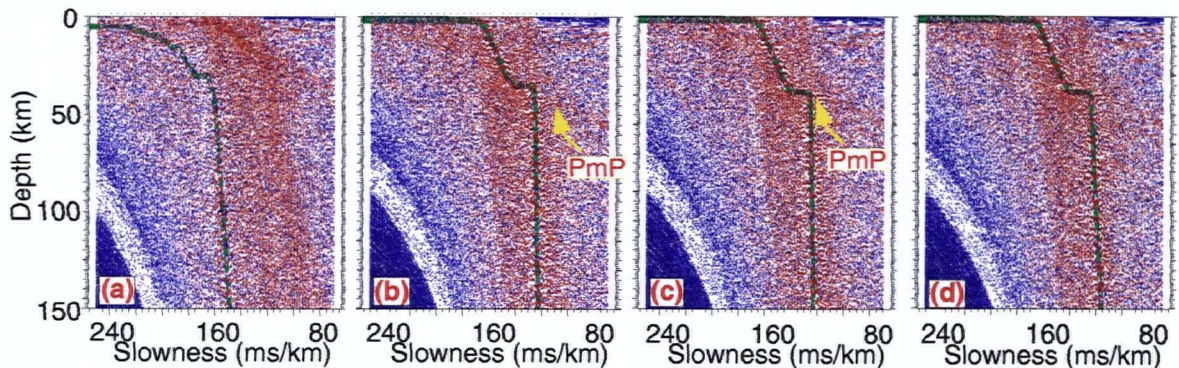


Figure 3.3: Downward continuations of the τ - p -transformed data into z - p space. Several velocity functions have been used; these are overlaid on the data in green. (a) The velocities used for the downward continuation are approximately 20% too low. (b) The velocity function used is corrected for crustal velocities. (c) The position of the Moho discontinuity is refined through iteration. (e) The upper mantle velocities used are refined through iteration. Plot parameters same as Fig. 3.2. In (b) and (c), the yellow arrows labelled P_mP indicate the crest of the hyperbolic-shaped transform of the P_mP reflection.

In the examples shown in Fig. 3.3, the τ - p section of Fig. 3.2 has been downward continued through several iterations. First, a velocity function was used that is $\sim 20\%$ too low at all depths (Fig. 3.3a). This velocity function was chosen to show the effect of downward continuation with an incorrect velocity function. In this example, it is apparent that the strong energy is to the right (greater in velocity) of the velocity function used (shown by a green line). By rerunning the downward continuation with a new velocity function, an improved match can be made. A second downward continuation was performed, this time using velocity information determined through preliminary analysis of the SAREX crustal data set [M.J.A. Burianyk, pers. comm., 1997]. This second downward continuation (Fig. 3.3b) shows good agreement at crustal depths, but poor agreement for the crust-mantle boundary (the Moho) and the upper mantle. The third downward continuation (Fig. 3.3c) shows the result of iterating to find an appropriate depth for the Moho. This was achieved at 38 km for these data. Note how the velocity function passes through the higher amplitudes at this depth. In addition, the τ - p transformed reflection from the base of the crust (P_mP) can be seen to tie well with the depth chosen. The fourth downward continuation shown (Fig. 3.3d) is the result of iteration to fit the velocity function through the uppermost mantle. Due to the small velocity gradient in the mantle, velocity picking is difficult. It is important that a sufficient number of slowness traces are created in the initial τ - p transform so that there are enough for a successful interpretation of the upper mantle velocity function.

3.2.3 Forward modelling

In order to check the 1-D velocity model developed by the τ - p to z - p downward continuation, time-distance curves can be calculated from the model and overlaid on the input data. In this case, the one-dimensional ray-theoretical forward modelling technique, WKBJ [Chapman 1978], has been used. A perfect match between the predicted and observed arrivals is not expected. Variations in arrival times are very likely the result of two- or three-dimensional velocity effects. Fig.

3.4 shows P_g (crustal refraction), P_mP and P_n (mantle refraction) arrival times as calculated by the WKB routine based on the velocity function used for the downward continuation in Fig. 3.3d. These are overlain on the input data in Fig. 3.4 (1) and show good agreement.

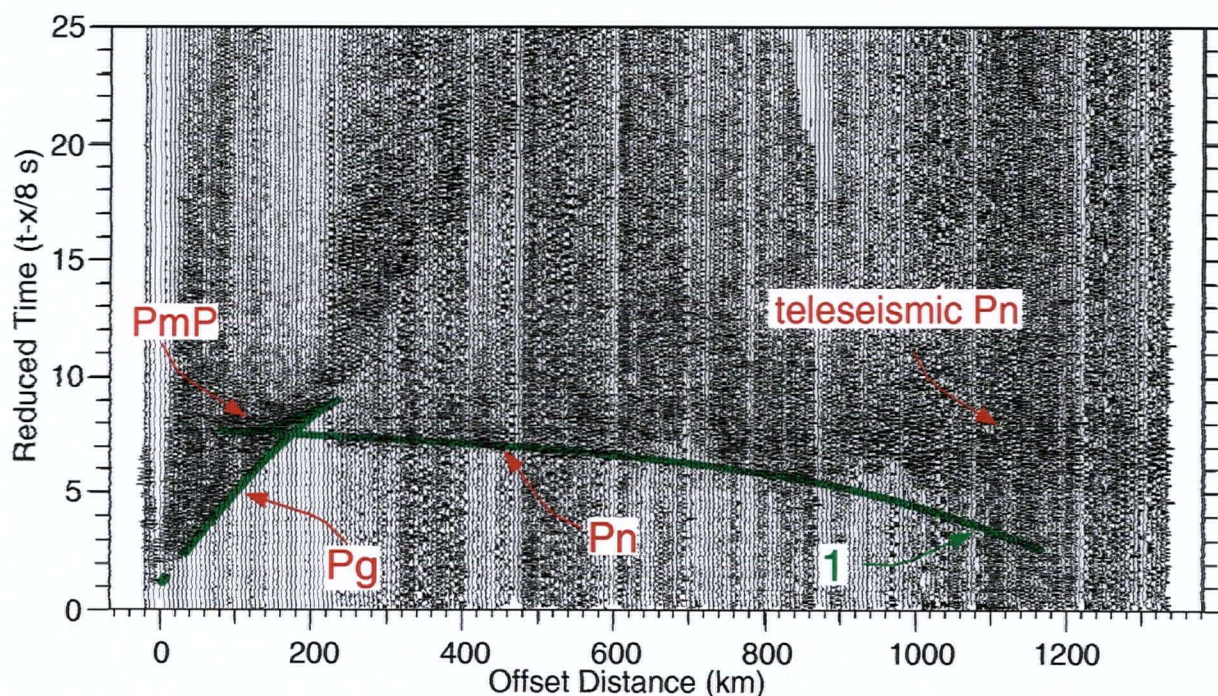


Figure 3.4: WKBJ-calculated travel times for P_g , P_mP and P_n phases (1, in green) overlaid on the input data.

3.2.4 Synthesis for a 2-D velocity model

The τ - p analysis of a single shot gather results in a one-dimensional velocity function, $v(z)$. However, in a typical modern refraction study, many shots are commonly recorded by several arrays of receivers to increase the volume of the subsurface which is sampled. If this happens along a linear profile, as was the case with Deep Probe and SAREX, a two-dimensional velocity model can be created by combining the one-dimensional velocity functions determined for each shot point. In the case of a split spread (the source located part way along the line of receivers), the data set

should be divided in two at the source location and analysed separately, so that offset direction can be considered.

To convert the individual 1-D velocity models to two dimensions, each 1-D function, $v(z)$, is converted to $v(x, z)$ where x is the offset of the particular refracted ray which turns at a depth z . Given the scale of the Deep Probe experiment, effects of the Earth's curvature must be considered. Using ray theory for a spherical Earth, this offset can be readily calculated for each depth, z , in the input $v(z)$ function by:

$$x(r_p) = r_E \frac{r_p}{v(r_p)} \int_{r_p}^{r_E} \frac{dr}{r \sqrt{\frac{r^2}{v^2(r)} - \frac{r_p^2}{v^2(r_p)}}} \quad (3.4)$$

where r_E is the radius of the Earth and r_p is the distance from the centre of the Earth to the turning point of the ray (*i.e.*, $r_p = r_E - z$). The resulting 2-D functions are then superimposed on a grid and contoured using GMT contouring routines [Wessel and Smith 1995] to provide a 2-D velocity model of the entire profile. For the Deep Probe data set, the model derived following this procedure is shown in Fig. 3.5. Note in this figure that the depth of the Moho is controlled by breaks in the individual 2-D functions for each shot (indicated by a green dot on each profile.)

3.3 Discussion

The model generated by this technique is quite coarse and strongly varying structures will have a negative effect on the accuracy of the technique. Even so, numerous features are readily identified in the model which are confirmed by later work. The three main lithospheric provinces, the Archean-aged Hearne and Wyoming provinces and the Proterozoic accretionary lithosphere of the southwestern U.S. (Fig. 3.5), are distinct on the model. These features correlate closely to the more detailed interpretation of the Deep Probe data set [Deep Probe Working Group 1998]. The Hearne Province shows a variable crustal thickness and relatively high upper mantle velocities.

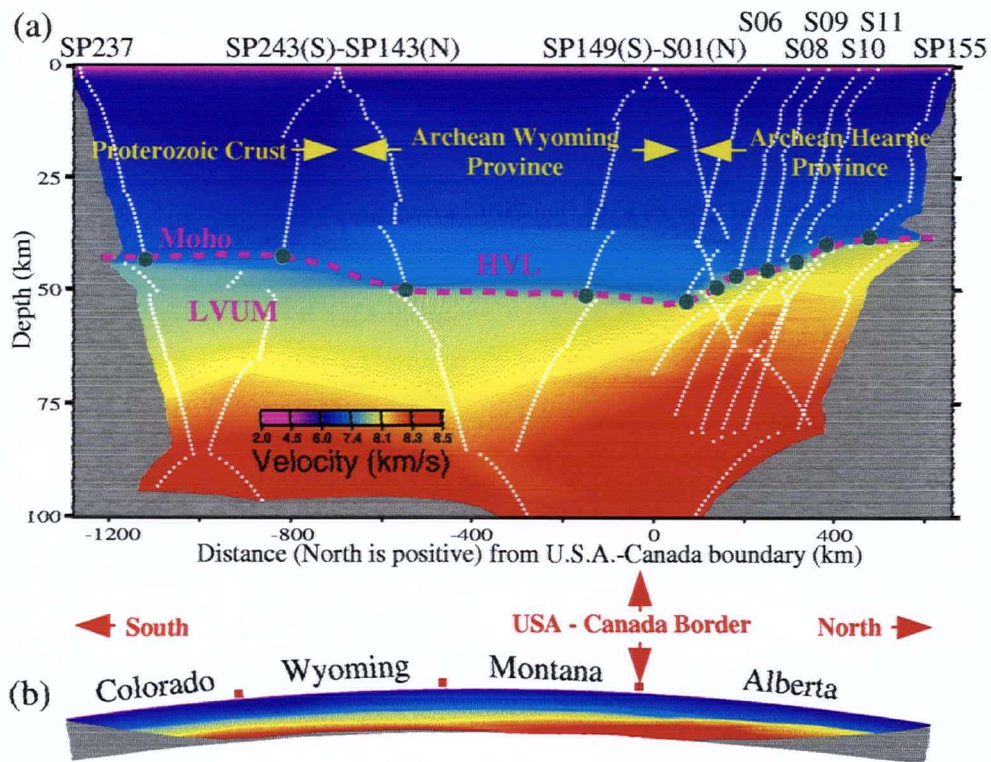


Figure 3.5: 2-D model derived from merging the results of all analysed profiles from the data set. (a) Model at 10:1 vertical exaggeration. Contour control points are indicated by white dots. Major continental basement domains are labeled. Interpreted Moho depth is indicated by dashed line running between green control points. A major high velocity layer (HVL) at the base of the Wyoming crust and the low velocity upper mantle (LVUM) within the lithosphere immediately below the Proterozoic crust are identified. (b) Same model including curvature of Earth and no vertical exaggeration.

The Wyoming Province shows a very thick crust (~ 50 km) and a high velocity layer (HVL) in the lower 20 km. The Proterozoic crust shows a normal and relatively constant crustal thickness with a low velocity upper mantle (LVUM). The positions of the Moho and other velocity discontinuities are constrained by breaks in the piecewise-continuous plot of bottoming locations.

The τ - p analysis routine is very useful as a first stage in obtaining upper mantle velocities, but it does have several limitations. First, since the τ - p transform technique is defined through ray theory, scattered energy in the input will not be handled correctly. This is particularly a concern when considering the teleseismic P_n event (Fig. 2.2(b)), interpreted in other studies to be either

the result of a scattering layer in the upper mantle [Tittgemeyer *et al.* 1996] or for its coda to be caused by scattering in the crust [Morozov *et al.* 1998]. Second, the velocity gradients in the mantle are much lower than in the crust. This makes picking velocities difficult and introduces an increased likelihood of degrading the interpretation of the velocity function due to the effects of spatial aliasing. Third, velocity picking is very interpretive; no automated picking routines are available. There is still a need to check picked velocity models against forward-modeled time-distance calculations.

With these limitations in mind, the two-dimensional model generated by this technique should only be considered as preliminary. It does not involve any correlation between shots. However, a model such as this can be generated in a comparatively short time and it may be used appropriately as a starting model for a more rigorous two-dimensional velocity analysis such as travel-time inversion techniques [Zelt and Smith 1992, Hole 1992] or waveform finite-difference forward modelling methods [Levander 1989].

Chapter 4

Considering Earth Curvature:

Modification of the Ray-Theoretical Travel-Time Inversion Routine

Regarding Lilliputians....

They bury their dead with their heads directly downwards, because they hold an opinion, that in eleven thousand moons they are all to rise again, in which period the earth (which they conceive to be flat) will turn standing on their feet. The learned among them confess the absurdity of this doctrine, but the practice still continues, in compliance to the vulgar.

– Jonathan Swift (Gulliver's Travels, Chapter VI, 1726).

Controlled-source seismic data are typically modelled with the assumption that energy propagates from a source to a receiver through a flat Earth, *i.e.*, an Earth, with a planar, horizontal surface, parameterised in Cartesian co-ordinates. In 2-D, it is assumed that the 'depth' co-ordinates, z , and the 'horizontal offset distance' co-ordinates, x , lie on an orthogonal grid (*i.e.*, that the z -axis is vertical or 'straight down' and the x -axis is horizontal – a straight line along the surface). This approximation is adequate for most modelling situations. However, for seismic surveys of extended length, the Earth's sphericity can introduce significant error. In such a case, surveyed surface positions and depths beneath the surface cannot be assumed to lie along axes of a Cartesian grid. A new parameterisation of the Earth is required in terms of radius, r , and angle, Δ (Fig. 4.1).

If the Earth's sphericity is not taken into consideration, then error will be present in the velocity structure of the forward model. This error will increase with depth as ray paths are systematically lengthened due to the inappropriate parameterisation. In the past, this error has been

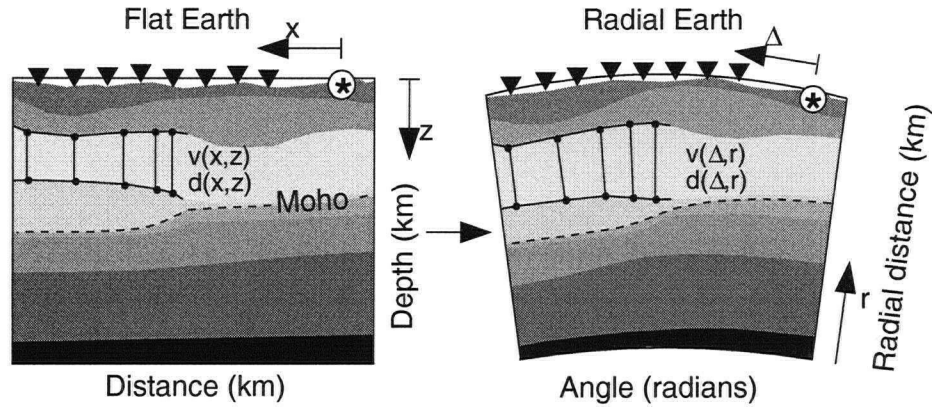


Figure 4.1: Schematic illustration summarising change from Cartesian to cylindrical co-ordinates.

accommodated by applying an Earth flattening approximation [*e.g.*, Müller 1971] that modifies depth and velocity values in a given model as follows:

$$z_{\text{flat}} = r_{\text{Earth}} \ln \frac{r_{\text{Earth}}}{r_{\text{Earth}} - z_{\text{cylindrical}}}, \quad (4.1)$$

$$v(z_{\text{flat}}) = \frac{r_{\text{Earth}}}{r_{\text{Earth}} - z_{\text{cylindrical}}} v(z_{\text{cylindrical}}). \quad (4.2)$$

These modifications shift calculated travel times through the Earth by an amount equal to the difference between modelled travel times through one-dimensional spherical and flat models. The main concern with this approach is that the approximation does not take lateral variations in velocity into consideration. A better approach is to perform the ray tracing in an appropriate curvilinear co-ordinate system. To this end, the widely-used ray-theoretical travel-time inversion routine, RAYINVR [Zelt and Smith 1992], has been modified in the present study. Specific details of the required code modifications are outlined in Appendix B. This chapter develops the theory required for these codes.

4.1 Ray tracing

RAYINVR [Zelt and Smith 1992] applies zero-order asymptotic ray theory to trace rays through a two-dimensional (2-D) velocity model. The system of ray tracing equations, given a set of initial conditions, is solved numerically to map the path of a particular ray through the velocity model. Travel times can then be calculated by integrating slowness (reciprocal velocity) along the ray path.

4.1.1 Ray tracing through a 'flat' Earth

First, consider how the ray tracing equations are formulated in a 2-D 'flat' Earth, *i.e.*, where geometries are expressed using the Cartesian co-ordinate system (Fig. 4.2). In this system, the ray tracing equations are a pair of ordinary differential equations (ODE's) [Červený *et al.* 1977] which in the case of RAYINVR are cast in terms of 'depth', z , and 'offset distance', x , as the independent variables. For trigonometric convenience, the orientation of the ray can be taken into consideration to avoid very large values of the trigonometric functions ($\tan\theta$ or $\cot\theta$). This results in two equivalent pairs of ODE's: one pair when the ray is mostly horizontal (Eq. 4.3) (*i.e.*, incidence angle, θ , between 45° and 90°), and another when the ray is mostly vertical (Eq. 4.4) (*i.e.*, incidence angle, θ , between 0° and 45°).

$$45^\circ \leq \theta \leq 90^\circ : \quad \frac{dz}{dx} = \cot\theta \quad \text{and} \quad \frac{d\theta}{dx} = \frac{v_z - v_x \cot\theta}{v}, \quad (4.3)$$

$$0^\circ \leq \theta \leq 45^\circ : \quad \frac{dx}{dz} = \tan\theta \quad \text{and} \quad \frac{d\theta}{dz} = \frac{v_z \tan\theta - v_x}{v}, \quad (4.4)$$

$$\text{where} \quad v_x = \frac{\partial v(x, z)}{\partial x} \quad \text{and} \quad v_z = \frac{\partial v(x, z)}{\partial z},$$

and with initial conditions

$$x = x_0, \quad z = z_0, \quad \text{and} \quad \theta = \theta_0.$$

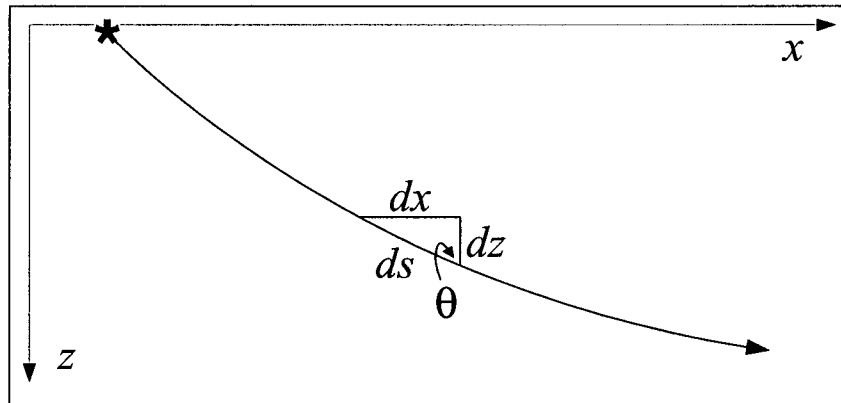


Figure 4.2: Ray traced in Cartesian co-ordinates.

In the RAYINVR routine, rays are traced through a 2-D velocity model made up of trapezoids with sides that are vertical and upper and lower boundaries that may or may not have an associated dip. The depth (z), horizontal position (x) and P-wave velocity (v) are defined at the corners of each trapezoid. Velocities internal to the trapezoids are calculated as necessary by a weighted average of the four corner velocities. Ray paths are calculated through the model in two ways: (1) between layer boundaries, where velocity is smoothly variable, a Runge-Kutta method is used to numerically solve the equations (4.3 or 4.4) for x , z and θ , and (2) at layer boundaries, where velocity changes are discontinuous, Snell's law is applied. The step length of the ray is controlled so that it is small enough to avoid significant error and large enough to avoid unnecessary computations.

Travel times are calculated by integrating slowness along the ray path, s (Eq. 4.5),

$$t = \int_{(x_0, z_0)}^{(x_R, z_R)} \frac{1}{v(x, z)} ds, \quad (4.5)$$

where (x_0, z_0) is the source location and (x_R, z_R) is the receiver location. The discrete form,

$$t = \sum_{x=x_0, z=z_0}^{x_R, z_R} \frac{\Delta s(x, z)}{v(x, z)}, \quad (4.6)$$

is used in the practical application.

4.1.2 Ray tracing through a cylindrical Earth

Now consider a more accurate parameterisation of the Earth by approximating it as cylindrical in cross-section, *i.e.*, that gradients in the transverse direction are negligible (Fig. 4.3). In this system, 'depth' is converted to radial distance (distance from the centre of the Earth) and 'offset distance' between the source and receiver is recast as an angle. Table 4.1 summarises the corresponding quantities in each parameterisation.

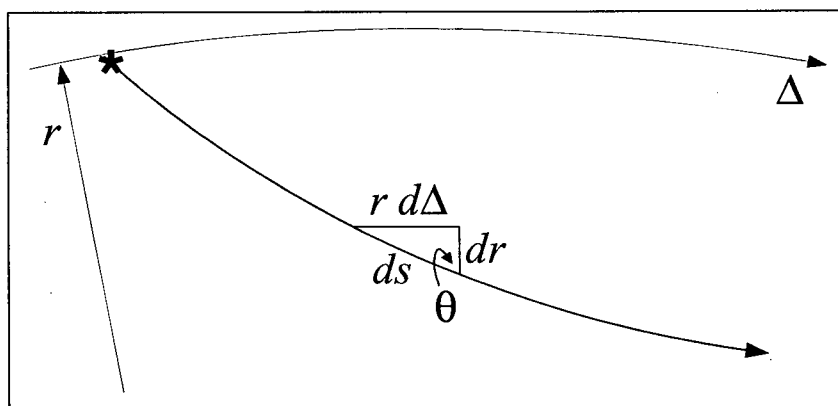


Figure 4.3: Ray traced in cylindrical co-ordinates.

Table 4.1: Corresponding flat Earth and cylindrical Earth quantities

Flat Earth	Cylindrical Earth
dx	$r d\Delta$
dz	$-dr$
$v_x = \frac{\partial v}{\partial x}$	$\frac{\partial v}{r \partial \Delta} = \frac{v_\Delta}{r}$
$v_z = \frac{\partial v}{\partial z}$	$-\frac{\partial v}{\partial r} = -v_r$

A new set of ordinary differential equations (Eqs. 4.7 and 4.8) can now be produced using

the corresponding quantities presented in Table 4.1.

$$45^\circ \leq \theta \leq 90^\circ : \quad \frac{dr}{d\Delta} = -r \cot \theta \quad \text{and} \quad \frac{d\theta}{d\Delta} = \frac{r(-v_r - \frac{v_\Delta}{r} \cot \theta)}{v}, \quad (4.7)$$

$$0^\circ \leq \theta \leq 45^\circ : \quad \frac{d\Delta}{dr} = -\frac{\tan \theta}{r} \quad \text{and} \quad \frac{d\theta}{dr} = \frac{v_r \tan \theta + \frac{v_\Delta}{r}}{v}. \quad (4.8)$$

4.1.3 Application of the cylindrical parameterisation

In order to avoid the reparameterisation of a RAYINVR input model in terms of radial distance (r) and angle (Δ), it is useful to establish equivalents between r and Δ and parameters l and ζ , where l is the arc length along the surface of the Earth (corresponding to surveyed surface locations, x , in the flat Earth RAYINVR method) and ζ is the radial depth (corresponding to depth, z , in the flat Earth RAYINVR method). This is done by including the radius of the Earth, r_E as a normalising factor (Fig. 4.4). Table 4.2 summarises the equivalencies that are used.

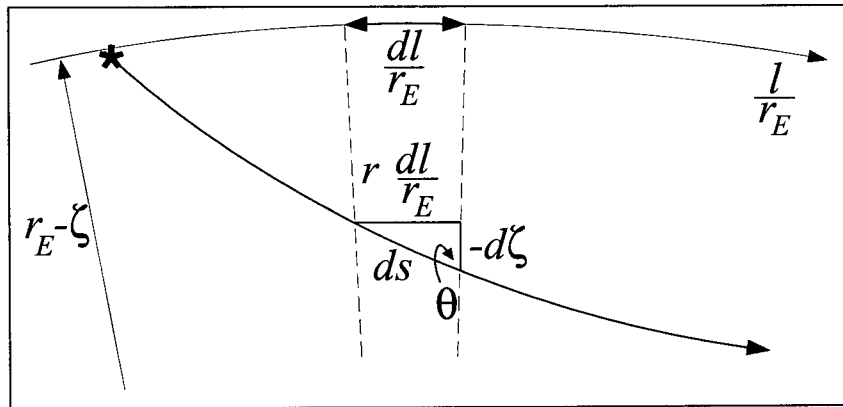


Figure 4.4: Ray traced in cylindrical co-ordinates which are parameterised in terms of l and ζ .

By applying the equivalents in Table 4.2, two pairs of cylindrical earth ODE's are produced (Eqs. 4.9 and 4.10) which are parameterised in terms of depth and offset distance.

$$45^\circ \leq \theta \leq 90^\circ : \quad \frac{d\zeta}{dl} = \frac{r}{r_E} \cot \theta \quad \text{and} \quad \frac{d\theta}{dl} = \frac{\frac{r}{r_E} v_\zeta - v_l \cot \theta}{v}, \quad (4.9)$$

Table 4.2: r , Δ and l , ζ parameterisation equivalents for a cylindrical Earth

r , Δ parameterisation	l , ζ parameterisation
$d\Delta$	$\frac{dl}{r_E}$
dr	$-d\zeta$
$v_\Delta = \frac{\partial v}{\partial \Delta}$	$r_E \frac{\partial v}{\partial l} = r_E v_l$
$v_r = \frac{\partial v}{\partial r}$	$\frac{\partial v}{-\partial \zeta} = -v_\zeta$

$$0^\circ \leq \theta \leq 45^\circ : \quad \frac{dl}{d\zeta} = \frac{r_E}{r} \tan \theta \quad \text{and} \quad \frac{d\theta}{d\zeta} = \frac{v_\zeta \tan \theta - \frac{r_E}{r} v_l}{v}. \quad (4.10)$$

Note the similarity between these ODE's (Eqs. 4.9 and 4.10) and the ODE's used for a flat Earth (Eqs. 4.3 and 4.4). The significant difference is the application of a scaling factor involving the ratio of the Earth's radius (r_E) to the radial distance (r).

An additional modification is required in the method of calculating travel times (Eq. 4.6) due to the cylindrical geometry. In the original flat-Earth RAYINVR method, the incremental travel time, Δt_i , for a single step of the ray path is calculated assuming Cartesian co-ordinates,

$$\Delta t_i = \frac{\Delta s_i}{v_i}, \quad (4.11)$$

$$\text{where } \Delta s_i = \sqrt{(x_{i+1} - x_i)^2 + (z_{i+1} - z_i)^2},$$

$$\text{and } v_i = \frac{v(x_i, z_i) + v(x_{i+1}, z_{i+1})}{2}.$$

In the modified cylindrical-Earth method, the incremental step-length of the ray, Δs_i , is determined in a similar manner. However, the ratio of the radial distance (r) to the Earth's radius (r_E) must also be considered in the calculation. For this case,

$$\Delta s_i = \sqrt{\left(\frac{r_{i+1} l_{i+1} - r_i l_i}{r_E} \right)^2 + (\zeta_{i+1} - \zeta_i)^2},$$

$$\text{and } v_i = \frac{v(l_i, \zeta_i) + v(l_{i+1}, \zeta_{i+1})}{2}.$$

4.2 Modelling results

4.2.1 Synthetic example: 1-D comparison of RAYINVR and WKBJ algorithms

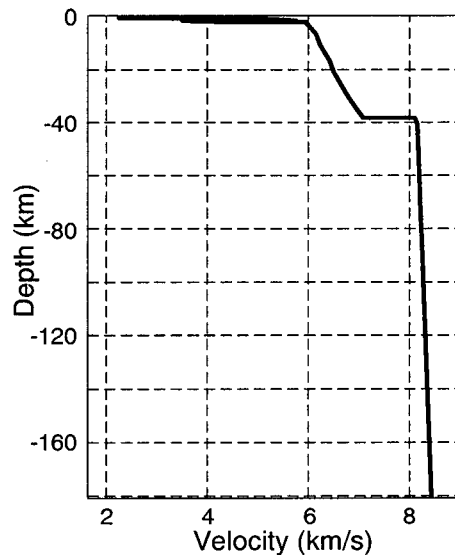


Figure 4.5: 1-D input model.

A few simple 1-D tests are instructive as to the relative behaviour of the flat Earth and cylindrical Earth routines. A simple 1-D crustal model (Fig. 4.5), which is typical of Archean platform such as that seen at the northern end of the Deep Probe profile beneath southern Alberta, has been chosen for these tests.

Flat Earth Model

Standard flat-Earth RAYINVR forward modelling has been performed on a hypothetical 2000-km-long model with a vertical velocity profile as shown in Fig. 4.5 and no lateral velocity variations (Fig. 4.6). The travel times predicted by RAYINVR are compared to those predicted by the WKBJ method [Chapman 1978], which traces rays through a Cartesian co-ordinate system after modifying the input 1-D velocity profile by the flat Earth transform (Eqs. 4.1 and 4.2). As can be clearly seen in Fig. 4.6, the arrival times for the flat Earth RAYINVR model lag the expected times

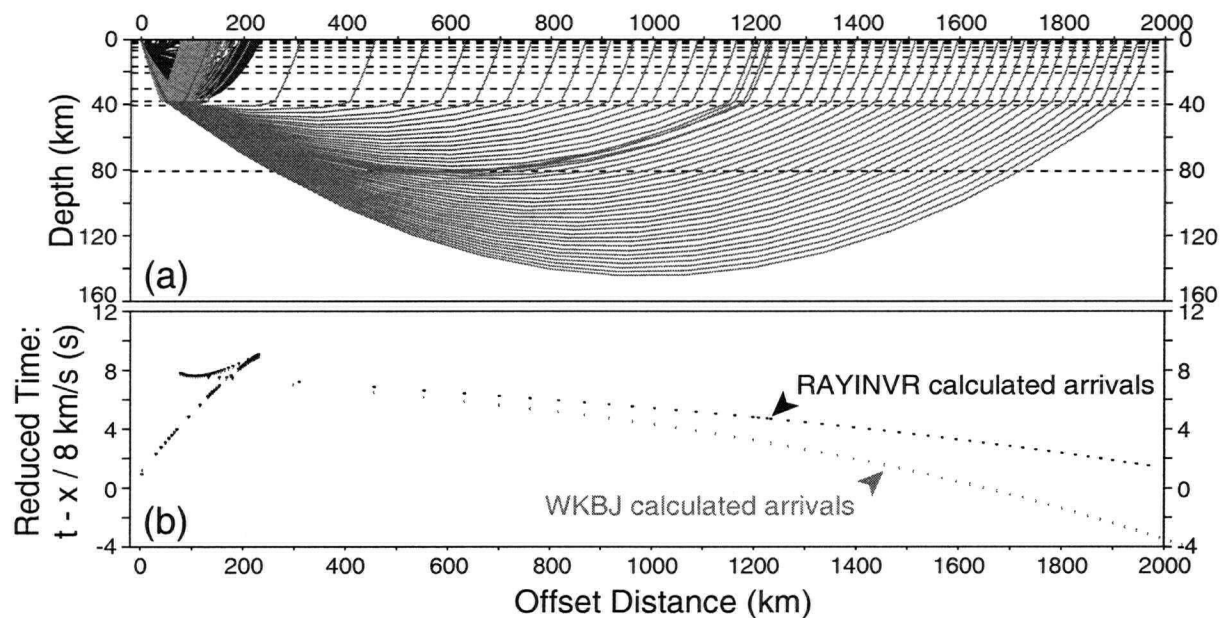


Figure 4.6: Flat Earth RAYINVR modelling of 1-D input model. (a) Example ray paths (P_g - black, P_mP - light grey, and P_n - dark grey). (b) Ray theoretical arrival times for a flat Earth (black dots) as compared to WKBJ-calculated arrival times (grey dots) calculated for a spherical Earth.

based on WKBJ. The lag becomes noticeable in the P_mP phase at about 180 km and becomes significant at about 400 or 500 km where the lag (~ 0.3 s) becomes greater than the expected errors in first arrival picks.

For a 1-D model, the flat-Earth RAYINVR method can also be used to calculate travel times which are correct for a cylindrical Earth. This is done by applying the Earth flattening transform (Eqs. 4.1 and 4.2) to the input RAYINVR model prior to tracing rays through the model. A comparison of the flat-Earth transformed velocity profile to the original cylindrical-Earth velocity profile (Fig. 4.7) gives an indication of the ‘error’ which must be introduced to the velocity model in order to accurately represent rays travelling through a spherical Earth.

The result of RAYINVR forward modelling on the flat-Earth transformed model (Fig. 4.8) shows agreement of travel-times with those calculated by the WKBJ method. This result confirms the ability of the Earth flattening transform method to accurately account for the sphericity of a

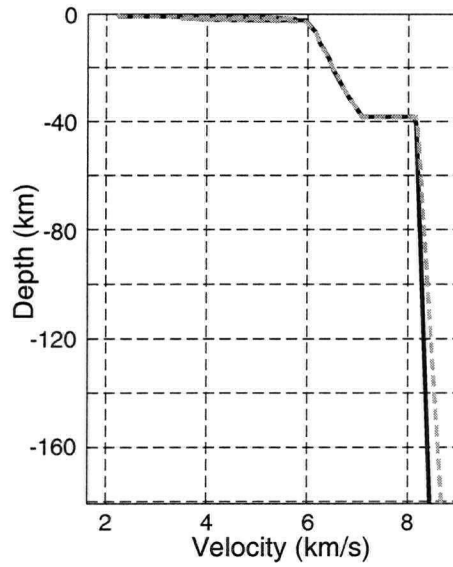


Figure 4.7: Comparison of flat-Earth transformed velocity profile (dashed grey line) to original cylindrical-Earth velocity profile (Fig. 4.5, black line).

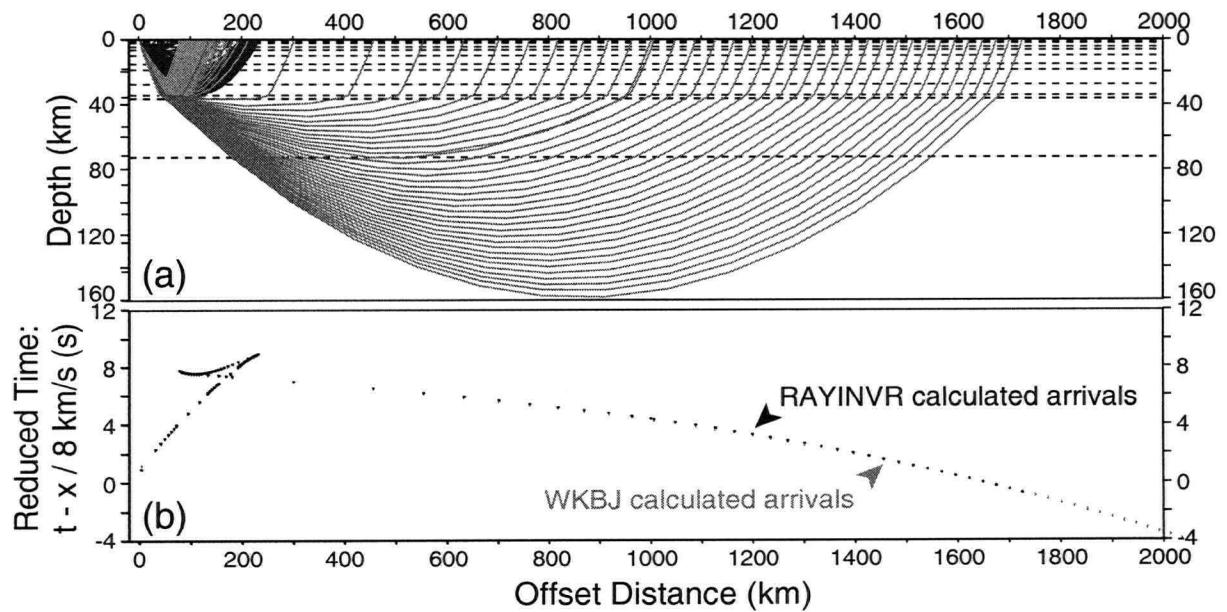


Figure 4.8: Flat Earth RAYINVR modelling of flat-Earth transformed input model. (a) Example ray paths (P_g - black, P_mP - light grey, and P_n - dark grey). (b) Ray theoretical arrival times for a flat-Earth transformed model (black dots) as compared to WKBJ-calculated arrival times (grey dots) calculated for a spherical Earth.

1-D Earth. Even though the Earth flattening transform is only exact for a 1-D representation of the Earth, it is often used as an approximation for a 2-D model of the Earth because the variability of the Earth in the horizontal direction is a major objective of modern controlled-source seismic surveys. It is the search for a more exact determination of the 2-D nature of the Earth which has led to the modifications made to the RAYINVR routine.

Cylindrical Earth Model

RAYINVR forward modelling has again been performed on the same hypothetical 2000-km-long model used for the flat-Earth example (Fig: 4.6) with no lateral velocity variations. This time, however, the RAYINVR model is parameterised using the cylindrical co-ordinate modifications developed in this chapter (Fig. 4.9).

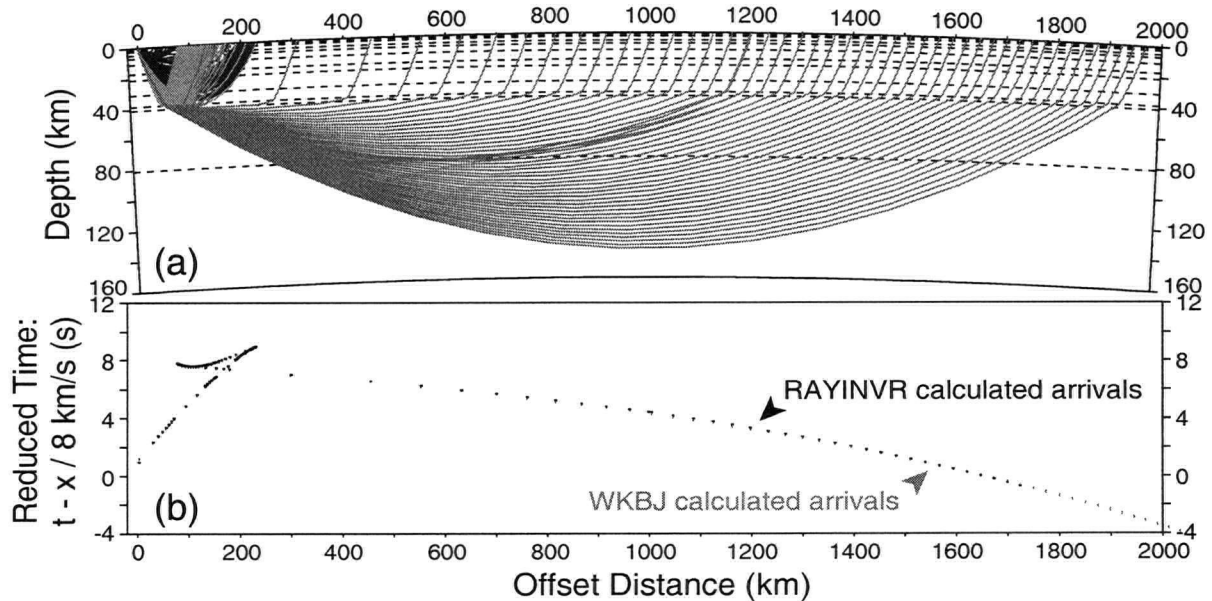


Figure 4.9: Cylindrical Earth RAYINVR modelling of 1-D input model. (a) Example ray paths (P_g - black, $P_m P$ - light grey, and P_n - dark grey). (b) Ray theoretical arrival times for a cylindrical Earth (black dots) as compared to WKBJ-calculated arrival times (grey dots) calculated for a spherical Earth.

In contrast to the flat-Earth RAYINVR modelling of the 1-D input model, and consistent with the flat-Earth RAYINVR modelling of the 1-D model with an Earth flattening transform applied, the predicted arrival times for the cylindrical-Earth RAYINVR model tie the expected times based on WKBJ. Such agreement in arrival times, calculated by RAYINVR in this 1-D model, provides confidence that the results seen in the 2-D case will be accurate.

4.2.2 Experimental example: the Deep Probe experiment

A simple illustration of the power of this technique can be seen by tracing rays through a

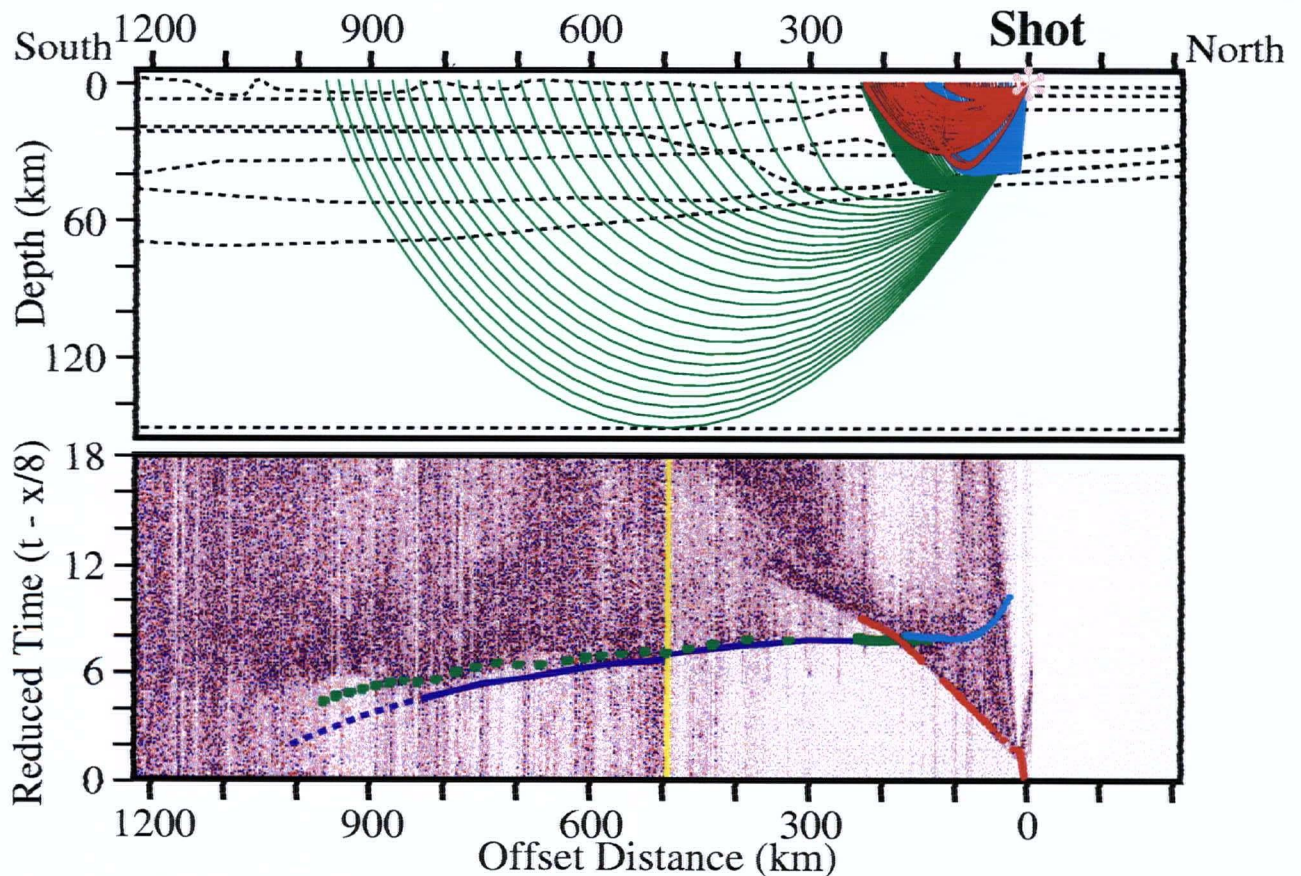


Figure 4.10: Flat Earth RAYINVR model of Shot 55. Upper plot: P_g (red), P_mP (blue), and P_n (green) ray paths through a skeleton plot of the Deep Probe velocity model. Lower plot: forward modelled travel-times (colour as before) overlain on data from shots S11 (offsets to 490 km) and DP55 (offsets > 490 km.) Interpreted P_n arrivals (dark blue) lie before predicted arrivals due to error caused by not considering curvature of Earth.

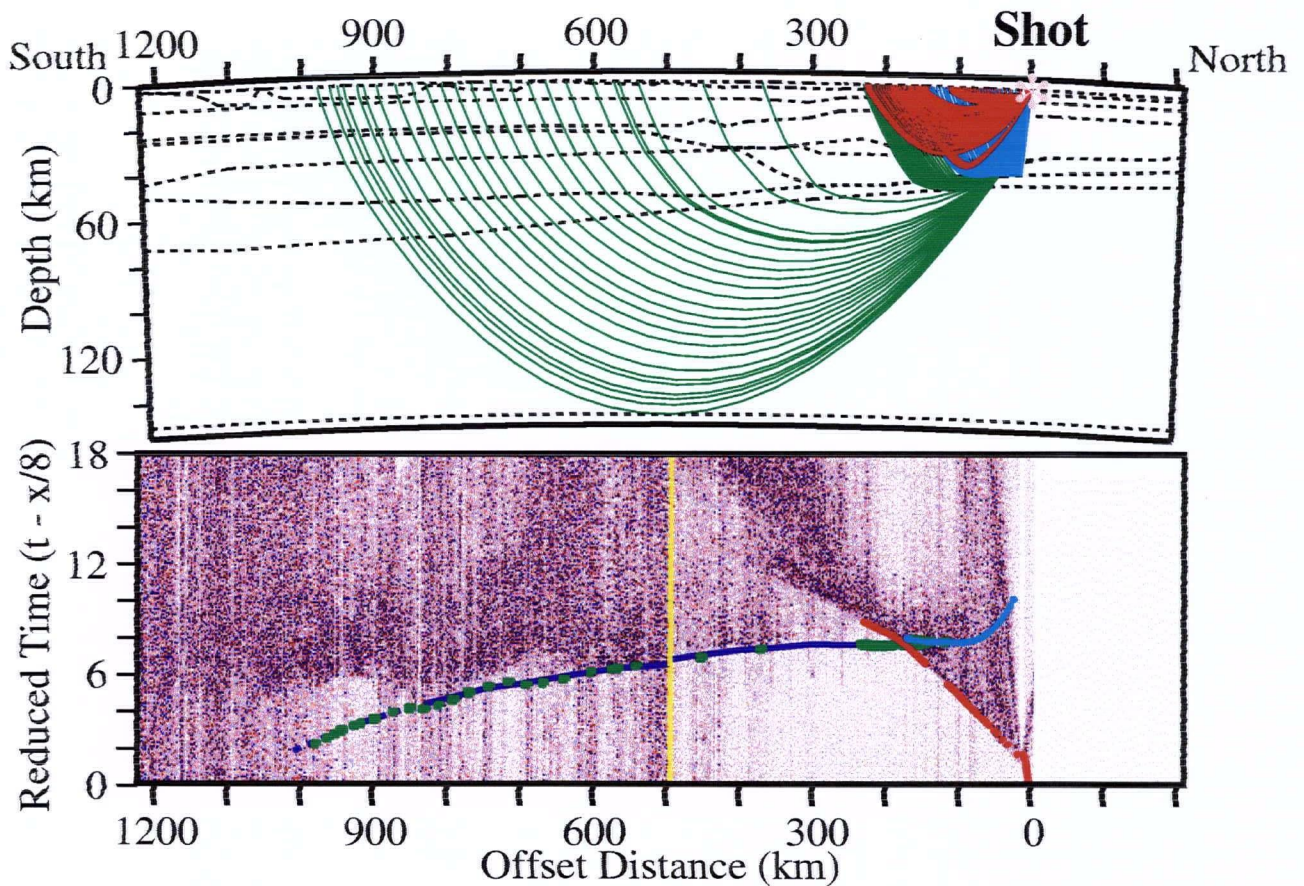


Figure 4.11: Cylindrical Earth RAYINVR model of Shot 55. Upper plot: P_g (red), P_nP (blue), and P_n (green) ray paths through a skeleton plot of the Deep Probe velocity model. Lower plot: forward modelled travel-times (colour as before) overlain on data from shots S11 (offsets to 490 km) and DP55 (offsets > 490 km.) Interpreted P_n arrivals (dark blue) coincide with predicted arrivals.

RAYINVR velocity model parameterised first as a flat Earth and then as a cylindrical Earth. The velocity model shown here is a preliminary model developed using the cylindrical Earth modifications to the RAYINVR code. Note that in the flat Earth case (Fig. 4.10), the arrival of P_n energy is predicted later than the observed arrival beyond offsets of 350 km. This divergence of the predicted and observed arrivals increases with offset and is >2 s at 900 km offset. In the cylindrical Earth case (Fig. 4.11), the predicted and observed arrivals coincide.

4.3 Discussion

Results indicate that for seismic refraction analysis of data with offset distances greater than 350 km, it is beneficial to use the cylindrical Earth modifications to RAYINVR. The primary technical success of these modifications has been the ability to maintain the program framework and model input structure established for the original code, which enables users to quickly upgrade their existing routines and models.

Empirical observations suggest that not accounting for the curvature of the Earth, either through the application of an Earth flattening transform method or the utilisation of the cylindrical-Earth ray-tracing method developed here, will result in a velocity error of +0.1 to +0.2 km/s at the depth of the Moho with errors increasing with depth. This difference is significant when interpreting lithologies at such depths, or when considering thermal effects on velocity values in the uppermost mantle. While applying the Earth-flattening approximation to a flat-Earth-derived 2-D model will reduce the error, there will still be error due to 2-D effects which are not considered by the Earth flattening transform method.

While 1-D tests are instructive in confirming the abilities of the modified code, the analysis of 2-D velocity structures can also benefit from these techniques in ways that are not so easily tested. Situations involving significant lateral variations of physical properties cannot be modelled accurately by the application of Earth flattening transform methods. In these cases, the cylindrical-Earth parameterisation of the modified RAYINVR method, which can accommodate significant lateral changes, will result in a more accurate model.

Chapter 5

Imaging the Lithosphere of Western Laurentia

The most exciting phrase to hear in science, the one that heralds the most discoveries, is not "Eureka!", but "That's funny..."

– Isaac Asimov, 1920-1992

State-of-the-art seismic refraction/wide-angle reflection (R/WAR) experiments using explosive or marine airgun sources have enabled the development of high-quality interpretations of crustal velocity cross sections on many continents and oceans. However, only a few R/WAR experiments have been of adequate length to provide velocity sections for the lithospheric mantle of the continents [*e.g.*, Iyer *et al.* 1969, BABEL Working Group 1990, Thybo and Perchuc 1997, Németh and Hajnal 1998, and references therein]. A notable exception is the series of experiments sourced with peaceful nuclear explosions in the former Soviet Union that are now being analyzed using modern procedures [Ryberg *et al.* 1996, Tittgemeyer *et al.* 1996, Morozov *et al.* 1998, Morozova *et al.* 1999]. Nevertheless, most upper mantle velocity information for the continents is derived from teleseismic earthquake studies that generate either one-dimensional (1-D) velocity-depth curves representative of a large area [*e.g.*, Hales 1981, LeFevre and Helmberger 1989] or three-dimensional (3-D) tomographic volumes that have poor lateral resolution [*e.g.*, Grand 1994, Grand *et al.* 1997, van der Lee and Nolet 1997.] The *LITHOPROBE* Deep Probe R/WAR experiment was designed to bridge the gap between regional crustal studies and earthquake mantle studies, improving constraints on velocity and structure within the lithospheric mantle.

In this chapter, the SAREX and Deep Probe data sets are used to derive a comprehensive 2-D lithospheric velocity structure section from SP 43 in central Wyoming to SP 55 in northern Alberta

(Fig. 1.1) and relate results to the major domains and subdomains along the profile. This analysis builds on (1) preliminary lithospheric velocity models for the Deep Probe corridor that illustrate the major lateral variations in structure associated with three major tectonic domains [Deep Probe Working Group 1998; Snelson *et al.* 1998] and (2) a detailed crustal velocity model for southern Alberta based on the SAREX data set [Clowes *et al.* 2000]. The analysis required modification of a well-utilized procedure for inversion and forward modelling of R/WAR data [Zelt and Smith 1992] to enable computations in radial (cylindrical) coordinates, necessary for the large offset distances being used, as described in Chapter 4. This chapter is based on a manuscript submitted in February 2000 to the *Canadian Journal of Earth Sciences* as one contribution to a thematic issue on *LITHOPROBE's* Alberta Basement Transect [Gorman *et al.* 2000].

5.1 Data

5.1.1 Acquisition Details

As detailed in Chapter 2, two consecutive and complementary seismic refraction experiments were conducted along the Deep Probe corridor in Western North America during July and August, 1995 [Gorman *et al.* 1997]. The lithospheric-scale Deep Probe experiment consisted of ten large shots ranging in size from 2400 to 17,000 kg detonated at seven locations. Fig. 1.1 shows the shot point locations in southern New Mexico (DP33), southern Colorado (DP37), central Wyoming (DP43), at the Canada-US border (DP49), central and northern Alberta (DP55 and DP57), and near Great Slave Lake in the Northwest Territories (DP61). The shots were recorded by 756 portable seismographs deployed in two arrays (Deployment 1 from central Wyoming to central Alberta and Deployment 2 from northern New Mexico to southern Montana) at a nominal interval of 1.25 km in the United States and 2 km in Canada. Table 2.1 provides the details of the shot locations and deployment of receivers. The recording arrays, which utilised almost all

portable refraction seismographs available at the time in North America, as well as some from Europe, extended across approximately 2100 km or 19° of latitude from central New Mexico to central Alberta (Fig. 1.1).

The more detailed crustal-scale experiment, SAREX, was centred on the Medicine Hat Block and conducted along the same profile as Deep Probe in the southern half of Alberta. Ten shot points with charges ranging in size from 800 to 2400 kg were positioned along the line in Canada at an average separation of 55 km. The shots were recorded by 661 portable seismographs deployed from central Alberta to southern Montana at an interval of 1 km in Canada and 1.25 km in the U.S. No U.S. shots were recorded during the SAREX experiment.

5.1.2 Seismic Observations

The data recorded during Deep Probe and SAREX varied greatly in quality depending on the source-receiver offset, near-surface conditions at the receivers, near-surface conditions at the sources and variable weather conditions along the lengthy profile. As mentioned in Chapter 2, the SAREX data set is of a more consistent quality than the Deep Probe data set since the source and receiver conditions were similar for all shots. Considerable effort was expended to merge seismic data from several different field recording systems, match their amplitudes and phases, delete poor traces, mute spurious noise, and enhance the signal-to-noise content where possible [Gorman *et al.* 1997]. Amplitude spectra show that, in regions of high or fair signal-to-noise content, coherent data are present in the frequency range of 0.5 to 8 Hz. This bandpass window has been used to filter all the data from Deep Probe and SAREX.

A representative set of data from the experiment is presented in Fig. 5.1. (All data used in the analysis are shown in Appendix A.) The primary seismic phases are labelled (P_g - energy refracting within the crust, P_mP - energy reflecting off the Moho, P_n - energy refracting in the

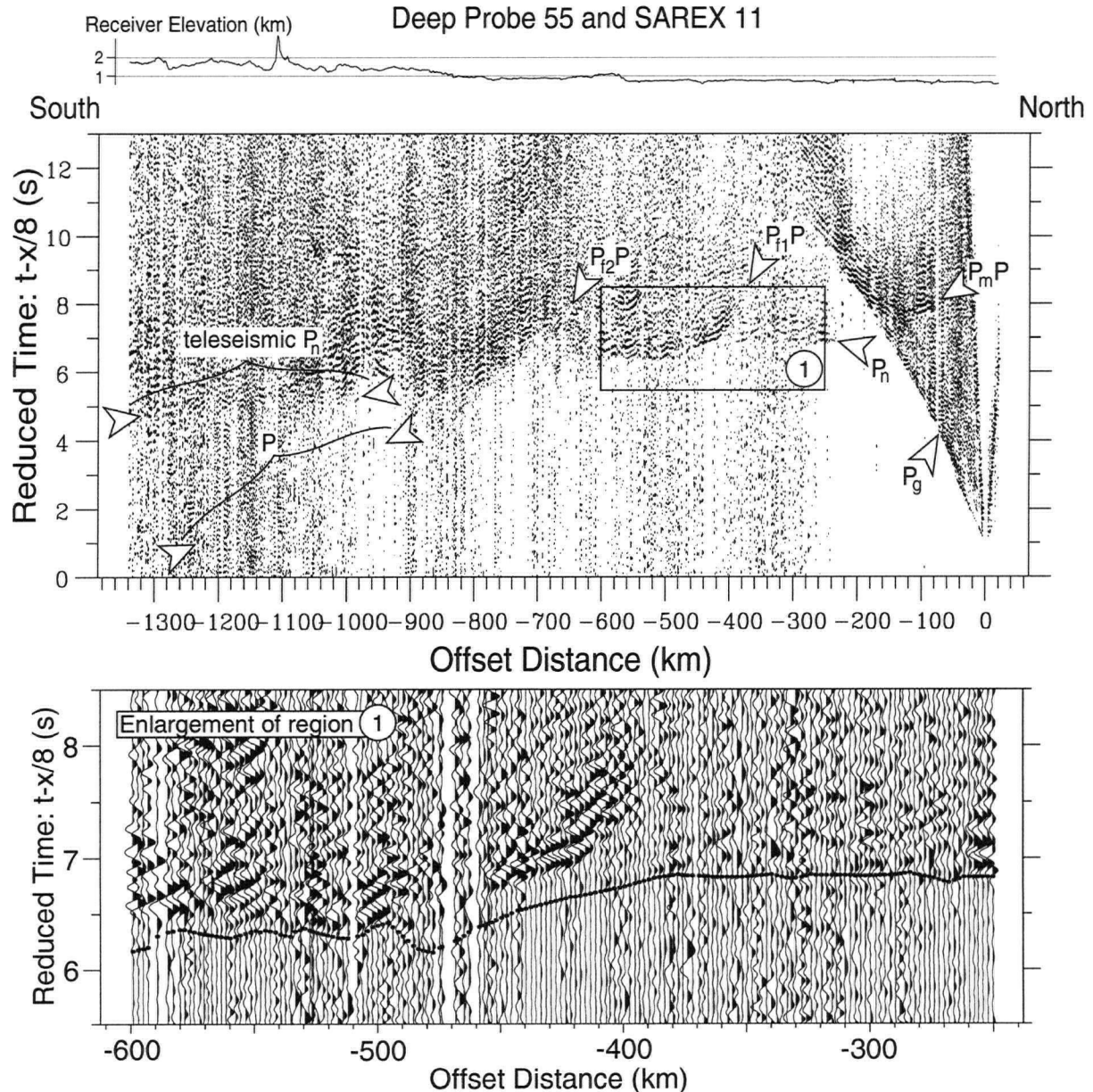


Figure 5.1: Merged data set: offsets between 0 and 282 km from SAREX 11, offsets beyond 282 km from Deep Probe 55. Significant phases are indicated (see text). Data are filtered with a 0.5-8.0 Hz bandpass filter and plotted in variable area, positive offsets only with a slight bias to remove low amplitudes. Enlargement of Region 1 (plotted in wiggly-trace variable area with no bias) details picks of the P_n -phase travel times.

uppermost mantle and P - the extension of P_n as the P body wave propagates deeper in the upper mantle.) Two significant reflections from the upper mantle, labelled $P_{f1}P$ and $P_{f2}P$ are also

indicated. These phases are visible on the south side of several of the profiles from shots located in southern Alberta. The teleseismic- P_n phase is also clearly visible at offsets between 700 and 1300 km. This phase, which is also identified in many other long-offset refraction data sets and in some earthquake-sourced data sets recorded over similar offsets, is most likely the result of energy propagating within the uppermost mantle at a relatively constant velocity, although the mechanism for its propagation is in debate [*e.g.*, Tittgemeyer *et al.* 1996, Morozov *et al.* 1998]. The phase is dealt with in more detail in Chapter 6.

The P_n phase has a ubiquitously weak amplitude in these data and can be difficult to pick. As a result, confidence in the P_n travel-time picks varies from high (enlargement in Fig. 5.1) to low (Fig. 5.2). Errors, in the range of ± 25 ms to ± 125 ms are assigned accordingly. A discussion of the picking process is included as part of Section 5.2.2.

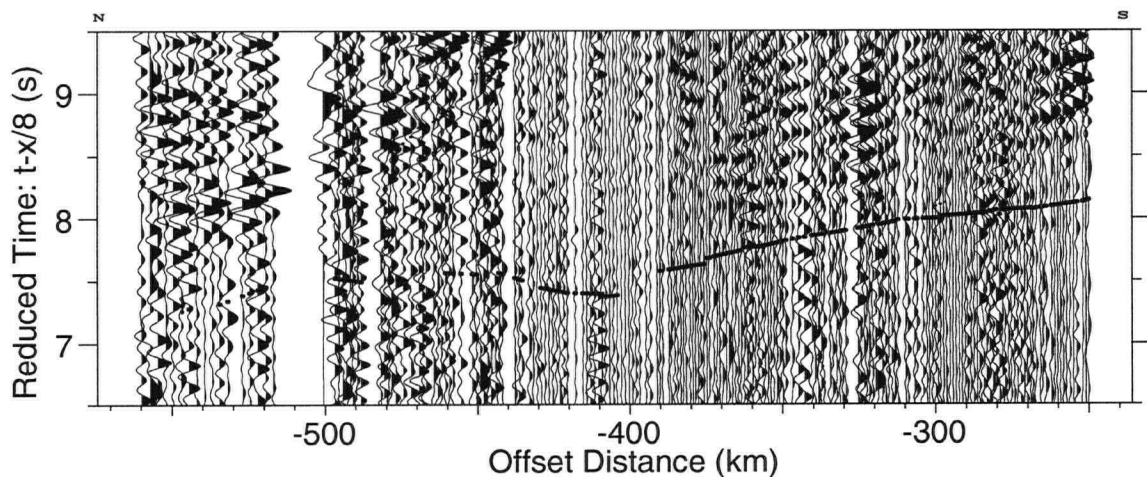


Figure 5.2: P_n phase extracted from SAREX 9 (See Fig. A.9 in Appendix A for the complete shot record). Data are filtered with a 0.5-8.0 Hz bandpass filter and plotted in wiggle-trace variable area with no bias. Picks of the P_n -phase travel times are denoted. Additional examples of shorter offset P_n arrivals are shown in Fig. 5.10.

5.1.3 Preliminary Interpretations

Using evidence from direct analysis of the shot records, 1-D reflectivity modelling [Fuchs and Müller 1971] of several of the large shot gathers, tau-p analysis on a shot-by-shot basis [Chapter 3, Gorman and Clowes 1999] and forward ray-trace modelling [Luetgert 1992], a 2-D image of the lithosphere along the Deep Probe corridor was developed (Fig. 5.3; Deep Probe Working Group 1998). Three well-defined provinces are identifiable in the crustal section: the Hearne Province in the north, the Wyoming Province in the centre of the profile and the accreted terranes of the Yavapai - Mazatzal Province in the south. In the upper mantle, two distinctly different velocity structures are interpreted, one beneath the Wyoming and Hearne provinces, the other beneath the accreted terranes. 1-D velocity profiles extracted from the 2-D model summarise the province-wide crustal and mantle structure of the three distinctly different lithospheric regions (Fig. 5.3).

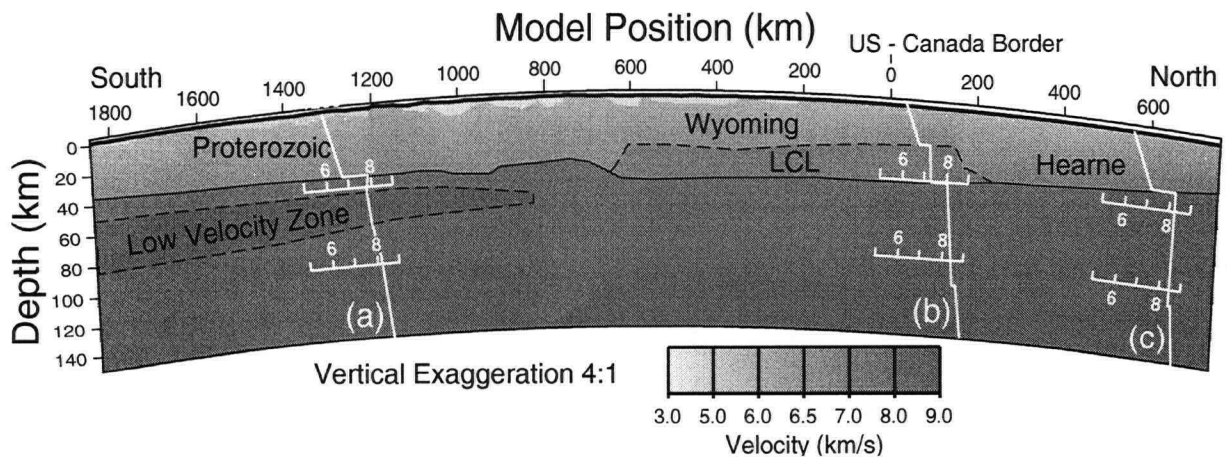


Figure 5.3: Initial 2-D interpretation of Deep Probe [Deep Probe Working Group 1998] used as input model to current study. Earth curvature is correct for any given depth but is exaggerated vertically 4:1. Three characteristic 1-D velocity curves are extracted from the model: (a) Yavapai - Mazatzal Province (-1260 km), (b) Wyoming Province (50 km), (c) Hearne Province (610 km). LCL – lower crustal layer. In this and subsequent figures, the model position in km is indicated north (positive) and south (negative) of the Canada-U.S. border.

Hearne Province

The Hearne Province beneath south-central Alberta has velocity characteristics very similar to those determined for regions of Canada where the shield is exposed [*e.g.*, Boland and Ellis 1989; Winardhi and Mereu 1997]. The northernmost velocity-depth profile in Fig. 5.3 shows a typical Moho (averaging ~ 40 km depth) for an Archean region. The crustal velocity ranges from 6.0 to 7.2 km/s and it is characterized by a simple vertical velocity gradient. Velocities immediately below the Moho are ~ 8.2 km/s and increase smoothly with depth with a gradient of 0.0046 km/s/km. This compares closely to upper mantle velocity profiles that have been observed beneath the Canadian Shield to the northeast [LeFevre and Helmberger 1989] and other Archean cratons around the world.

Wyoming Province

The central profile in Fig. 5.3 shows an average velocity profile for the crust and upper mantle for the region capped by the Archean Wyoming Province. The crustal thickness is much greater (approximately 50 km) with a high velocity layer ($V_p \sim 7.1-7.3$ km/s) in the lower ~ 25 km of the crust. At 6.6 km/s, the mean crustal velocities are the highest observed in the data set. The significance of the lower crustal layer will be discussed later in this chapter. At 8.1 km/s, the uppermost mantle velocity is almost the same as that of 8.2 km/s beneath the Hearne Province to the north. The velocity profile for the uppermost mantle is very similar to that observed beneath the Hearne Province.

Yavapai - Mazatzal Province

The southernmost velocity curve in Fig. 5.3 shows average velocities through the region of Proterozoic accreted terranes underlying the Southern Rocky Mountains / Colorado Plateau

[Karlstrom and Bowring 1988]. In this region, the crust is 40-45 km thick, with little change in crustal velocity other than an approximately linear increase in velocity with depth. The mean crustal velocity is 6.3 km/s. Although ray coverage, and hence resolution of crustal velocity structure, is limited by recordings from only three shot points (Fig. 1.1), these observations are somewhat puzzling for two reasons. A simple velocity profile is surprising for a region that presumably has undergone crustal-scale Laramide tectonism [Burchfiel *et al.* 1992], and the thickness of the crust does not appear to be great enough to support the present-day regional topography. A possible solution to these problems may be found in the velocities modelled in the upper mantle. Near the top of the mantle, a low velocity zone that may represent buoyant mantle sufficient to support the high elevations observed in the overlying crust is interpreted. The upper mantle profile from the southern Rocky Mountains is comparable to Walck's [1983] velocity profile for the Gulf of California, a part of the East Pacific Rise spreading system. This suggests that an 'oceanic' or extensional style hot and low-velocity upper mantle is in place beneath this part of the continent.

Comparison of crustal and uppermost mantle signatures

On a global basis, shields and platforms are seen to have an average crustal thickness of 41.5 ± 5.8 km with a mean crustal velocity of 6.42 ± 0.20 km/s, whereas orogenic crust has thicknesses of 46.3 ± 9.5 km with velocities of 6.39 ± 0.25 km/s [Christensen and Mooney 1995, Rudnick and Fountain 1995]. The Yavapai - Mazatzal Province crust is of typical thickness but has lower velocities compared to these averages. The Wyoming Province crust is thicker and faster than the averages for shields and platforms, but matches fairly well with the averages for orogens. The Hearne Province crust conforms to global averages for thickness and velocity.

One of the first significant observations made on the Deep Probe data set was that there were extreme differences in the P_n phase to the north and south of Deep Probe shot 43 [Deep Probe Working Group 1998]. To the north, the mantle underlying the Wyoming and Hearne provinces

has a velocity that is 8.1-8.2 km/s just below the Moho, increases with depth, and shows no evidence for a low velocity zone. To the south, a 1-2 km thick mantle lid with velocities of 7.95-8.0 km/s overlies a ~40-km-thick low velocity zone with a minimum velocity of 7.75 ± 0.1 km/s at a depth of 60 km. In general terms, this agrees well with regional-scale teleseismic models for the mantle of North America [Grand 1994, Grand *et al.* 1997, and van der Lee and Nolet 1997]. However, all three of these continental-scale lithospheric velocity models appear to show the transition from hot, low-velocity, 'oceanic' mantle to cold, fast, 'continental' mantle to occur below the middle of the Wyoming Province, rather than at the boundary between the Wyoming Province and Proterozoic orogens to the south. This could be the result of the lateral resolution of the teleseismic technique and/or the extraordinary thickness of the Wyoming crust.

The analysis presented in this chapter focuses primarily on the lithosphere capped by the Archean crustal provinces (*i.e.*, the Hearne and Wyoming provinces). Many questions remain concerning the tectonic relationship between these two provinces. By combining the data sets from SAREX and Deep Probe, the resolution of this study is greater than in other parts of the Deep Probe profile and is sufficient to draw some significant conclusions about the tectonic history of the region.

5.2 Radial Earth Ray-Theoretical Travel-Time Inversion

5.2.1 Method

Controlled-source seismic data are often modelled by ray-theoretical methods in a Cartesian reference frame. However, as detailed in Chapter 4, a better approach for seismic surveys of extended length is to perform the ray tracing in a radial co-ordinate system. To this end, a modification to the ray-theoretical travel-time inversion routine, RAYINVR, of Zelt and Smith [1992] has been implemented for the Deep Probe analysis. In this modified routine, the ordinary differential equations

used to trace rays through a model are rewritten in a radial co-ordinate system and the method for calculating distances between points in the model (and hence calculating total travel times for any given ray) is modified to reflect radial geometries.

Subsequent steps in the development of the velocity model follow the accepted RAYINVR method [Zelt and Forsyth 1994]. The comparison of travel times observed in recorded data to travel times predicted by tracing rays through a hypothetical model of the Earth is the fundamental operation. The procedure strives to minimise the difference between these two times within a specified error for all the observed travel times picked by the modeller. This is accomplished by modifying the input velocity model, constructed by a framework of nodes which specify velocity and depth, in one of two ways: permitting the depth node of a layer boundary to change, or permitting the boundary velocity in the layer above or below a node to change. For any particular iteration of the routine, the modeller has explicit control over the type of modifications and positions of nodes which are permitted to be changed. After each iteration of the routine, three important statistical parameters are calculated and used by the interpreter to assess the changes done.

1. The number of picks used indicates whether or not picks are being excluded due to the new geometry of the model.
2. The RMS travel-time residual provides a value for the average difference in travel times between observed and modelled arrivals. The inversion routine attempts to minimise this value.
3. The normalised chi-squared value indicates if modelled travel times lie within the anticipated error in the observed travel times. The inversion routine seeks to make this value as close to unity as possible.

These statistical indicators help to quantify the accuracy of the final model, but they should also

be used in concert with (1) considerations of model resolution (*e.g.*, minimum observable length scales at depth) and (2) effective ray coverage (*e.g.*, ray paths successfully traced for all observed arrivals) [Zelt and Forsyth 1994].

5.2.2 Data Analysis

Travel times were picked on the records from the ten SAREX shot points and three of the Deep Probe shot points (55, 49, and 43 North) which had data of usable quality. On all records, three primary phases were picked, P_g - crustal refractions, P_mP - reflections from the Moho and P_n - upper mantle refractions. On several records additional phases were interpreted and picked. These included reflections from the top of a lower crustal layer in the Medicine Hat Block (MHB) and Wyoming Province, P_iP ; refractions from within this layer, P_i ; and two enigmatic reflectors in the uppermost mantle beneath the north and south margins of the MHB, $P_{f1}P$ and $P_{f2}P$. The $P_{f1}P$ and $P_{f2}P$ events are included in the RAYINVR model as floating reflectors, defined as reflecting boundaries by a series of depth nodes which are not necessarily accompanied by a change in modelled velocities. Floating reflectors are a useful feature within RAYINVR structural models as they are used to represent changes in local physical properties which result in reflections not caused by bulk shifts in velocity (*e.g.*, fault planes). Table 5.1 summarises the picks included in this study.

The 'layer-stripping' approach [Zelt and Forsyth 1994] was used as the basis for the modelling method. In addition, several over-riding conditions were considered during this procedure to make use of *a priori* information [Zelt 1999]. The starting model for the inversion was based largely on analysis done by the Deep Probe Working Group [1998]. In addition, preliminary results from the travel-time inversion of the SAREX data set [Burianyk *et al.* 1997] were incorporated into the larger model for Deep Probe. The Deep Probe model has a considerably simpler upper crust than that of the SAREX model, which incorporates several significant layers

Table 5.1: The number of picks made for each phase followed by the average uncertainty (ms) in parentheses.

Shot Point	P_g	P_iP	P_i	P_mP	P_n	P_{f1}	P_{f2}	Total
55	–	–	–	6 (47)	680 (134)	42 (131)	109 (143)	837 (134)
11	241 (47)	–	–	94 (111)	348 (118)	41 (126)	32 (150)	756 (97)
10	282 (51)	–	–	110 (87)	309 (124)	40 (111)	70 (155)	811 (96)
9	373 (71)	–	–	195 (110)	200 (142)	40 (102)	71 (111)	879 (100)
8	404 (49)	–	–	169 (113)	135 (143)	–	84 (141)	792 (89)
6	411 (56)	–	–	178 (139)	152 (141)	43 (135)	–	784 (95)
5	405 (48)	–	–	215 (130)	143 (136)	–	–	763 (88)
4	330 (49)	69 (110)	–	200 (128)	144 (131)	–	–	743 (92)
3	358 (41)	39 (147)	–	186 (137)	194 (127)	–	–	777 (91)
2	381 (52)	50 (88)	–	96 (129)	192 (147)	–	–	719 (90)
1 / 49	645 (60)	257 (122)	57 (74)	293 (112)	443 (140)	–	–	1695 (100)
43(N)	78 (33)	44 (66)	76 (58)	77 (117)	496 (140)	–	–	771 (115)
Total	3908 (53)	459 (114)	133 (65)	1819 (120)	3436 (135)	206 (121)	366 (139)	10327 (99)

within the Western Canada Sedimentary Basin [Clowes *et al.* 2000]; the Deep Probe model has limited the representation of the sediments to a single layer of average properties. For the uppermost crust, published basin studies and well analyses were used to constrain the model [Snelson 1998, Snelson *et al.* 1998, Mossop and Shetsen 1994]. Depths within the uppermost crust were not allowed to vary where they were controlled by well data; velocities were only permitted to

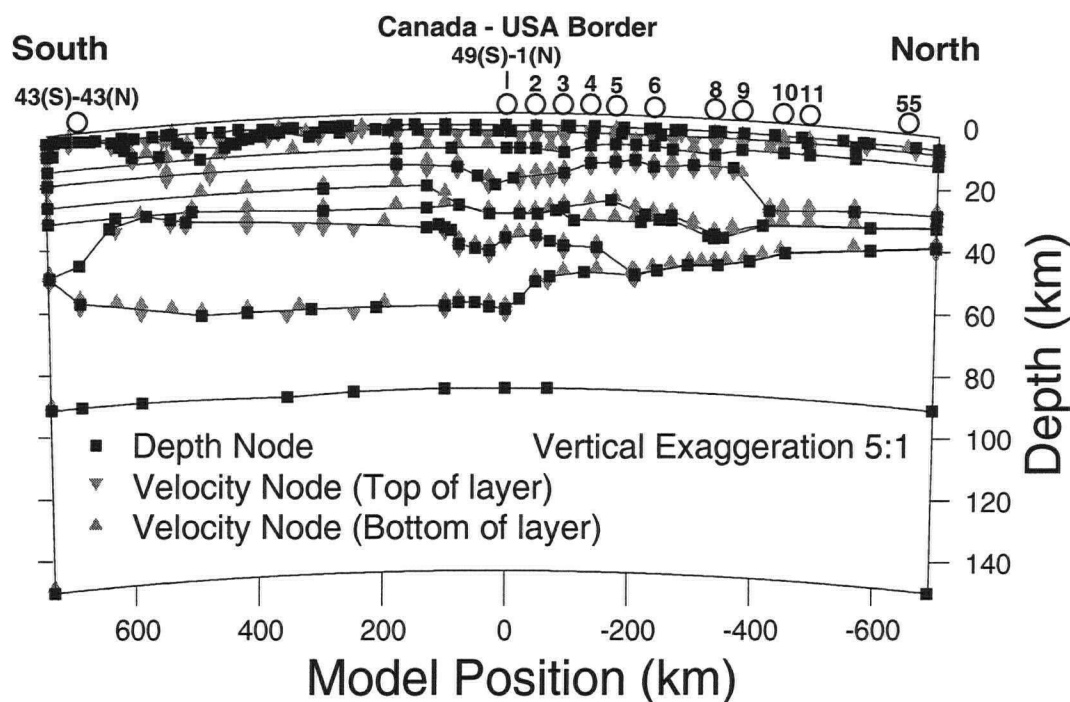


Figure 5.4: Model node distribution (squares and triangles) superimposed on a skeleton of the Deep Probe model. Increased density of nodes in north due to higher resolution of model.

vary slightly. In a few cases where shot and receiver positions were at some distance perpendicular to the line of the Deep Probe profile, this resulted in poor travel-time fits. This is especially evident, for example, in the crustal phases recorded from shot 43 in central Wyoming. This shot was more than 50 km off-line in a region where near-surface basin geology is greatly variable due to dramatic uplifts of Archean rocks interspersed with very deep Phanerozoic basins. Velocity and depth node positions along each layer were initially limited to be no more frequent than two for every shot position. However, as modelling progressed, additional nodes were added in a limited number of instances. This was especially necessary for modelling curved reflectors. Unnecessary structures were avoided. The depth and velocity node distribution for the final model is seen in Fig. 5.4.

To develop the final Deep Probe velocity structure model, the modified RAYINVR forward modelling and inversion procedure was carried out in an iterative manner. Rays traced through

the model illustrate model coverage for the different phases (Fig. 5.5). Due to shot point coverage, the top of the lower crustal layer is defined only at the north and south ends by observations of the P_iP and P_i phases. At the north end, within the Medicine Hat Block, good ray coverage enables a moderately-well-constrained interpretation of an upper boundary to the lower crustal layer which has considerable structure, suggesting a dynamic tectonic history. Observations of the P_mP phase are more widespread, with the exception of the central part of the Wyoming Province and immediately south of the Canada-U.S. border (0 km on the model). The former case is expected due to shot point coverage, but the latter case suggests that the Moho immediately south of the Canada-U.S. border is structurally complex. Observations of the P_n phase are consistent from shot to shot and surprisingly clear for the smaller SAREX shots. As a result, control of uppermost mantle velocities in this study is improved over the preliminary regional interpretation of the Deep Probe Working Group [1998].

Statistical results of the travel-time inversion provide a measure of how well the model fits the data (Table 5.2). As previously mentioned, one of the major causes of error in this model is the greatly variable nature of the shallow crust in the Wyoming Province. This can be clearly seen by removing Deep Probe shot 43 from the statistical calculations. When this is done, the normalised χ^2 error is reduced and the RMS misfit times for the model are much closer to the expected average uncertainty in the observed data. Even with this consideration, the errors for most phases are high. Only for one minor phase do normalised χ^2 values approach unity and often the model misfit is much greater than measured uncertainty. The cause of this partly lies in the method used for quantifying uncertainty in the seismic travel-time picks. An automated routine which assigns an uncertainty for each pick based on comparing the energy of envelopes before and after the pick on each seismic trace is used. This technique is well suited to assigning uncertainties for first arrival picks in relatively noise-free data. However, this method is partially flawed when assigning error for much of the Deep Probe data set for three reasons.

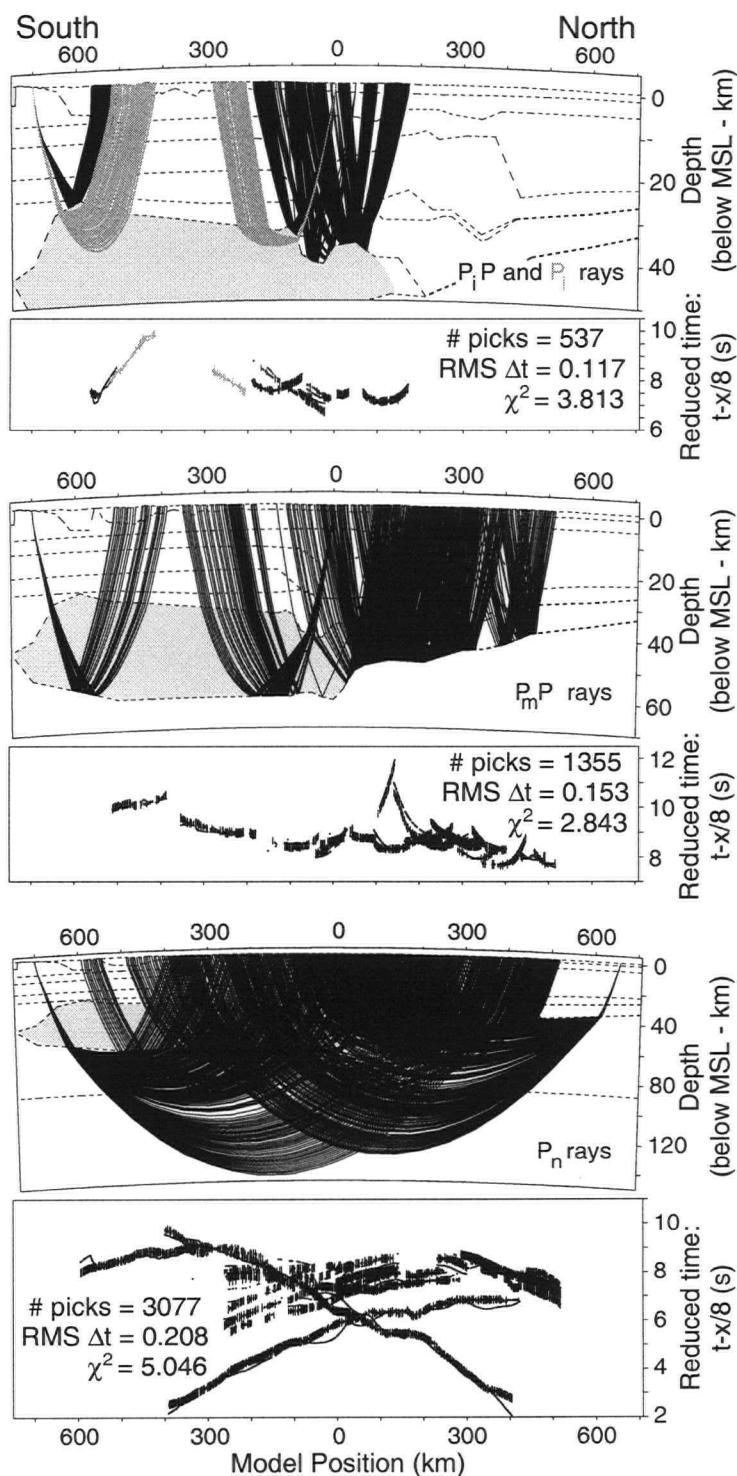


Figure 5.5: Summary of ray tracing results by phase: P_iP , P_i , P_mP , and P_n . Ray paths are plotted on sketches of the velocity model which show dashed lines for boundaries. The lower crustal layer discussed in this chapter is shown in grey. Time-distance plots show calculated (small dots) and interpreted (vertical bars with length corresponding to error) arrival times. Horizontal distance and time scales are constant for all plots; depth scales on ray diagrams vary to emphasize coverage.

Table 5.2: Statistical modelling results. ^aResults excluding Deep Probe shot 43.
^bResults for floating reflectors f_1 and f_2 .

Phase	Number of Picks	Average Uncertainty (s)	Number of Picks Used	RMS Misfit (s)	Normalised χ^2
P_g	3908	0.053	3835 (98.1%)	0.126	12.566
P_g^a	3830	0.054	3705 (96.7%)	0.098	6.649
P_iP	459	0.114	404 (88.0%)	0.126	4.055
P_iP^a	415	0.119	362 (87.2%)	0.118	2.893
P_i	133	0.065	133 (100.0%)	0.082	3.169
P_i^a	57	0.074	57 (100.0%)	0.052	0.786
P_mP	1819	0.120	1353 (74.4%)	0.152	2.828
P_mP^a	1742	0.121	1276 (73.2%)	0.155	2.846
P_n	3436	0.135	3077 (89.6%)	0.208	5.046
P_n^a	2940	0.134	2585 (87.9%)	0.201	5.097
Total	9755	0.097	9006 (92.3%)	0.165	7.960
Total ^a	8984	0.096	8089 (90.0%)	0.151	5.363
P_f^b	572	0.133	344 (60.1%)	0.198	5.223

1. Many of the picks used are secondary arrivals which are picked on the basis of trace-to-trace characteristics. Therefore, energy envelopes before and after these secondary phases will be 'contaminated' with noise and energy from other phases.
2. Especially in low signal-to-noise, far-offset data, picks are often very interpretive. The automated technique used for assigning error cannot take interpretive error into consideration.
3. The method does not consider localised variations (*e.g.*, near-surface variations) which may not be resolvable by the model but are present in the data.

Even with these shortcomings, the automated assigning of error was used to provide consistency and to avoid the effects of assigning error in an *ad hoc* fashion.

Two significant floating reflectors were added to the model once the velocity determinations were finalised. These reflectors, corresponding to the P_{f1} and P_{f2} events observed on five shot

records (Deep Probe 55, Fig. 5.1; and SAREX 8, 9, 10 and 11, Fig. 5.6), are dipping to the north and lie in the upper mantle beneath southern Alberta. While both have similar dips and lengths, the northern, f_1 , reflector (between model positions 175 and 310 km and depths 48 and 83 km) is significantly shallower than the southern, f_2 , reflector (between model positions 25 and 150 km and depths 85 and 124 km). The reflections have fair to good signal-to-noise characteristics. In order to keep the model as simple as possible, the floating reflectors were defined by only two depth nodes, one on each end.

Amplitude modelling was not used as a constraint in producing a final lithospheric velocity model for two reasons. First, the amplitude responses of some instruments used during data acquisition were never determined satisfactorily. Estimations of instrument responses were made, but these were complicated by the varied near-surface conditions observed along the profile. It is estimated that amplitude information between instrument types in the Deep Probe data set is accurate only within a factor of two or three. Second, for most of the upper mantle phases observed in the data, the signal-to-noise ratio is close to unity. Only by observing several traces side-by-side can interpretations be made. Therefore, error in assigning travel times to these phases is higher than for typical crustal phases and accordingly amplitudes cannot readily be measured. The lack of amplitude control in the model is partially offset by ensuring that rays are traced for all locations where travel times were picked. Table 5.2 readily shows that for most phases a great majority of the picked events are traced in the model.

5.2.3 A Cross-Section of Platformal Western Laurentia

The final Deep Probe velocity structure model is displayed in Fig. 5.7. It represents a north-south slice through the lithosphere of western Laurentia capped by the Archean platforms of the Hearne and Wyoming provinces and their overlying sedimentary basins. The issue of model resolution will be dealt with quantitatively in the next section, but qualitatively, the resolution decreases,

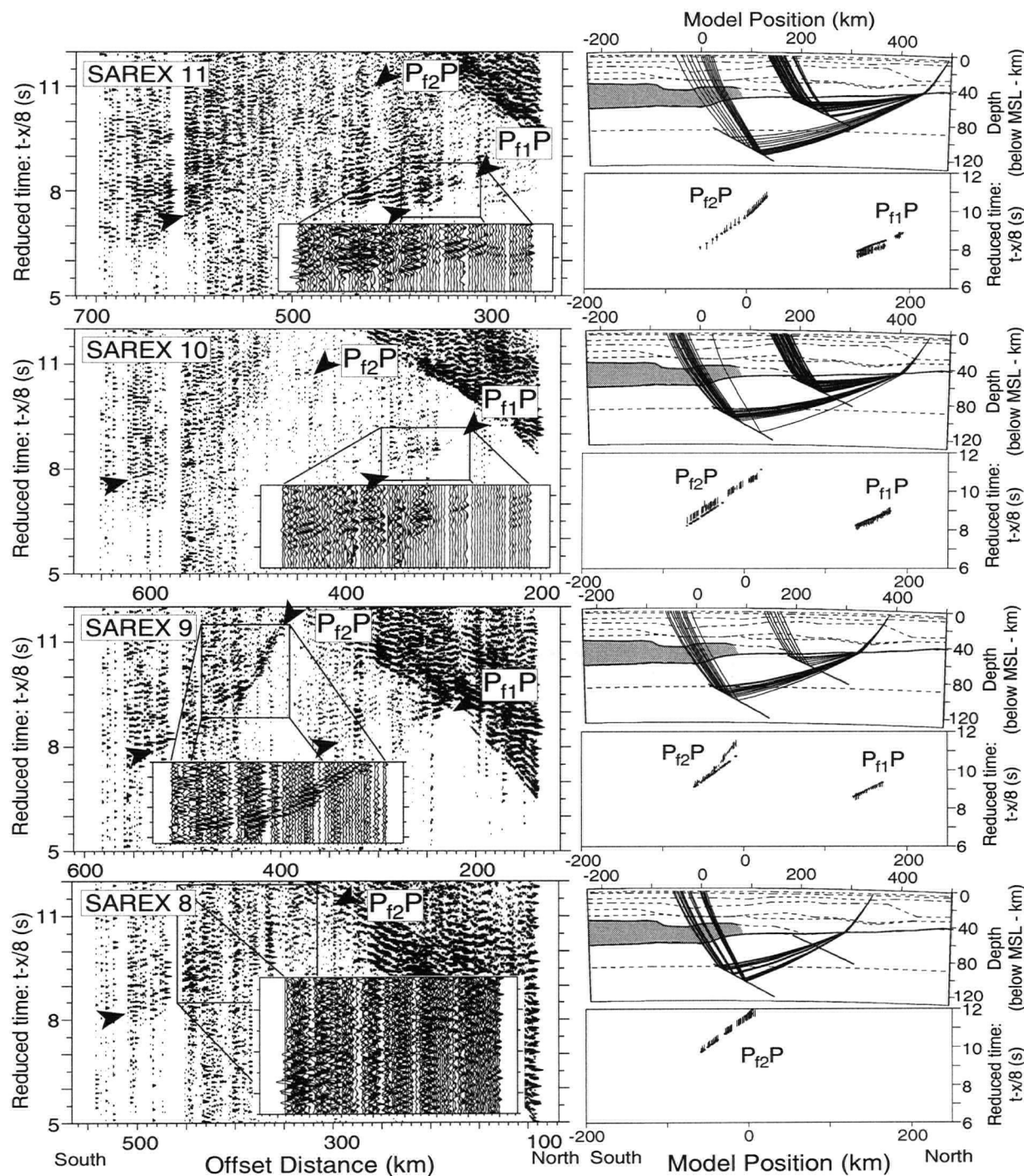


Figure 5.6: Data examples: upper mantle reflectors f_1 and f_2 beneath southern Alberta. Data from four shots are shown (variable area, positive amplitudes only, 15% bias) to highlight the deep, northward-dipping reflectors seen to the south of SAREX shots 8, 9, 10 and 11. Offset distances are indicated for each plot; these correspond to model positions 200-km south to 250-km north. Exemplary phases are shown in close-up (wiggle-trace, variable area). Ray paths are plotted on sketches of the velocity model which show dashed lines for boundaries within the model and solid lines for reflectors. The lower crustal layer discussed in this chapter is shown in grey. Time-distance plots, covering the same $t-x$ windows as in the data plots, show calculated (small circles) and interpreted (vertical bars with length corresponding to error) arrival times.

and hence the length scales at which meaningful interpretations can be made increase, from north to south. There are several contributing factors to this, the most important being the distribution of shot points. The presence of the SAREX data set in Alberta greatly increases ray coverage in the Hearne crust. This can be clearly seen in the velocity model (Fig. 5.7) as the intensity of the velocity colour-scale is controlled by the ray coverage at any point within the model. A second factor is that the near-surface geology in the north, that of the Western Canada Sedimentary Basin, is much more regular than that of the region deformed by the Laramide orogeny to the south (Fig. 5.3), thereby facilitating seismic acquisition and interpretation. A third consideration, while not affecting model resolution directly, does affect the scale at which the northern portion of the model beneath the Western Canada Sedimentary Basin can be interpreted. In this region, high-resolution gravity, aeromagnetic and seismic reflection data, combined with basement core sample measurements and observations of the exposed shield to the northeast, define characteristics of the Hearne Province and Medicine Hat Block at a level of detail greater than those observed to the south.

A schematic structural interpretation of the velocity model is shown in Fig. 5.8 and discussed in the remainder of this section. First-order structures identified include the major crustal divisions which were identified in preliminary modelling but resolved more clearly in these results. This interpretation also shows numerous more subtle features, such as the shape and distribution of reflecting surfaces. The geometry of reflectors at boundaries within the crust and at the Moho and those which correspond to hypothesised relict subduction zones in the upper mantle provide additional constraints on the origin and tectonic history of the lithosphere in this region.

The Crust

The present interpretation of the lower crust and upper mantle beneath the Wyoming and Hearne provinces greatly enhances previously published results through the incorporation of the SAREX data set and the use of the travel-time inversion technique. Although more complex than in the

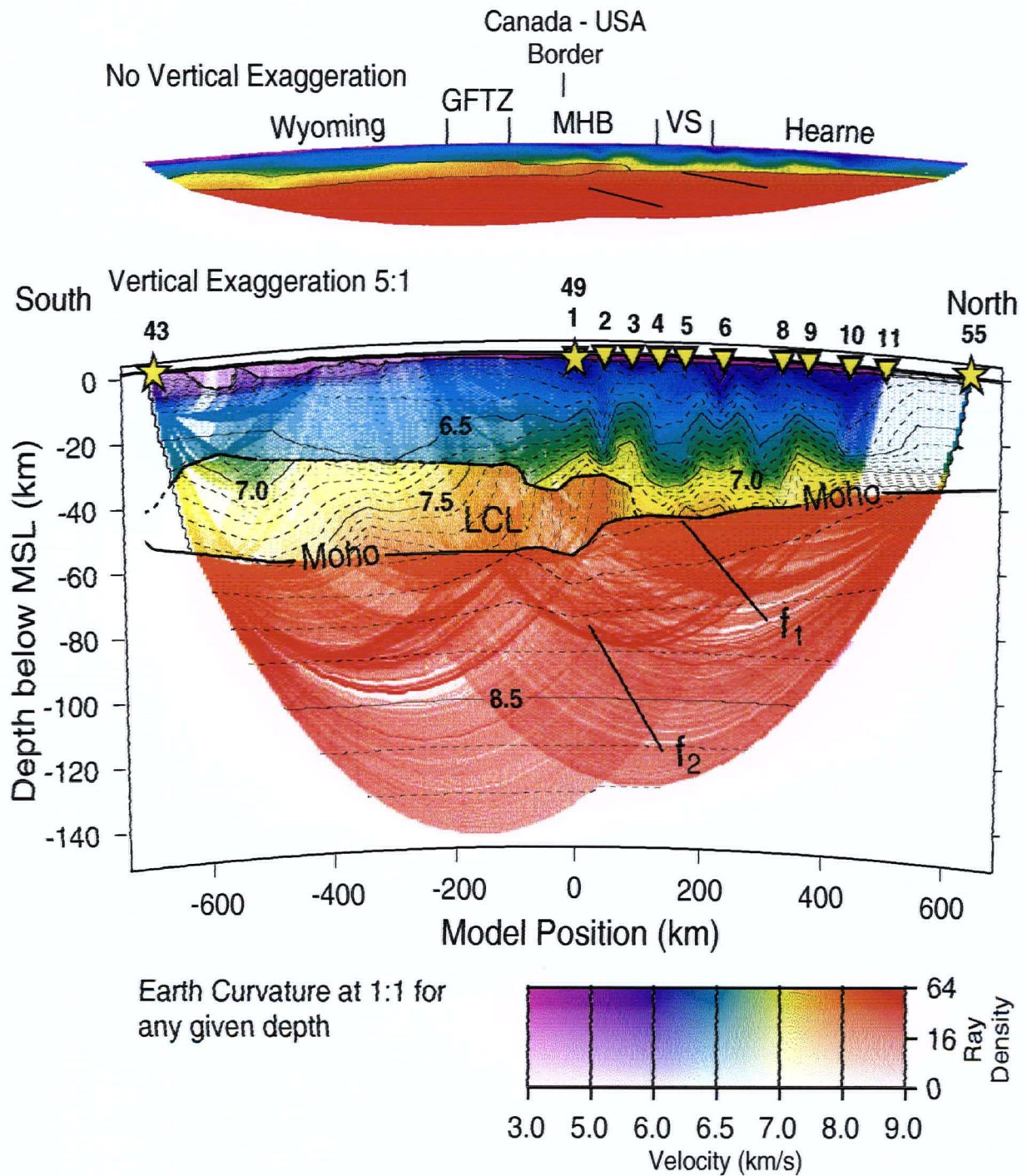


Figure 5.7: Interpreted Deep Probe velocity model. Velocities are shown in colour with significant contour lines overlain. Contour interval: 0.1 km/s. Labelled features include: LCL – lower crustal layer, f1 and f2 – upper mantle floating reflectors. Intensity of colour is a logarithmic representation of the number of rays traced through a particular cell (cell size: 5 km laterally and 500 m vertically); full intensity is at 64 rays per cell. Model position in km is indicated north (positive) and south (negative) of the Canada-USA Border. Deep Probe (stars) and SAREX (triangles) shot points are shown. Moho depth south of SP 43 is determined from Deep Probe Working Group [1998]. Positions of major crustal features are indicated on the 1:1 representation of the model at the top: GFTZ – Great Falls Tectonic Zone, MHB – Medicine Hat Block, VS – Vulcan Structure.

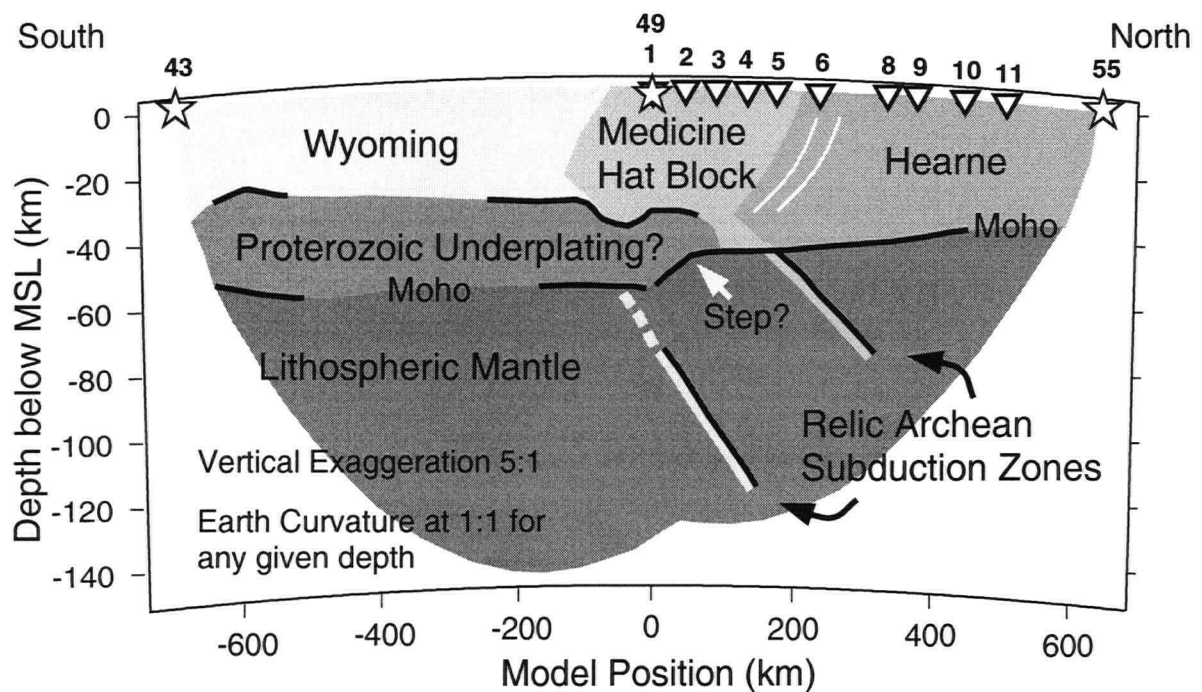


Figure 5.8: Schematic structural interpretation of the Deep Probe velocity model in Fig. 5.7. Reflective boundaries indicated by solid black lines. Model position in km is indicated north (positive) and south (negative) of the Canada-USA Border. Deep Probe (stars) and SAREX (triangles) shot points are shown.

initial model (Fig. 5.3) [Deep Probe Working Group 1998], the two distinct crustal signatures for the Hearne and Wyoming provinces remain well defined. The final model also exhibits the following, more subtle features not observed in the preliminary analysis.

- The velocity structure of the Medicine Hat Block is seen to be distinct from that of the Wyoming and Hearne provinces. Its upper crustal section has velocities similar to those seen in the Hearne Province whereas the lower crustal layer has velocities higher than those seen in the lower crustal layer within the Wyoming Province.
- The reflective top of the lower crustal layer within the Medicine Hat Block and the Moho at its base are seen to have considerable structural relief.
- The southern end of the lower crustal layer, although admittedly poorly constrained relative to other parts of the model, has significantly lower velocities than those interpreted at the

north end of the lower crustal layer.

- The modelled depth of the Moho at the base of the Wyoming Province, at ~ 56 - 58 km, is deeper than the original model, which indicates that the Wyoming Province is considerably thicker than global averages (see 5.1.3 Preliminary Interpretations).

In general terms, the final RAYINVR model can be described as follows. From north to south, the crust of the Hearne Province thickens considerably from 34 to 50 km. The velocity structure of the Hearne crust, which is the subject of a more detailed investigation [Clowes *et al.* 2000], appears to have considerable variability. The variations are dominated by horizontal velocity changes which undulate with a period of approximately 150 - 200 km. This is consistent with previous geological and potential field interpretations which define several Archean-aged crustal domains in the platformal Hearne Province beneath the Western Canada Sedimentary Basin [*e.g.*, Ross *et al.* 1991]. These domains have a similar length scale to the velocity undulations seen in the model. For the most part, velocity values modelled in the Hearne crust match those from the preliminary interpretations (6.0 - 7.2 km/s). However, there is a small high-velocity region (~ 7.5 km/s) at the base of the crust between SAREX shots 5 and 6 which has been identified in the current detailed model and corresponds to the location of the Vulcan Structure as identified by potential field methods (Fig. 1.2). At the approximate location of the Vulcan Structure, the crustal velocity structure changes dramatically. A lower crustal layer with anomalously high velocities in the range of 6.9-7.8 km/s underlies the Medicine Hat Block and the entire Wyoming Province. The top of the layer produces a marked mid-crustal reflection and exhibits significant structure. This is well constrained in the Medicine Hat Block and northernmost Wyoming Province by Deep Probe shot 49 and SAREX shot 1 (Fig. 5.9) as well as SAREX shots 2, 3, and 4 (Fig. 5.10). Due to shot and receiver geometries, control on the velocity structure of the lower crustal layer is weak beneath the centre of the Wyoming Province, but near Deep Probe shot 43 in central Wyoming, reflections are again observed from the top of a lower crustal layer. The termination of the lower

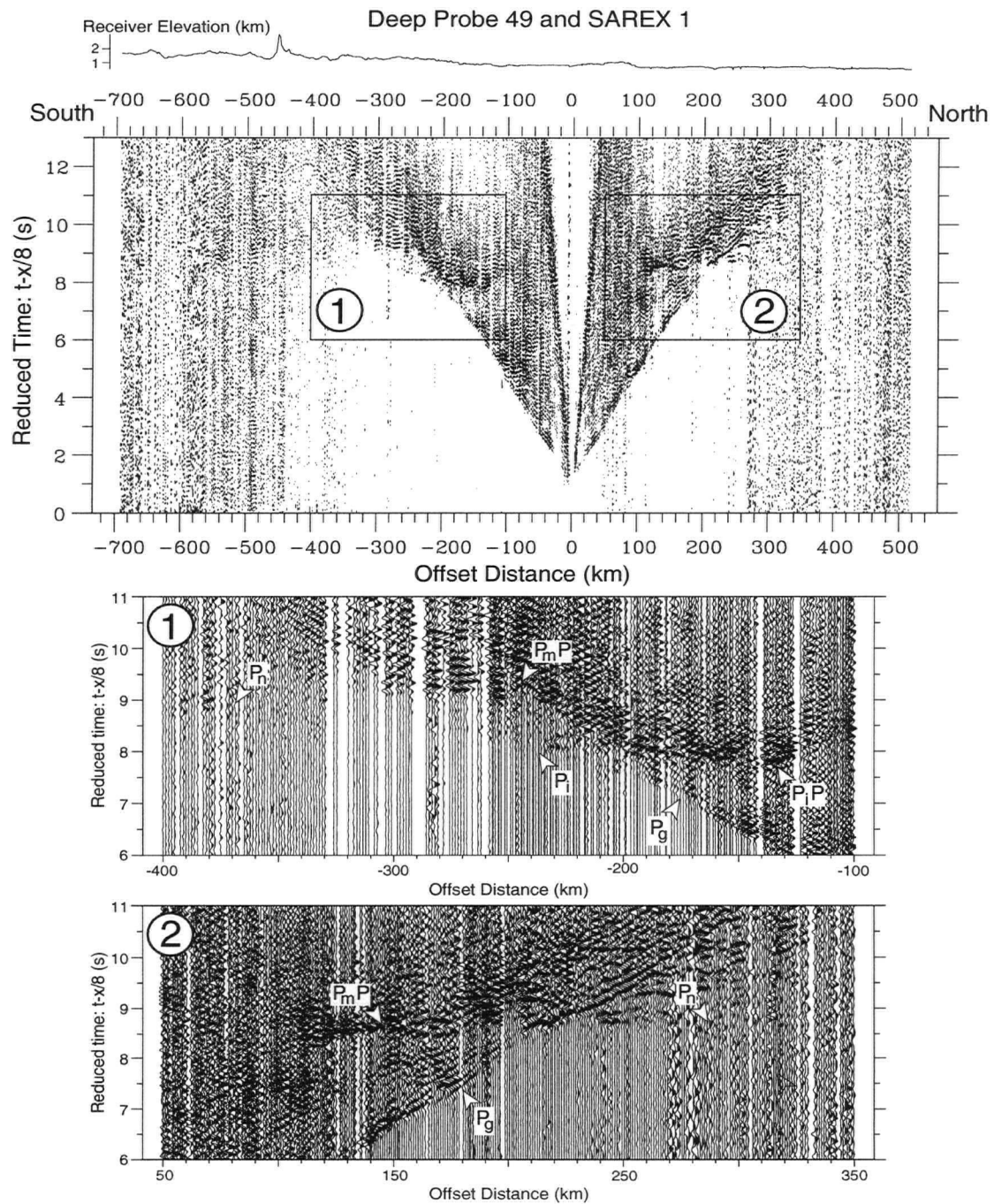


Figure 5.9: Merged data set: Deep Probe 49 and SAREX 1 (Shot point location at Canada - USA Border). Data are merged and filtered with a 0.5-8.0 Hz bandpass filter. Data are plotted in variable area, positive offsets only with a slight bias to remove low amplitudes. Two close-ups (Wiggle-trace, variable area, no bias) are shown to highlight the differences in the lower crustal reflector and Moho reflection and refraction characteristics to the north and south of the shot point.

crustal layer, as shown in the previous interpretation [Deep Probe Working Group 1998], is north of the Cheyenne Belt in southern Wyoming, the boundary between the Wyoming and Yavapai - Mazatzal provinces.

The dramatic difference between the crustal signature to the south of the Canada – U.S.A. boundary, where the lower crustal layer is present, and to the north where it is not, is apparent even in first-order observations of the data (Fig. 5.9). South of the shot point, two strong reflectors, one from the top of the lower crustal layer (P_iP) and one from the Moho (P_mP) can be distinguished along with a first-arrival refracted event (P_i), with an apparent velocity of 7.3 km/s, from within the lower crustal layer. The cross-over distance from the P_g to P_i phase occurs ~ 185 km south of the shot while the cross-over from P_i to P_n occurs at ~ 310 km. To the north only the P_mP reflection is seen. The cross-over from P_g to P_n occurs at ~ 225 km north of the shot. These observations on their own indicate the presence of thicker crust and a high-velocity lower crustal layer south of the Canada-US border. No observable difference can be seen in the apparent velocity of P_n , ~ 8.1 km/s, north and south of the shot.

This interpretation corroborates the results of two pre-digital, crustal-scale seismic refraction studies, the only studies of comparable size that tie directly to the Deep Probe profile. In southern Alberta, within the Medicine Hat Block, an east-west refraction study [Chandra and Cumming 1972] crosses the Deep Probe profile at the location of SAREX shot 4. In this early study, a lower crustal layer with a velocity of 7.17 km/s was interpreted between depths of 37.5 and 47.0 km using the plus-minus method to position planar features between reversed seismic sources. The current model at this position shows a layer between depths of 41.0 and 49.3 km with velocities smoothly varying from 7.10 to 7.30 km/s. The uppermost mantle velocity in both the early study and the current model is 8.10 km/s. In Montana, another east-west study, analysed using the same techniques as the Canadian study, crosses the Deep Probe profile about 100 km south of the Canada-U.S. border in the vicinity of the Great Falls Tectonic Zone [McCamy and Meyer

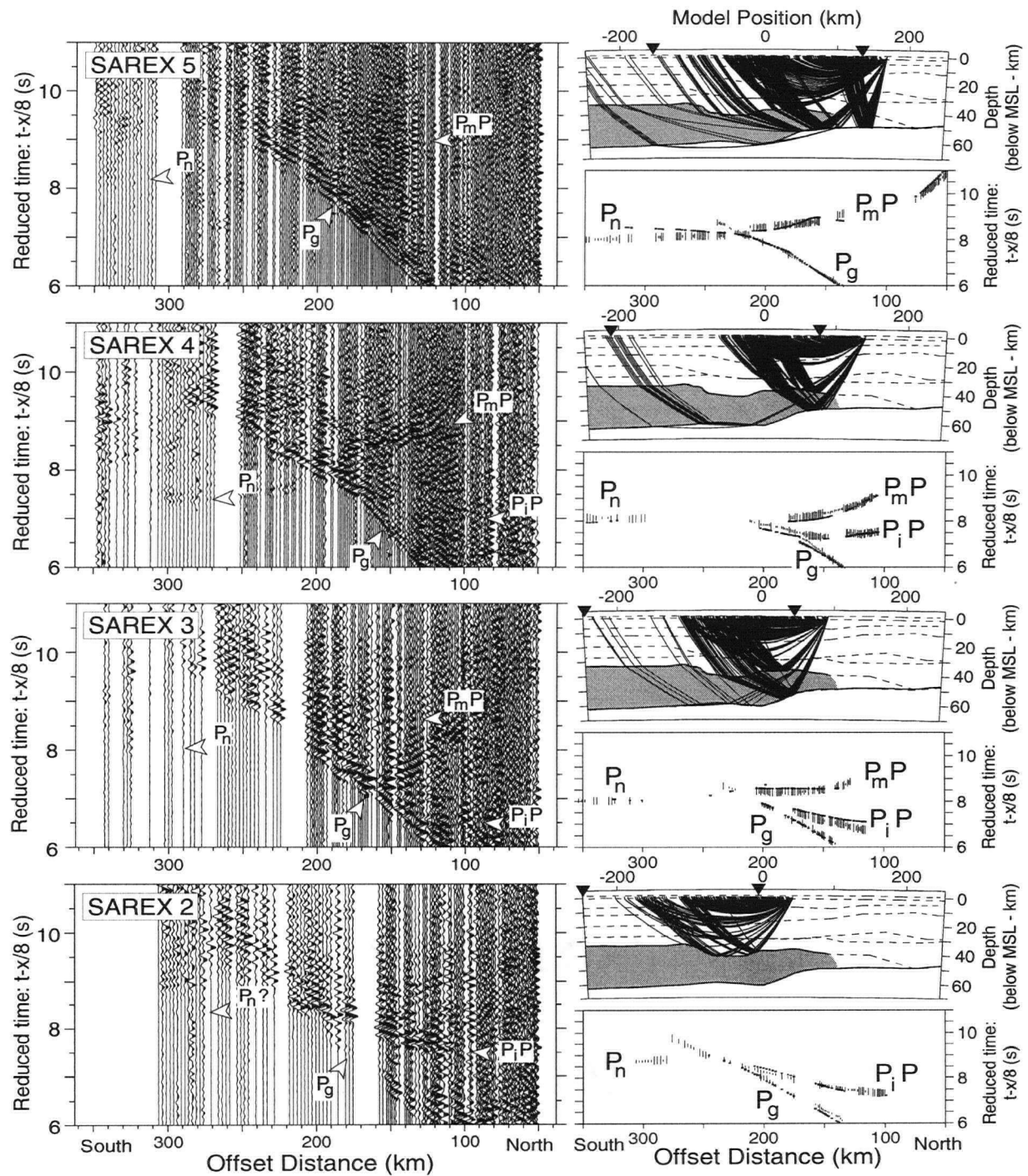


Figure 5.10: Data examples: lower crustal layer of the Wyoming Province and Medicine Hat Block. Four subsets of the data are shown (wiggle-trace, variable area) to highlight the changes in the character of the P_iP and P_mP reflections to the south of SAREX shots 2, 3, 4 and 5. Only offsets between 50 and 350 km south of each shot are shown. Ray paths are plotted on sketches of the velocity model which show dashed lines for boundaries within the model and solid lines for reflectors. The lower crustal layer is shown in grey. Offsets of plotted seismic data lie between the triangles on each ray diagram. Time-distance plots showing calculated (small circles) and interpreted (vertical bars with length corresponding to error) arrival times are shown for each example.

1964]. Unfortunately the positioning of shots and receivers for the earlier study leaves a gap in the interpretation at its intersection with the Deep Probe profile. However, the region of western Montana lying to the west of the tie point is characterised by a very thick lower crustal layer extending from 20 to 50 km depth with an average velocity of 7.3 km/s. Considering the offset distance ($\sim 100 - 200$ km), this early model ties well to the Deep Probe model in central Montana where a similarly thick lower crustal layer lies between depths of 33 and 58 km with velocities ranging from 7.6 to 7.8 km/s. The interpreted upper mantle velocity in the original model is 8.2 km/s; the same as that determined in the current study.

In interpreting the seismic data, the P_iP , P_i and P_mP phases needed to be picked in a consistent manner from shot to shot. This was especially important for the closely spaced SAREX shots and Deep Probe shot 49 beneath the MHB and northernmost Wyoming Province. Even with a shot spacing of ~ 50 km, the three phases which define the lower crustal layer were variable. The secondary arrivals were generally difficult to pick since they often were complicated by spurious coherent energy in the records. In order to produce a final model that had picks that were consistent with modelled arrivals, it was necessary to iteratively repick several of the events. It is likely that the surfaces imaged for the Moho and the top of the lower crustal layer have a 3-D geometry that cannot be fully recovered with this 2-D technique. Due to the geometry of the experiment, P_iP and P_i phases were only recorded by receivers south of the shot points. Three of the shot gathers shown in Fig. 5.10 (SAREX 2, 3 and 4) and the lower left enlargement in Fig. 5.9 (Deep Probe 49) show a well defined P_iP phase. SAREX 5 (Fig. 5.10) does not show this phase. Only Deep Probe 49 shows a well defined P_i phase as a first arrival, in a region corresponding to the thickest part of the lower crustal layer within the Wyoming Province.

The top of the lower crustal layer beneath the Medicine Hat Block varies in depth from 37.4 km in the north to 41.0 km in the south. Crossing the Great Falls Tectonic Zone to the south, the

depth decreases to 33.8 km beneath the northernmost part of the Wyoming Province. In the southernmost part of the Wyoming Province, the depth to the top of the lower crustal layer shallows to 27.3 km. The lower crustal layer is modelled to be variable in thickness with an average of 16 km within the Medicine Hat Block and 25 km within the Wyoming Province. Structure on the Moho is similar in length scale to that seen on the top of the lower crustal layer, plunging from a depth of 49 km beneath the Vulcan Structure to a maximum of 60 km beneath north-central Wyoming before rising dramatically to 45 km beneath the Cheyenne Belt [Deep Probe Working Group 1998].

The Upper Mantle

The velocity structure of the uppermost mantle is shown to have little variability in velocity beneath the Hearne and Wyoming provinces. An important difference between this model and previous work is that velocities are slightly lower (approximately 0.1 km/s slower at the top of the mantle). This is primarily due to modelling the profile using the radial Earth method. The interpretation is also improved by the addition of the SAREX data that includes well-defined P_mP and P_n phases. In general, uppermost mantle velocities appear to be slightly faster at locations where the Moho is deeper. There does appear to be a slight deviation from this trend, although at the limit of velocity resolution, beneath the Great Falls Tectonic Zone extending from the Moho (~ 58 km deep) to a depth of ~ 80 km, where relative velocities are ~ 0.1 km/s higher than in neighbouring regions. This may be an indicator of different tectonic regimes north and south of this region.

Two strong upper-mantle reflections are observed on several of the profiles from SAREX (Fig. 5.6). Due to the linear geometry of the data set, out-of-plane sources for these reflections cannot be ruled out. However, there are no apparent features in current interpretations of the crust

of southern Alberta and northern Montana with orientations that could generate the observed arrivals. Therefore, it is assumed that the reflections are from features lying in the plane of the profile. This is a simplification that is used to evaluate these features using a ray-theoretical method.

Both reflections are modelled as being roughly 125 km in length and dipping to the north with slopes of $\sim 15^\circ$ for the northern reflector and $\sim 18^\circ$ for the southern one. The northern reflector extends down from just beneath the crust-mantle boundary, whereas the deeper southern reflector descends from 85 km depth. Up-dip extrapolation of the northern reflector ties it with the Vulcan Structure; a similar extrapolation for the southern reflector projects it to the Great Falls Tectonic Zone (Figs. 5.7 and 5.8). This suggests that these mantle features may be related to sutures between the Medicine Hat Block and the Hearne Province to the north and the Wyoming Province to the south. The dips of the reflectors are suggestive of subduction to the north.

Previous R/WAR experiments have also observed reflectors in the upper mantle beneath western Canada and the contiguous states to the south. COCORP reflection data in Montana [Best 1991] and *LITHOPROBE* R/WAR data in Saskatchewan [Németh and Hajnal 1998] have recorded upper mantle reflectors that were associated with events in the uppermost mantle beneath the Trans-Hudson Orogen, just to the east of the current study area. However, unlike the reflectors seen on the Deep Probe / SAREX data, the Trans-Hudson Orogen reflectors were modelled to have little dip, suggesting a different origin than the reflectors seen in the current study.

5.2.4 Resolution

The Deep Probe seismic data were acquired and interpreted on a scale that bridges the gap between earthquake-sourced tomographic modelling of North America and several crustal-scale, controlled-sourced seismic experiments that have been conducted along its length. These experimental methods have varied abilities to resolve features of different length scales, so assessing

the resolving power of Deep Probe in comparison to other experimental methods is necessary to evaluate the current model and compare it to previous studies.

As previously noted, continental-scale tomographic experiments [*e.g.*, Grand 1994, Grand *et al.* 1997, and van der Lee and Nolet 1997] all show a transition from high-velocity and cold to low-velocity and hot upper mantle occurring beneath the middle of the Wyoming Province, whereas the Deep Probe results show this transition ~ 300 km farther south, at the boundary between the Wyoming and Yavapai - Mazatzal Provinces. This difference is within the error bounds of the tomographic studies (about 500 km horizontally, and 100 km vertically.)

Previous crustal-scale controlled-source seismic studies conducted near the Deep Probe profile possessed lower resolving power than Deep Probe / SAREX. The ambitious Project Early Rise [Iyer *et al.* 1969] and several regional refraction studies [McCamy and Meyer 1964, Chandra and Cumming 1972] had poor lateral resolution due to limited numbers of shots and large receiver spacings. They were most useful in developing regional 1-D models similar to what would be derived from teleseismic studies. The only detailed refraction survey in the region [Kanasewich *et al.* 1969], was acquired in an era when analogue recording and limited processing power yielded low-resolution models of the velocity structure of the basement rocks. No modern high-resolution crustal refraction studies have been conducted along the study profile.

In contrast, high-resolution seismic reflection surveys have been acquired near the Deep Probe corridor. In Alberta, the *LITHOPROBE* Southern Alberta Lithospheric Transect, SALT 95, runs parallel to the Deep Probe profile [Eaton *et al.* 1999]. However, although these data are very successful at imaging the deep crust, they do not image major features in the upper mantle. South of the border, the most significant regional reflection studies, COCORP's Montana transect and Wind River Uplift seismic reflection studies [Best 1991], unfortunately are oriented perpendicular to the Deep Probe profile. Seismic reflection data sets provide poor constraints on velocity, but effectively resolve the geometry of impedance contrasts (on the order of 4 km laterally and

<2 km vertically at the depth of the Moho.)

The resolution of the P-wave velocity model developed for Deep Probe lies between the two extremes described above. Laterally, resolution is variable, as previously mentioned, due to the unequal distribution of shot points along the profile. In general, resolution and uncertainty in the upper crust are dependent on shot spacing while at deeper parts of the model, ray path geometries are the dependent factor [Zelt and Forsyth 1994]. Ray coverage can be observed directly in the final model (Fig. 5.7) where the colour intensity is related to the number of rays passing through a particular cell of the velocity model. Standard procedures have been developed to quantitatively evaluate the resolution and uncertainty of a model produced by ray-theoretical travel-time inversion [Zelt 1999]. These procedures involve perturbing specific velocity and depth nodes of the model to test local spatial resolution and absolute parameter uncertainty. These tests have been applied in an *ad hoc* manner to significant portions of our model. In regions of good ray coverage, errors in depths and velocities are estimated to be <1.5 km and <0.1 km/s for the lower crust and Moho and <4 km and <0.2 km/s for the upper mantle; lateral resolution of structures in the lower crustal and upper mantle is <25 km. In regions of poor ray coverage, *e.g.*, the central Wyoming Province, errors in depths and velocities are estimated to be <8 km and <0.3 km/s for the lower crust and Moho.

In addition to observations of ray coverage, a general appreciation for the resolution of the RAYINVR model can be gained from the distribution of velocity and depth nodes that specify the velocity model used (Fig. 5.4). The distribution of nodes can be compared directly to the number of shots used in the model. The region of SAREX has ten shot locations distributed over 496 km while the southern region has only one shot in ~700 km. In general, the model has more nodes defined than should be necessary for a well constrained model. However, to avoid a geologically unreasonable model containing sharp breaks and bends, the additional model control points were added.

Additional evaluation of resolution and uncertainty is desired for some of the more significant structural features within the model. For example, at the north end of the lower crustal layer within the Wyoming Province and Medicine Hat Block, the Moho and top of the lower crustal layer show features exhibiting changes of up to 10 km vertically over as short as 50 km laterally. The topography on the top of the lower crust and on the Moho is intrinsically linked with the thickness of the lower crustal layer and the velocities present within it. For features such as these, the non-uniqueness of the RAYINVSR method is utilised to produce multiple models with equal uncertainties. In some of these test models, velocities are relatively constant above and below a very irregular boundary, while in others velocities vary greatly around a boundary free of structure. All test models must show adequate ray coverage where it is expected based on the recorded seismic data. Trade-offs between structures and velocities are required, but finally a velocity-depth model is chosen which provides acceptable RMS travel-time residuals and χ^2 values while conforming to geological and geophysical expectations.

5.3 Implications for the History of Lithospheric Assemblage in Western Laurentia

The velocity structural model from the combined Deep Probe and SAREX R/WAR data sets not only adds detail to the existing tectonic models for this region [Hoffman 1989] but provides evidence supporting several modifications. The model identifies three independent Archean crustal blocks which are interpreted to have collided with each other accompanied by limited subduction, evidence for which is preserved as reflective features in the upper mantle. In addition, the model supports the presence of a high-velocity lower crustal layer beneath the southern two blocks which is interpreted to be Proterozoic in age. This section details the interpretation of these major model features. Fig. 5.11 summarises the proposed tectonic assemblage history of western Laurentia.

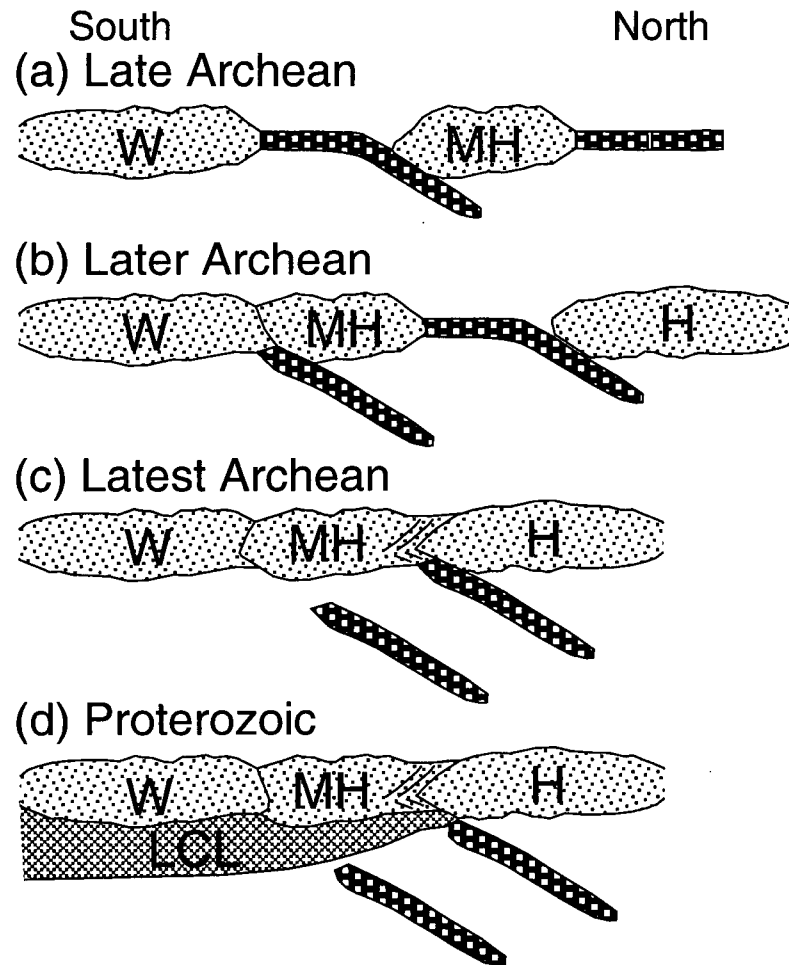


Figure 5.11: Cartoon summarising the tectonic assemblage of western Laurentia. (a) Wyoming Province (W) and Medicine Hat Block (MH) collide accompanied by limited north-dipping subduction. (b) Amalgamated Wyoming Province / Medicine Hat Block and Hearne Province (H) collide accompanied by limited north-dipping subduction. (c) Hearne wedge delaminates upper and lower crust of MHB. Assembly of western Laurentia is complete; remanent subducted slabs locked in place. (d) Proterozoic underplating results in addition of lower crustal layer (LCL) to the Wyoming Province and Medicine Hat Block.

5.3.1 Three Crustal Blocks Develop Independently

The Wyoming Province, Medicine Hat Block, and Hearne Province are interpreted to be three independent crustal fragments that developed sequentially and independently during the Archean.

Although the Medicine Hat Block is commonly deemed to be a northern part of the Wyoming

Province or a southern part of the Hearne Province (based mainly on which side of the political boundary that a particular study was conducted), the current model identifies enough differences between it and its two larger neighbours (*i.e.*, velocity and structural characteristics and the suggestive positioning of hypothesised relict subduction zones) to let it stand alone as an Archean continental fragment. This interpretation of the refraction data is supported by the direct geological evidence discussed earlier as well as by other geophysical characteristics including magnetic, gravity and seismic reflection data (see also Lemieux *et al.* 2000).

Although the Wyoming Province has been the unit most tectonically modified during the Phanerozoic, dating of exposed basement, as discussed in the introduction, suggests that, apart from the lower crustal layer, it is the oldest of the three (3.8 - 2.6 Ga). Ages determined for the Medicine Hat block (again not including the lower crustal layer) show it to be slightly younger (3.27 - 2.58 Ga) and ages from the Hearne Province are shown to be younger still (2.71 - 1.78 Ga). Only the Hearne Province conforms with the 42-km-thick global averages for Archean platform crust [Christensen and Mooney 1995]. The crust of the MHB and Wyoming Province is much thicker, increasing from 49 to 60 km. However, this thick crust is interpreted to be at least partially due to the addition of the distinctive lower crustal layer during the Proterozoic. If this lower crustal layer is ignored, the thickness of the upper crust observed in the current model (~25 km) is thinner than the global averages for Archean cratonic crust. This suggests that if the lower crustal layer is entirely composed of Proterozoic material, then the thickening must have involved the removal or alteration of some deep Archean crust from the MHB and Wyoming Province.

5.3.2 Hearne - Medicine Hat Block - Wyoming Assemblage

The positions of sutures between the three blocks are readily apparent on geophysical data at the Great Falls Tectonic Zone (GFTZ; Wyoming - MHB suture) and the Vulcan Structure (MHB - Hearne suture), the latter of which has been the focus of several recent and current research

projects for its relationship to the overlying Western Canada Sedimentary Basin and its tectonic significance [e.g., Eaton *et al.* 1999 (crustal reflection and gravity modelling), Lemieux *et al.* 2000 (seismic reflection), Ross *et al.* 2000 (tectonic history)]. The extension of both the Vulcan Structure [Price 1996] and the GFTZ [O'Neill and Lopez 1985] beneath the Cordillera also has been a focus of study for their relationship to Phanerozoic tectonic events. The variable topography of the reflective upper and lower boundaries of the lower crustal layer interpreted within the MHB may be the result of reactivation of Phanerozoic fault systems coincident with the sutures.

The two north-dipping upper mantle reflectors interpreted in the Deep Probe model, which extrapolate up-dip to the crustal positions of the suture zones, add significantly to the understanding of the two sutures. The reflectors strongly suggest that the aggregation of the three blocks was accompanied by north-dipping subduction or underthrusting of material into the upper mantle. These reflections provide the first concrete evidence to support this hypothesis. Neither of the suture zones appears to have a co-linear magmatic arc associated with it. This could imply that the three blocks formed in close proximity to one another; aggregation could have involved short-lived subduction of narrow intervening oceanic crustal material without the development of arc magmatism. However, the lack of a co-linear magmatic arc is also consistent with gravity modelling based on interpretations of seismic reflection data which propose Pyrenees-like suturing for the Vulcan Structure that involves oblique convergence and only limited subduction [Eaton *et al.* 1999]. Additional analyses of crustal seismic reflection and potential field data support upward thrusting of the Medicine Hat Block to the north over the Hearne Province [Lemieux *et al.* 2000]. These studies combined with our results necessitate a collisional history which involves wedging of the Hearne crust between upward- and downward-thrusting parts of the Medicine Hat Block. This geometry is similar to that proposed for the upward and downward delamination of the Fort Simpson Terrane by the crust of the Hottah Terrane in northwestern Canada [Cook *et al.* 1998, 1999]. Regions of deformation, which are associated with reflectivity, that have opposing dips

in the crust and upper mantle also are consistent with results of subduction / delamination from numerical modelling [Beaumont *et al.* 1994].

The timing and geometry of these suturing events remain enigmatic due to the lack of direct geological evidence. The absence of electrical conductivity anomalies between the blocks, generally anticipated for subducted foredeeps, suggests one of two possibilities: development of the sutures in the Archean, prior to the development of an oxygen-rich atmosphere in which case subducted foredeeps would not be conductive; or less likely, development of the sutures in the Proterozoic between continental fragments with no foredeep sedimentation or sedimentation that was removed [Boerner *et al.* 1998]. If we assume Archean accretion, then this makes the Wyoming – MHB – Hearne system one of the oldest and largest of the continental fragments which came together to form Laurentia in the early Proterozoic. Two questions then require consideration.

- What is the relative timing of the two suture zones?
- Is the position of the Vulcan Structure suture above the termination of the lower crustal layer coincidental or somehow related to the feature?

If it were not for the assumption of Archean accretion, then the fact that a lower crustal layer extends through the Wyoming Province and MHB would strongly support the interpretation that the GFTZ suture is older. However, since the lower crustal layer is interpreted to have been added later (during the Proterozoic), it cannot be used to constrain the ages of the sutures. The most obvious difference between the two reflectors is that the one associated with the GFTZ is deeper than the northern one, suggesting that more time was available to allow a subducted slab to penetrate deeper or that upper mantle conditions were different at the two locations at the time of subduction. The gap between the top of the southern slab and the Moho suggests either (1) a slab of similar size to the northern one which separated from the crust and sank before becoming locked

in place in the upper mantle, or (2) a slab of larger size than the northern one which was affected by a tectonic process that erased the slab's reflective signature in the uppermost mantle. Thus a weak argument can be made for the southern suture being older, but a better knowledge of the original nature of the oceanic plates which subducted would be necessary to use the present slab geometry to interpret age definitively.

The interpretation shown in Fig. 5.11 is limited in geometry to two dimensions: the strike of the Deep Probe profile and depth. Analyses of metamorphic patterns in Precambrian outcrops within and adjacent to the Wyoming Province add information in the dimension perpendicular to the profile [Dahl *et al.* 1999] and suggest a strike-slip component to the GFTZ suture which cannot be seen in the model. This adds support for Pyrenees-like convergence for the Great Falls Tectonic Zone as well as for the Vulcan Structure [Eaton *et al.* 1999].

5.3.3 Proterozoic vs. Archean lithosphere development

Previous studies have aimed to establish a set of generalised physical conditions for the continental lithosphere based on either localised 1-D models of the Earth's structure or tomographic images of the Earth with poor lateral resolution. The tectosphere model [Jordan 1975] conceptualised the notion that lithospheric roots were tectonically fused with their overlying Archean cratons. By compiling the results of numerous seismic refraction and teleseismic studies, additional characterisations of Archean and Proterozoic continental lithosphere have been made [Durrheim and Mooney 1994]. In their characterisations, they observed Archean crust to be thinner than Proterozoic crust, although this generalisation has been questioned and shown not to apply in several locations [Clowes *et al.* 1996]. However, accepting that the crustal-thickness generalisation has a degree of merit, it is contrasted by earlier seismic and petrological studies which found that the subcrustal lithosphere beneath Archean crust is, in general, thicker than the Proterozoic equivalent [*e.g.*, Jordan 1975, Boyd 1987]. The explanation for this is that due to higher mantle

temperatures in the Archean, the subcrustal lithosphere was depleted in FeO and volatiles, and as a result is more buoyant and less susceptible to delamination. These 'roots' acted as barriers to convection and as a result, underplating of crustal material was not possible, as it was beneath younger crust [Jordan 1975].

The Deep Probe and SAREX R/WAR data sets provide an opportunity to study more dynamic elements of the continental lithosphere with much higher resolution. Along the Deep Probe profile a combination of the two lithospheric characters defined by Durrheim and Mooney [1994] is observed. In the Wyoming Province, the upper crust is observed to be Archean and in fact to contain some of the oldest rocks on Earth [Frost and Frost 1993]. However, other geologic evidence supports the interpretation that the lower, high-velocity crust is Proterozoic [Ross and Davis 2000]. The implications of these observations are that if the Wyoming and MHB ever had an Archean lithospheric root, then it must have been removed in some manner to make way for the Proterozoic lower crustal layer that is inferred to be present today. However, if the Wyoming Province and MHB that we see today are only remnants of marginal regions of a larger amalgamated Archean continent, the absence of an Archean root beneath them could be explained.

5.3.4 Lower Crustal Layer Emplacement

Geological evidence from xenolith studies in the Sweet Grass Hills of northern Montana suggests that the lower crustal layer within the Medicine Hat Block is Proterozoic in age [Ross and Davis 2000]. The mineralogy of the xenoliths (Fig. 5.12) suggests a combination of crustal-sourced (garnet paragneiss) and mantle-derived (mafic granulite) material.

If these observations from the Medicine Hat Block are interpreted to extend south to the Wyoming Province, then the emplacement of this layer was independent of both the Wyoming Province's Archean assembly and Phanerozoic tectonism (*e.g.*, Laramide orogeny). However, the

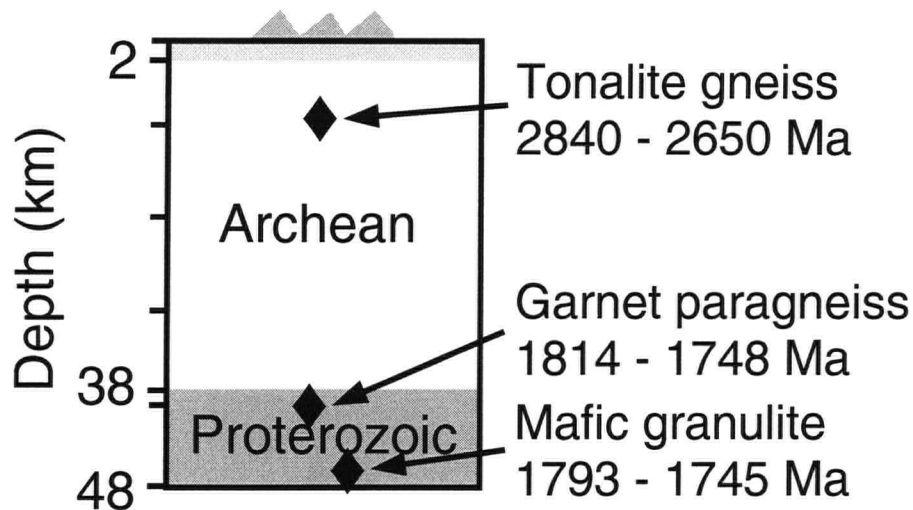


Figure 5.12: Cartoon summarising Sweet Grass Hills xenolith ages and source depths (adapted from Ross and Davis 2000). Interpretation of Archean and Proterozoic crustal divisions derived from the Deep Probe model at the location of the Canada-U.S. border.

resolution of the model decreases to the south as do the velocities modelled in the lower crustal layer. This suggests that the physical nature of the lower crustal layer and its method of emplacement could be different to the south.

Questions still remain concerning the source of the ‘underplating’ and the nature of ‘new’ Proterozoic material versus partially reworked Archean material. Possibilities range from the addition of a subducted oceanic slab to the simple accumulation of upper mantle magmatic material through convective processes. In either of these cases, the process could have been accompanied by the alteration of or mixing with the lowest part of the original crust. One possibility is that the underplating could be the result of tectonic processes acting on the margin of a large pre-Laurentian Archean craton comprised of the Wyoming Province, Medicine Hat Block, Hearne Province and other continental fragments that have now rifted off to the east, west and south. Even though the lower crustal layer stops at the boundary between the MHB and Hearne Province, the

Trans-Hudson Orogen should not be ruled out as a possible source of this underplating. The general observation that thickening of the crust due to underplating processes is rare during Archean time but common during Proterozoic time is intrinsic to the concepts of physical and chemical changes in the upper mantle at the end of the Archean. However, if we consider the Wyoming Province and MHB as marginal regions of a pre-Laurentian continent, then it is possible to imagine that the Vulcan Structure coincidentally falls at the point where the Archean lithospheric root develops. If this is the case, then the Wyoming - MHB - Hearne system may indeed have been established prior to the positioning of the lower crustal layer beneath the Wyoming and MHB. The original Archean continental margin could have trended SW to NE with the present-day Hearne being more central to the continent and therefore well positioned over the root, which would have impeded the subsequent underplating that occurred below the MHB and Wyoming Province. The nature of the underplating features, *i.e.*, magmatic accumulation or subducted oceanic crust, remains enigmatic.

Recent geochronological and isotopic studies indicate Proterozoic alteration of the sub-crustal lithosphere beneath much of the Hearne Province as a result of collisional processes with the Trans-Hudson Orogen to the east and other Proterozoic terranes to the north-west [Boerner *et al.* 1999, Ross *et al.* 2000.] If this is the case, then the region of the current study becomes an important laboratory for the comparison of continent-ocean collision with and without the presence of a lithospheric root beneath the continent (*i.e.*, the effect of the westward subduction of an eastern ocean beneath the Hearne, with its interpreted Archean root, should be different than that seen beneath the MHB and Wyoming Province where no Archean root is interpreted.)

5.4 Summary

Image of the lithosphere of western Laurentia

The analysis of the Deep Probe and SAREX R/WAR data sets, focussing on the region between Deep Probe shots 43 and 55, has resulted in a continental-scale velocity structural model of the lithosphere of platformal western Laurentia reaching depths of ~ 150 km. Radial Earth modifications to the existing ray-theoretical, travel-time inversion techniques were instrumental in accurately positioning boundaries and assigning velocities in the model. Crustal velocities are variable but general crustal structures define three independent blocks representing the Hearne Province, the Medicine Hat Block and the Wyoming Province. The sub-crustal lithosphere along the profile is homogeneous in velocity structure but two significant northward-dipping reflectors are apparent and interpreted as relict subduction zones.

The Hearne crust is typical of an Archean shield or platform both in thickness (34 - 50 km) and seismic velocity structure (6.0 - 7.4 km/s). Moving to the south, the crust of the Medicine Hat Block and Wyoming Province ranges in thickness from 49 to 60 km. The 10-30-km thick high-velocity (7.0 - 7.8 km/s) layer, interpreted beneath the Archean Medicine Hat Block and Wyoming Province to be Proterozoic in age, is unexpected beneath Archean crustal provinces, but is possibly explained by being a feature related to a cratonic margin. The variable topography along the reflective upper and lower boundaries of this layer, especially within the MHB, suggests considerable variability in its emplacement and subsequent tectonic history.

The relatively homogeneous velocity structure observed in the uppermost mantle (velocities of 8.1 - 8.2 km/s at the Moho with a gradient of 0.064 - 0.093 km/s/km) is intruded upon by two well-defined reflectors which descend to 124 and 83 km with dips of $\sim 18^\circ$ and 15° . This is the only direct evidence derived to date that suggests subduction as a past process in the amalgamation of the Wyoming Province, MHB and Hearne Province.

Western Laurentian accretionary history

Previous interpretations of the tectonic history of this region can be modified on the basis of the new observations from the Deep Probe and SAREX data sets. The following tectonic assemblage history for western North America in the region of the Deep Probe experiment is proposed.

- Archean: The Wyoming Province, Medicine Hat Block, and Hearne Province develop, in that order, as three independent crustal fragments.
- Late Archean: Accretion of the Wyoming Province and MHB as the result of north-dipping subduction beneath the MHB.
- Simultaneous with or shortly after the preceding stage: Accretion of the MHB and the Hearne Province in a wedge-delamination process, completing the aggregation of a pre-Laurentian continent with the Hearne Province being more central to the continent.
- Proterozoic: Rifting develops along the eastern margin of the Wyoming – MHB – Hearne system.
- Proterozoic: Development of the Trans-Hudson Orogen is coincident with lower crustal underplating beneath the Wyoming Province and MHB. No thickening of the Hearne Province is possible due to the presence of a lithospheric root.
- Proterozoic: Rifting to the south is followed by island arc accretion of the Yavapai - Mazatzal Province.
- Proterozoic and Early Phanerozoic: Rifting to west is followed by island arc accretion of the Cordillera.
- Phanerozoic: Vertical movement in the MHB / Montania is controlled by the position of ancient sutures (Vulcan Structure and Great Falls Tectonic Zone).

- Mesozoic to Early Tertiary: Magmatism of the Montana Alkalic Province is controlled by the position of the Wyoming - MHB suture (Great Falls Tectonic Zone); Laramide tectonism modifies crust of Wyoming Province.

Chapter 6

Beyond Ray Theory

To try and find out the reason for everything is dangerous and leads to nothing but disappointment and dissatisfaction, unsettling your mind and in the end making you miserable.

– Queen Victoria, 1819 - 1901.

Due to their geometry and length scales, several features apparent in the Deep Probe data have likely sources that cannot be properly described using ray theory. In such cases, finite difference forward modelling can be utilised to calculate wave field responses and thus to evaluate the effects and contributions of scattering to the generation of these features. This chapter examines three specific features seen in the Deep Probe data: reflections from the Moho, dipping reflections from the upper mantle and the teleseismic P_n phase. Each of the three features is currently the subject of intensive research efforts by many investigators in several Earth science disciplines. The intention of the work presented in this chapter is to explore some aspects of this research pertaining to the Deep Probe data set, as noted below.

- The nature of the crust – mantle boundary, or Moho, is investigated through the evaluation of a series of models constructed to test various styles of transition between crustal and mantle properties (*e.g.*, a discrete boundary, a transitional boundary zone, a discrete boundary overlying a constant velocity layer.)
- Dipping bodies in the upper mantle, identified in Chapter 5, are examined with regard to their thickness and velocity contrast with surrounding upper mantle material.
- A mechanism for the effective propagation of the teleseismic P_n phase and its associated

coda is modelled to conform with the waveform characteristics seen in the Deep Probe data.

The primary objective of this chapter is to evaluate particular aspects of the features of the interpreted velocity structure model listed above, not to carry out a comprehensive study of each of them. Note should be made of the fact that the finite-difference method is a forward modelling technique based on a simplified representation of the real Earth and as such it cannot be expected to produce synthetic seismograms which match the ones recorded in the field. However, the method has proven very successful as a technique for evaluating specific characteristics and testing end-member models. Prior to the discussion of the finite-difference modelling, the first part of this chapter will detail background information on this technique and how it has been applied to the Deep Probe investigation.

6.1 Preliminary Modelling Concerns

6.1.1 A Word or Two on Scales of Observation

The relationship between length scales present in a medium (*e.g.*, layer thicknesses, widths of

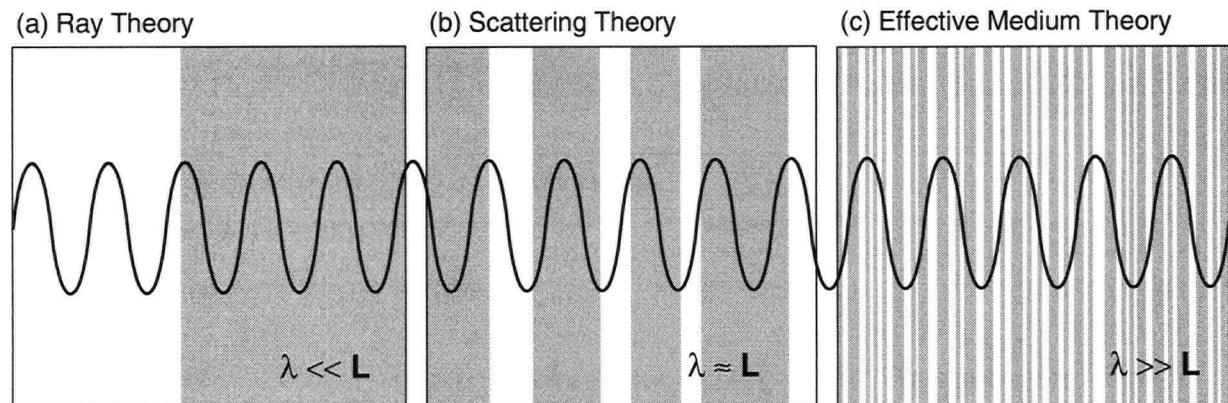


Figure 6.1: Length-scales of heterogeneity in the physical properties of the Earth, L , as compared to the wavelength of the investigating seismic wave, λ . Varying physical properties are indicated by alternating white and grey bars.

velocity transitions, or the size of geologic bodies) and the wavelengths of the energy type used to investigate them (*e.g.*, electromagnetic or seismic) is fundamental in determining an appropriate approach to the interpretation of the data. These relationships are summarised in Fig. 6.1.

At one extreme, when length scales are much longer than the wavelengths involved ($L \gg \lambda$), ray theory is routinely used to investigate the physical properties of the medium. This is commonly the case in seismological investigations. In the Deep Probe data set, seismic wave frequencies are observed in the range 0.5 to 8 Hz. In the lower crust and upper mantle, where P-wave velocities are in the range of 6.5 to 8.5 km/s, this corresponds to wavelengths of 0.8 to 17 km (Table 6.1). The dominant frequency in the data, ~ 4 Hz, corresponds to wavelengths between 1.5 and 2.1 km. Thus ray theoretical approaches are appropriate for the interpretation of features with dimensions larger than a few kilometres.

Table 6.1: Frequency vs. wavelength of various seismic waves.

Frequency (Hz)	Velocity (km/s)	Wavelength (km)
0.5	6.5	13
0.5	8.5	17
4.0	6.5	1.51
4.0	8.5	2.13
8.0	6.5	0.75
8.0	8.5	1.06

At the other extreme, when length scales are much shorter than the investigative wavelengths ($L \ll \lambda$), effective medium theory is appropriate. An effective medium, as the name suggests, refers to a composite medium made up of two or more constituent media. The composite, as a whole, has physical properties which are controlled by the volume fractions and physical properties of the constituents as well as the geometric details of how they are combined [Mavko *et al.* 1998, p. 106]. What this means for the Deep Probe data set is that the distribution and physical properties of features with length-scales smaller than those seen in the seismic data (*e.g.*,

stratigraphic layers, mineral heterogeneity or localised fault related structures) are combined to produce effective physical properties of the aggregate medium; the resulting averaged properties of the Earth are dependent on the wavelengths of the seismic energy used to investigate them.

The calculation of averaged elastic properties for an effective medium can be complicated. However if volume fractions and constituent properties are assumed, it is reasonable to quantify bounds for effective elastic properties. For example, consider the simple Voigt-Reuss bounds [Mavko *et al.* 1998, p. 110] for horizontally interbedded layers with elastic properties, M_i , and an incident ray perpendicular to bedding. At one extreme, the Reuss lower bound of the effective elastic moduli, M_R , is appropriate for determining average elastic properties of the composite system with the assumption that all layers have the same strain.

$$\frac{1}{M_R} = \sum_i \frac{\theta_i}{M_i}, \quad (6.1)$$

where θ_i is the thickness fraction of a particular layer. This lower bound also applies to ray-theory average properties (such as velocity, V_{rt}), as can be seen by considering that the total travel time for a wave travelling through a series of layers is the sum of the travel times in each layer. The ray theory average velocity is therefore

$$\frac{1}{V_{rt}} = \sum_i \frac{\theta_i}{V_i}. \quad (6.2)$$

At the other extreme, the Voigt upper bound of the effective elastic moduli, M_V , is appropriate for determining average elastic properties of the composite system with the assumption that all layers have the same stress.

$$M_V = \sum_i \theta_i M_i. \quad (6.3)$$

The Voigt average weighs higher-valued properties more heavily in determining the effective property. Considering velocity and travel time, this means that the average velocity of a Reuss

effective medium will be lower than through a Voigt effective medium, and hence the travel time will be longer. In experimental results, it has been found that as the layer thicknesses within the effective medium decrease, the measured effective elastic moduli move from the Reuss lower bound to the Voigt upper bound [Marion *et al.* 1994], *i.e.*, travel times will decrease.

The Voigt-Reuss bounds consider only vertically incident rays travelling through isotropic, linear and elastic constituent media. Several situations which are likely in the lower crust and upper mantle – non-orthogonal incident rays, anisotropy, visco-elasticity and an effective medium that is constructed in some way other than layers – are not considered with these equations. However, more realistic effective media can be considered to have elastic properties which lie between these extremes [Hill 1952]. The evaluation of the seismic response to effective media is an important consideration in this chapter. This is especially significant in evaluating velocity structures in the vicinity of the Moho which are imaged by rays with a broad range of incident angles and frequency content.

Between the extremes of ray theory and effective medium theory lie length scales which are approximately the same as the wavelength used to investigate them. Waves travelling through a medium with length scales such as this (*e.g.*, a 1 - 3 km transitional Moho, or a subducted oceanic crustal layer) cannot accurately be represented as rays, and yet the length scales present are long enough that they cannot be averaged with those of surrounding material to produce an effective medium. In this case, scattering theory can be used to glean extra information about the medium. Finite difference methods [Alterman and Karal 1968, Claerbout 1970] make use of scattering theory by parameterising the model as a matrix of small cells. Energy is propagated from cell to cell and from time step to time step by a discretisation of the wave equation.

6.1.2 Finite Difference Theory

The finite difference technique numerically models the propagation of a seismic wave through a gridded model by approximating the time and spatial derivatives of the wave equation (1.1) in each grid of the model, using these results to advance the wave field in time, and then iterating. In conventional finite-difference routines, such as the one used for this thesis, approximation of the second spatial derivative in the wave equation is accomplished through a Taylor series expansion at each gridded cell of the instantaneous wave field using the elastic attributes of the cell in question and of the neighbouring orthogonal cells. A similar technique is used to approximate the second time derivative; therefore, at a minimum, initial conditions for the wave field must be specified for the first two time steps. In practice, an input source function generally is specified that covers a length of time much longer than two time steps.

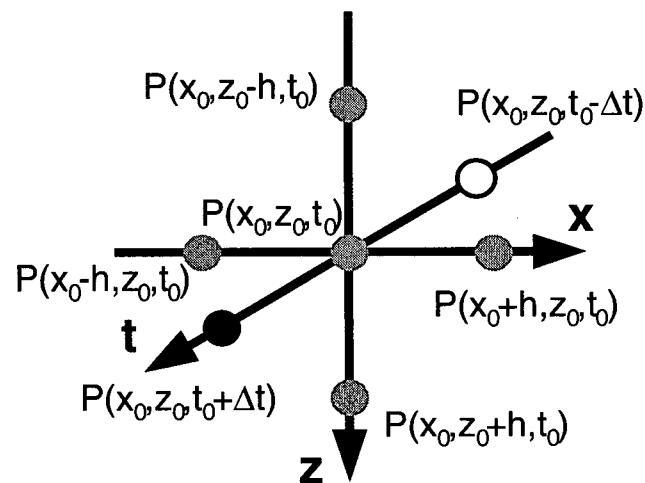


Figure 6.2: Finite-difference grid about a point (x_0, z_0, t_0) . The pressure field, $P(x, z, t)$, is advanced from the t_0 to $t_0 + \Delta t$ level using values from the t_0 and $t_0 - \Delta t$ levels.

In order to understand the significance of time-step size, Δt , and the grid dimension, h , it is illustrative to examine the explicit discretisation of the wave equation in more detail. Consider the expansion of the wave equation around a point (x_0, z_0, t_0) . For simplicity, this examination is

restricted to an acoustic example with constant density. In this situation, the pressure field can be expanded outwards from (x_0, z_0, t_0) , as shown in Fig. 6.2, by simple Taylor series expansions. In the positive direction of the x-axis, the 1-D Taylor series expansion can be written as:

$$P(x_0 + h) = P(x_0) + h \frac{\partial P(x_0)}{\partial x} + \frac{h^2}{2} \frac{\partial^2 P(x_0)}{\partial x^2} + \frac{h^3}{6} \frac{\partial^3 P(x_0)}{\partial x^3} + \dots \quad (6.4)$$

If this process is repeated in the other three axial directions ($-x$, $+z$, and $-z$) and the resulting expansions are added, then the resulting sum provides a centred approximation to the second spatial derivative in two dimensions, which is second-order accurate in mesh size h .

$$\begin{aligned} & \left(\frac{\partial^2}{\partial x^2} + \frac{\partial^2}{\partial z^2} \right) P(x_0, z_0) \\ &= \frac{P(x_0+h, z_0) + P(x_0-h, z_0) + P(x_0, z_0+h) + P(x_0, z_0-h) - 4P(x_0, z_0)}{h^2} + \dots \end{aligned} \quad (6.5)$$

In a similar way, the second time derivative can be approximated. The 1-D Taylor series expansion of the pressure field in the positive direction of the time axis would be

$$P(t_0 + \Delta t) = P(t_0) + \Delta t \frac{\partial P(t_0)}{\partial t} + \frac{\Delta t^2}{2} \frac{\partial^2 P(t_0)}{\partial t^2} + \frac{\Delta t^3}{6} \frac{\partial^3 P(t_0)}{\partial t^3} + \dots \quad (6.6)$$

Repeating the process in the negative time direction and summing the two provides the second derivative in time

$$\frac{\partial^2 P(t_0)}{\partial t^2} = \frac{P(t_0 + \Delta t) + P(t_0 - \Delta t) - 2P(t_0)}{h^2} + \dots \quad (6.7)$$

which by the wave equation can be equated to (6.5) by incorporating a compressional velocity field, $v_p(x_0, z_0)$. An explicit value for each (x, z) location in the pressure field at $t_0 + \Delta t$ can then be readily calculated from spatial wave fields at the previous two time steps, t_0 and $t_0 - \Delta t$,

$$\begin{aligned} P(x, z, t_0 + \Delta t) &= 2P(x, z, t_0) - P(x, z, t_0 - \Delta t) \\ &+ v_p^2(x, z) \left(\frac{\Delta t}{h} \right)^2 [P(x+h, z) + P(x-h, z) \\ &+ P(x, z+h) + P(x, z-h) - 4P(x, z)] + \dots \end{aligned} \quad (6.8)$$

In this synopsis of the finite-difference method, only the first few terms of the Taylor series expansions have been detailed. The number of terms preserved in a particular finite-difference routine determines the accuracy of the code. However, additional terms will have an adverse affect on computation time. It therefore becomes important to choose values for Δt and h which will avoid grid dispersion even with a low degree Taylor series expansion.

The application of this technique in an acoustic medium with unvarying density is relatively simple; only compressional velocity, v_p , must be defined at each cell in the model. However, the application becomes more complicated numerically with the consideration of other elastic parameters and attenuation [Levander 1989]. In this case, shear velocity - v_s , density - ρ , P-wave attenuation - Q_p and S-wave attenuation - Q_s also must be known at each cell. Also the propagation of each parameter relies on a coupled relationship between it and the other visco-elastic parameters.

6.1.3 Selection of Finite Difference Parameters

The determination of the finite difference time step, Δt , and the maximum frequency, f_{max} , for the model is affected by the stability and dispersion characteristics of the particular finite difference routine used [Levander 1989]. Grid, or numerical, dispersion is the dependence of the finite difference routine on the spatial sampling dimension, h . In effect, it is the physical result of short wavelength waves sensing the discrete medium. For fourth-order finite-difference routines (where order refers to the number of terms in the Taylor series expansion used to approximate the second spatial derivative in the wave equation), parameter selection should be based on the following two rules of thumb [Levander 1989].

$$\Delta t \leq 0.75 \sqrt{\frac{3}{8}} \frac{h}{v_{max}} \quad (6.9)$$

where h is the dimension of a single cell in the grid (they must be square cells), and

$$f_{max} = \frac{v_{min}}{5h}. \quad (6.10)$$

To ensure insignificant grid dispersion, it is recommended that the 5 in the denominator of (6.10) should be changed to 10.

For most of the the finite-difference models presented in this chapter, the grid dimension, h , and time step, Δt , have been set to 120 m and 0.005 s respectively. Substituting these values into (6.9) and solving for v_{max} gives:

$$v_{max} \leq 11.02 \text{ km/s}, \quad (6.11)$$

which is more than sufficient for upper mantle models.

The modelled source signature selected for this work is a Ricker wavelet with a central frequency of 1.75 Hz and an effective upper frequency of two times the central frequency (*i.e.*, 3.5 Hz.) Substituting $f_{max} = 3.5$ Hz and $h = 120$ m into (6.10) and solving for v_{min} gives:

$$v_{min} = 2.1 \text{ km/s}, \quad (6.12)$$

(or 4.2 km/s to be absolutely sure of no grid dispersion.) This value is satisfactory for lower crustal and mantle velocities, but lies close to the velocities seen in the shallower sedimentary basins. This concern is reduced by stripping off the upper layer of the model and starting the model at a depth of 1 km beneath sea level (about 1.8 km beneath the surface). In this way, v_{min} was restricted to 3.9 km/s. S-wave velocities have not been considered in this argument. They will be lower than the P-wave velocities, but still should not be affected by grid dispersion because of the conservative rules-of-thumb used and the modifications made to remove the shallowest (and slowest) part of the model.

6.1.4 Procedural Details

The visco-elastic finite-difference modelling code utilised in this chapter has been provided by Professor Alan Levander of Rice University. This code is fourth-order accurate in x and z and second-order accurate in t . Models were calculated on two platforms: a *Sun Enterprise 450* computer with 4×300 MHz central processing units (CPU's) and 4 Gbytes of Random Access Memory (RAM) at the Department of Geology and Geophysics at Rice University; and a *Sun Ultra 60* computer with 2×360 MHz CPU's and 1.25 Gbytes of RAM at the Department of Earth and Ocean Sciences at the University of British Columbia. The code itself is that of Robertsson *et al.* [1994] and accompanying documentation was provided by Robertsson and Akerberg [Akerberg, pers. comm. 1999].

The characteristics of the computer platform upon which the finite-difference modelling is performed limit the size of models possible and the speed at which they can be calculated. Two parameters, the CPU speed and the number of CPU's utilised in parallel, primarily affect the speed of the calculation. However, the amount of RAM available (~ 1.75 Gb on the Rice computer and ~ 1.1 Gb on the UBC computer) limits the dimensions of the models calculated on the platform. This can be quantified in the following way.

$$\text{Largest model area (km}^2\text{)} = \frac{\text{Available RAM (bytes)}}{62 \left(\frac{\text{bytes}}{\text{cell}} \right) \times \frac{1}{h^2} \left(\frac{\text{cells}}{\text{km}^2} \right)} \quad (6.13)$$

Therefore, the largest model areas possible using the parameters discussed in the previous section are $\sim 390,000$ km² (*e.g.*, 2339 km long by 167 km deep) on the Rice computer and $\sim 255,000$ km² on the UBC computer. Models run to simulate the source and receiver geometry of the SAREX field deployment required an x -dimension of 784 km (the length of the SAREX deployment) while those simulating Deep Probe Deployment 1 required 1359 km (the distance between the northernmost shot used, DP155, and the southernmost receiver deployed). The maximum depth of the

SAREX models is thereby limited to ~ 497 km on the Rice computer or ~ 325 km on the UBC system, more than sufficient for modelling the uppermost mantle. In contrast, because of the longer x-dimension required, the maximum depth of the Deep Probe models is limited to ~ 287 km on the Rice computer or ~ 188 km on the UBC system. While this is sufficient for modelling the features of interest in the uppermost mantle, it is considerably shallower than the modelling depths possible for the shorter SAREX models.

In general, the double-CPU UBC computer system was used for routine modelling of the SAREX data, with a single model typically taking between 15 and 18 hours to run. The Rice system, using all four available processors, could run the jobs in half the time. The larger Deep Probe models were run exclusively at Rice where, even with the larger computer system, a single run would take as long as 60 hours.

A summary of the procedure utilised to produce each finite-difference model follows.

6.1.4.1 Input Model Set-up

In order to preserve continuity from the results of the ray-theoretical travel-time inversion (RAYINVR), a number of utility routines, either newly developed or modified from existing routines, were used to convert the RAYINVR acoustic model into a gridded finite-difference visco-elastic model. Additional utility routines were developed and/or utilised to modify and plot the finite-difference model (Table 6.2).

The first step required is to consider the radial Earth characteristics of the RAYINVR model to be used for input. The RAYINVR modelling was performed in radial co-ordinates, but since the finite-difference modelling scheme used here operates only in a Cartesian grid, an Earth-flattening transform must be applied to the RAYINVR model before it can be used as an input model for the finite difference scheme. By doing this, the waveforms modelled will have the same travel-time

Table 6.2: Utility routines used to modify and plot the finite-difference models.

Routine	Purpose
vrad2cart	Converts a 'radial' RAYINVR <i>v.in</i> file to 'flat-Earth' <i>v.in</i> file (new routine).
conv_vout	Windows a RAYINVR <i>v.out</i> file and formats boundary limits as required (modified Rice University routine conv_vin).
setupa3	Converts a <i>v.out</i> file to an <i>MTRPRP</i> (material properties) acoustic file (used Rice University routine).
vmodify	Adds trapezoidal velocity anomalies to an <i>MTRPRP</i> acoustic file (new routine).
mmod	Adds elliptical velocity anomalies to an <i>MTRPRP</i> acoustic file (modified routine from B. Németh).
ac2gmt	Produces a GMT grid of the <i>MTRPRP</i> acoustic model for plotting (new routine).
convert_ac_vefd2	Converts an <i>MTRPRP</i> file to an <i>MTRPRP.VE</i> visco-elastic file (used Rice University routine).
seistrans_seggy	Converts output seismogram file to SEG-Y format for plotting, <i>etc.</i> (used Rice University routine).

characteristics as the RAYINVR modelled travel-time curves and the real data which will enable their direct comparison. This transformation has been performed on the final model of Chapter 5 (Fig. 5.7) using the utility program **vrad2cart** which transforms all depth and velocity nodes in the model by applying Eqs. (4.1) and (4.2).

The next procedure is to produce a standard discretised output file from RAYINVR to be the model used for input to the finite difference routine. The boundaries of this model must correspond exactly with the domain used in the finite difference model. It must start at a depth of 0 units and contain only positive offset distances in the x direction. The code does not handle topography, so a sensible datum must be chosen.

RAYINVR software contains a routine for converting the familiar velocity and depth nodes of a *v.in* acoustic model file to a discretised *v.out* model file. However, a simple utility, **conv_vout**,

was developed to facilitate the extraction of a subset of a *v.out* model consistent with the requirements of the finite-difference code. Its function is simply to window the original *v.out* model and adjust the boundaries to start at zero depth and zero offset. Cell size for the *v.out* file deserves consideration. Ideally, the discretisation used to create the *v.out* model should be the same as that which will be used in the finite-difference model. However, for large models this may be impossible if the resulting *v.out* file size is too large. To avoid this problem, a multiple of the desired finite-difference cell size can be used and a later utility will interpolate. Another point to consider is that the discretisation of the *v.out* file must be the same in *x* as it is in *z*. Care must be taken when selecting the discretisation size to avoid smearing the acoustic characteristics of small features. For the Deep Probe modelling, a *v.out* discretisation of $1.2 \text{ km} \times 1.2 \text{ km}$ was chosen; a finer discretisation size could not be chosen due to the size limitations of the *v.out* file. This length scale is approximately the same as the dominant wavelengths in the data. The result of this is that velocity discontinuities, such as the Moho, will not in general be first order discontinuities in the discretised model.

6.1.4.2 Creation of the Acoustic Model

The utility program **setupa3** creates an initial acoustic model by interpolating the preconditioned RAYINVR *v.out* model to a desired cell size. In addition, the routine populates any empty cells from the *v.out* model with values calculated from neighbouring cells or specified in the input to **setupa3**. An acoustic model file named *MTRPRP* (an abbreviation of ‘material properties’) is created. All models shown here were created using a cell size of 120 m.

Modifications or enhancements can be added to the acoustic model using a variety of utility routines. The routine **vmodify** modifies the velocity of regions of the model by either adding to them or changing them by a percentage of their original value. This was used extensively during the Deep Probe modelling process to make variations to the original model. For example, dipping

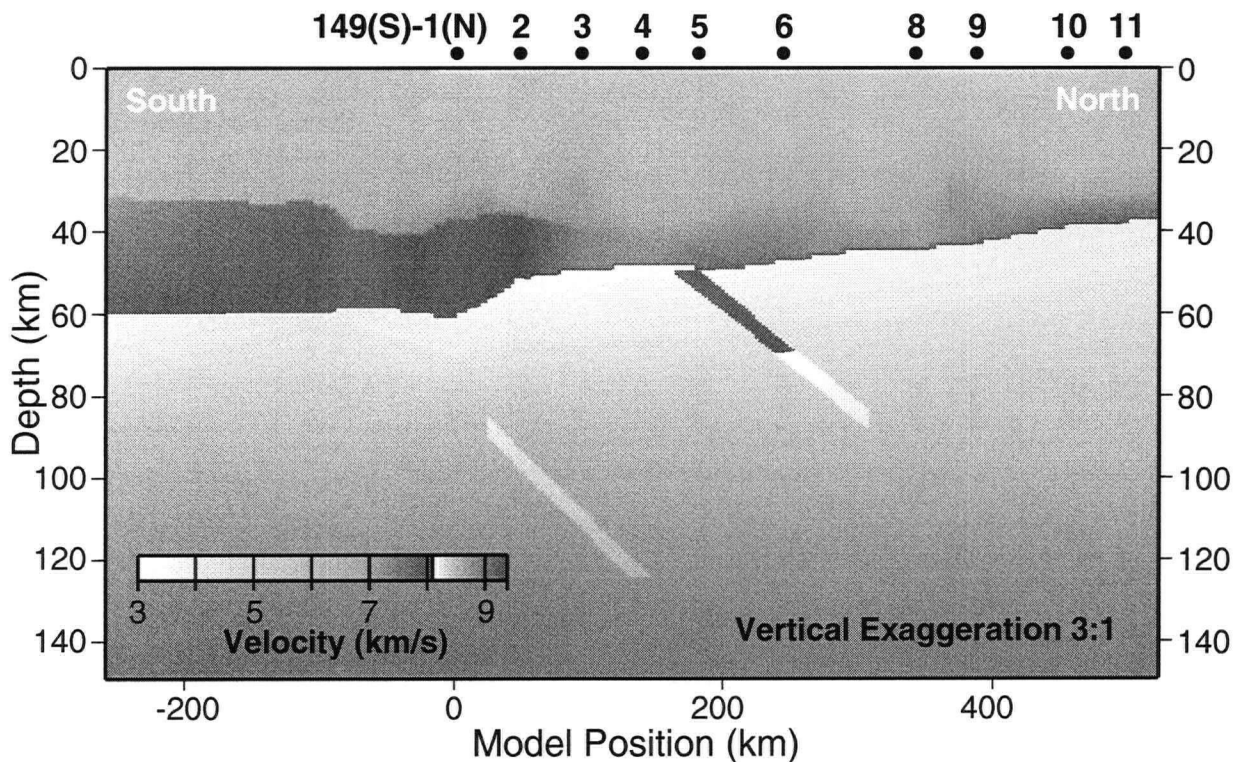


Figure 6.3: Model 4 - RAYINVNR model for the SAREX deployment with the Earth flattening transform applied and a discretisation of 120 m. 5-km thick dipping layers have been added as shown with a velocity contrast of -0.25 km/s from surrounding rock. SAREX and Deep Probe shot locations are shown along top of model. Top of model is at 1000 m below sea level (~ 2000 m below the surface). The apparent (not real) velocity change in the northern dipping slab at a depth of 70 km is due to the modest velocity increase along the slab and the change in the grey scale at 8.1 km/s (see scale bar and comments in text.)

reflective bodies (Fig. 6.3) were added to the upper mantle. Another suite of utilities, collectively referred to as the **mmod** routines, modified from an original routine by Balázs Németh [Németh 1999 and pers. comm. 2000], adds ellipses of statistically defined distributions and dimensions to the model in order to simulate geological phenomena.

Note that the acoustic models plotted in this chapter are plotted in a grey scale with shading varying from light to dark over two velocity ranges: 3.0 - 8.1 km/s and 8.1 to 9.4 km/s. This has the advantage of showing a distinct line for the Moho. However, it is important to keep the grey scale in mind when examining the representation of the dipping slabs. For example, the northern slab

in Fig. 6.3), which has a velocity defined as being 0.25 km/s less than the surrounding material, varies in velocity linearly from ~ 8.0 km/s near the Moho to 8.2 km/s at its base. The switch from dark to light shading is a result of crossing the 8.1 km/s contour and does not represent a discrete velocity contrast. Also, note that model numbers in this chapter refer to the order in which they were created during the development of this work. Some models have been dropped and others have been presented in an order different to that in which they were created to present a coherent flow of ideas.

6.1.4.3 Creation of the Visco-elastic Model

A series of assumptions is required to convert an acoustic model into a suitable visco-elastic model. This involves establishing relationships between the P-wave velocity, v_p , and the other four visco-elastic parameters, v_s , density, Q_p and Q_s . The utility program `convert_ac_vefd2` uses a user-specified table of relationships to calculate a full visco-elastic model. This produces a large file, *MTRPRP.VE*, which contains each of the five visco-elastic parameters specified for every cell.

The relationships specified for the Deep Probe modelling are shown in Table 6.3. These relationships are loosely based on the 1-D Preliminary Reference Earth Model (PREM) [Dziewonski and Anderson 1981] with modifications made for the crustal velocities interpreted along the Deep Probe model [Henstock, pers. comm. 1999]. The major boundary apparent in this table is the Moho; crustal visco-elastic parameters are determined for v_p less than 8.1 km/s and upper mantle parameters are determined for v_p greater than 8.1 km/s.

6.1.4.4 Execution of the finite difference code

The execution of the program is controlled by the 24 quantities, specified in Table 6.4, included in a control file that is read during the execution of the program. The values shown in the table are

Table 6.3: Viscoelastic parameter relationships.

v_p Low (m/s)	v_p High (m/s)	v_p/v_s Low	v_p/v_s High	Density (kg/m ³)	Q_p	Q_s
3600	4200	1.73	1.73	2700	50	10
4200	5000	1.73	1.73	2700	100	25
5000	6500	1.73	1.73	2750	400	200
6500	8100	1.78	1.78	3000	400	200
8100	9400	1.81	1.81	3380	2000	1000

typical of those used for the Deep Probe modelling. Care is taken to ensure that these parameters meet the conditions set out in section 6.1.3. Parameters that were varied most often are:

- 1. The central frequency was varied from 1.75 to 3.25 Hz for testing purposes and to resolve shorter length-scale features. The central frequency is one of the parameters used to determine the input source signature which is also affected by parameters 11 (type of source) and 12 (source wavelet). The nature of the source signature will be discussed in section 6.1.4.5.
- 9. The number of time steps calculated depended on the farthest offset required for the shot point being modelled. This value was minimised for each run to reduce the computation time.
- 10. Snapshots were produced every 2 seconds for movies of the propagating wave field; otherwise, this value was set to be greater than the number of time steps so that valuable disk space would not be used storing images.
- 22. The source location was varied as needed depending on the SAREX or Deep Probe shot point being modelled.

Table 6.4: Finite difference input parameters. * repeated for each HLA and/or VLA designated.

	Value	Description
1	1.75	Central frequency of wavelet (in Hz)
2	10000.	Width of absorbing boundary (in m)
3	5000.	Width of taper (in m)
4	2.	Q_p in boundary
5	2.	Q_s in boundary
6	1	Specification of material properties: (1) MTRPRP file.
7	5.0×10^{-3}	Time step (in s)
8	0	Output material properties on cfl-files (1=yes/0=no)
9	29500	Number of time steps
10	30000	Time steps between snap shots
11	4	Source: (1) Plane IC (2) point IC (3) BC (4) insertion of point source at one point
12	1	Wavelet: (1) Ricker wavelet (2) impulsive CW (3) time-series specified on file (4) integrated Ricker wavelet
13	2	Quantity to output in seismogram. (0) pressure (acoustic medium), (1) P/S energy, (2) horizontal/vertical component of velocity)
14	.016	Time step between samples in seismogram (in sec)
15	1	How many Horizontal Line Arrays (HLA)?
16	0	How many Vertical Line Arrays (VLA)?
17	0.	z co-ordinate of HLA 1* (in m)
18	0000.	x_1 co-ordinate of HLA 1* (in m)
19	750000.	x_2 co-ordinate of HLA 1* (in m)
20	1000.	Δx for HLA 1* (in m)
21	1000.	Source: Amplitude
22	163000.	Source: x-centre (in m)
23	40.	Source: z-centre (in m)
24	-.20	Source: Time shift (should be < 0)

6.1.4.5 Output

The program produces vertical and horizontal seismogram files, *seismogram_ver* and *seismogram_hor* simulating the velocity of ground motion at the locations specified in Table 6.4 (parameters 17-19). For convenience, since the data being modelled are vertical-component data, a symbolic link:

seismogram → *seismogram_ver*

is made so that the utility routine, **seistrans_segy**, will demultiplex the vertical-component seismograms into a SEG-Y file named *hse01.sgy*; no input parameters are required. This procedure can be undertaken while the finite-difference code is still running in order to check on progress. This is often desirable after a few seconds of data have been modelled to ensure that the output is being generated appropriately.

SEG-Y formatted data can be readily plotted for detailed examination of the output. The PLOTSEC suite of routines has again been utilised for this purpose. Display parameters used for plotting the finite difference seismograms are important, especially with regard to the absence of noise in the synthetic data. The main goal in selecting suitable plotting parameters is to show the same features in the synthetic as can be seen in the real data. To this end, the following parameters have been selected for the grey-scale synthetic seismograms plotted in this chapter. The data are plotted in 'true' amplitude, *i.e.*, the velocity of ground motion 'measured' at the receiver scaled by a geometric spreading factor, $\frac{x^{1.9}}{2 \times 10^6}$, where x is the offset distance in km. The amplitudes are then clipped so that the gradational grey-scale displays the range between -10% and +10% of the maximum scaling value. Amplitudes below and above these limits are plotted as the same shade of grey (negative troughs) or black (positive peaks). These settings were determined in an *ad hoc* manner in order to mimic the general amplitudes seen in the field data (Fig. 6.4).

In Fig. 6.4, note that even though the frequency content of the (a) real and (b) synthetic data

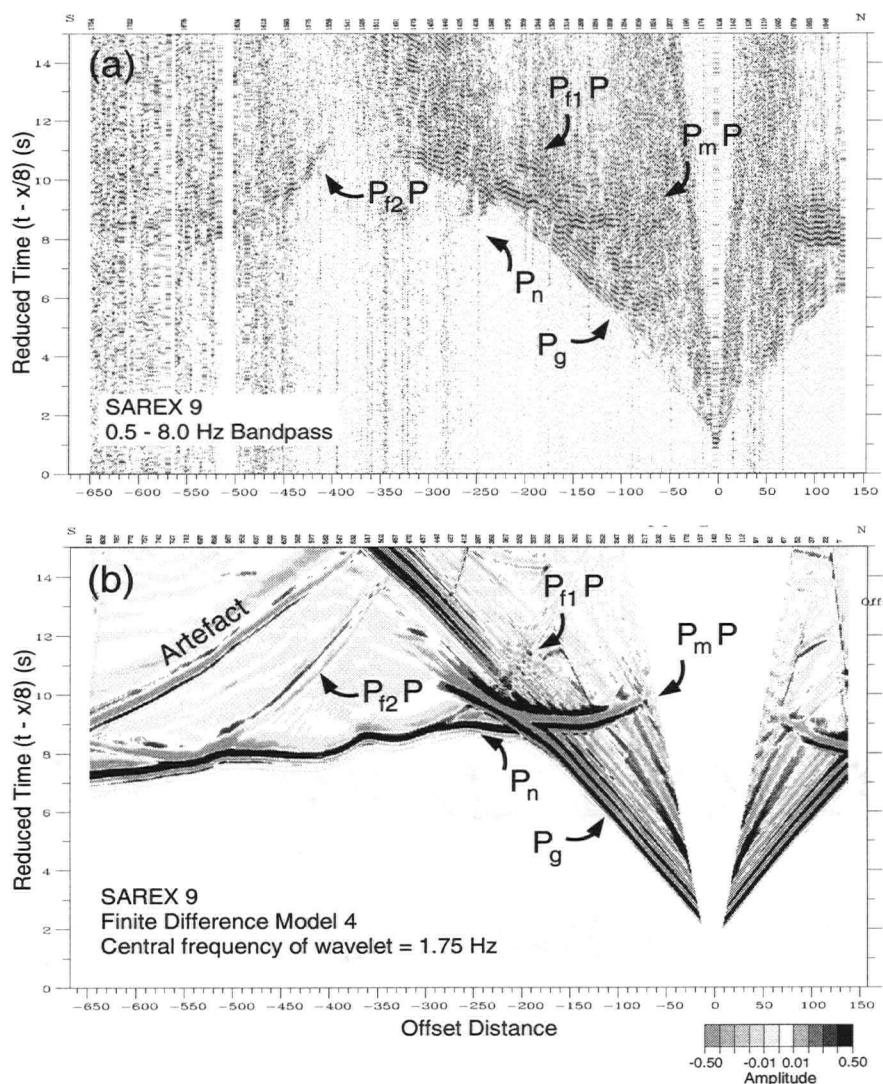


Figure 6.4: Amplitude considerations: (a) SAREX Shot 9 (b) Finite difference synthetic seismogram of SAREX Shot 9. Both sections plotted with a geometric spreading factor of $x^{1.9}$. The 'artefact' is a reflection from the base of the model. In subsequent figures where it is present, this feature will not necessarily be identified or discussed. All real data in this chapter are plotted with the same parameters as the synthetic data: true amplitude, variable density grey scale, no trace normalisation.

is very different, there is a relatively good match between the real and synthetic reflecting phases in regard to the arrival times, distribution with offset distance and amplitude for most phases. However, there is a poor match between the amplitudes seen for the real and synthetic P_n refraction. This indicates that conditions in the uppermost part of the mantle are not as conducive to the refraction of seismic energy as the model would predict; this will be considered later in this

chapter.

6.1.5 Model Parameter Testing Issues

In order to establish bounds on the modelling process, several parameters of the model were tested in an *ad hoc* manner. The first of these was the length dimension, h , of an individual cell in the model. As previously determined through consideration of the rules of thumb (Eqs. 6.9 and 6.10), a cell dimension of 120 m is considered satisfactory. To test this, three models were generated with cell dimensions of 100, 120 and 150 m (Fig. 6.5). While all three of these cell sizes meet the criteria of the rule-of-thumb equations, it is apparent from the resulting modelled seismograms that high-frequency noise artefacts increase with cell size. In addition, even with identical plotting parameters, increases in cell size appear to increase the amplitude of reflection and refraction events. This can be explained by the way in which boundaries within the model are discretised when converting the sparsely-defined RAYINVR model to a finite-difference grid model. The continued use of a 120-m cell size was confirmed as a tradeoff between the higher noise level in the 150-m cell-size seismogram and the longer calculation time in the 100-m cell-size model.

Another model parameter to be considered is the depth of the model. For SAREX, a maximum depth of 150 km was chosen. This resulted in a model which is deep enough such that reflections from the bottom of the model would not interfere with the modelled first arrivals. As can be seen in Fig. 6.6a, the reflector from the bottom of the model interferes with the coda of the P_n -phase at farther offset distances when the model is only 125 km deep. Moving the lower boundary of the model to 150 km shifts the reflection later in time and away from the P_n -coda (Fig. 6.6b).

The source wavelet for most plots in this chapter has been defined as a zero-phase Ricker

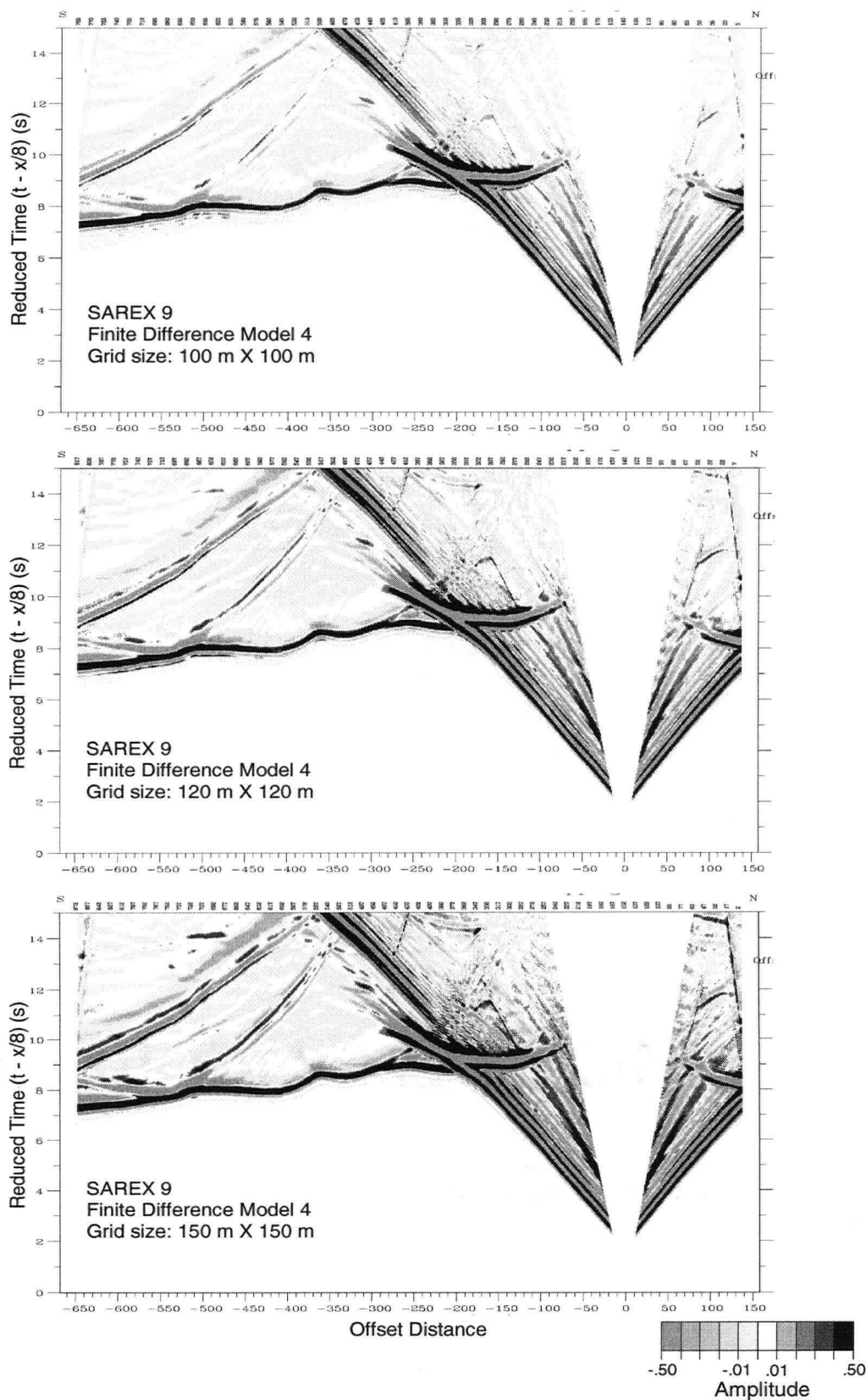


Figure 6.5: Grid size comparison. Grid dimensions of 100, 120 and 150 m.

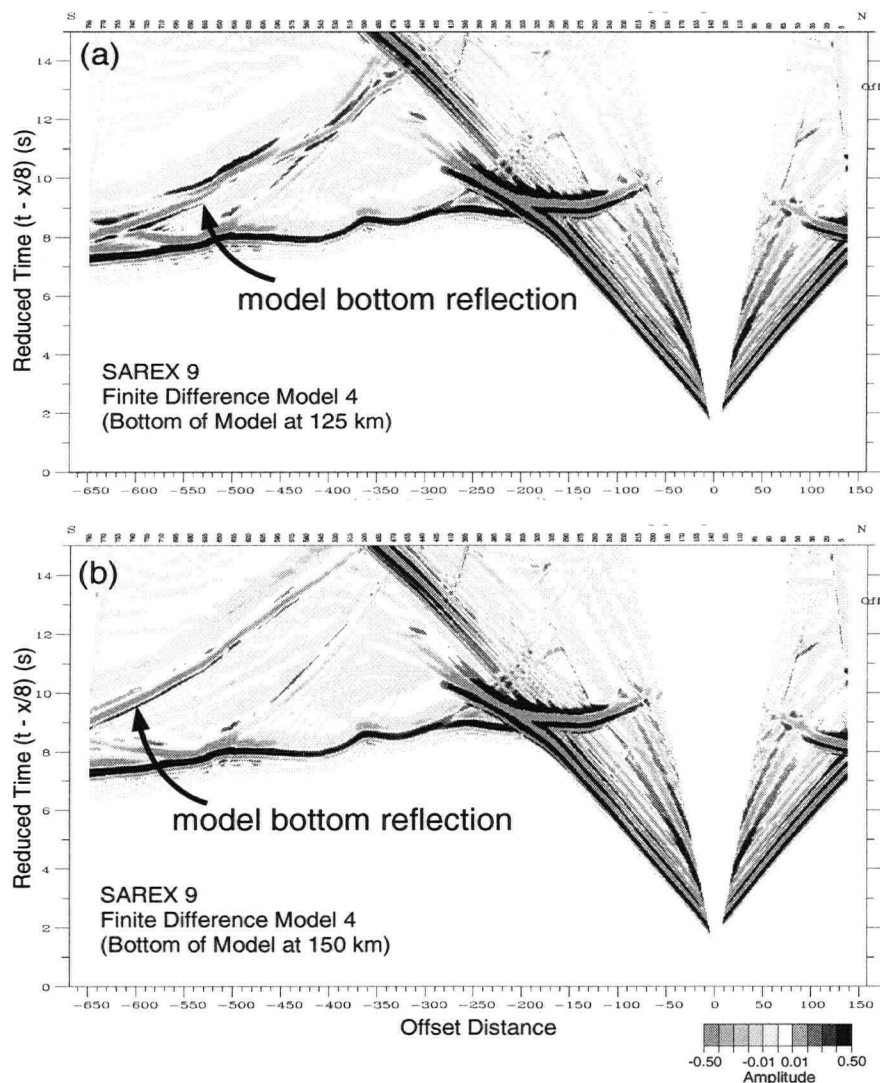


Figure 6.6: Model depth comparison: (a) 125 km vs. (b) 150 km.

wavelet,

$$A(t) = (1 - 2\pi^2\nu_M^2 t^2)e^{-\pi^2\nu_M^2 t^2}, \quad (6.14)$$

with a central frequency, ν_M , of 1.75 Hz. This wavelet has an effective upper frequency limit of two times the central frequency, in this case, 3.5 Hz. While this is lower than what is seen in the real data, most of the major features are still clearly apparent in the lower-frequency synthetic seismograms with the added advantage that grid dispersion is not a concern. As well, higher frequency content requires considerably longer computation times, which can be a limiting factor

for testing different models.

In some cases, however, a higher central frequency is justified to more accurately evaluate particular features. For these models, a frequency of 3.25 Hz is chosen. With a highest effective frequency of 6.5 Hz, this approaches the limit of the finite difference grid, *i.e.*, substituting $f_{max} = 6.5$ Hz and $h = 120$ m into (6.10) and solving for v_{min} gives:

$$v_{min} = 3.9 \text{ km/s.} \quad (6.15)$$

which is equal to the lowest velocities included in the model.

As mentioned previously, the uppermost ~ 1800 m of the original Deep Probe model have been removed so that the minimum velocity in the finite-difference grid is ~ 3.9 km/s. This reduces the time needed for a single model run and also helps to avoid grid dispersion. The removal of this layer does have two unfortunate effects. First, the uppermost part of the model is not as attenuative as the sedimentary layer that has been stripped off would be. This generates artificially-high-amplitude surface waves and probably causes amplitudes of all other phases to be greater than they otherwise would be. The surface waves have been surgically muted in the plots of finite-difference synthetic data in this chapter. Second, the missing layer results in a shift in travel times between the real and synthetic data. This can be corrected by assuming a vertical path for seismic energy in the sedimentary layer. Then a constant time shift can be added to the synthetic data to correct for the missing layer. A trial-and-error method resulted in determining a static time shift of 1.4 s which has been added to all plots. Fortunately, the removal of a sedimentary layer of constant thickness in the region of this study does not adversely affect the model. Southern Alberta and northern Montana have a very uniform, relatively undisturbed sedimentary section which can be effectively approximated in the model by a static time shift.

6.2 The Nature of the Moho

The crust-mantle boundary, the Mohorovičić Discontinuity – now universally referred to as the Moho – was originally identified by seismic refraction analysis [Mohorovičić 1910] to be one of the most distinct boundaries within the differentiated Earth. Initially defined as a sharp chemical and physical discontinuity between predominantly mafic crustal rocks (6.5 – 6.8 km/s) and predominantly ultramafic upper mantle rocks (7.6 – 8.6 km/s), modern seismology has shown the boundary to be much more complex. For example, a generalised model of the continental Moho invokes a transition zone of variable thickness composed of interbedded anastomosing layers which progress from predominantly crustal mafic granulites to predominantly mantle ultramafic rocks with depth [Jarchow and Thompson 1989]. Numerous studies have proposed that the boundary may include such features as partial melts and recrystallised melts, igneous layering, metasedimentary or oceanic crustal residuum from subduction processes, eclogitisation along shear zones, and intrusions or thrust material from lower in the mantle, all of which would affect the seismic signature of the boundary on length scales as small as ten metres and as large as tens of kilometres [Hammer and Clowes 1997].

Ray-theoretical inversion methods, such as the one used to derive the velocity model in Chapter 5, do not provide a means for examining many of the features expected in a transitional, as opposed to sharp, Moho. And, as already seen, (Fig. 6.4), there are distinct differences between the amplitudes of the P_n phase seen in real data as opposed to synthetic finite-difference data using the ray-theoretical model as input. In addition, occurrences of a coda to the P_n phase are not seen in the ray-theory model. In this section, the final RAYINVR model is modified in some simple ways and used as input to the finite-difference routine to investigate the response of various characteristics of the Moho and to evaluate whether or not they are occurring in the real data. These modifications can be divided into two categories: modifications to the nature of a Moho

transition zone and modifications to regional structure of the Moho surface from one geographic area to another.

6.2.1 Investigations of a Moho Transition Zone

In this section, four relatively simple models will be evaluated to explore some of the effects of specific features incorporated in a transitional Moho. Comparisons with the Deep Probe data set (SAREX shot 9) are made in order to ascertain the plausibility of each model. The four models are characterised as follows.

- Transitional interbedding of layers. The transitional Moho in this model is represented by a system of layers with constant thickness. The layers have physical properties that alternate between those of the crust and those of the mantle.
- Transitional interbedding in 2-D. In this model, randomly distributed elliptical bodies of statistically determined size with physical properties different from those of the background rock are used to represent a transitional Moho which is more geologically reasonable than the previous model and conforms to the generalised model for a transitional Moho mentioned above [Jarchow and Thompson 1989].
- Moho overlying zero velocity gradient. The effects of a zero velocity gradient in the upper 10 km of the mantle are modelled in order to investigate a possible cause of low amplitudes observed for the P_n phase in the real data.
- Transitional 2-D interbedding with zero background velocity gradient. For this model, the previous two models were combined in order to test the joint application of a geologically reasonable 2-D transition model with a zero background velocity gradient.

Transitional interbedding of layers

A simple model for a transitional Moho is a series of layers of varying thickness with material properties which alternate between those of the crust and those of the mantle. To this end a model has been constructed (Fig. 6.7) which contains eight layers ranging in thickness from 250 to 1000 m. Four layers with crustal material properties which successively thin out with depth are interbedded with four layers with upper mantle properties which successively thicken with depth (Fig. 6.8).

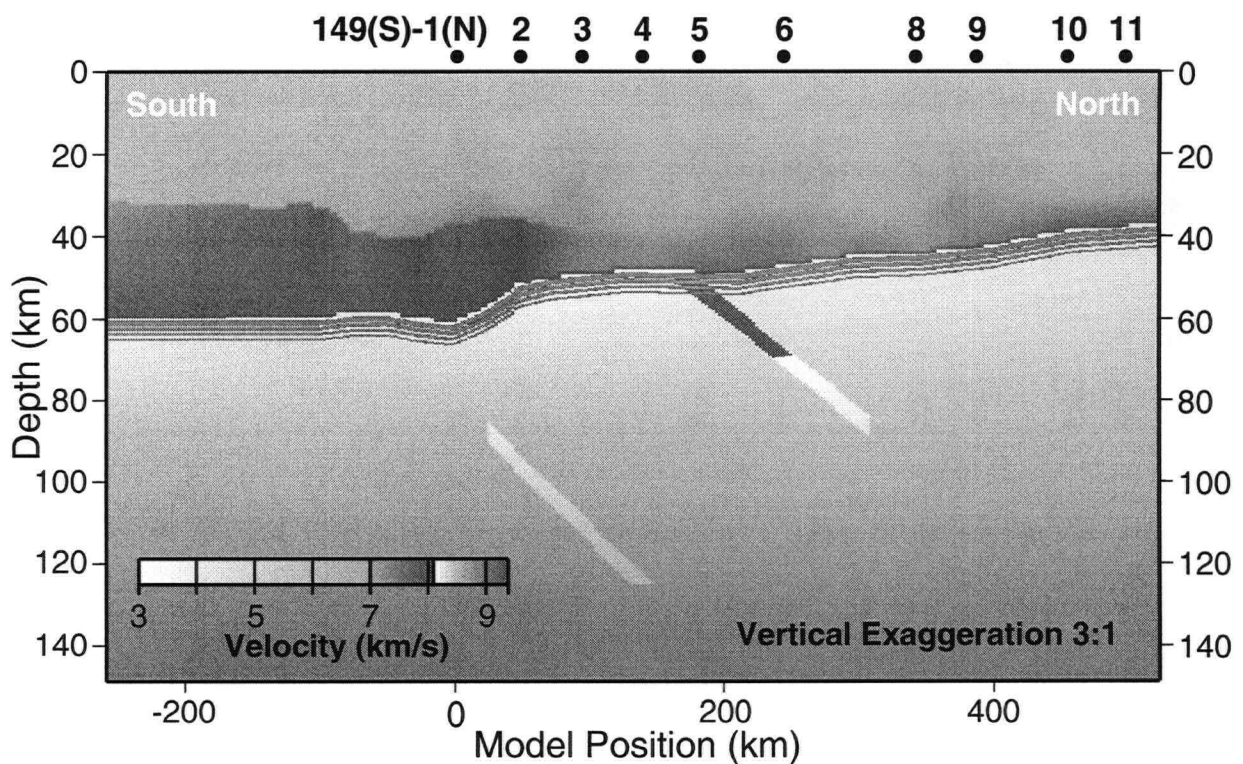


Figure 6.7: Model 5 - Transitional Moho. Model 4 (Fig. 6.3) has been modified by the addition of alternating layers of crustal and mantle elastic properties as shown.

The resulting synthetic seismogram for SAREX Shot 9 (Fig. 6.9b) from this model shows an interesting complication to the coda patterns of the $P_m P$ (labelled A in figure) and P_n (labelled C) phases when compared to the result of modelling with a discrete Moho discontinuity (Fig. 6.9a). As a relevant check on the final Deep Probe / SAREX model, note that the offset position of large

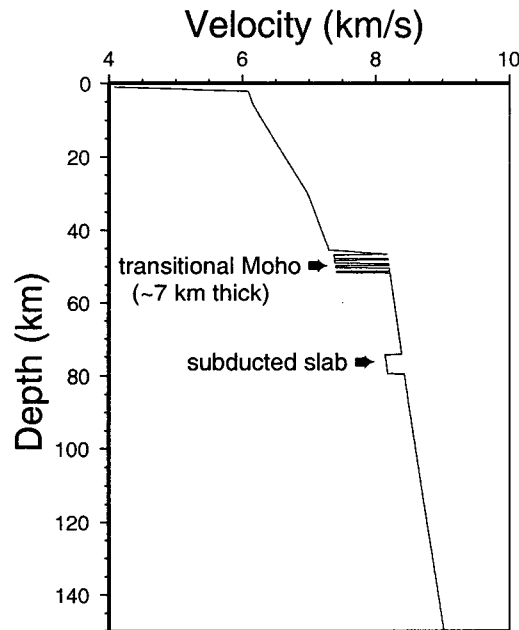


Figure 6.8: 1-D profile through Model 5 at model position 274 km.

amplitudes associated with $P_m P$ both to the south and the north of the shot point are consistent with the data. The ringy character of the $P_m P$ reflection coda is similar to that seen in the real data (enlargement of area 1 in Fig. 6.9a). In addition, a second strong $P_m P$ -like reflection is seen (labelled B in Fig. 6.9b) which is a manifestation of the base of the Moho transition zone. This reflection corresponds to a region of disturbed signal in the real data, but has a more coherent character than that seen in the real data. The amplitude of the P_n coda at offsets between 250 and 350 km (labelled C) is higher than that seen in the real data (enlargement of area 2 in Fig. 6.9b), but it is interesting to note that the amplitude of the P_n first arrival in this same range (labelled D) is decreased in the transitional Moho model from that seen in the sharp Moho model. As one of the major goals of this section is to examine the low amplitude P_n in this offset range, this is a gratifying observation. However, these P_n amplitudes are still much higher than those seen in the real data, so it would appear that interbedded layers alone will not provide a complete explanation.

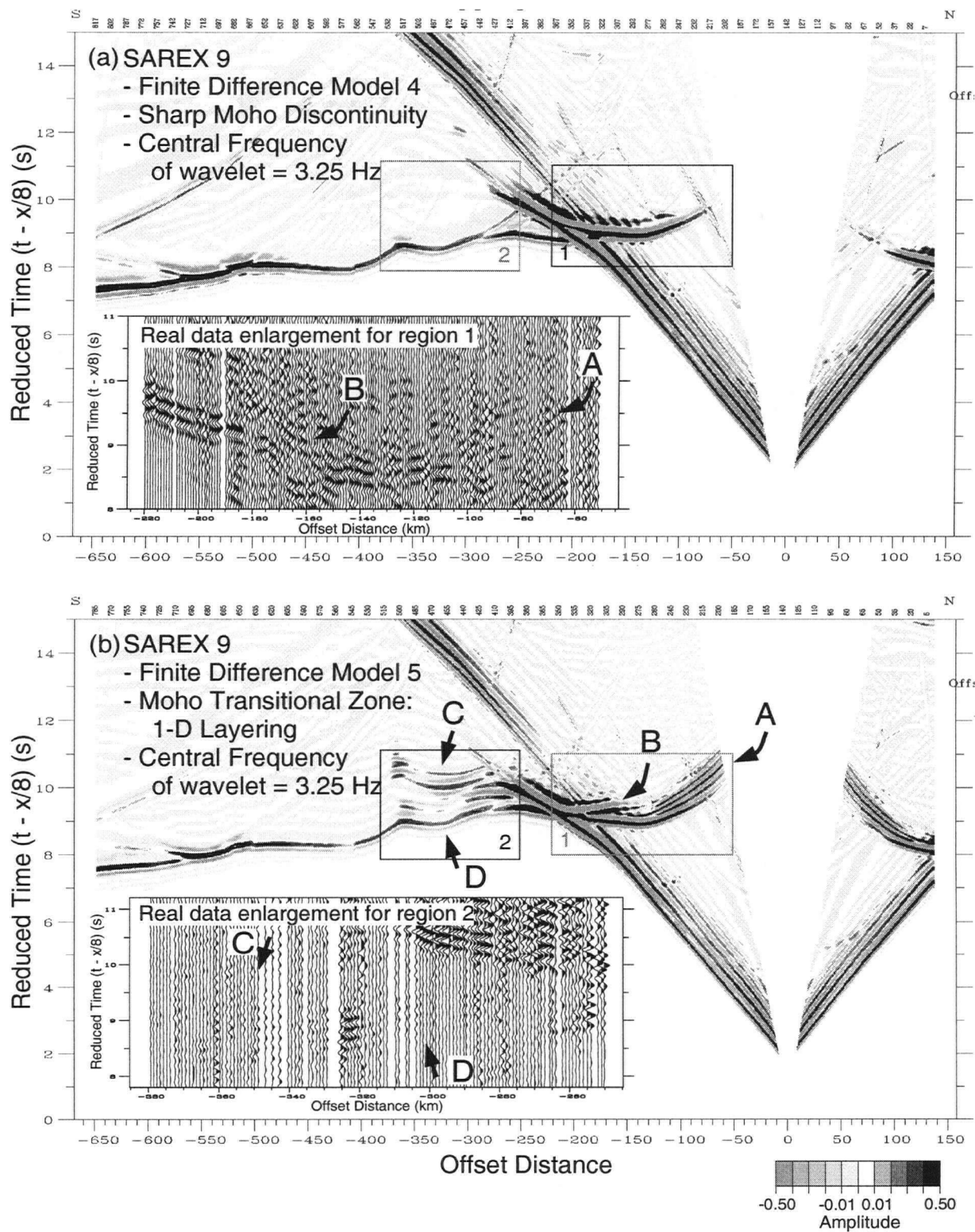


Figure 6.9: SAREX 9 finite difference synthetics. Comparison of (a) Model 4: a discrete Moho discontinuity to (b) Model 5: a layered transitional Moho boundary zone. Letters refer to features discussed in text. Enlargements of real data from the time-offset windows labelled 1 and 2 in both (a) and (b) are included for comparison. Data are trace normalised and plotted in variable-area wiggle-trace.

Transitional interbedding in 2-D

A more geologically reasonable model for a transitional Moho requires the consideration of the 2-D velocity structure of the transition zone. A model has been constructed by adding a layer of statistically defined ellipses with lower-crustal properties to the upper mantle (Fig. 6.10). A velocity function extracted from a single position in this model (Fig. 6.11) shows that in 1-D the model is very similar to the layered model previously examined (Fig. 6.8). The choice of parameters for the ellipses (as specified in the caption of Fig. 6.11) was initially based on those used to successfully model Moho features in the Trans-Hudson Orogen Refraction Experiment [Németh 1999]. The dimensions and distribution of the ellipses and the thickness of the transitional layer

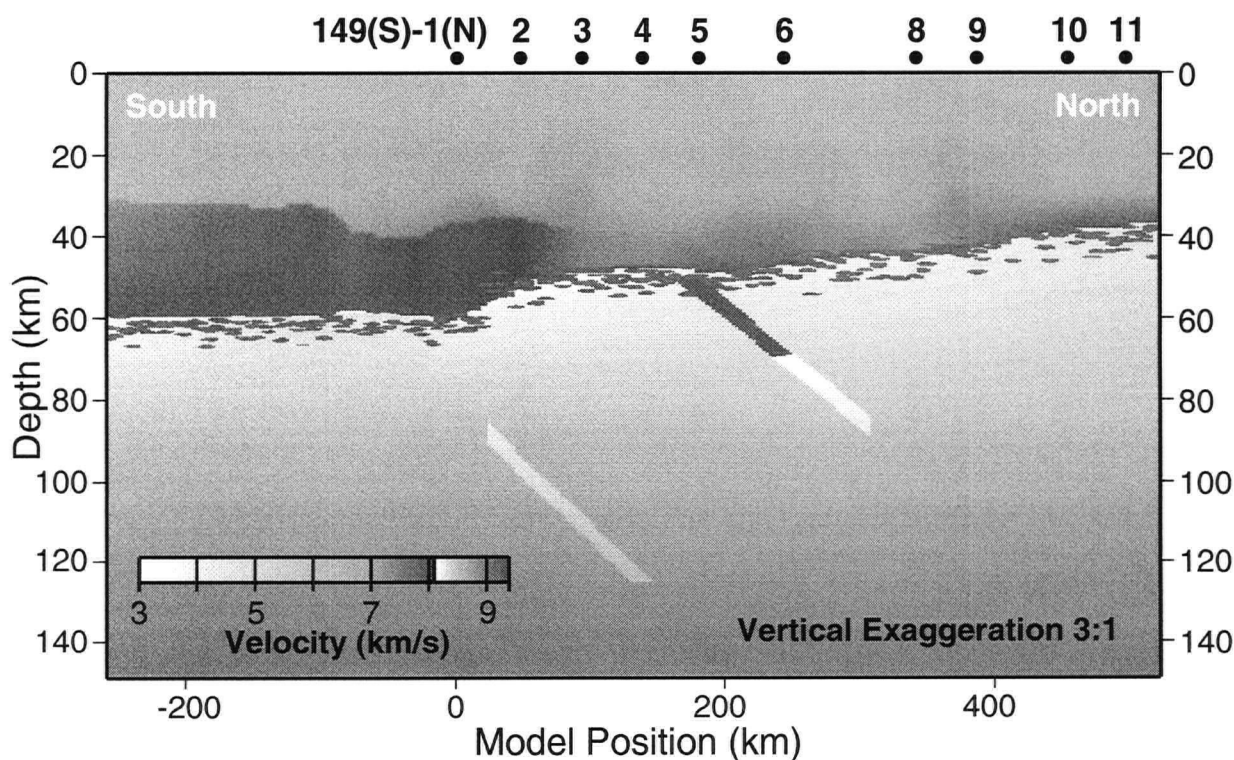


Figure 6.10: Model 11 - Transitional Moho. Model 4 has been modified by the addition of statistically defined elliptical structures in the uppermost 6 km of the mantle with velocities characteristic of the lower crust. (Ellipse dimensions: $x=6\pm.12$ km, $z=0.36\pm.12$ km. Ellipse velocities: $v=7.85\pm.05$ km/s at Moho depth with an increment of $.0083$ km/s/km. Ellipse distribution - horizontal: 1 per 3.0 ± 1.2 km, vertical: 1 per 5.0 ± 1.2 km.)

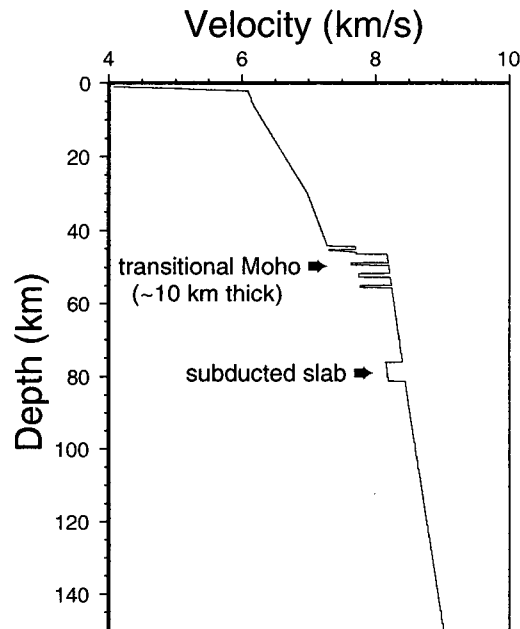


Figure 6.11: 1-D profile through Model 11 at model position 274 km.

were then modified in an *ad hoc* manner in order to produce phase characteristics in the finite-difference model which compared in offset and time to those seen in the real data.

The resulting seismogram (Fig. 6.12) shows characteristics similar to those generated with a 1-D layered Moho transitional zone. The P_mP reflections have a ringy character (labelled A in figure), similar to that seen in the previous synthetic (Fig. 6.9b) and in the real data (enlargement of area 1 in Fig. 6.9a). In fact, the more random nature of this P_mP coda, especially at offset distances less than 100 km, is more like the real data. The secondary P_mP reflection (labelled B), although not as distinct as in the previous synthetic, is still present; its non-distinctness again makes it more like the phase seen in the real data. While this model seems to replicate the real P_mP phase, it does not do as well with the P_n phase. The amplitudes of the P_n first arrivals in the 250 to 350 km offset range (labelled D) do not appear to be appreciably lower than in the model with a sharp Moho transition; they are much higher than in the real data (enlargement of area 2 in Fig. 6.9b). However, the amplitude of the P_n coda (labelled C) in the same offset range is much lower than that seen in the layered Moho model (Fig. 6.9b); this is in better agreement with the

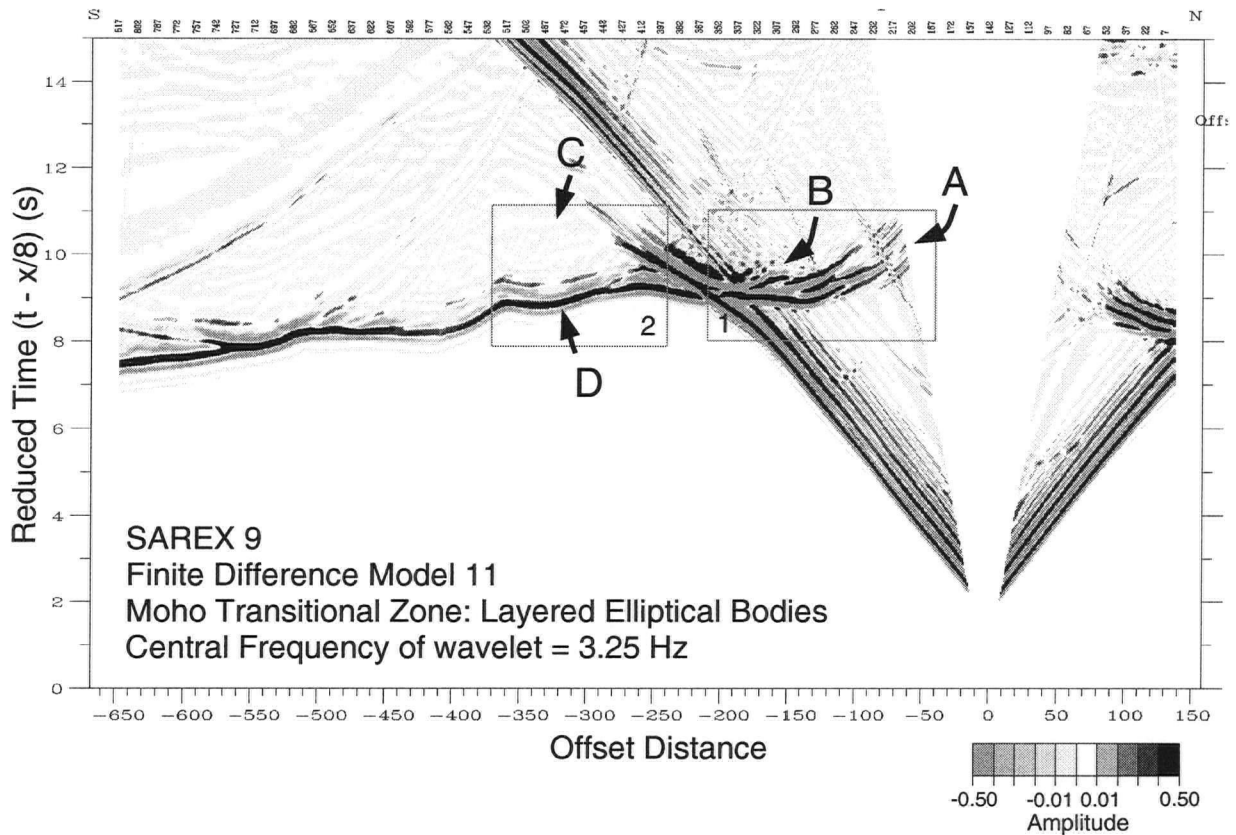


Figure 6.12: SAREX 9: Model 11 finite-difference synthetic. Moho boundary zone statistically defined by a layer of ellipses in the uppermost mantle with velocities characteristic of the lower-crust. Letters refer to features discussed in text. Grey boxes labelled 1 and 2 correspond to the time-offset windows of the real data examples in Fig. 6.9.

real data.

Moho overlying zero velocity gradient

As already mentioned, one of the major discrepancies between the finite-difference models and the real data is that the amplitude of the P_n phase, especially at offset distances less than 450 km, is higher in the models than in the real data (Fig. 6.4a). By modifying the uppermost 10 km of the mantle in the input model to have a zero velocity gradient (Fig. 6.13), the low amplitudes seen in the real data are successfully modelled. The determination of a 10-km thickness for this uppermost mantle lid was again determined in an *ad hoc* manner. Several finite-difference models were generated and evaluated for their ability to match the offset-distribution of low amplitude

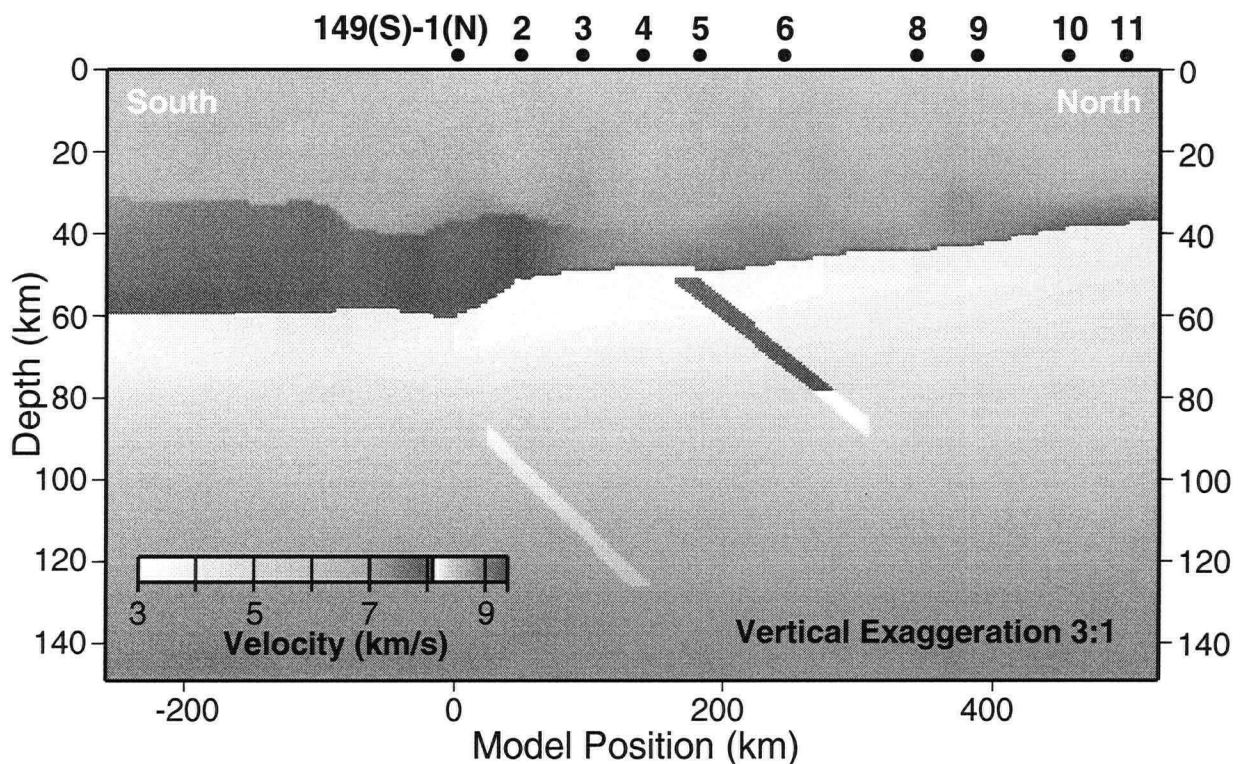


Figure 6.13: Model 10 - Sharp Moho discontinuity overlying a 10-km thick lid in upper mantle with no velocity gradient.

P_n arrivals while still maintaining an upper mantle velocity structure that did not deviate far from the original model at greater depths.

The comparison of P_n amplitudes in the real and modelled data is much more satisfactory in this example (Fig. 6.14) than in the previous examples (Fig. 6.4). Note that the amplitudes of the P_n first arrivals between offsets of 250 and 450 km (labelled A in Fig. 6.14b) are greatly reduced from those seen in the models with a positive velocity gradient in the uppermost mantle (*e.g.*, Fig. 6.12). Interestingly, at an offset of about 350 km (labelled B) the amplitude of P_n increases due to the significant structure on the Moho beneath the Medicine Hat Block. This amplitude feature is also observed in the real data. Unfortunately, the high-amplitude P_n phase observed at near offset distances between 200 and 250 km (labelled C) cannot be simply explained. Possibly, these arrivals are strong head-waves which persist at near-critical distances due to the large impedance

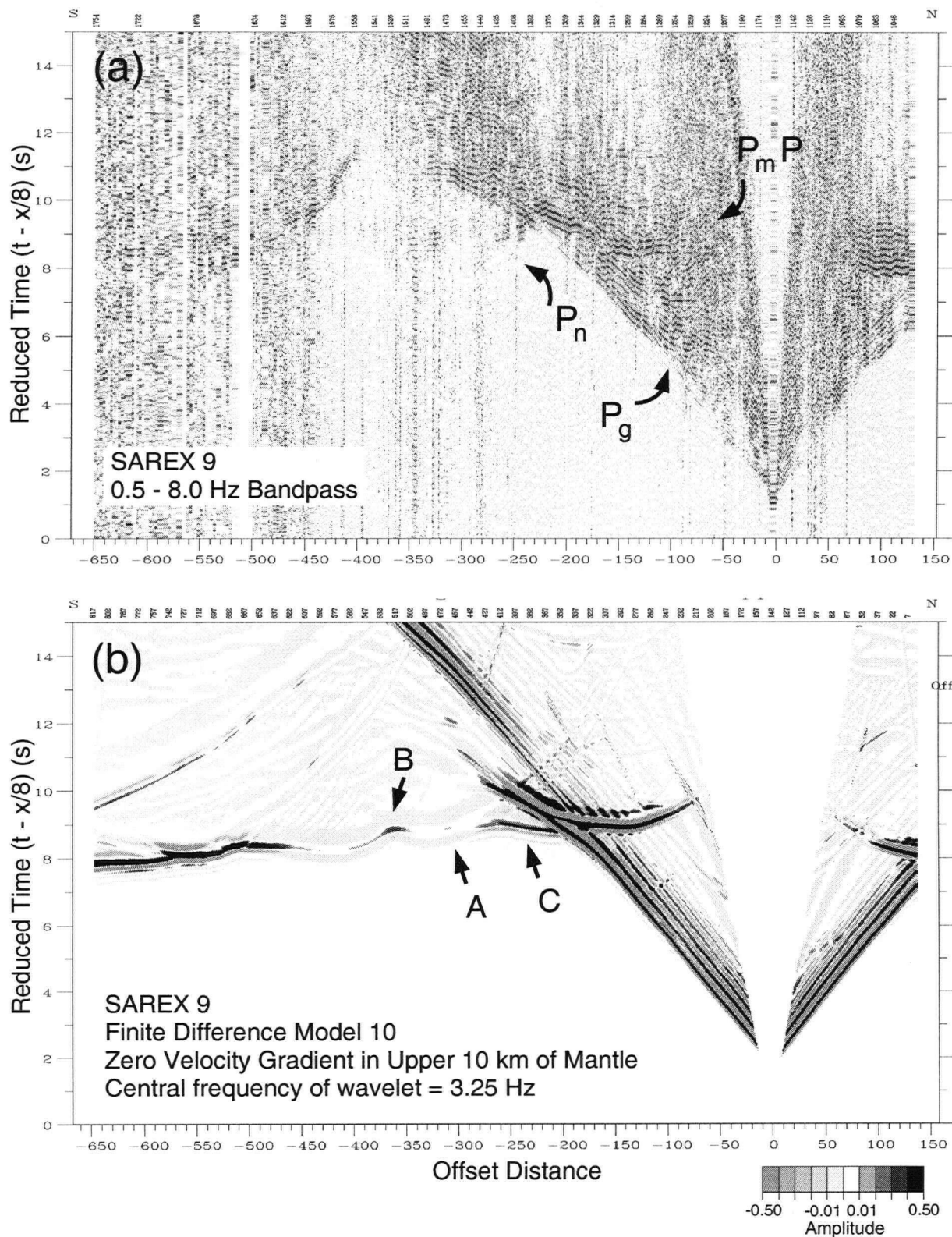


Figure 6.14: SAREX 9. Comparison of (a) real data to (b) Model 10: a Moho boundary zone defined by a 10-km thick layer of zero velocity gradient. Letters refer to features discussed in text.

contrast which exists at the top of the Moho transition zone; this again suggests that the entire story has not been explained.

Transitional 2-D interbedding with zero background velocity gradient

As a final exercise in the modelling of a Moho transition zone, the previous two models have been combined. Both of these examples successfully modelled aspects of the wave field that are seen in various parts of the real data. It is likely that the real Earth contains elements of both. This new model (Fig. 6.15) contains the same statistical distribution of elliptical bodies as used in the 2-D interbedded transitional Moho model (Fig. 6.10). However, in this case, the background velocity gradient in the upper 10 km of the mantle is zero, as in the zero gradient model (Fig.

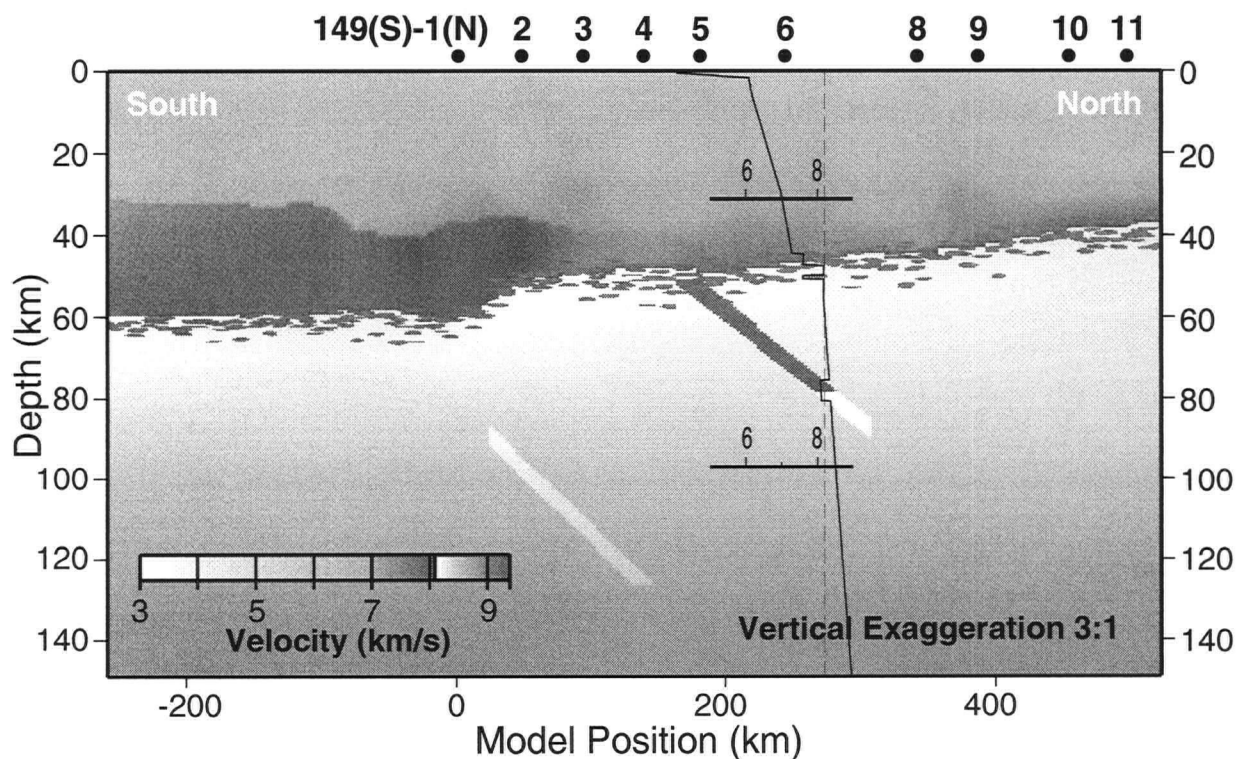


Figure 6.15: Model 12 - 2-D transitional Moho (as in Model 10) within a 10-km thick lid in upper mantle with zero velocity gradient. (Ellipse dimensions: $x=6\pm.12$ km, $z=0.36\pm.12$ km. Ellipse velocities: $v=7.85\pm.05$ km/s at Moho depth with an increment of $.0083$ km/s/km. Ellipse distribution - horizontal: 1 per 3.0 ± 1.2 km, vertical: 1 per 5.0 ± 1.2 km.) A 1-D velocity profile extracted at a model position of 274 km (dashed line) is overlaid on the model.

6.13). A 1-D velocity profile (overlaid on Fig. 6.15) shows in simple terms how the model is constructed.

As expected, elements of both the low velocity gradient in the upper mantle and the interbedded elliptical bodies are apparent in the synthetic seismogram section (Fig. 6.16). The ringy character of the P_mP (labelled A in Fig. 6.16) and the secondary P_mP reflection (labelled B) are both apparent. Their somewhat distorted character, which is also seen in the real data (Fig. 6.14a), suggests that the interbedded 2-D-bodies model may be a closer approximation to the real Earth than a layered model would be. There is no evidence of strong P_n coda in the offset range between 250 and 350 km (labelled C); this is in agreement with what is observed in the real data and is another line of evidence supporting interbedded 2-D bodies rather than layers (the modelling of

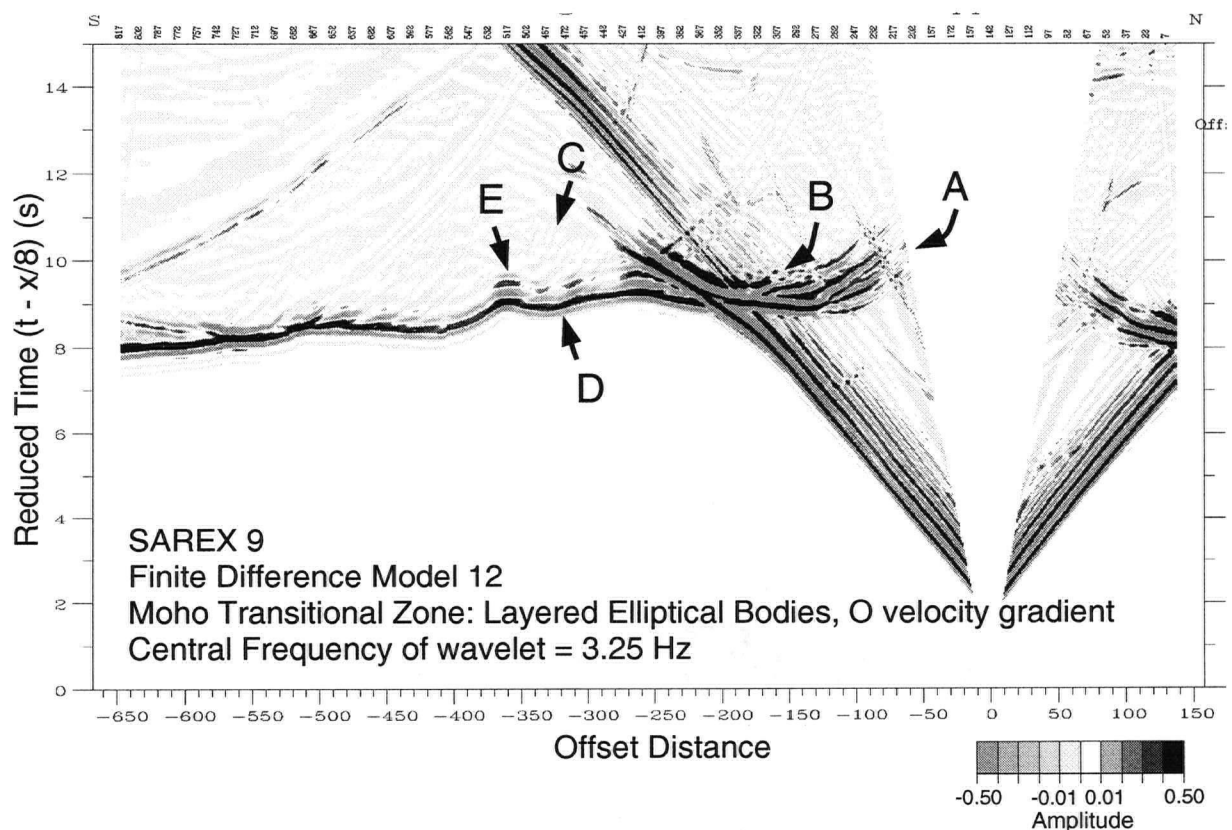


Figure 6.16: SAREX 9: Model 12 finite-difference synthetic. Moho boundary zone defined by elliptical bodies within a 10-km-thick lid in the upper mantle with zero velocity gradient. Letters refer to features discussed in text.

which supported high P_n -coda amplitudes here). As for the P_n phase, amplitudes at offsets between 250 and 450 km are higher than those modelled for the previous model with a simple zero-velocity gradient in the upper 10 km of the mantle (Fig. 6.14b), and comparable to that seen for a simple sharp Moho (Fig. 6.9a). The addition of a 2-D transitional Moho to the zero-velocity-gradient model was unsuccessful in obtaining the low P_n amplitudes needed to match the real data. Indubitably, a rigorous search of geometrical and physical parameters for the interbedded 2-D bodies could result in a synthetic seismic section more closely resembling the real data. It is gratifying, though, to see such features as the high velocity later arrival in the P_n (labelled E) preserved in the synthetic data. A rigorous investigation of a transitional Moho should also be accompanied by the evaluation of each model for its near-vertical seismic response in order to ensure concordance with crustal common mid-point (CMP) stacked reflection data in the area.

6.2.2 Structures on Moho: Distinct vs. smooth change

As already mentioned in Chapter 5, one of the most dramatic features in the final Deep Probe velocity model is the large step that occurs in the Moho beneath the Medicine Hat Block. At this location, the thickness of the crust changes by as much as 15 km over a distance of ~ 75 km. Due to the small number of rays that are traced in this region in the RAYINVR velocity model, the shape of the Moho is not well constrained. In this section, finite-difference synthetics are generated for SAREX shots 4, 5, 6, 8 and 9 in order to compare the expected response for a model with a laterally smooth Moho (as seen in all previous finite-difference models, *e.g.*, Fig. 6.3) and one with a vertical offset of the Moho (Fig. 6.17). Note that for SAREX shot 4, the offset of the step in the Moho is only ~ 75 km south. This offset increases to ~ 325 km for SAREX shot 9.

Examples of the specific features targeted by the finite difference modelling of this section are seen in the data from SAREX shots 4 and 9 (Fig. 6.18). The southward travelling waves from SAREX shot 4 (Fig. 6.18a), sample a complicated section of the lower crust in the region of the

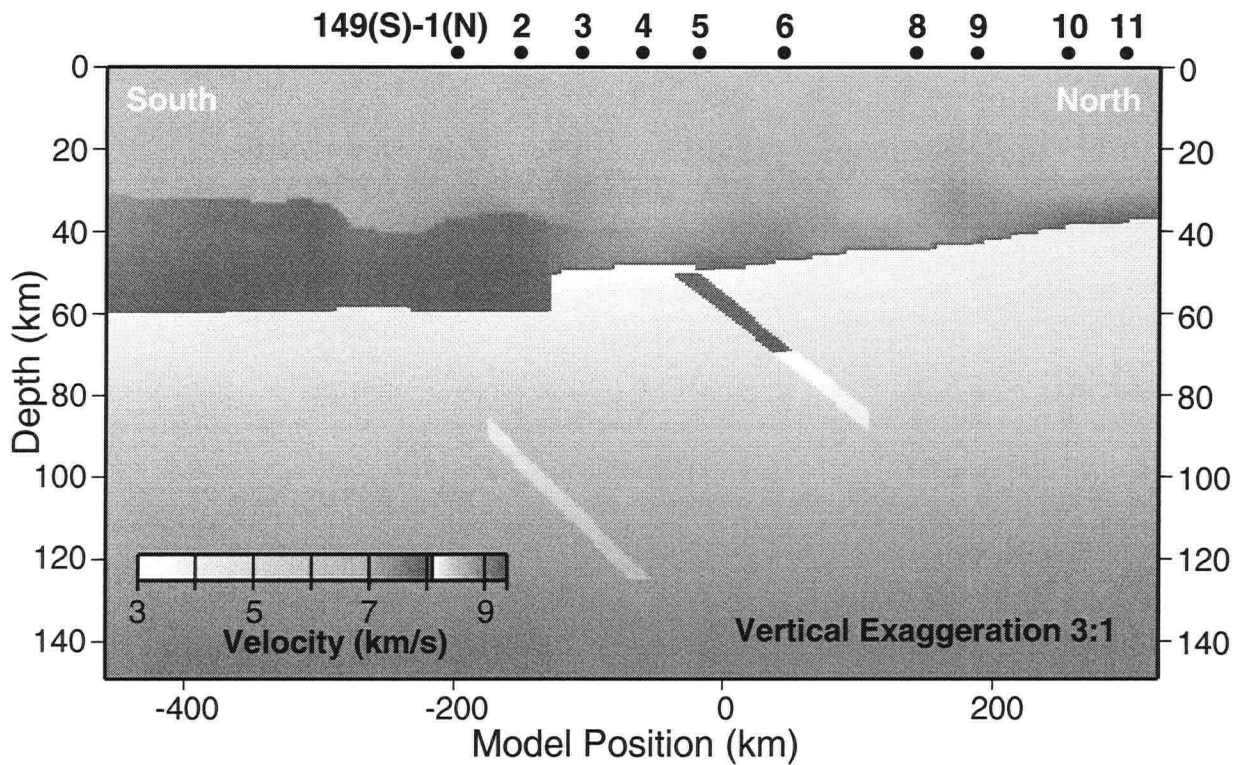


Figure 6.17: Model 6 - Sharp Moho break. Model 4 has been modified by inserting a sharp break in the Moho at the location where a smooth change occurs in the original model.

step in the Moho. Well developed reflections from the top of the lower crustal layer (P_iP) and the Moho (P_mP) are identified. These reflections are generated just to the north of the Moho step (see Appendix A, Fig. A.5 for ray diagram). The amplitudes of expected refracted arrivals from within the lower crustal layer (P_i) are low and contrast with refracted arrivals from the uppermost mantle (P_n) which have relatively strong amplitudes at offsets beyond 330 km. Of particular interest to the finite-difference modelling in this section is the coherent seismic character of the region labelled A in Fig. 6.18a; this character will be discussed in more detail later in this section. SAREX shot 9 (Fig. 6.18b), samples the step in the Moho at a greater offset distance. From this distance, reflections from the Moho (P_mP) to the north of the step are recorded. No reflections from the top of the lower crustal layer beneath the MHB are identified. At this greater offset distance, the step in the Moho is manifested by a bend (labelled 'step' in Fig. 6.18b) in the refracted arrivals

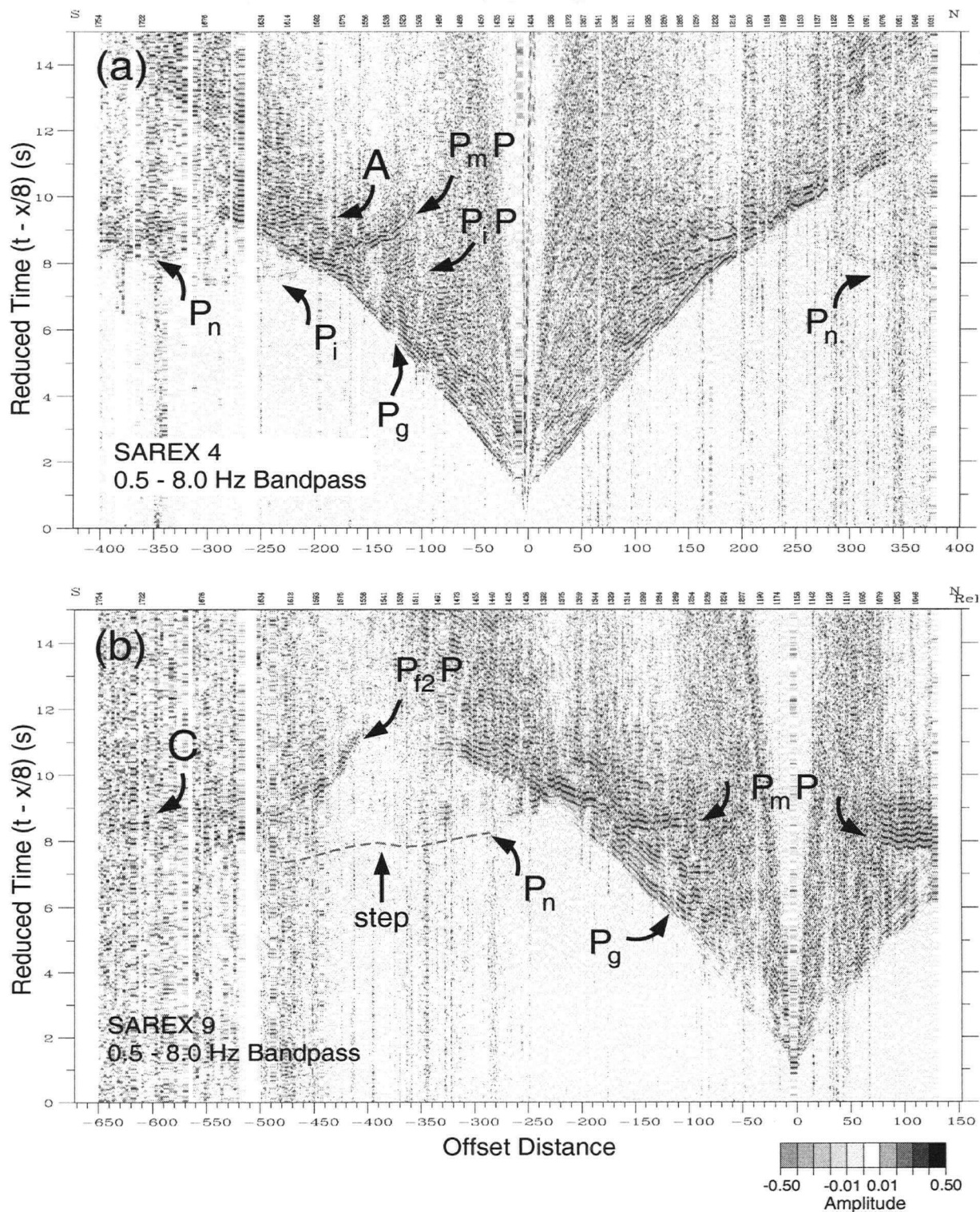


Figure 6.18: Comparison of SAREX shots 4 (a) and 9 (b) to highlight features in the data resulting from the steep structure in the Moho beneath the Medicine Hat Block. SAREX 4 is located ~ 75 km north of the structure which is sampled by pre-critical reflections. SAREX 9 is located ~ 325 km north of the structure which is sampled by wide offset reflections and refractions. Letters, phase identifications and other labels refer to features discussed in the text. Travel-time picks in the region of the 'step' in the P_n are shown in Fig. 5.2.

from the uppermost mantle (P_n). The characteristics of this bend are investigated by modelling presented in this section. In addition, the seismic character of the region labelled C in Fig. 6.18b will be examined.

In the models presented in this section, a distinct Moho boundary has been used, rather than the more likely Moho transition zone. This has been done to keep the model as simple as possible, the intent being to vary only one unknown at a time from the original ray-theoretical model which is used as input. For each of the five modelled SAREX shot points (Figs. 6.19 to 6.23), part (a) of the figure shows the finite-difference synthetic response for the smooth-step model and part (b) shows the response for the sharp step model. The major statement that can be made at the outset is that the observed differences in the responses are much more significant when the $P_m P$ reflected phase samples the region than when either lower crustal or upper mantle refracted phases do.

For the shot with the nearest offset expected to record a response, SAREX shot 4 (Fig. 6.19), note the obvious difference in the boxed area of the two plots. In this region a distinct arrival (labelled A) is seen in the sharp Moho model. This can be attributed to a diffraction from the sharp Moho boundary. This feature is also apparent on the real data for SAREX shot 4 (labelled A in Fig. 6.18a). The unusual feature with a very low apparent velocity (labelled B) seen on both the smooth and sharp Moho models for SAREX shots 4, 5 and 6 (Figs. 6.19 to 6.21) appears to be an unfortunate diffraction artefact resulting from a small region of erroneously high velocity at the top of the lower crustal high-velocity layer beneath the Medicine Hat Block. The region of this velocity error is very small and was not evident in plots of the ray-theoretically derived model, but the error has the observed effect on the finite-difference synthetic seismograms. The erroneous region of the model is not large enough to have greatly affected the development of the original RAYINVR model. Note that both the lower-crustal-layer and Moho refractions (P_i and P_n) have amplitudes that are much higher than those seen in the real data (Fig. 6.18a). This amplitude concern has been addressed, in part, for the P_n by the previous section; it would appear

that a similar approach should be applied to the study of P_i amplitudes.

SAREX shots 5 and 6 (Figs. 6.20 and 6.21) show very little difference between the responses to the smooth and sharp Moho models. The only minor difference of note is for SAREX shot 5, where a higher amplitude P_n coda is observed in the sharp Moho synthetic seismogram over a limited offset distance range (260 - 320 km). This again can be attributed to diffracted energy from the sharp step in the Moho. However, the differences seen in the outlined boxes, and enlarged in each plot, are very small and would not be conclusive features if seen in the real data. In addition, an examination of the P_n phase at these offsets in the real data reveals that they have very low amplitudes; there is no evidence for diffraction features in the real data.

SAREX shots 8 and 9 (Figs. 6.22 and 6.23) also do not have a significantly different P_n response for the smooth vs. sharp Moho models. As shown in the outlined boxes and the accompanying enlargements, the responses are almost identical. Only subtle changes in amplitude are noted and these would not be observable in real data. However, a significant difference is seen about 100 km farther from the shot, where a much stronger, low-apparent-velocity feature is seen dipping up and away from the P_n phase (labelled C) on the smoothly varying Moho synthetics. This can be attributed to the smoothly undulating geometry of the Moho surface in the region of interest. This feature has a significant amplitude and arrival time pattern that should be identifiable in the real data. Examination of the real data (Fig. 6.18b) shows an event at the appropriate location (labelled C) but with a different geometry and amplitude from that of the synthetics. In fact an alternate source for this feature will be proposed and supported in section 6.4. These last two models therefore support a sharp step in the Moho.

In summary, the finite-difference modelling of a Moho transition zone (section 6.2.1) supported the likelihood of a zone made up of interbedded 2-D structures of a specific size, physical nature and distribution. However, several significant observations in the real data were left unexplained, most particularly being low amplitude P_n phases. Fewer significant questions remain

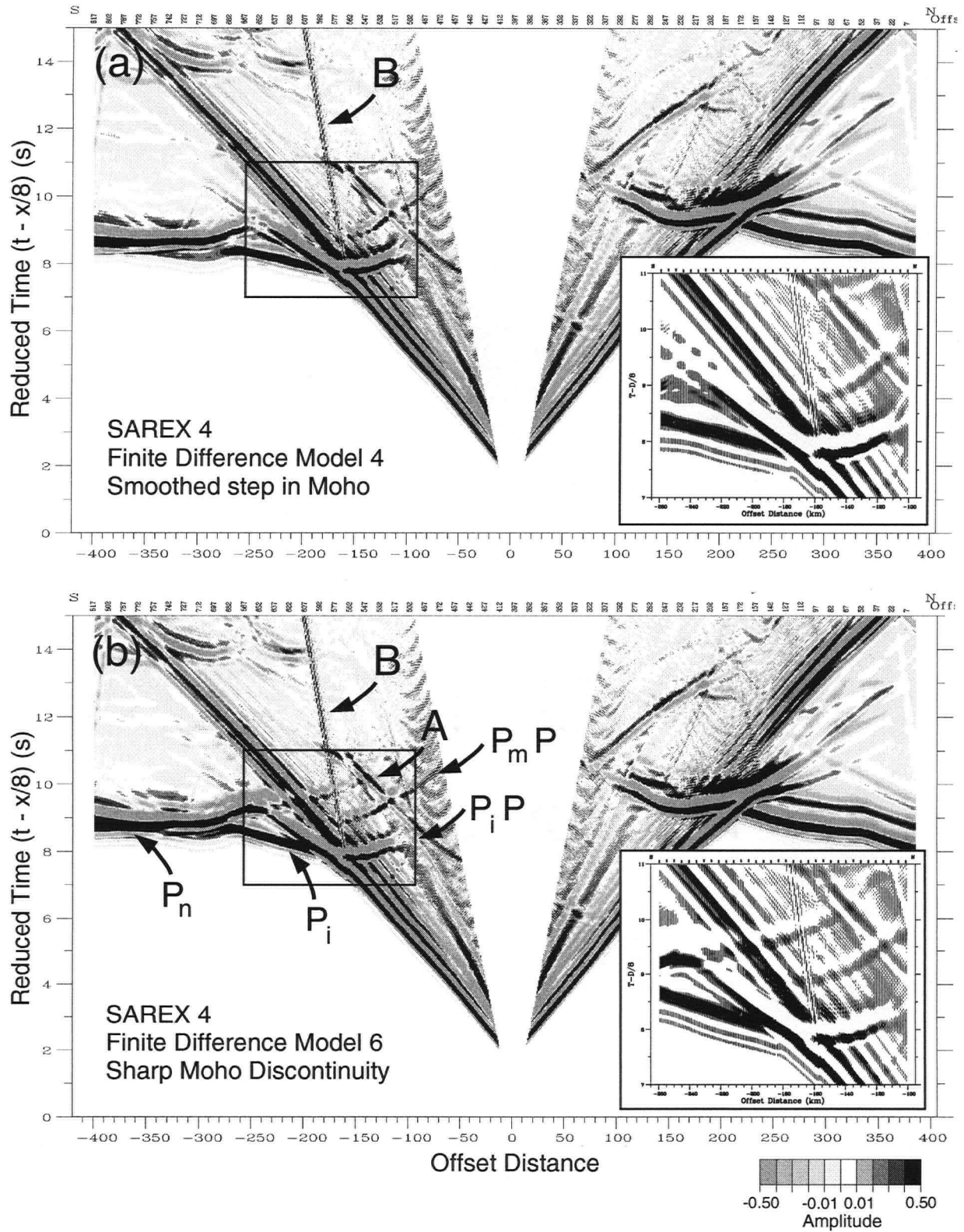


Figure 6.19: SAREX 4 finite difference synthetics. Comparison of (a) Model 4: a smooth step in the Moho beneath the MHB to (b) Model 6: a sharp step. Enlargements of the region of interest are added to the appropriate plot. Letters and phase identifications refer to features discussed in text.

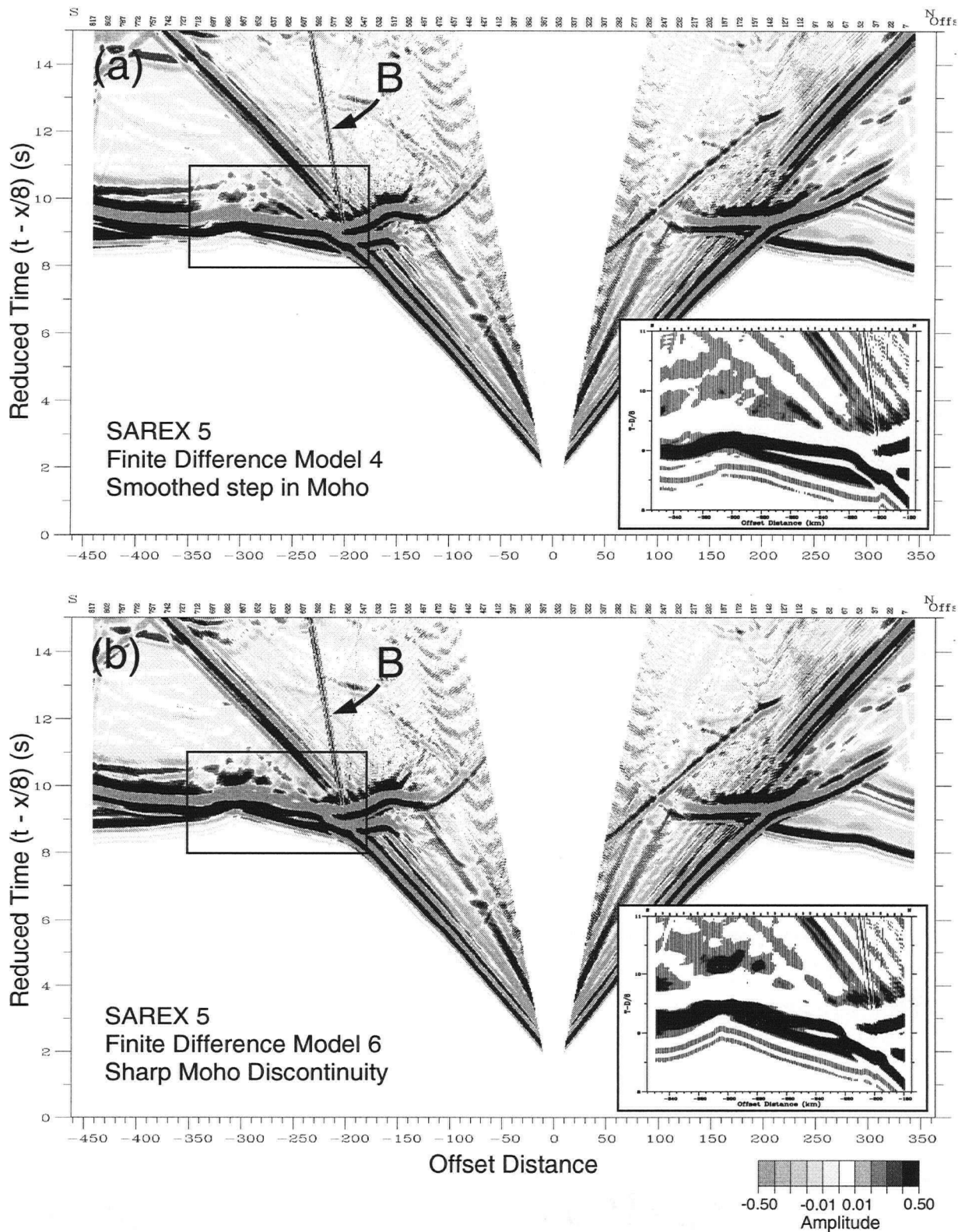


Figure 6.20: SAREX 5 finite difference synthetics. Comparison of (a) Model 4: a smooth step in the Moho beneath the MHB to (b) Model 6: a sharp step. Enlargements of the region of interest are added to the appropriate plot. Letter refers to feature discussed in text.

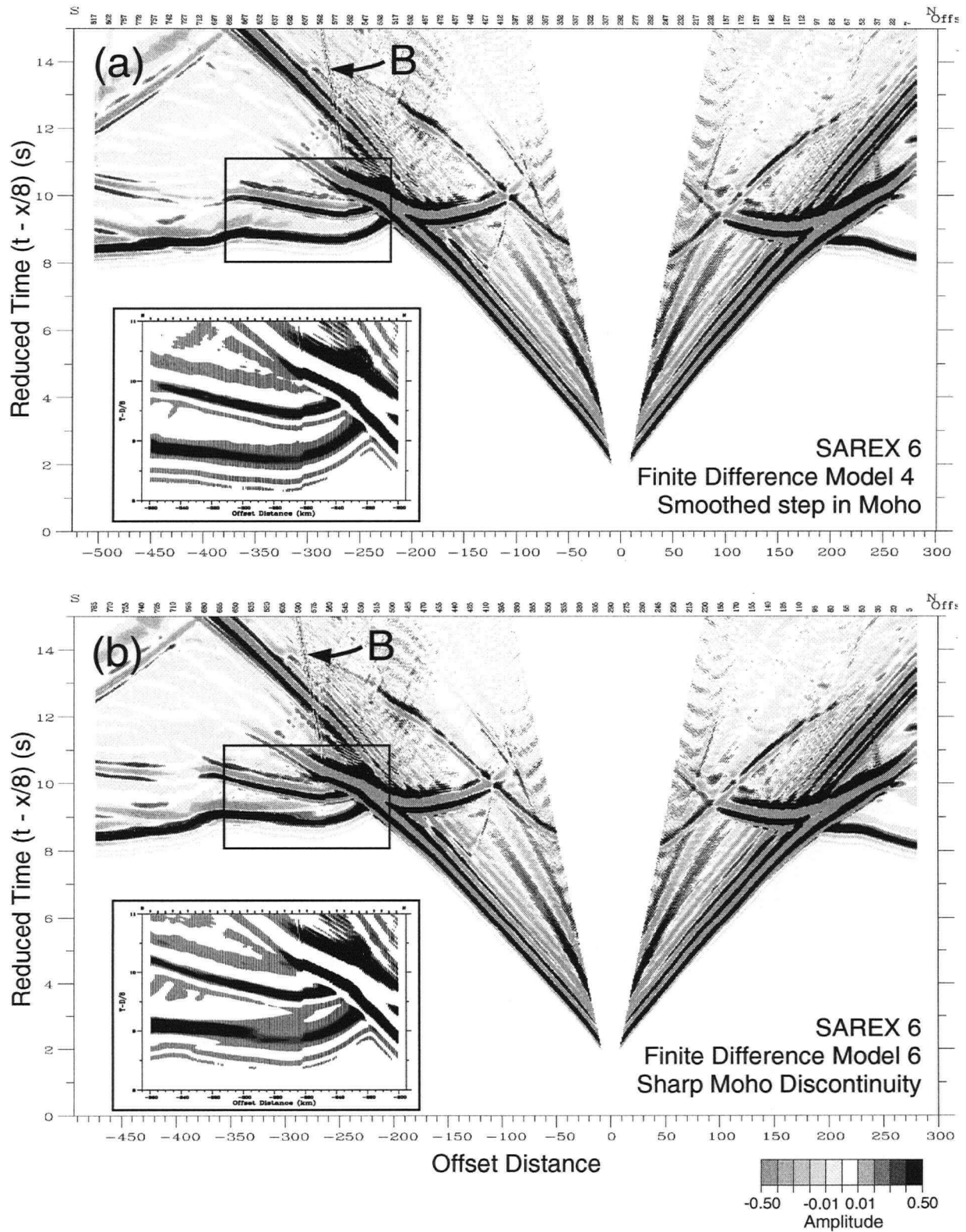


Figure 6.21: SAREX 6 finite difference synthetics. Comparison of (a) Model 4: a smooth step in the Moho beneath the MHB to (b) Model 6: a sharp step. Enlargements of the region of interest are added to the appropriate plot. Letter refers to feature discussed in text.

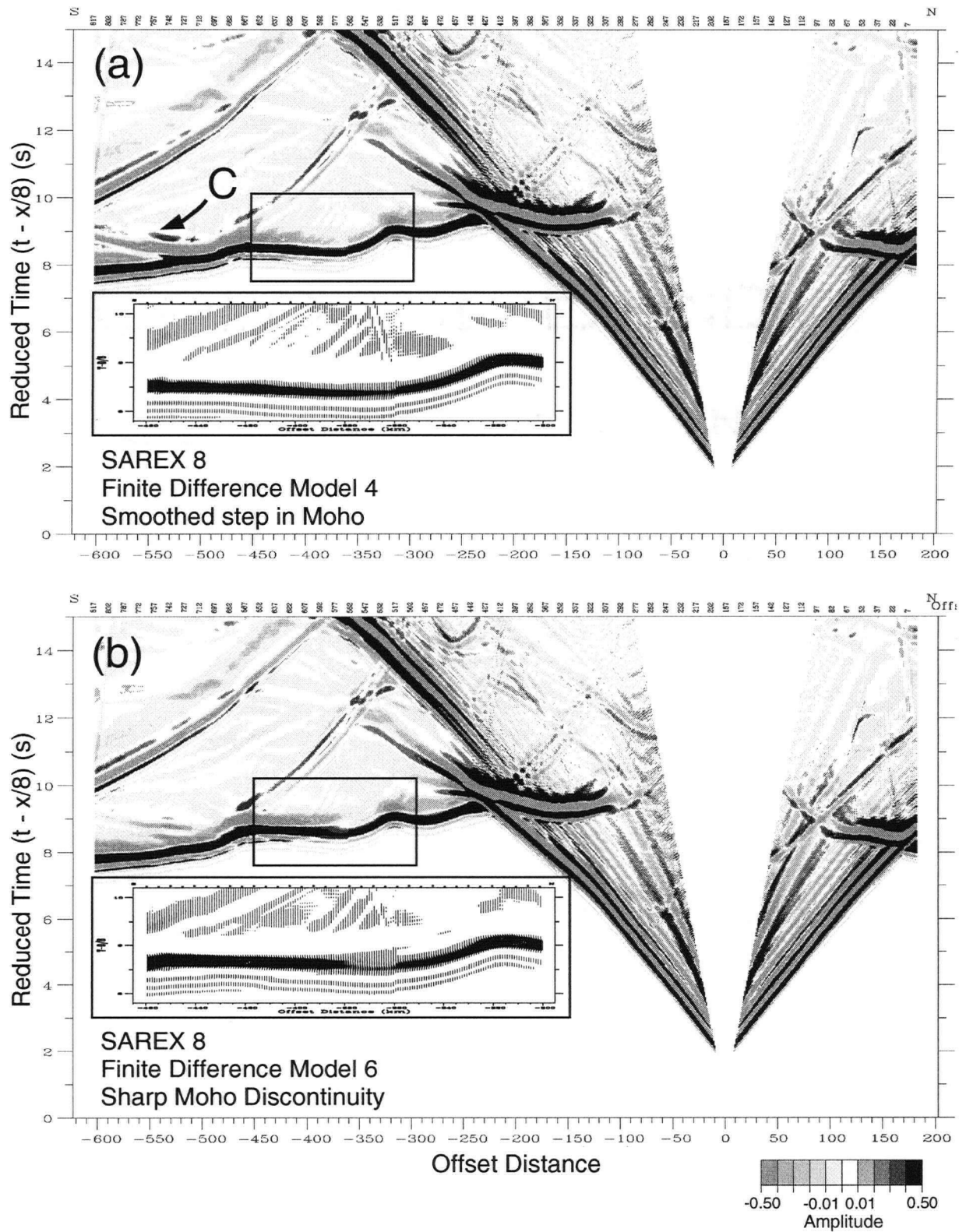


Figure 6.22: SAREX 8 finite difference synthetics. Comparison of (a) Model 4: a smooth step in the Moho beneath the MHB to (b) Model 6: a sharp step. Enlargements of the region of interest are added to the appropriate plot. Letter refers to feature discussed in text.

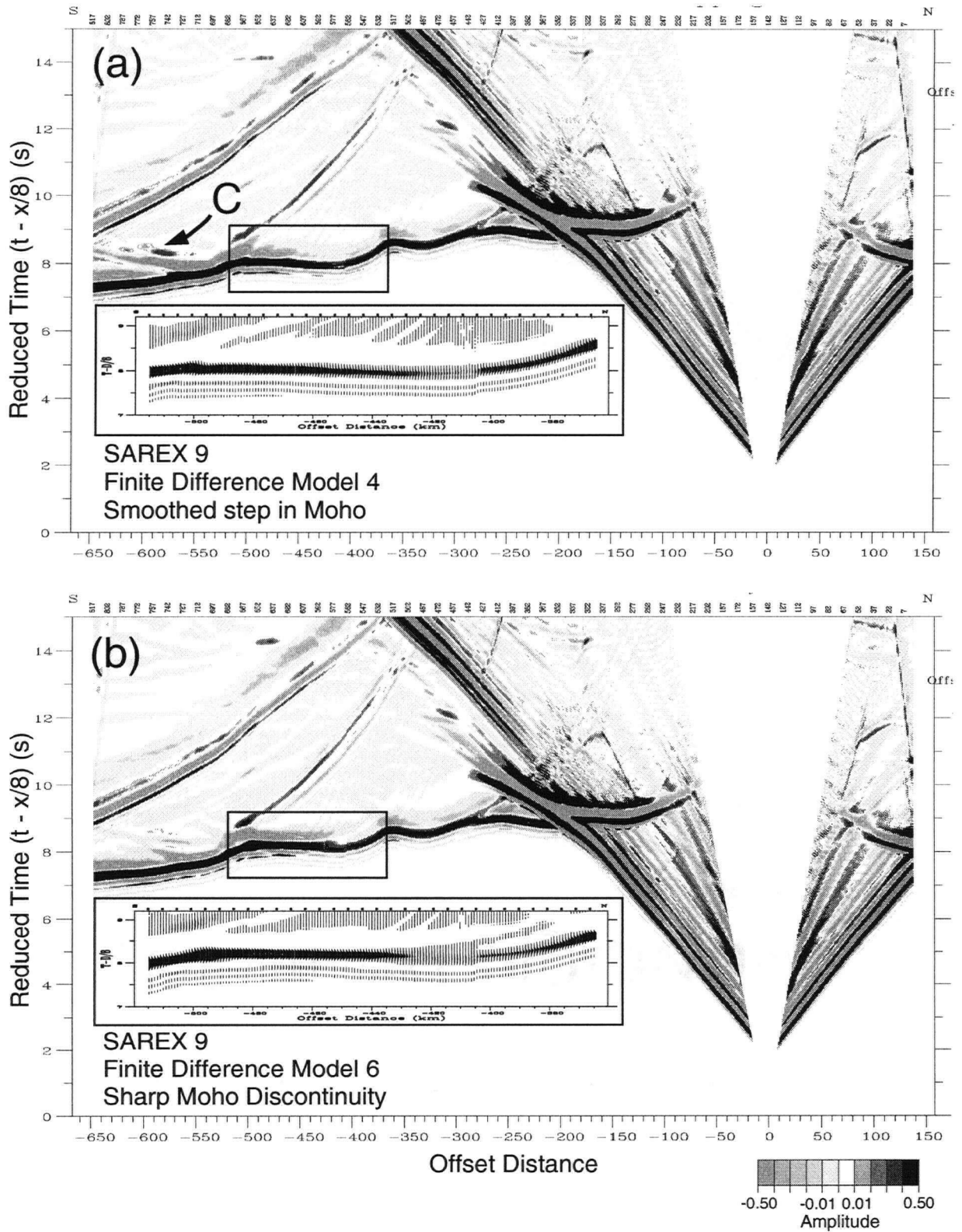


Figure 6.23: SAREX 9 finite difference synthetics. Comparison of (a) Model 4: a smooth step in the Moho beneath the MHB to (b) Model 6: a sharp step. Enlargements of the region of interest are added to the appropriate plot. Letter refers to feature discussed in text.

from the modelling of the structural step in the Moho beneath the MHB (section 6.2.2). All of the modelling supports the suggestion that the step is sharp rather than smooth. This is a good example of the ability of the finite-difference method to evaluate small, specific features.

6.3 Dipping Reflectors in the Upper Mantle

In 1981, the Flannan reflector [Smythe *et al.* 1982], beneath the Scottish Caledonides, was the first extensive upper-mantle reflector to be imaged by near-vertical seismic profiling methods. This inclined (25° to 35° of dip) reflector was recorded by the British Institutions Reflection Profiling Syndicate (BIRPS) Moine and Outer Isles Seismic Traverse (MOIST) reflection profile. In the intervening years, many common mid-point (CMP) stacked near-vertical seismic-reflection investigations of the continental lithosphere worldwide have identified structures in the upper mantle and a few of these have identified shallow dipping structures similar to the Flannan reflector [Steer *et al.* 1998]. Examples of these include the Gulf of Bothnia [BABEL Working Group 1990, 1993], the Superior Province of eastern Canada [Calvert *et al.* 1995], the European-Asian continental suture in the Urals [Knapp *et al.* 1996] and the Slave Province of northern Canada [Cook *et al.* 1998, 1999]. The work presented in this thesis suggests that these rare upper-mantle dipping reflectors seen in CMP data are analogues to the dipping reflectors seen in the R/WAR Deep Probe data set.

Several hypotheses have been developed for the development and preservation of these dipping upper mantle features. Dominating these hypotheses are several which suggest that the features are related to Precambrian subduction processes. This is strongly supported by the fact that all of the features can be correlated to known crustal sutures and also by the geometry of the features themselves. Although limited to a certain extent by the depth of penetration of the CMP method, all but one of the aforementioned examples show reflections extending to depths

of 70 to 100 km with apparent dips between $\sim 15^\circ$ and $\sim 35^\circ$. In the case of the Flannan reflector, subsequent cross-lines to the original MOIST profile have given additional control on the true dip (25° to 35°) of the feature. Suggestions for the cause of the reflectors include: the subduction of partially hydrated peridotitic oceanic lithosphere into an otherwise anhydrous mantle [Warner and McGearry 1987], the subduction of eclogitised oceanic crust [Warner *et al.* 1996], and subduction-related shear-zone development with or without subsequent mafic intrusion from the mantle [Warner and McGearry 1987]. The recent interpretation of the well-resolved upper-mantle reflections beneath the Slave Province and adjoining Paleoproterozoic domains in northern Canada suggests that at least two different geologic units contribute to the reflectivity of the dipping body: (1) the subducted sedimentary wedge within the subduction zone and (2) the down-going oceanic crust [Cook *et al.* 1999].

The Nikolaevka Reflection Sequence (NRS) observed beneath the Trans-Uralian hinterland surpasses the 100-km depth limit for upper-mantle dipping reflectors on CMP data [Knapp *et al.* 1996]. The east-dipping reflector lies between depths of ~ 130 and ~ 170 km and has a slope between $\sim 13^\circ$ and $\sim 20^\circ$. Globally, this is the deepest upper mantle reflection imaged by CMP data. While corresponding to the location of the Paleozoic suture between the Archean crust of the East European craton and the Paleozoic crust of central Eurasia, another plausible explanation for this feature is that it represents the base of the thermal lithosphere. The dip to the east may correspond to the thickening of the lithosphere beneath the Archean East European craton.

Recent data from the Vibroseis Augmented Listen Time (VAuLT) experiment in southwestern Alberta show an isolated, reflection at ~ 120 km depth [Eaton *et al.* 2000]. The reflection is ~ 15 km long and dips to the north with an apparent dip of $\sim 15^\circ$. Positioned beneath the southern edge of the Vulcan Structure approximately 300 km west of the Deep Probe profile, this feature corresponds in depth and inclination to the southern upper mantle dipping reflector interpreted in the Deep Probe data. While limited in extent as compared to the longer feature in the Deep Probe

interpretation, an argument can be made for a common source for both reflections. This suggests that the interpreted north-dipping subduction feature associated with the collision of the Wyoming Province and Medicine Hat Block extends across several hundred kilometres in southern Alberta.

The thickness and physical properties of the zones responsible for the dipping upper-mantle reflectors are important parameters to extract from the data. Subducted eclogitised crust would be expected to have higher velocities and densities than the surrounding peridotitic mantle. Their thicknesses would be controlled by the amount of material subducted and the amount of deformation (stretching or squeezing) that the material experienced during subduction. For example, seismic modelling of the Flannan reflector suggests an eclogitised layer > 2 km thick [Warner *et al.* 1996]. Shear zones within an otherwise homogeneous peridotitic mantle or shear zones with accompanying mafic intrusions could have a range of velocity and density characteristics which could be higher or lower than the surrounding mantle [Knapp *et al.* 1996]. In thickness, these zones could be thinner or thicker than in the case of subducted material depending on the deformation process and possible subsequent invasion by mafic magma. Reflections from the base of the thermal lithosphere would be the result of a bulk shift in physical properties, rather than the insertion of a layer. Reflections from such a boundary would be affected by both the impedance contrast and the width of the transition.

There are no previously published instances of refraction / wide-angle reflection (R/WAR) seismic surveys recording significant dipping reflectors in the upper mantle. While it is possible that such features could have been overlooked or misinterpreted in earlier experiments, the Deep Probe data set provides a unique opportunity to study these features due to the observation of the reflections in data from six adjacent shot locations spanning more than 400 km. All of the models shown in this chapter have included the two north-dipping subducted slabs (*e.g.*, Fig. 6.3), as interpreted in the previous ray-theoretical analysis of Chapter 5. In the RAYINVR interpretation, the subducted slabs were represented as 'floating reflectors' which were dimensionless in

the z-direction. Rays were reflected off these surfaces to calculate ray-paths and accompanying travel times. In order to produce a reflection in the finite-difference modelling procedure (and in the real Earth) these reflecting surfaces must be accompanied by a contrast in physical properties. Since the ray-theoretical modelling does not support a bulk shift in physical properties to occur at these surfaces, then the remaining option is that they represent relatively thin bodies with different physical properties than the surrounding mantle. In this chapter, the models used as input to the finite-difference routine were produced by using the 'floating reflectors' mapped by RAYINVR as the upper bounds for a slab 5 km thick in the vertical direction and with a P-wave velocity that is 0.25 km/s less than the surrounding material. The thickness and velocity chosen were constrained in an *ad hoc* manner by iteratively modelling slabs of various thicknesses and velocity contrasts and comparing the synthetic response to the real data. One possibility for the thickness and velocity contrast chosen could be that they are representative of a subduction-related shear zone which was subsequently intruded by a lower velocity material.

Many factors, such as tuning, AVO effects, and frequency content, are involved in the evaluation of these reflectors. For the simple models shown in this section, the thickness of the subducted slabs has been left constant at 5 km and the velocities within the slabs have been varied in two simple ways in order to examine the response. The first model was constructed by reversing the polarity of the velocity contrast within the slab. The second model increased the magnitude of the velocity contrast by a factor of four. Several interesting observations can be made.

Simply reversing the sign of the velocity contrast in the subducted slabs (*i.e.*, a velocity contrast of +0.25 km/s), a situation that could be representative of subducted oceanic crust that has undergone eclogitisation, produces a model (Fig. 6.24) which is as geologically reasonable as the original negative-velocity-contrast model (Fig. 6.3). A comparison of the synthetic responses to the two models shows some distinct differences in the characters of the dipping reflectors (Fig. 6.25). These differences are especially evident in the $P_{f_2}P$ reflector (the southern one) which is

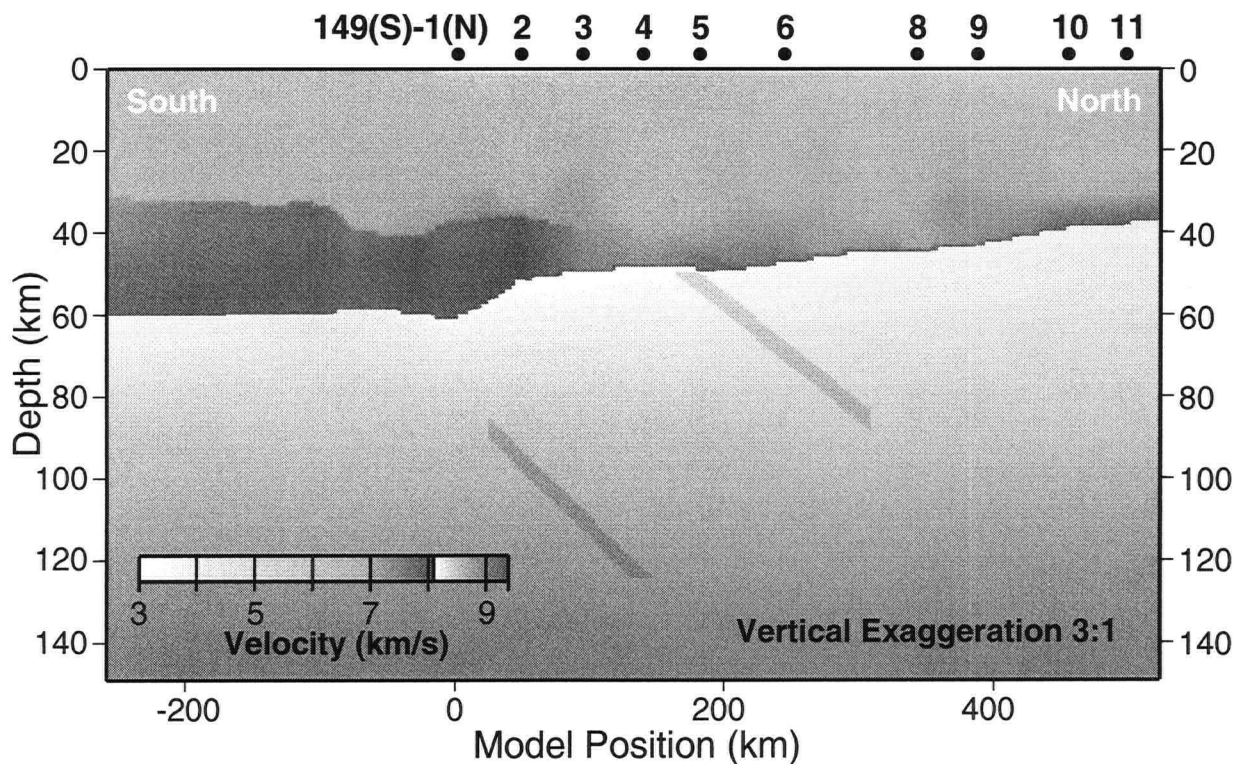


Figure 6.24: Model 4a - RAYINVR model for SAREX deployment with Earth flattening transform and 120 m discretisation. 5-km thick dipping layers have been added as shown with a velocity contrast of +0.25 km/s from surrounding rock. SAREX and Deep Probe shot locations shown along top of model. Top of model is 1000 m below sea level (~ 2000 m below the surface).

undisturbed by P_g and $P_m P$ energy. In the positive-velocity-contrast model, the $P_{f_2} P$ reflector has a 'peak – trough – weak peak' character (labelled A) while in the negative-velocity contrast model, the $P_{f_2} P$ reflector has a more diffuse 'trough – peak' character (labelled B). In addition, tuning effects result in the amplitude of B being lower than that of A. While it is difficult to make a direct comparison between these data and the real data (enlarged region in Fig. 6.25a) due to phase content and noise, it can be argued that the $P_{f_2} P$ reflector in the real data has a low-frequency trough-peak character. This supports the negative-velocity-contrast model. However, additional modelling at frequencies matching the real data would be required to conclusively support this interpretation.

The effect of changing the magnitude of the velocity contrast can be quite dramatic. If the

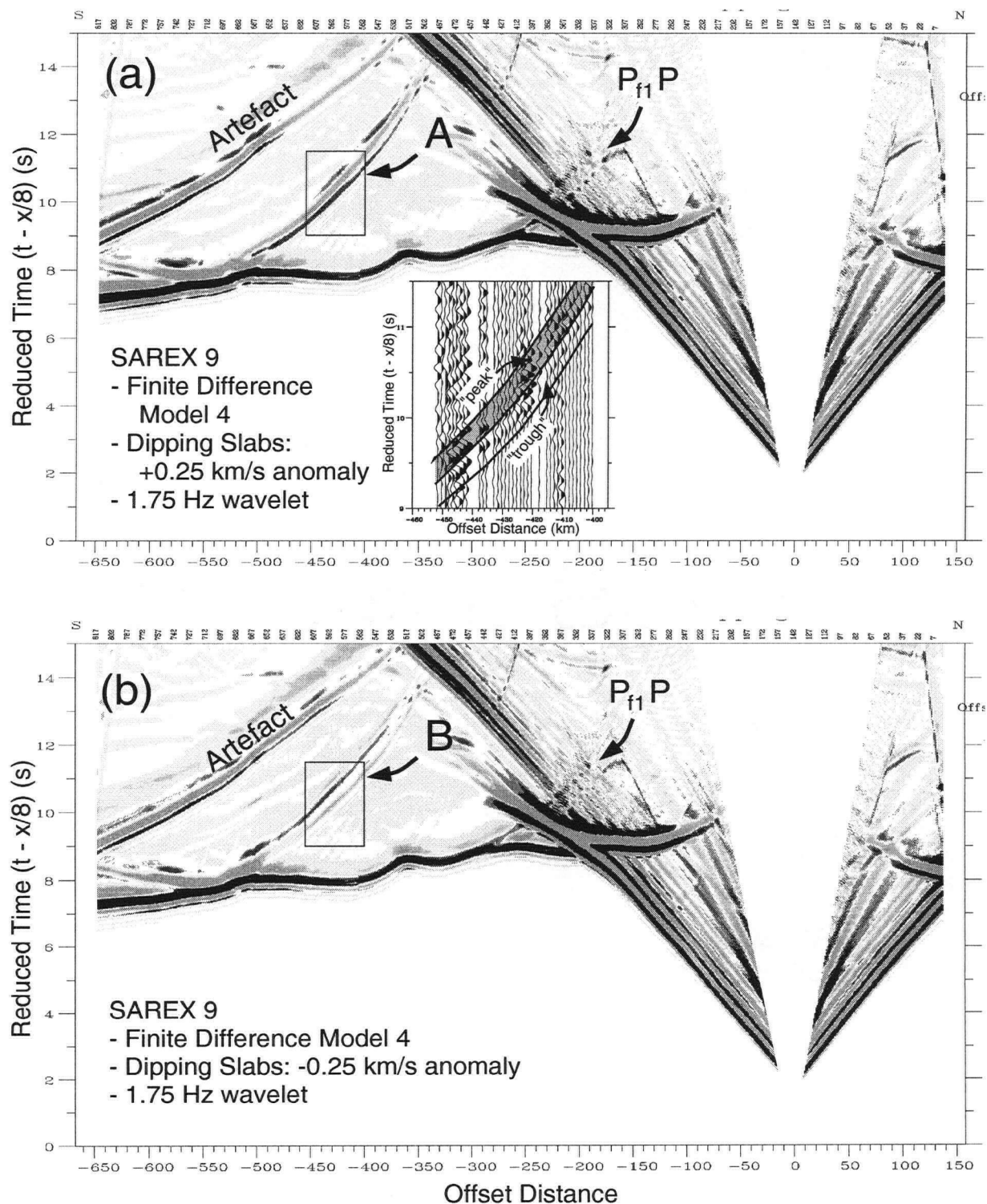


Figure 6.25: SAREX 9 finite difference synthetics. Comparison of (a) Model 4a: positive velocity anomaly slabs to (b) Model 4: negative velocity anomaly slabs. Central frequency = 1.75 Hz. Letters refer to the character of the $P_{f2}P$ reflection as discussed in the text. Boxed regions in synthetic sections corresponds to the enlargement of the real data (wiggle-trace variable-area plot) shown in (a).

negative-velocity-contrast in the last example is changed to -1.0 km/s from -0.25 km/s, the resulting synthetic shows considerable differences (Fig. 6.26). Where the $P_{f_2}P$ reflection was diffuse in the original model (labelled B in Fig. 6.25b) it is now sharp and well defined by a ‘trough – peak – peak – trough’ character (labelled C in Fig. 6.26). Also, the $P_{f_1}P$ reflection has very strong amplitudes at near offset distances. Such high amplitude events as these are not seen in the real data, but it is possible that the true amplitude contrast could lie within the range of 0.25 to <1.0 km/s.

In comparing the time duration of the dipping reflection events in the three synthetic data examples (1.0 to 1.5 s in Figs. 6.25 and 6.26) to the duration of the reflections in the real data

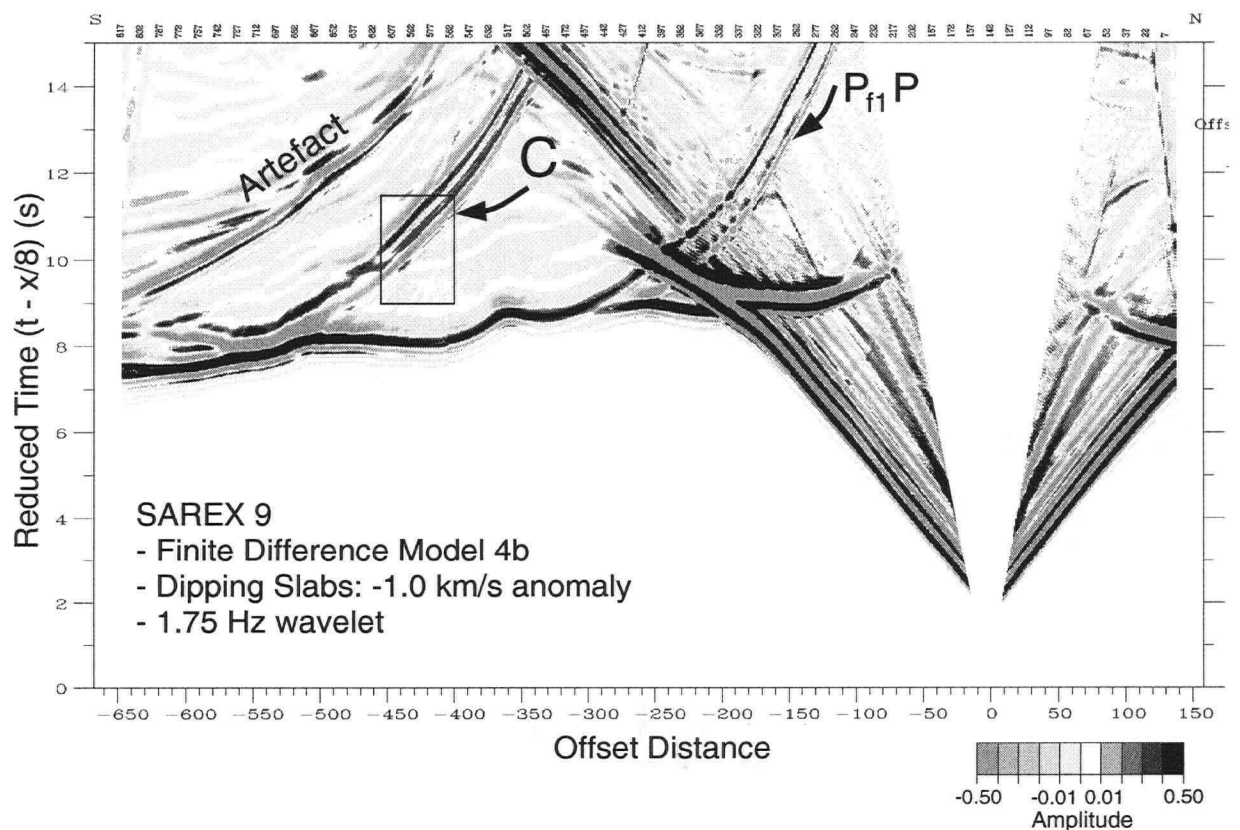


Figure 6.26: SAREX 9: Model 4b finite difference synthetic. Subducted slabs defined by a -1.0 km/s velocity anomaly. Central frequency = 1.75 Hz. ‘C’ refers to the character of the $P_{f_2}P$ reflection as discussed in the text. Boxed region in synthetic section corresponds to the enlargement of the real data shown in Fig. 6.25a.

(~ 0.5 s in the real data enlargement in Fig. 6.25a), a significant discrepancy is noted. The calculated duration of the reflection is affected by numerous parameters including the frequency content of the data (the synthetic examples are lower in dominant frequency than the real data), the extent of velocity heterogeneity within the slab, and by the thickness of the slab itself. The longer time duration of the $P_{f_1}P$ and $P_{f_2}P$ reflections in modelled data, as compared to the real data, suggests that the slab widths utilised in the model are too thick.

To summarise the conclusions that have been reached in regard to the dipping reflectors interpreted from the Deep Probe data set, the simple finite-difference models generated in this section support the interpretation of relict subducted slabs with a velocity contrast from the surrounding mantle of -0.25 to >-1.00 km/s. The thickness of these slabs is interpreted to be less than 5 km. A possible geologic scenario supporting these parameters could involve a subduction-related shear zone subsequently intruded by low velocity magmatic material. This contrasts with recent models of the Flannan reflector, developed with the use of CMP data, which suggest a positive velocity contrast within the slab (indicative of eclogitisation of subducted oceanic crust) and a thickness of greater than 2 km [Warner *et al.* 1996]. A more thorough evaluation of the dipping reflector features in the Deep Probe data would require the investigation of other more complex controlling parameters (*e.g.*, velocity heterogeneity within the slab, or a slab with a two-layer composition such as that previously discussed for the reflector beneath the Slave Province [Cook *et al.* 1999]).

6.4 P_n Coda and Teleseismic P_n Considerations

Long-range (>600 km) observations of refractions travelling at upper mantle velocities are not predicted by most homogeneous or smoothly varying models of the upper mantle. However, such observations are made to offsets as great as 3000 km in some regions of the Earth [Pavlenkova

1996]; the region of the Deep Probe data set is one of these. The source of this so-called 'teleseismic P_n ' phase can be shown to be related to the same features which produce a coda, or tail, on the P_n phase at nearer offsets (300 - 600 km). Models for the source of the teleseismic P_n phase fall into two major categories: whispering gallery models and upper mantle wave guide models.

Whispering gallery models involve multiple reflections of the P_n wave off the underside of the Moho; the P_n coda is explained by invoking lower crustal heterogeneities [Morozov *et al.* 1998]. However, modelling of whispering gallery events has not successfully reproduced either the amplitude characteristics of the teleseismic P_n and P_n coda or the coherent energy in the P_n coda while simultaneously preserving lower crustal characteristics observed in real data [Tittgemeyer, pers. comm. 1998]

Upper mantle wave guide models involve inserting a layer of heterogeneity within the upper mantle. Multiple reflections and scattering within this layer can be shown, by a variety of modelling methods, to affect the observations recorded by numerous R/WAR studies including the Russian PNE data [*e.g.*, Tittgemeyer *et al.* 1996; Ryberg *et al.* 1995], the FENNOLORA data from the Baltic Shield [*e.g.*, Perchuc and Thybo 1996; Thybo and Perchuc 1997], and the Trans-Hudson Orogen of western Canada [Németh 1999]. As detailed in the Introduction (section 1.4.2), a few hypotheses have been proposed for the emplacement and preservation of scattering bodies in the upper mantle which would result in the proposed upper mantle wave guide layer. These range from low-fraction partial-melt models [Thybo and Perchuc 1997] to petrological models combined with shear-induced anisotropy [Bostock 1998].

Due to its long offset distances and short spatial sampling interval, the Deep Probe data set is especially well suited to examining the characteristics of the P_n coda and teleseismic P_n . As observed in other data sets [*e.g.*, Thybo and Perchuc 1997; Németh 1999], the Deep Probe P_n first arrival data (Fig. 6.27) show a characteristically low amplitude over the offset range of less than ~ 400 km (the exact value varies from one shot record to another). The first arrivals experience

an increase in amplitude at offset distances greater than these, coincident with the development of a coherent coda. In the Deep Probe data, the series of events which make up the coda can be identified as a package of intermittently coherent arrivals with apparent velocities between 8.0 and 8.5 km/s which are continuous over tens of kilometres (lying between dashed lines in Fig. 6.27). Where this coda package coincides with the previously discussed dipping mantle reflections, the coda features are clearly seen to have less dip than the upper mantle reflections. The P_n coda has a variable amplitude which is often lower than that of the mantle reflections and can make their interpretation difficult. The teleseismic P_n phase corresponds to the line where the P_n coda events converge.

The teleseismic P_n and P_n coda have been effectively modelled by previous researchers [Tittgemeyer *et al.* 1996, Thybo and Perchuć 1997, Németh 1999, Tittgemeyer *et al.* 2000], who

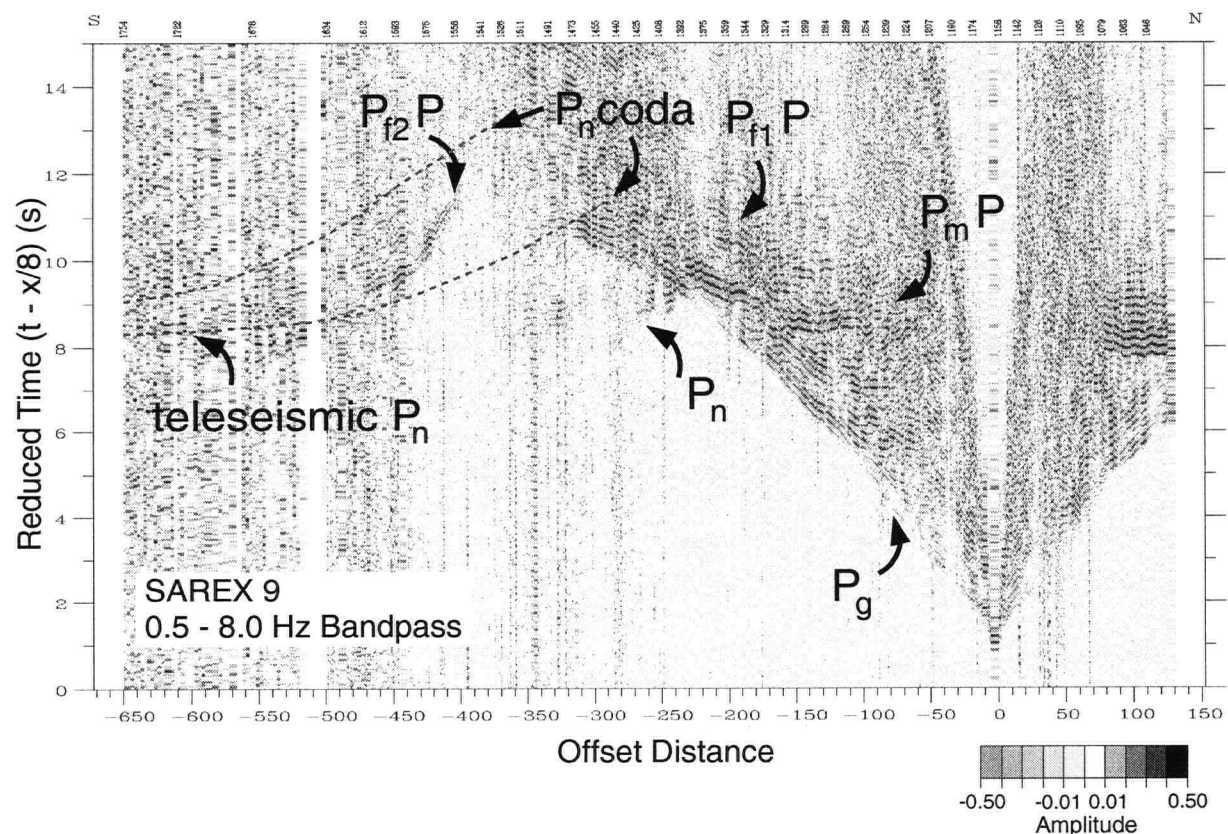


Figure 6.27: SAREX 9 with teleseismic P_n and P_n coda features highlighted. Coherent P_n coda events associated with an upper mantle wave guide lie between the grey dashed lines.

invoke an upper mantle wave guide composed of a variety of layered or statistically defined media superimposed on a relatively transparent uppermost mantle. In this section, a series of finite-difference models has been constructed with the purpose of delineating some of the properties of such a heterogeneous upper mantle wave guide specific to the area of Deep Probe. First, three models are evaluated to provide constraints on the size and distribution of heterogeneous bodies within the wave guide. These models have been constructed with dimensions similar to those of the SAREX experiment. Following this, a model has been constructed with the larger Deep Probe dimensions in order to investigate the effects of such a wave guide at greater offset distances.

SAREX Models

In order to constrain the statistical properties of heterogeneous bodies within an upper mantle wave guide specific to the Deep Probe data set, a series of three models was developed, using the dimensions of the SAREX experiment. The models presented here add a layer of elliptical anomalies between depths of 100 and 140 km. The depth extent of the wave guide layer was constrained by an *ad hoc* iterative modelling procedure; several different combinations of upper and lower bounds were modelled to find a match for the distribution of coherent events in the P_n coda. The first model shown in this section is constructed using elliptical bodies that are roughly 24 km long by 0.5 km thick (Fig. 6.28), dimensions that correspond to the preferred interpretation of similar features in the Trans-Hudson Orogen Refraction Experiment data [Németh 1999].

Two finite-difference synthetic seismograms for SAREX shot 9 have been produced using this first model, one with a central frequency of 1.75 Hz (Fig. 6.29b) and the other with a central frequency of 3.25 Hz (Fig. 6.30b). These can be compared with the synthetic seismograms from the standard model with a transparent upper mantle (Figs. 6.29a and 6.30a). The comparison is especially useful for identifying features related to the upper mantle dipping reflector as opposed to specific features of the P_n coda. In the first synthetic seismogram produced using this technique

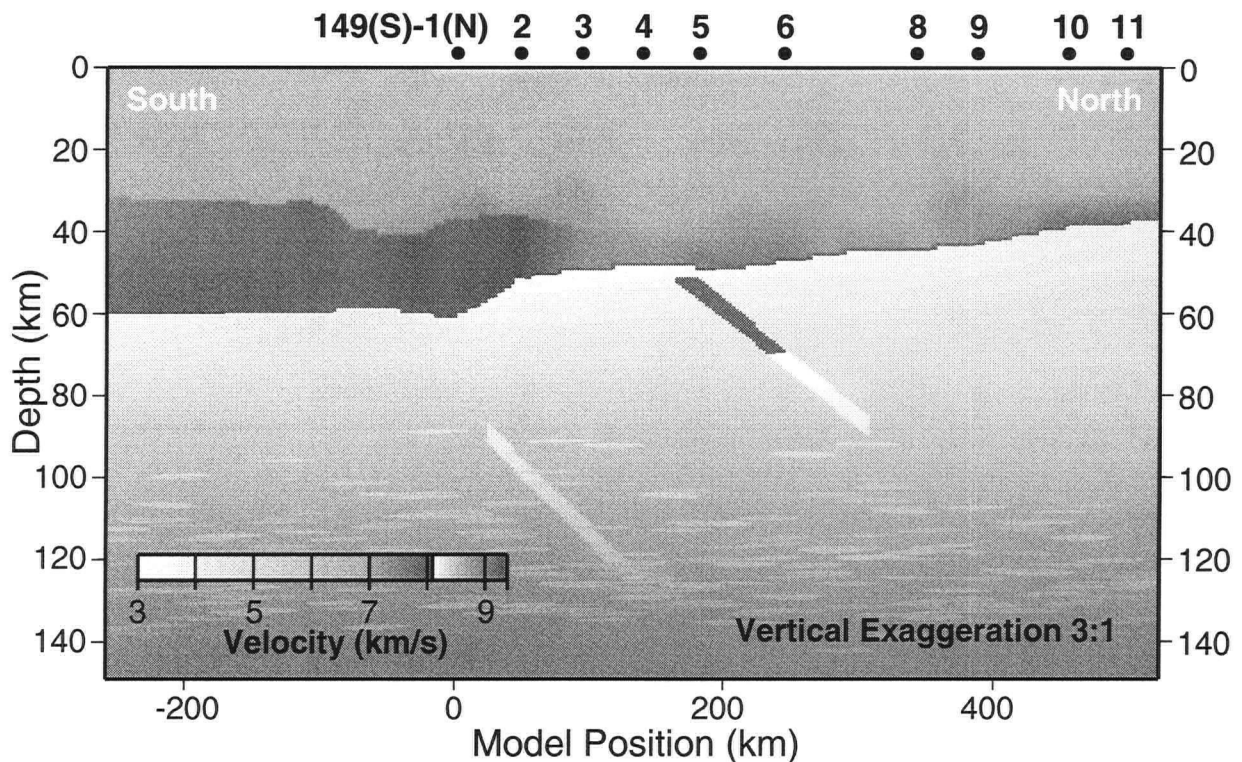


Figure 6.28: Model 7 - Elliptical velocity anomalies inserted between depths of 100 and 140 km. (Ellipse dimensions: $x=24\pm.012$ km, $z=0.48\pm.012$ km. Ellipse velocities: $v=8.38\pm.05$ km/s at 100 km depth with an increment of $.0083$ km/s/km. Ellipse distribution - horizontal: 1 per $12\pm.012$ km, vertical: 1 per $9.6\pm.012$ km, cutoff depth: 90 km.)

(Fig. 6.29b) which had a central frequency of 1.75 Hz, it is apparent that the layer of elliptical anomalies was observed as an effective medium by the examining wave field. With a central frequency of 1.75 Hz and velocities of ~ 8.4 km/s, the dominant wavelength in the data at the depth of the upper mantle wave guide is ~ 4.8 km, a length considerably greater than the thickness of the ellipses modelled. Continuous upper and lower reflections (labelled A and B respectively in Fig. 6.29b), marking the top and bottom of the zone of ellipses are clearly seen; reflections within the P_n coda are also continuous over long offset ranges. This 'continuous' coda pattern is a result of the effective medium characteristics of the system and is not representative of what is seen in the real data (Fig. 6.27) which shows intermittently continuous reflections with a much shorter length scale. As a result, the central frequency of the source wavelet was increased to 3.25 Hz to

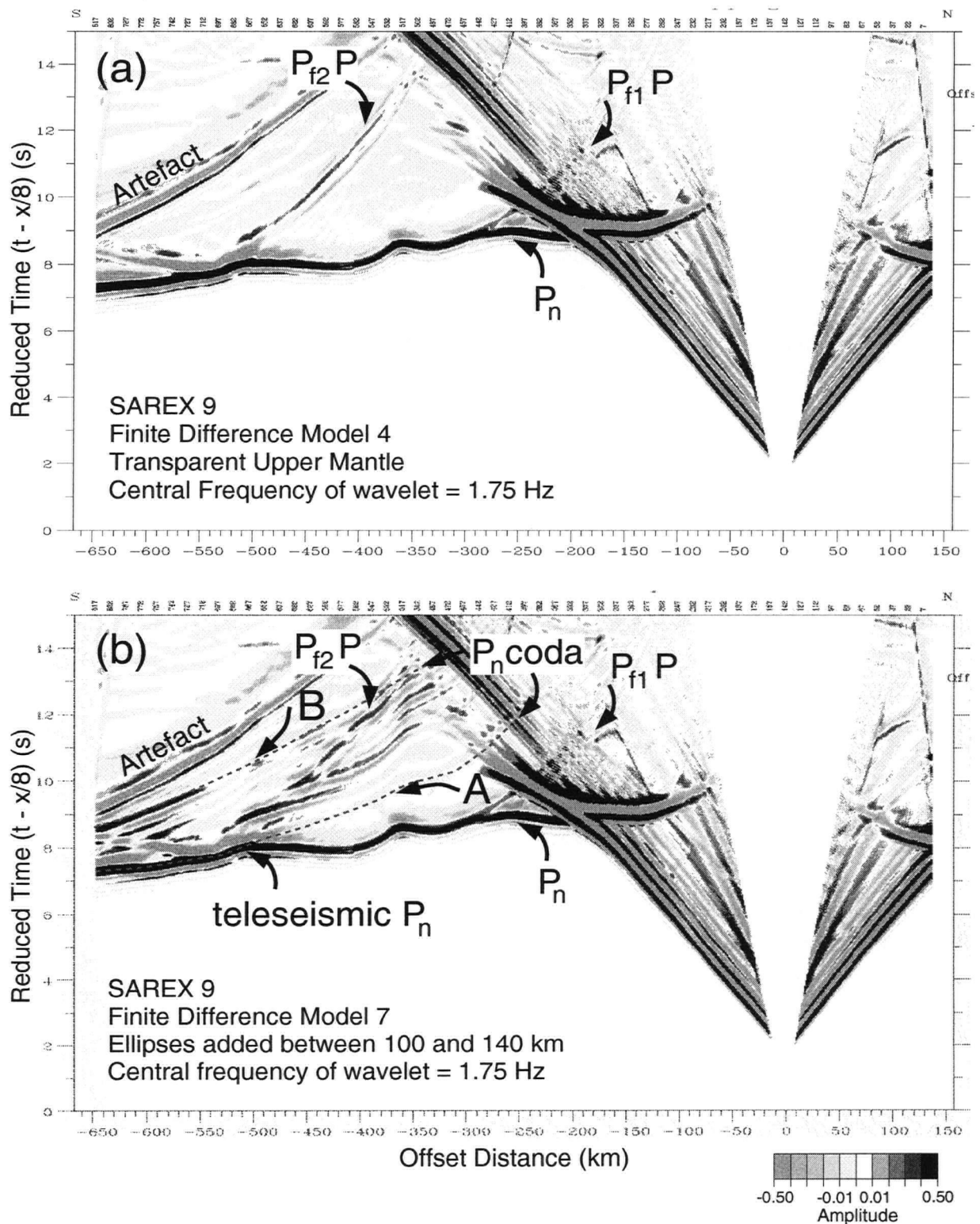


Figure 6.29: SAREX 9 finite difference synthetics. Comparison of (a) Model 4: a transparent upper mantle to (b) Model 7: a mantle with coarse elliptical anomalies added between 100 and 140 km depth. Central frequency = 1.75 Hz. Features related to the teleseismic P_n and P_n coda are labelled. Coherent P_n coda events associated with an upper mantle wave guide lie between grey dashed lines in (b).

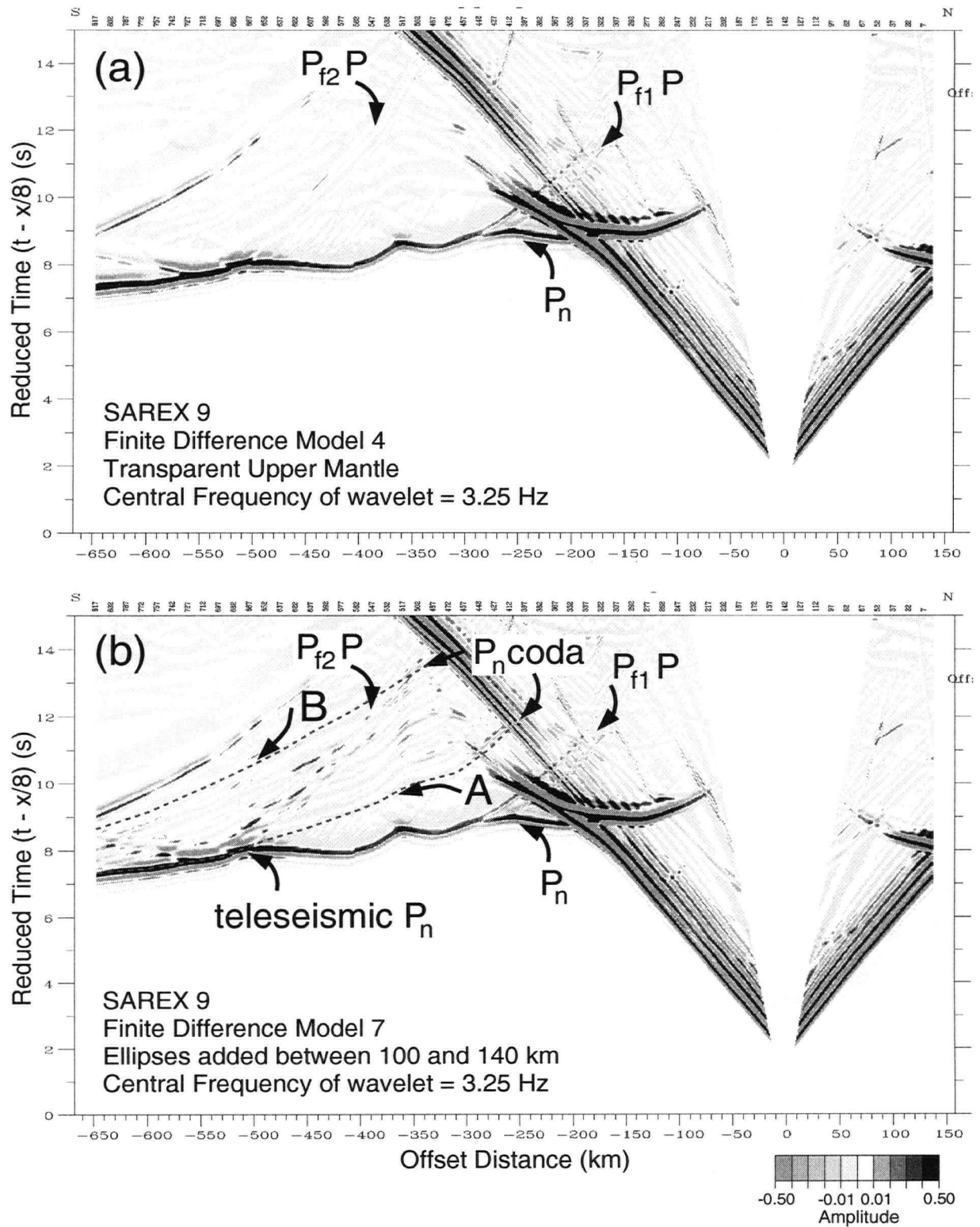


Figure 6.30: SAREX 9 finite difference synthetics. Comparison of (a) Model 4: a transparent upper mantle to (b) Model 7: a mantle with coarse elliptical anomalies added between 100 and 140 km depth. Central frequency = 3.25 Hz. Features related to the teleseismic P_n and P_n coda are labelled. Coherent P_n coda events associated with an upper mantle wave guide lie between grey dashed lines in (b).

reduce the effective medium characteristics observed in the lower frequency synthetic data. The resulting, higher frequency synthetic seismogram is a closer match to the real data, although it can be argued that the length over which events remain coherent in the P_n coda is shorter than observed in the real data. In this case, though, the short length scale is due to the dimensions of the ellipses used in the model rather than the frequencies used to model them.

Two additional models were subsequently developed to further constrain the ellipse dimensions and distributions within the wave guide layer. In the first of these models (Fig. 6.31a), the size of the ellipses was doubled, to 48 km long by ~ 1.0 km high. This resulted in a P_n coda with more significant coherence (Fig. 6.31b). Reflections within the coda are observed to be coherent over as much as 60 km, longer than that observed in the real data (Fig. 6.27). This suggests that the ellipse dimensions in this case are too large. In addition, the quantity of coda reflections in the synthetic data is observed to be lower than in the real data which suggests that the number of elliptical bodies inserted in the model is too low. (Note that ellipse distribution parameters are included in the figure captions for each model.) Interference between the upper mantle dipping reflection ($P_{f_2}P$) and coda reflections is apparent in both the real data and the synthetic examples. This aspect of the models has not been investigated further.

The middle ground was struck in the final SAREX model with ellipse lengths of 36 km and heights of 0.72 km (Fig. 6.32a). The density of intermittent coda reflections seen in the resulting synthetic seismogram (Fig. 6.32b) matches well with the real data, and the modelled and observed length scales of coda reflections (10 - 30 km in offset length) also appear to be a fairly close match.

The modelling performed here has partially constrained the dimensions and distribution density of heterogeneous bodies within the proposed upper mantle wave guide (36 km \times 0.72 km ellipses, with one ellipse per 324 km² on average.) The accuracy of these statistical parameters (especially the width of elliptical bodies) is affected by the wave lengths of the real and modelled seismic waves. Several parameters, such as ellipse orientation and velocity contrasts within the

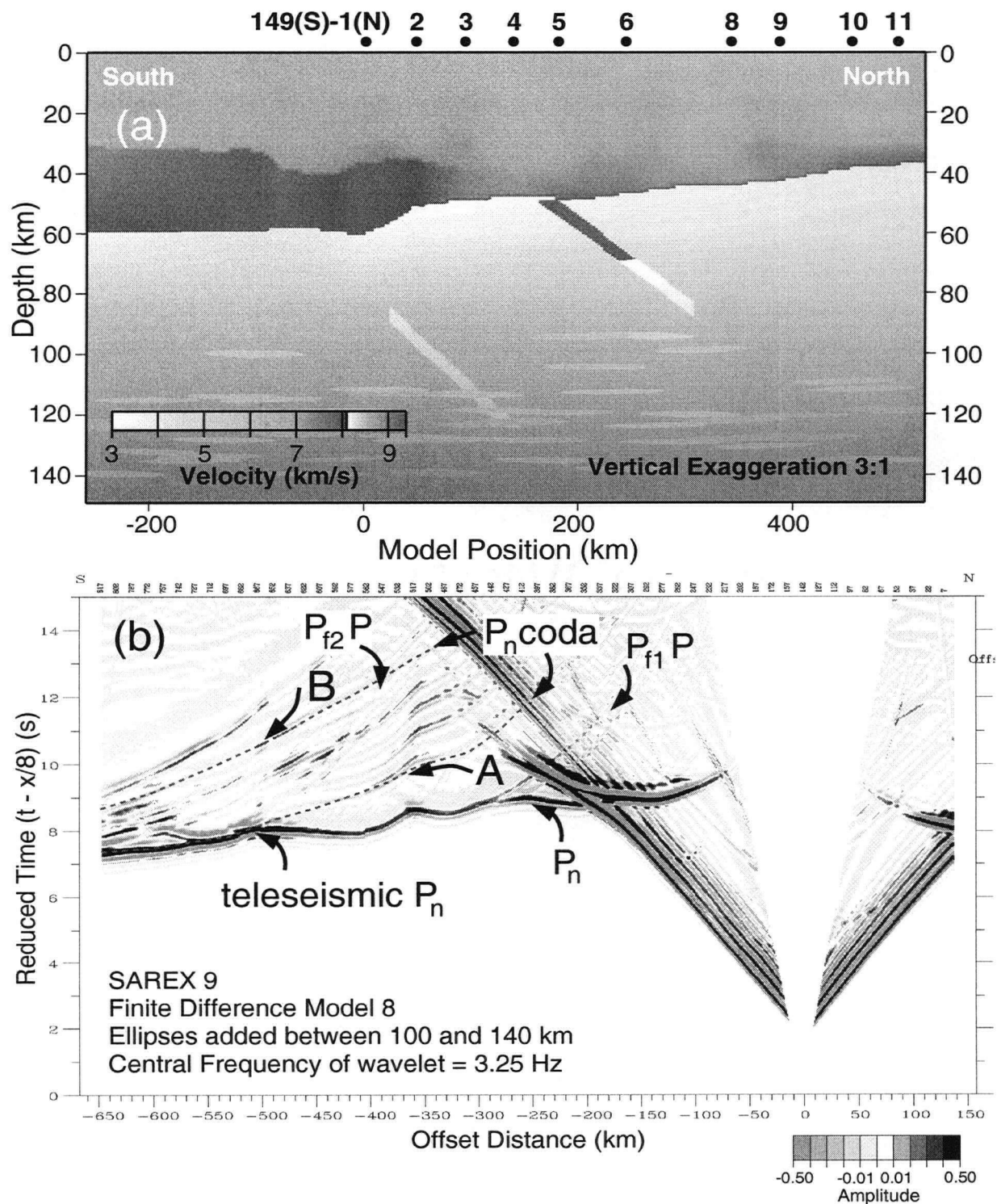


Figure 6.31: (a) Model 8 - Elliptical velocity anomalies inserted between depths of 100 and 140 km. (Ellipse dimensions: $x=48 \pm 1.2$ km, $z=0.96 \pm 1.2$ km. Ellipse velocities: $v=8.38 \pm 0.05$ km/s at 100 km depth with an increment of $.0083$ km/s/km. Ellipse distribution - horizontal: 1 per 24 ± 1.2 km, vertical: 1 per 24 ± 1.2 km, cutoff depth: 90 km.) (b) SAREX 9 finite difference synthetic for Model 8. Central frequency = 3.25 Hz. Features related to the teleseismic P_n and P_n coda are labelled. Coherent P_n coda events associated with an upper mantle wave guide lie between grey dashed lines.

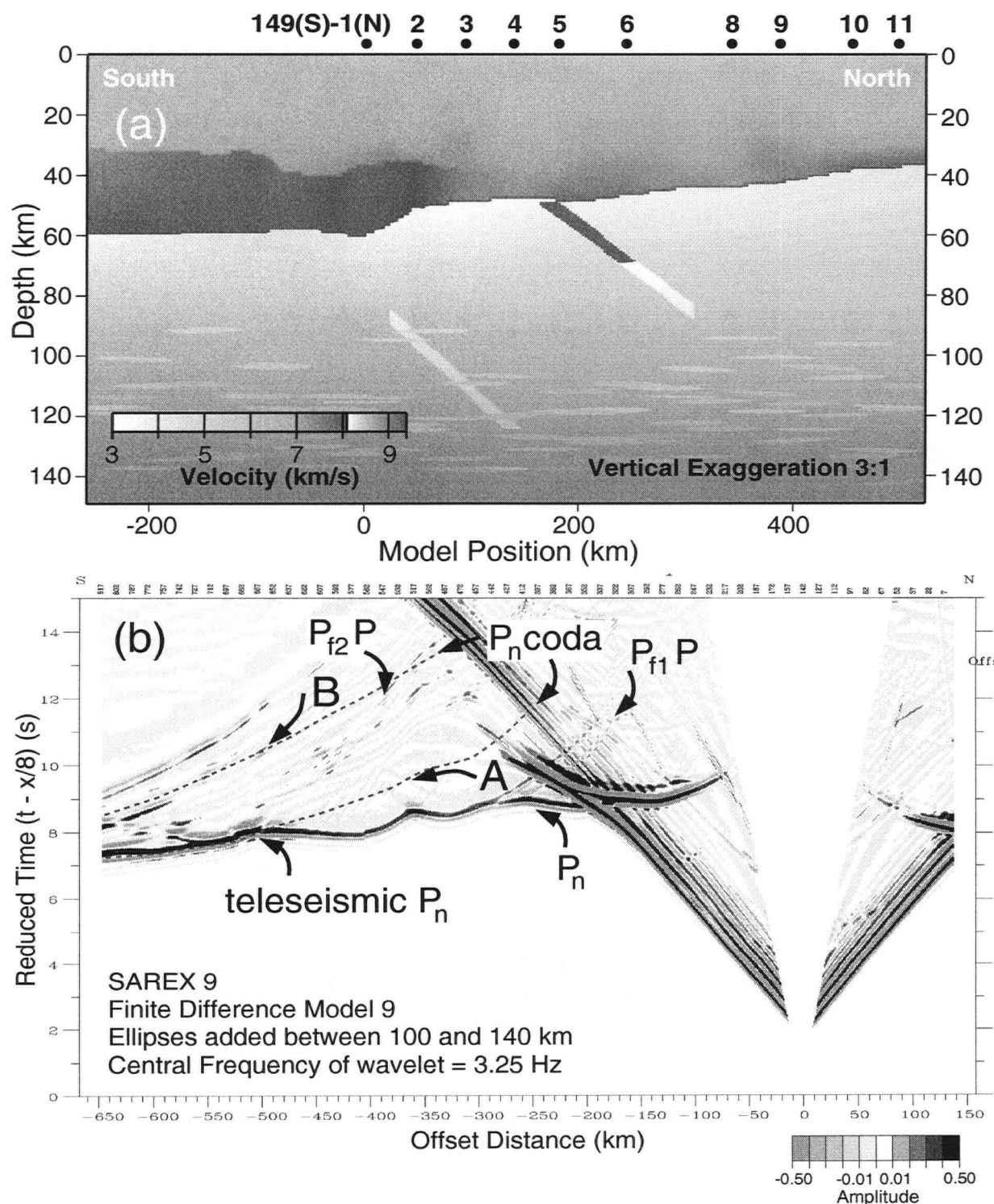


Figure 6.32: (a) Model 9 - Elliptical velocity anomalies inserted between depths of 100 and 140 km. (Ellipse dimensions: $x=36\pm 1.2$ km, $z=0.72\pm 1.2$ km. Ellipse velocities: $v=8.38\pm 0.05$ km/s at 100 km depth with an increment of $.0083$ km/s/km. Ellipse distribution - horizontal: 1 per 18 ± 1.2 km, vertical: 1 per 18 ± 1.2 km, cutoff depth: 90 km.) (b) SAREX 9 finite difference synthetic for Model 9. Central frequency = 3.25 Hz. Features related to the teleseismic P_n and P_n coda are labelled. Coherent P_n coda events associated with an upper mantle wave guide lie between grey dashed lines.

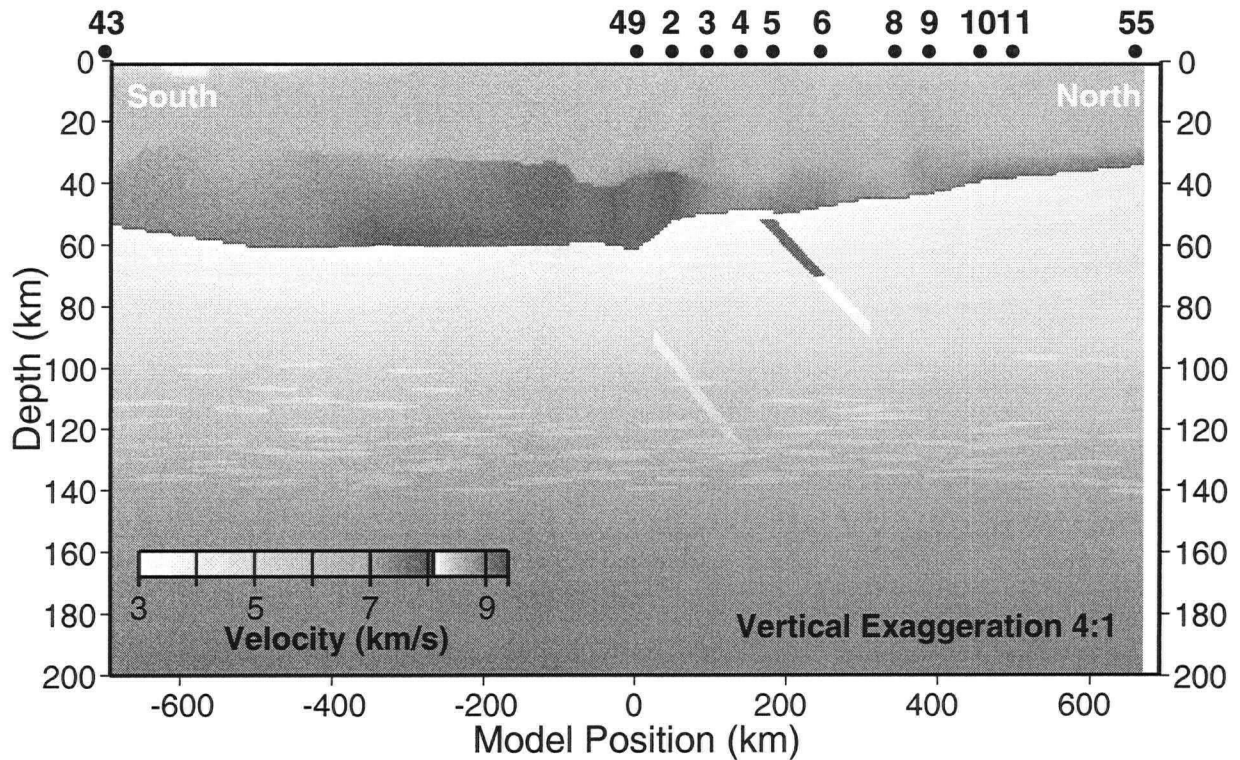


Figure 6.33: Model 9a: modified for the dimensions of Deep Probe 55 - Elliptical velocity anomalies inserted between depths of 100 and 140 km. (Ellipse dimensions: $x=36\pm.12$ km, $z=0.72\pm.12$ km. Ellipse velocities: $v=8.38\pm.05$ km/s at 100 km depth with an increment of .0083 km/s/km. Ellipse distribution - horizontal: 1 per 18 ± 1.2 km, vertical: 1 per 18 ± 1.2 km, cutoff depth: 90 km.)

heterogeneous bodies have not been evaluated in this limited investigation. For example, in the current models, the inserted ellipses are assumed to be horizontally oriented; inclined elliptical bodies could be representative of a particular method of emplacement or post-emplacement alteration.

Deep Probe Model

The previous models and the synthetic seismograms generated from them have examined the P_n phase and its associated coda at offsets less than 650 km. In order to investigate the seismic character at longer offset distances, the input model is expanded to the dimensions of Deep Probe profile 55. The bottom of the model was dropped to 200 km and the length increased to almost

1400 km. This triples the time required to run a single model to almost 48 hours on the higher-capacity Rice computer system. The preferred model from the SAREX tests (Fig. 6.32a) is recast in the Deep Probe dimensions (Fig. 6.33).

Comparing the real data for Deep Probe 55 (Fig. 6.34a) to the synthetic generated for this shot (Fig. 6.34b) reveals some enlightening features. In the real data, the same general upper mantle features observed in the data from SAREX shot 9 (Fig. 6.27) are identified. As was seen in the SAREX data, a P_n coda envelope comprised of intermittently coherent events with length scales in the order of 10 - 30 km and apparent velocities between 8.0 and 8.5 km/s can be identified. The two upper mantle dipping reflections, $P_{f1}P$ and $P_{f2}P$, are identified, both of which crosscut the P_n coda envelope. The formation of the teleseismic P_n by the convergence of P_n coda events into a narrow band, is clearly identified in the data, especially at offset distances greater than 750 km.

The most gratifying result of this finite difference model is that the teleseismic P_n phase observed in the synthetic seismogram (Fig. 6.34b) propagates as seen in the real data. The modelled P_n coda is also seen to occur at the anticipated position, based on the modelling of SAREX shot 9. However, the distribution of reflectivity within the coda has a different character than that seen in the real data, especially in the offset range between 480 and 850 km. This suggests that the model, as constructed based on the modelling of the SAREX data is not completely satisfactory for the farther offset distances seen in the Deep Probe data set. Therefore, the position of the upper mantle wave guide layer (between depths of 100 and 140 km) can be confirmed for both the shot positions modelled here, but the exact nature of the heterogeneities within this layer is not completely understood.

As seen for the previous SAREX examples, the modelled amplitudes of the P_n phase as compared with deeper mantle phases are the reverse of what is seen in the real data. In the real data example (Fig. 6.34a), the P_n coda and teleseismic P_n have a much greater amplitude than the P_n

or body wave P . These amplitudes have not been accurately modelled. 1-D reflectivity modelling of the teleseismic P_n phase [Tittgemeyer *et al.* 1996] indicates that several criteria control the relative amplitudes of these phases. These criteria include: (i) the distribution of hypothesised scattering bodies of various sizes within the upper mantle, (ii) the physical nature (*e.g.*, impedance contrast, anisotropic properties) of these scattering bodies, and (iii) the background velocity gradient. The first two criteria have been partially investigated for the SAREX example (Section 6.2.1), and the third criterion is controlled by the picks made in the real data for the body wave P phase; possible error in these picks has not been considered in the finite difference modelling. These models have been successful in exploring some of the geometric controls on the seismic response of the uppermost mantle, but clearly, an enhanced and extensive modelling program which examines all possible geometries and visco-elastic properties for the hypothesised scattering bodies should result in a better model for the P_n coda and teleseismic P_n .

6.5 Summary

The visco-elastic finite-difference modelling undertaken in this chapter has made several specific contributions to the interpretation of the Deep Probe data set, as noted in the following points.

- The Moho in this region has been shown to be more appropriately represented by a 5-10-km-thick transition zone composed of interbedded 2-D structures with properties that gradually change from those of the crust to those of the mantle.
- A structural step observed in the Moho beneath the Medicine Hat Block is more appropriately modelled as a sharp step, as evidenced by diffraction patterns, rather than a smoothed feature.
- The dipping reflectors, interpreted to be relict subduction features related to the boundaries between the MHB and the Hearne and Wyoming Provinces, can be modelled as slabs with a

thickness of less than 5 km and internal velocities less (0.25 - 1.0 km/s) than the surrounding mantle material. This is in accordance with reasonable geologic models for such features.

- The upper mantle wave guide layer, proposed to be the cause of the teleseismic P_n and its associated coda, is constrained to lie between depths of 100 and 140 km. This corresponds closely to the globally recognised 8° and Lehmann discontinuities, discussed in the introduction to this thesis as being boundaries of an upper mantle layer of heterogeneity. The heterogeneous nature of the layer has been partially investigated and shown to be composed of interbedded elongate 2-D structures, possibly with length scales on the order of 36 km.

In general, the contributions of the finite-difference method can be broken down into three main categories: (i) controls on the dimensions of small features, (ii) the evaluation of features not constrained by ray-theoretical methods, and (iii) amplitude concerns.

Control on dimensions of features

The modelling has been successful in empirically constraining the interpretation of smaller features. By comparing the results of finite-difference modelling to the real data, the Moho has been shown to not be a sharp boundary in this region; rather, it is better modelled as a transition zone composed of a layer of statistically distributed elliptical bodies with physical parameters distinct from the background. The thickness of this layer has been investigated suggesting a transition zone between 5 and 10 km thick. The thicknesses of the hypothesised relic subducted slabs, as modelled, have been shown to be too thick, suggesting a thickness less than 5 km. Finally, the dimensions and distributions of scattering bodies within an upper-mantle wave guide have been investigated suggesting that the length scales of heterogeneous features in this layer is much longer (roughly $36 \text{ km} \times 0.72 \text{ km}$) than that seen in the Moho transitional layer (roughly $6 \text{ km} \times 0.35$

km). Understanding the relationship between the seismic wavelength (in both the real and synthetic data) and the length scale of modelled features is vital for successful modelling.

Evaluation of non-ray-theoretical features

In addition to providing a way to evaluate small-length-scale features such as the heterogeneities within transitional layers, the finite-difference technique has also enabled the evaluation of diffractions such as those expected from a sharp step in the Moho beneath the Medicine Hat Block. Such an interpretation adds to the discussion of the tectonic history in this region as it provides additional information on the short-scale geometry of the feature. The sharp step in the Moho, in close proximity to the hypothesised relic subducted slabs, adds extra support to the suggestion that the uppermost mantle has experienced little horizontal motion, particularly in the direction of the profile, since shortly after the events which sutured the various Archean blocks together. North-south oriented tectonic processes in the crust and uppermost mantle would have smoothed such a sharp Moho feature.

Amplitude information

Amplitudes observed in the finite-difference synthetic seismograms can provide evidence, either supportive or contradictory, for the occurrence and positioning of certain features that are included in the ray-theoretical model. Most significantly in this chapter, the P_n - and body wave P -phase amplitudes modelled in the offset range beyond 250 km are shown to be much higher than those seen in the real data. Various strategies were explored to reduce this amplitude. The best technique involved inserting a layer in the uppermost 10 km of the mantle (with or without superimposed heterogeneities) with an average velocity gradient equal to zero.

The models developed in this chapter, as applied to the Deep Probe data set, show the benefit of utilising a wave-field forward-modelling scheme, such as the visco-elastic finite-difference routine, in conjunction with a more quantitatively constrained interpretation method, such as the ray-theoretical method used in Chapter 5. When tailored to study specific features (*e.g.*, the step in the Moho beneath the Medicine Hat Block), this method can make significant specific conclusions. When applied to more general features (*e.g.*, the statistical nature of a heterogeneous upper mantle wave guide layer), the technique is limited in its abilities to enable specific conclusions to be drawn, but can be very helpful in exploring and constraining the inter-related physical properties that define such features.

Chapter 7

Discussion, Conclusions and Recommendations

*There rolls the deep where grew the tree.
O earth, what changes hast thou seen!
There where the long street roars, hath been
The stillness of the central sea.*

*The hills are shadows, and they flow
From form to form, and nothing stands;
They melt like mist, the solid lands,
Like clouds they shape themselves and go.*

*But in my spirit will I dwell,
And dream my dream, and hold it true;
For tho? my lips may breathe adieu,
I cannot think the thing farewell.*

*– Alfred, Lord Tennyson, 1809-1892
(In Memoriam A.H.H. CXXIII).*

The Deep Probe experiment introduced to North America a new scale of controlled-source seismic investigation of the lithosphere. The use of very large chemical explosions recorded by a closely spaced array of seismographs to offset distances as great as 2800 km made it as much a test of the technique and methods as it was an investigative project. The experiment successfully met three of its scientific objectives – development of a 2-D velocity model of the crust and upper mantle, interpretation of the model in terms of tectonic history, and characterisation of heterogeneities in the sub-crustal lithosphere – as presented in the introduction to this thesis. The fourth objective, significant observations of the mantle transition zone, was unfortunately not clearly achieved. However, Deep Probe has succeeded in making new and significant contributions to the understanding of the lithosphere of western North America; it has had a large role in modifying our

understanding of Precambrian tectonic history in western North America. This final chapter reviews the successes and failures of the experiment, discusses the implications of the interpretation in the larger context of its setting within continental North America and makes recommendations for future large-scale refraction surveys.

7.1 Summary of Results

The Deep Probe experiment has made several new contributions to the understanding of the structure of the lithosphere of western North America. The interpretation of the data set has identified several major lithospheric features.

- A lower crustal layer underlying the Wyoming Province and Medicine Hat Block is delineated by strong reflections at its top and base, and by a significant velocity contrast from neighbouring lower crustal domains. The interpretation of this feature is further enhanced by current xenolith studies which identify a lower crust that is Proterozoic in age, younger than the overlying Archean rocks. North-south contrasts in modelled velocities (the velocity of the lower crustal layer is modelled to be higher beneath the MHB than beneath the Wyoming Province), suggest possible differences in the source and history of the layer.
- Significant (10-15 km) structural relief seen on the Moho beneath the MHB suggests strongly different dynamic systems to the north and south. This feature corresponds to the location of a hypothesised Archean subduction zone resulting from the collision of the MHB with the Hearne Province.
- Two north-dipping reflective bodies are hypothesised to be relict subduction zones in the upper mantle of southern Alberta. Modelling suggests that the reflectors are the result of subduction-related shear-zones less than 5 km thick which have been subsequently intruded

by upper-mantle magmatism observed to have a negative velocity contrast from neighbouring mantle rocks. The southern subduction zone represents the suture between the Wyoming Province and MHB while the northern subduction zone represents the suture between the MHB and the Hearne Province. Subduction in both cases is inferred to be limited in extent due to the absence of co-linear magmatism. Tectonic motions out of the plane of observation are not resolvable in this dataset but are incorporated into the interpretation based on other evidence. For example, the observed geometries of the subduction zone, combined with geologic evidence from the margin of the Wyoming Province, support a significant oblique component to the continental collisions analogous to the Pyrenean suture zone between the Iberian and European crustal blocks.

- Through the use of numerical forward-modelling techniques, an upper-mantle waveguide layer composed of scattering bodies between depths of 100 and 140 km has been identified as the likely source for the propagation of P_n coda and teleseismic P_n phases. As seen in a growing number of locations worldwide, this layer of heterogeneities is bounded by the so-called 8° and Lehmann discontinuities.

Several interpretation techniques, of increasing complexity have been successfully developed and utilised in the investigation of the Deep Probe data set.

- The combination of iterative downward-continuations of waveform $\tau - p$ transforms for each shot profile enabled the rapid calculation of a preliminary velocity model for the profile. These preliminary results were shown to be consistent with those of the more complete interpretations.

- The modification of the ray-theoretical travel-time inversion routine of Zelt and Smith [1992] to consider a cylindrical co-ordinate system parameterisation enabled the development of a velocity model that takes Earth curvature and 2-D velocity variation into consideration, thereby providing more accurate velocity structure information.
- The utilisation of finite-difference forward-modelling techniques enabled the further evaluation of specific features within the model which could not be fully examined with ray-theoretical methods due to their geometry or physical characteristics.

The Deep Probe experiment was not without its disappointments. Foremost among these was that although tantalising signals were initially observed with travel-time characteristics suitable for reflections from the mantle transition zone, these events could not be enhanced by the signal enhancement techniques used. This is partially due to: (i) the relatively high noise level in some portions of the data set which lowered the signal-to-noise ratio below the point where statistical methods could enhance the data and (ii) the lack of effective propagation from some of the very large sources which were detonated. The failure of three of the large shots in the Northwest Territories and northern Alberta was especially unfortunate. Although technical difficulties were partly to blame for the failure of these shots, partial blame must also lie with the regional geology of the region - including the possibility of absorptive effects caused by the Great Slave Lake Shear Zone (between the Archean Rae and Slave Provinces in the Northwest Territories close to Deep Probe shot 61) and the Snowbird Shear Zone (between the Archean Hearne and Rae Provinces in northern Alberta near Deep Probe shot 55). A better understanding of the seismic propagation characteristics of these regions would be helpful in future planning for similar surveys. The major effect that the shot failures had to the Deep Probe interpretation was loss of information at far offset distances which would have aided in the analysis of the teleseismic P_n phase and its associated coda.

7.2 North American Ramifications of the Experiment

Placing the Deep Probe interpretation in context with other lithospheric interpretations of North America, the feature which most stands out is the modelled thickness of the crust of the Wyoming Province and Medicine Hat Block. With thickness approaching 60 km, this interpretation is greater than most other estimates for the Wyoming Province and also greater than global averages for similar tectonic provinces. Much of this can be explained by the presence of the high-velocity lower-crustal layer interpreted to be the result of Proterozoic underplating marginal to a large Archean continent.

The concurrent acquisition and interpretation of the southern portion of the Deep Probe experiment over the Proterozoic accretionary terranes of the Yavapai-Mazatzal Province, while not a major part of this thesis, show a distinct southern lithospheric boundary between the Wyoming Province and its neighbours to the south. The velocity structure of the uppermost mantle in the southern portion of the Deep Probe profile (characterized by an extensive low velocity layer) resembles the velocity structure modelled beneath the Gulf of California, a region of crustal spreading. This suggests that the mantle beneath this portion of the Deep Probe profile could be actively convecting, in a manner similar to what is expected beneath the Gulf of California. In contrast, the mantle velocity structure in the northern portion of the Deep Probe profile, is relatively uniform; no low velocity zone is modelled. The interpretation of relict subduction zone features in the upper mantle leads to the invocation of a stable lithospheric mantle which has experienced little motion since the Proterozoic.

Due to the linear geometry of the Deep Probe experiment, the direct interpretation of the data is limited to two dimensions. However, the consideration of out-of-plane tectonic movements has not been ignored. The likelihood of oblique convergence during the amalgamation of the three Archean crustal blocks, based on the geometries of the interpreted relict subduction zones,

comparison to analogous suture zones in other parts of the world, and other supporting geological evidence, is an important part of the interpretation. In addition, out-of-plane processes must be invoked when considering the source of the interpreted Proterozoic lower-crustal layer and its positioning beneath Archean crust.

7.3 Recommendations

This thesis has focussed on the 'big picture' of lithospheric construction and composition along a slice of the Earth through Alberta, Montana and Wyoming. In addition, some questions regarding smaller-scaled features and 3-D aspects of tectonic history were answered. However, the course of this work has led to several new questions being posed and others remain unanswered from before. These questions lead to the following recommendations for future investigation.

1. Out-of-plane processes involved in the amalgamation of the Wyoming Province, MHB and Hearne Province and in the positioning of the lower crustal layer interpreted in this thesis deserve considerably more attention. Geological evidence from Precambrian outcrops in Montana, Wyoming and South Dakota provides only tantalising suggestions of rotational motion during the suturing of these Archean blocks. The understanding of the relationship between the Proterozoic Trans-Hudson Orogen and the Archean Hearne Province – MHB – Wyoming Province system in southern Alberta and Montana is poorly understood. The likelihood of Trans-Hudson involvement in the creation of the Wyoming and MHB lower crustal layer is anticipated but not proven. Additional east - west oriented R/WAR surveys straddling the border between Montana and Alberta combined with the possible enhancement of the Southern Alberta Lithospheric Transect (SALT) CMP data to examine upper mantle features may elucidate many of these issues.

2. Analysis should be expanded to examine the characteristics of the Moho along the length of the profile. In combination with with a good model for the tectonic assemblage of the crust in this region, insight should be gained into understanding the development and history of changes in Moho properties (*e.g.*, a transitional *vs.* a discrete boundary, a diffuse *vs.* a sharp seismic character) underlying Archean crustal blocks.
3. The interpretation of the lower crustal layer beneath the MHB and Wyoming Province is greatly affected by the sudden decrease in resolution beneath northern Montana due to the termination of SAREX shot points at the Canada-USA border. Some changes in the layer's thickness and velocity are apparent in the interpretation, but an improved interpretation would require a consistently acquired R/WAR and (preferably) a CMP seismic survey. In addition, a strong line of evidence for Proterozoic-aged underplating beneath the MHB comes in the form of xenolith evidence. Similar conclusions have not been forthcoming in the Wyoming province; xenoliths from this province should be evaluated and incorporated into a regional study.
4. Finally, although a substantial quantity of good-quality horizontal-component data was recorded during Deep Probe, these recordings and significant shear-wave arrivals within the vertical component data have not been involved in the interpretation. A shear-wave analysis of the lithosphere, which would complement the teleseismic study currently underway in southern Alberta, could add additional constraints to the interpreted tectonic history by providing information on Poisson's ratio for the lower crust and upper mantle which in turn would lead to a better interpretation of lithology.

The ability of seismology, over the last few decades, to make observations of the Earth with greater and greater detail has improved our understanding of how our planet was constructed. While the Deep Probe experiment did not push the envelope of observations as far as was hoped,

it did improve our detailed knowledge of the crust and uppermost mantle in unexpected ways. As seismic acquisition and processing techniques improve and interpretive abilities are refined, we undoubtedly will uncover new and exciting information to improve our knowledge of the tectonic history of this region and the Earth as a whole. The Earth has seen great changes. Our challenge is to effect great change in the way we study and interpret those changes.

References

- Alterman, Z. and F.C. Karal 1968. Propagation of elastic waves in layered media by finite difference methods. *Bull., Seis. Soc. Am.*, **58**: 367-398.
- Amor, J. 1996. PLOTSEC: Generalised software for seismic refraction data, *LSPF Newsletter*, University of Calgary, **23**: 1039-1043.
- Anderson, D.L. and J.D. Bass 1986. Transition region of the Earth's upper mantle. *Nature*, **320**: 321-328.
- BABEL Working Group 1990. Evidence for early Proterozoic plate tectonics from seismic reflection profiles in the Baltic shield. *Nature*, **348**: 34-38.
- BABEL Working Group 1993. Integrated seismic studies of the Baltic Shield using data in the Gulf of Bothnia region. *Geophys. J. Internat.*, **112**: 305-324.
- Baird, D.J., K.D. Nelson, J.H. Knapp, J.J. Walters and L.D. Brown 1996. Crustal structure and evolution of the Trans-Hudson orogen: Results from seismic reflection profiling. *Tectonics*, **15**: 416-426.
- Bank, C.-G., M.G. Bostock, R.M. Ellis, Z. Hajnal and J.C. VanDecar 1998. Lithospheric mantle structure beneath the Trans-Hudson Orogen and the origin of diamondiferous kimberlites. *J. Geophys. Res.*, **103**: 10,103-10,114.
- Beaumont, C., P. Fullsack and J. Hamilton 1994. Styles of crustal deformation in compressional orogens caused by subduction of underlying lithosphere. *Tectonics*, **232**: 119-132.
- Benz, H.M. and J.E. Vidale 1993. Sharpness of upper-mantle discontinuities determined from high frequency reflections. *Nature*, **365**: 147-150.
- Best, J.A. 1991. Mantle reflections beneath the Montana Great Plains on Consortium for Continental Reflection Profiling seismic reflection data. *J. Geophys. Res.*, **96**: 4279-4288.
- Bina, C.R. and G.R. Helffrich 1994. Phase transition Clapeyron slopes and transition zone seismic discontinuity topography. *J. Geophys. Res.*, **99**: 15,853-15,860.
- Boerner, D.E., R.D. Kurtz, J.A. Craven and F.W. Jones 1996. Electromagnetic results from the Alberta Basement *LITHOPROBE* Transect. In G.M. Ross, compiler, *1996 Alberta Basement Transects Workshop, LITHOPROBE Report 51*, *LITHOPROBE* Secretariat, University of British Columbia: 61-70.
- Boerner, D.E., J.A. Craven, R.D. Kurtz, G.M. Ross and F.W. Jones 1998. The Great Falls Tectonic Zone: Suture or intracontinental shear zone? *Can. J. Earth Sci.*, **35**: 175-183.
- Boerner, D.E., R.D. Kurtz, J.A. Craven, G.M. Ross, F.W. Jones and W.J. Davis 1999. Electrical conductivity in the Precambrian lithosphere of western Canada. *Science*, **283**: 668-670.
- Boland, A.V., and R.M. Ellis 1989. Velocity structure of the Kapuskasing Uplift, northern Ontario, from seismic refraction studies. *J. Geophys. Res.*, **94**: 7189-7204.
- Bostock, M.G. 1997. Anisotropic upper-mantle stratigraphy and architecture of the Slave craton *Nature*, **390**: 392-395.
- Bostock, M.G. 1998. Mantle stratigraphy and evolution of the Slave province. *J. Geophys. Res.*, **103**: 21,183-21,200.

- Boyd, F.R. 1987. High and low temperature garnet peridotite xenoliths and their possible relation to the lithosphere-asthenosphere boundary beneath southern Africa. In Nixon, P., ed., *Mantle Xenoliths*, John Wiley, New York: 403-412.
- Burchfiel, B.C. and G.A. Davis 1975. Nature and controls of Cordilleran orogenesis, western United States: Extensions of an earlier synthesis. *Am. J. Sci.*, **275**: 363-396.
- Burchfiel, B.C., D.S. Cowan and G.A. Davis 1992. Tectonic overview of the Cordilleran orogen in the western United States. In Burchfiel, B.C., P.W. Lipman and M.L. Zoback, eds., *The Geology of North America, bf G-3, The Cordilleran Orogen: Conterminous United States*, Geological Society of America, 447-512.
- Burianyk, M.J.A., Y. Bouzidi, S. Phadke and E. R. Kanasewich 1997. Seismic velocity models and depth migration imaging of the Alberta basement. In Ross, G.M., compiler, *1997 Alberta Basement Transects Workshop. LITHOPROBE Report 59*, LITHOPROBE Secretariat, University of British Columbia, 9-14.
- Calvert, A.J., E.W. Sawyer, W.J. Davis and J.N. Ludden 1995. Archean subduction inferred from seismic images of a mantle suture in the Superior Province. *Nature*, **375**: 670-674.
- Carlson, R.W. and A.J. Irving 1994. Depletion and enrichment history of subcontinental lithospheric mantle: an Os, Sr, Nd and Pb isotopic study of ultramafic xenoliths from the north-western Wyoming Craton. *Earth and Planet. Sci. Lett.*, **126**: 457-472.
- Cassidy, J.F. 1995. A comparison of the receiver structure beneath stations of the Canadian National Seismograph Network. *Can. J. Earth Sci.*, **32**: 938-951.
- Cassidy, J.F. and R.M. Ellis 1993. S-wave velocity structure of the northern Cascadia subduction zone. *J. Geophys. Res.*, **98**: 4407-4421.
- Cassidy, J.F., R.M. Ellis, C. Karavas and G.C. Rodgers 1998. The northern limit of the subducted Juan de Fuca plate system. *J. Geophys. Res.*, **103**: 26,949-26,961.
- Červený, V., I.A. Molotkov and I. Pšenvčík 1977. *Ray method in seismology*. Univerzita Karlova, Prague.
- Chandra, N.N. and G. L. Cumming 1972. Seismic refraction studies in western Canada. *Can. J. Earth Sci.*, **9**: 1099-1109.
- Chapman, C.H. 1978. A new method for computing synthetic seismograms. *Geophys. J. Roy. Astr. Soc.*, **54**: 481-518.
- Christensen, N. I. and W. D. Mooney 1995. Seismic velocity structure and composition of the continental crust: A global view. *J. Geophys. Res.*, **100**: 9761-9788.
- Claerbout, J.C. 1970. Coarse grid calculations of waves in inhomogenous media with applications to delineation of complicated seismic structure. *Geophysics*, **35**: 407-418.
- Clayton, R.W. and G.A. McMechan 1981. Inversion of refraction data by wave field continuation. *Geophysics*, **46**: 860-868.
- Clowes, R.M., E.R. Kanasewich and G.L. Cumming 1968. Deep crustal seismic reflections at near-vertical incidence. *Geophysics*, **33**: 441-451.
- Clowes, R.M., A.J. Calvert, D.W. Eaton, Z. Hajnal, J. Hall and G.M. Ross 1996. Lithoprobe reflection studies of Archean and Proterozoic crust in Canada. *Tectonophysics*, **264**: 65-88.

- Clowes, R.M., M.J.A. Burianyk, A.R. Gorman, E.R. Kanasewich and D.W. Schmitt, 2000. Crustal velocity structure from SAREX, the Southern Alberta Refraction Experiment. In preparation for *Can. J. Earth Sci.*.
- Cook, F.A., A.J. van der Velden, K.W. Hall and B. Roberts 1998. Tectonic delamination and sub-crustal imbrication of the Precambrian lithosphere in northwestern Canada, mapped by *LITHOPROBE*. *Geology*, **26**: 839-842.
- Cook, F.A., A.J. van der Velden and K.W. Hall 1999. Frozen subduction in Canada's Northwest Territories: *LITHOPROBE* deep lithospheric reflection profiling of the western Canadian Shield. *Tectonics*, **18**: 1-24.
- Crosson, R.S. and T.J. Owens 1987. Slab geometry of the Cascadia subduction zone beneath Washington from earthquake hypocentres and teleseismic converted waves. *Geophys. Res. Lett.*, **14**: 824-827.
- Dahl, P.S., D.K. Holm, E.T. Gardner, F.A. Hubacher and K.A. Foland 1999. New constraints on the timing of Early Proterozoic tectonism in the Black Hills (South Dakota), with implications for docking of the Wyoming Province with Laurentia. *Geol. Soc. Am. Bull.*, **111**: 1335-1349.
- Deep Probe Working Group 1998. Probing the depths of western North America: Contrasting Archean and Proterozoic lithosphere with controlled source seismology. *GSA Today*, **8** (7): 1-5.
- Deiss, C. 1941. Cambrian geography and sedimentation in the central Cordilleran region. *Geol. Soc. Am. Bull.*, **52**: 1085-1116.
- Durrheim, R. J. and W. D. Mooney 1994. Evolution of the Precambrian lithosphere: Seismological and geochemical constraints. *J. Geophys. Res.*, **99**: 15,359-15,374.
- Dutch, S.I. and P.A. Neilsen 1990. The Archean Wyoming province and its relations with adjacent Proterozoic provinces. In *The Early Proterozoic Trans-Hudson Orogen of North America*, Geol. Ass. of Can. Special Papers, **37**: 287-300.
- Dziewonski, A.M. and D.L. Anderson 1981. Preliminary reference Earth model. *Phys. Earth Planet Int.*, **25**: 297-356.
- Eaton, D.W. and G.M. Ross 1996. SALT and VAuLT: Summary of Data Acquisition and Processing over the Vulcan Low. In G.M. Ross, compiler, *1996 Alberta Basement Transects Workshop, LITHOPROBE Report 51*, *LITHOPROBE* Secretariat, University of British Columbia: 1-10.
- Eaton, D.W., G.M. Ross and R.M. Clowes 1999. Seismic-reflection and potential field studies of the Vulcan structure, Western Canada: A Paleoproterozoic Pyrenees? *J. Geophys. Res.*, **104**: 23,255-23,269.
- Eaton, D.W., G.M. Ross, F.A. Cook and A.J. van der Velden 2000. Seismic imaging of the upper mantle beneath the Rocky Mountain foreland, southwestern Alberta. *Can. J. Earth Sci.*, in press.
- Egorkin, A.V. and N.M. Chernyshov 1983. Peculiarities of mantle waves from long-range profiles. *J. Geophys.*, **54**: 30-34.

- Egorkin, A.V. and N.I. Pavlenkova 1981. Studies of mantle structure of USSR territory on long-range seismic profiles. *Phys. Earth Planet Int.*, **25**: 12-26.
- Egorkin, A.V., S.K. Zaganov, N.I. Pavlenkova and N.M. Chernyshov 1987. Results of lithospheric studies from long-range profiles in Siberia. *Tectonophysics*, **140**: 29-47.
- EUGENO-S Working Group 1988. Crustal structure and tectonic evolution of the transition between the Baltic Shield and North German Caledonides (the EUGENO-S project). *Tectonophysics*, **150**: 253-348.
- Fernandez Viejo, G., R.M. Clowes and J.R. Amor 1999. Imaging the lithospheric mantle in north-western Canada with seismic wide-angle reflections. *Geophys. Res. Lett.*, **26**: 2809-2812.
- Frederiksen, A.W., M.G. Bostock, J.C. VanDecar and J.F. Cassidy 1998. Seismic structure of the upper mantle beneath the northern Canadian Cordillera from teleseismic travel-time inversion. *Tectonophysics*, **294**: 43-55.
- Frost, C.D and B.R. Frost 1993. The Archean history of the Wyoming province. *Geological Survey of Wyoming Memoir 5*: 58-76.
- Fuchs, K, and G. Müller 1971. Computation of synthetic seismograms with the reflectivity method and comparison with observations. *Geophys. J. Roy. Astr. Soc.*, **23**: 417-433.
- Gorman, A.R. 2000. Ray-theoretical travel-time inversion in a cylindrically parameterised Earth. In preparation.
- Gorman, A.R. and R.M. Clowes 1999. Wave-field tau-p analysis for 2-D velocity models: Application to western North American lithosphere. *Geophys. Res. Lett.*, **26**: 2323-2326.
- Gorman, A.R., R.M. Clowes, and R.M. Ellis 1996. Deep Probe seismic refraction imaging of the crust and upper mantle in the Archean Hearne Craton, Southern Alberta. In G.M. Ross, compiler, *1996 Alberta Basement Transects Workshop, LITHOPROBE Report 51*, LITHOPROBE Secretariat, University of British Columbia: 27-38.
- Gorman, A.R., T.J. Henstock, R.M. Clowes and 8 others 1997. Southern Alberta Refraction Experiment (SAREX) and Deep Probe Refraction Experiment 1995: Field Acquisition and Preliminary Data Processing Report. *LITHOPROBE Report 52*, 26 pp, 11 apps.
- Gorman, A.R., R.M. Clowes, R.M. Ellis, M.J.A. Burianyk, E.R. Kanasewich, I. Asudeh, Z. Hajnal, G.D. Spence, T.J. Henstock, A.R. Levander, G.R. Keller, K.C. Miller and C.M. Snelson 2000. Deep Probe - Imaging the roots of western North America. *Can. J. Earth Sci.*, in review.
- Grand, S.P. 1994. Mantle shear structure beneath the Americas and surrounding oceans. *J. Geophys. Res.*, **99**: 11,591-11,621.
- Grand, S.P., R.D. van der Hilst and S. Widiyantoro 1997. Global seismic tomography: A snapshot of convection in the earth. *GSA Today*, **7** (4): 1-7.
- Guggisberg, B. and A. Berthelsen 1987. A two-dimensional velocity model for the lithosphere beneath the Baltic Shield and its possible tectonic significance. *Terra Cognita*, **7**: 631-638.
- Gurrola, H., J.B. Minster and T. Owens 1994. The use of velocity spectrum for stacking receiver functions and imaging upper mantle discontinuities. *Geophys. J. Internat.*, **117**: 427-440.

- Hajnal, Z., B. Németh, R.M. Clowes, R.M. Ellis, G.D. Spence, M.J.A. Burianyk, I. Asudeh, D.J. White and D.A. Forsyth 1997. Mantle involvement in lithospheric collision: Seismic evidence from the Trans-Hudson Orogen, western Canada. *Geophys. Res. Lett.*, **24**: 2079-2082.
- Hales, A.L. 1981. The upper mantle velocity distribution. *Phys. Earth Planet Int.*, **25**: 1-11.
- Hammer, P.T.C. and R.M. Clowes 1997. Moho reflectivity patterns – a comparison of Canadian LITHOPROBE transects. *Tectonophysics*, **269**: 179-198.
- Hill, R. 1952. The elastic behaviour of crystalline aggregate. *Proc. Phys. Soc., London*, **A65**: 349-354.
- Hoffman, P.F. 1988. United plates of America, the birth of a craton: Early Proterozoic assembly and growth of Laurentia. *Annu. Rev. Earth Planet. Sci.*, **16**: 543-603.
- Hoffman, P.F. 1989. Precambrian geology and tectonic history of North America. In Bally, A.W. and A.R. Palmer, eds., *The Geology of North America - An overview*, **A**, *The Geology of North America*, Geological Society of America, 447-512.
- Hole, J.A. 1992. Non-linear high-resolution three dimensional seismic travel time tomography. *J. Geophys. Res.*, **97**: 6553-6562.
- Houston, R.S., E.A. Erslev, C.D. Frost, K.E. Karlstrom, N.J. Page, M.L. Zientek, J.C. Reed Jr, G.L. Snyder, R.G. Worl, B. Brant, M.W. Reynolds and Z.E. Peterman 1993. The Wyoming Province. In Reed, J.C. Jr, M.E. Bickford, R.S. Houston, P.K. Link, D.W. Rankin, P.K. Sims and W.R. Van Schmus, eds., *Precambrian: Conterminous U.S.*, Geological Society of America, *The Geology of North America*, **C-2**, 121-170.
- Ita, J. and L. Stixrude 1992. Petrology, elasticity, and composition of the mantle transition zone. *J. Geophys. Res.*, **97**: 6849-6866.
- Iyer, H.M., L.C. Pakiser, D.J. Stuart and D.H. Warren 1969. Project Early Rise: Seismic probing of the upper mantle. *J. Geophys. Res.*, **74**: 4409-4441.
- Jarchow, C.M. and G.A. Thompson 1989. The nature of the Mohorovičić discontinuity. *Annu. Rev. Earth Planet. Sci.*, **17**: 475-506.
- Jordan, T.H. 1975. The continental tectosphere. *Rev. Geophys. and Space Phys.*, **13** (3): 1-11.
- Kanasewich, E.R. 1968. Precambrian rift: Genesis of strata-bound ore deposits. *Science*, **161**: 1002-1005.
- Kanasewich, E.R. and G.L. Cumming 1965. Near-vertical-incidence seismic reflections from the 'Conrad' discontinuity. *J. Geophys. Res.*, **70**: 3441-3446.
- Kanasewich, E.R., R.M. Clowes and C.H. McLoughlan 1969. A buried Precambrian rift in Western Canada. *Tectonophysics*, **8**: 513-527.
- Karlstrom, K. E. and R. S. Houston 1984. The Cheyenne belt: analysis of a Proterozoic suture in southern Wyoming. *Precambrian Research*, **25**: 415-446.
- Karlstrom, K. E. and S.A. Bowring 1988. Early Proterozoic assembly of tectonostratigraphic terranes in southwestern North America. *J. Geol.*, **96**: 561-576.
- Knapp, J.H., D.N. Steer, L.D. Brown, R. Berzin, A. Suleimanov, M. Stiller, E. Lüschen, D. Brown, R. Bulgakov and A.V. Rybalka 1996. A lithosphere-scale seismic image of the southern Urals from explosion-source seismic reflection profiling. *Science*, **274**: 226-228.

- Kopylova, M.G., J.K. Russell and H. Cookenboo 1998. Upper-mantle stratigraphy of the Slave craton, Canada: Insights into a new kimberlite province. *Geology*, **26**: 315-318.
- Kopylova, M.G., J.K. Russell and H. Cookenboo 1999. Mapping the lithosphere beneath the north central Slave craton. In *Proc. 7th Intern. Kimb. Conf.*, Rad Roof Design, Cape Town: 468-479.
- LeFevre, L. V., and D.V. Helmberger 1989. Upper mantle P velocity structure of the Canadian shield. *J. Geophys. Res.*, **94**: 17,749-17,765.
- Lemieux, S., F.A. Cook and G.M. Ross 2000. Crustal geometry and tectonic evolution of the southern Alberta basement, from new seismic reflection and potential-field studies of the Archean Medicine Hat Block. *Can. J. Earth Sci.*, in press.
- Levander, A.R. 1989. Finite-difference forward modeling in seismology. In James, D., ed., *The Encyclopedia of Solid Earth Geophysics*, Van-Nostrand-Reinhold: 410-431.
- Lucas, S.B., D. White, Z. Hajnal, J. Lewry, A. Green, R.M. Clowes, H. Zwanzig, K. Ashton, D. Schledewitz, M. Stauffer, A. Norman, P.F. Williams, and G. Spence 1994. Three-dimensional collisional structure of the Trans-Hudson Orogen, Canada. *Tectonophysics*, **232**: 161-178.
- Lucas, S.B., E.C. Syme and K.E. Ashton 1999. Introduction to Special Issue 2 on the NATMAP shield margin project: The Flin Flon Belt, Trans-Hudson Orogen, Manitoba and Saskatchewan. *Can. J. Earth Sci.*, **36**: 1763-1765.
- Luetgert, J.H. 1992. MacRay: Interactive two-dimensional seismic raytracing for the Macintosh. *U.S. Geological Survey Open File Report 92-356*: 1-2.
- Marion, D., T. Mukerji and G. Mavko 1994. Scale effects on velocity dispersion: From ray to effective medium theories in stratified media. *Geophysics*, **59**: 1613-1619.
- Mavko, G., T. Mukerji and J. Dvorkin 1998. *The Rock Physics Handbook: Tools for Seismic Analysis in Porous Media*. Cambridge University Press, Cambridge, 329 pp.
- McCamy, K. and R.P. Meyer 1964. A correlation method of apparent velocity measurement *J. Geophys. Res.*, **69**: 691-699.
- McMechan, G.A., R.W. Clayton and W.D. Mooney 1982. Application of wave field continuation to the inversion of refraction data, *J. Geophys. Res.*, **87**: 927-935.
- Melbourne, T., D. Helmberger and J. Mori 1995. Evidence for a diffuse 410-km discontinuity. *Trans. AGU, Eos, 1995 Fall Meeting*, **76** (46): S22E-11.
- Milkereit, B. and C. Spencer 1989. Noise suppression and coherency enhancement of seismic data. In Agterberg, F.P. and G.F. Bonham-Carter, eds., *Statistical Application in the Earth Sciences*, Geological Survey of Canada, Paper **89-9**: 243-248.
- Mohorovičić, A. 1910. Das Beben vom 8. *X. Jahrb. Meteorol. Obs. Zagreb*. 9. Teil 4. Abschn., **1**: 63.
- Morozov, I.B., E.A. Morozova, S.B. Smithson and L.N. Solodilov 1998. On the nature of the teleseismic Pn Phase observed on the ultralong-range profile Quartz, Russia. *Bull., Seis. Soc. Am.*, **88**: 62-73.

- Morozova, E.A., I.B. Morozov, S.B. Smithson and L.N. Solodilov 1999. Heterogeneity of the uppermost mantle beneath Russian Eurasia from the ultra-long-range profile QUARTZ. *J. Geophys. Res.*, **104**: 20,329-20,348.
- Mossop, G.D. and I. Shetsen (compilers) 1994. *Geological Atlas of the Western Canada Sedimentary Basin*. Canadian Society of Petroleum Geologists and Alberta Research Council, Calgary, 510 pp.
- Müller, G. 1971. Approximate treatment of elastic body waves in media with spherical symmetry. *Geophys. J. Roy. Astr. Soc.*, **23**: 435-449.
- Neele, F. 1996. Sharp 400-km discontinuity from short period P reflections. *Geophys. Res. Lett.*, **23**: 419-422.
- Németh, B. 1999. *Structure of the Lithosphere within the Trans-Hudson Orogen (Results of the 1993 LITHOPROBE Trans-Hudson Refraction Experiment)*. PhD Thesis, University of Saskatchewan, Saskatoon, 143 pp.
- Németh, B. and Z. Hajnal 1998. Structure of the lithospheric mantle beneath the Trans-Hudson Orogen, Canada. *Tectonophysics*, **288**: 93-104.
- Nielsen, L., H. Thybo and L. Solodilov 1999. Seismic tomographic inversion of Russian PNE data along profile Kraton. *Geophys. Res. Lett.*, **26**: 3413-3416.
- O'Neill, J.M. and D.A. Lopez 1985. Character and regional significance of Great Falls Tectonic Zone, east-central Idaho and west-central Montana. *Am. Ass. Petr. Geol. Bull.*, **69**: 437-447.
- Pavlenkova, N.I., 1996. General features of the uppermost mantle stratifications from long-range seismic profiles. *Tectonophysics*, **264**: 261-278.
- Pavlenkova, N.I. and A.V. Egorkin 1983. Upper mantle heterogeneity in northern part of Eurasia. *Phys. Earth Planet Int.*, **33**: 180-193.
- Peltier, W.R. and L.P. Solheim 1992. Mantle phase transitions and layered chaotic convection. *Geophys. Res. Lett.*, **19**: 321-324.
- Perčuć, E., and H. Thybo 1996. A new model of upper mantle P-wave velocity below the Baltic Shield: Indication of partial melt in the 95 to 160 km depth range. *Tectonophysics*, **253**: 227-245.
- Pike, C.J. 1986. A seismic refraction study of the Hecate Sub-Basin, British Columbia. MSc Thesis, University of British Columbia, Vancouver, 133 pp.
- Pilkington, M., R.A.F. Grieve, J.D. Rupert and J.F. Halpenny 1992. Gravity anomaly map with shaded relief of gradient of North America. Geologic Survey of Canada, Map 1807A, scale 1:10 000 000.
- Price, R.A. 1996. Tectonic heredity of the Crowsnest Pass cross-strike discontinuity: Mesozoic-Cenozoic tectonic inversion of Paleozoic structures with Eocambrian, Neoproterozoic, Mesoproterozoic and Archean antecedents. In Ross, G.M., compiler, *1996 Alberta Basement Transects Workshop, LITHOPROBE Report 51*, LITHOPROBE Secretariat, University of British Columbia, 213-214.
- Pysklywec, R.N. and J.X. Mitrovica 1998. Mantle flow mechanisms for the large-scale subsidence of continental interiors. *Geology*, **26**: 687-690.

- Pysklywec, R.N. and M.C.L. Quintas 2000. A mantle flow mechanism for the late Paleozoic subsidence of the Paraná Basin. *J. Geophys. Res.*, **105**: 16,359-16,370.
- Pysklywec, R.N., C. Beaumont and P. Fullsack 2000. Modeling the behavior of the continental mantle lithosphere during plate convergence. *Geology*, **28**: 655-658.
- Reiter, E.C., G.M. Purdy and M.N. Toksöz 1993. 2-D velocity inversion/imaging of large offset seismic data via the tau-p domain. *Geophysics*, **58**: 1002-1016.
- Robertsson, J.O.A., J.O. Blanch and W.W. Symes 1994. Viscoelastic finite-difference modeling. *Geophysics*, **59**: 1444-1456.
- Ross, G.M. 1991. Tectonic setting of the Windermere Supergroup revisited. *Geology*, **19**: 1125-1128.
- Ross, G.M. and W.J. Davis 2000. Proterozoic underplating of Archean microcontinents, western Laurentia: Seismic and geochronological constraints. In preparation for *Geology*.
- Ross, G.M. and E.R. Kanasewich 1992. Southern Alberta Mantle Experiment: A proposal to LITHOPROBE. In *LITHOPROBE Alberta Basement Transects Workshop, Workshop Report 28*, LITHOPROBE Secretariat, University of British Columbia, 139-163.
- Ross, G.M., R.R. Parrish, M.E. Villeneuve and S.A. Bowring 1989. Tectonic subdivision and U-Pb geochronology of the crystalline basement of the Alberta Basin, western Canada. *Geological Survey of Canada, Open File 2103*.
- Ross, G.M., R.R. Parrish, M.E. Villeneuve and S.E. Bowring 1991. Geophysics and geochronology of the crystalline basement of the Alberta Basin, western Canada. *Can. J. Earth Sci.*, **28**: 512-522.
- Ross, G.M., D.W. Eaton, D.E. Boerner, W. Miles 2000. Tectonic entrapment and its role in the evolution of continental lithosphere: An example from the Precambrian of western Canada. Submitted to *Tectonics*.
- Rudnick, R.L. and D.M. Fountain 1995. Nature and composition of the continental crust: A lower crustal perspective. *Rev. Geophys.*, **33**: 267-309.
- Ryberg, T., K. Fuchs, A.V. Egorkin and L. Solodilov 1995. Observation of high-frequency teleseismic Pn on the long-range Quartz profile across northern Eurasia. *J. Geophys. Res.*, **100**: 18,151-18,163.
- Ryberg, T., F. Wenzel, J. Mechie, A. Egorkin, K. Fuchs and L. Solodilov 1996. Two-dimensional velocity structure beneath Northern Eurasia derived from the super long-range seismic profile Quartz. *Bull., Seis. Soc. Am.*, **86**: 857-867.
- Shearer, P.M. and T.G. Masters 1992. Global mapping of topography on the 660-km discontinuity. *Nature*, **355**: 791-796.
- Smythe, D.K., A. Dobinson, R. McQuillin, J.A. Brewer, D.H. Matthews, D.J. Blundell and B. Kelk 1982. Deep structure of the Scottish Caledonides revealed by the MOIST reflection profile. *Nature*, **299**: 338-340
- Snelson, C.M. 1998. *An Integrated Lithospheric Study of the Rocky Mountain Region Along the Deep Probe Seismic Profile*. MS Thesis, University of Texas at El Paso, El Paso, Texas, 150 pp.

- Snelson, C.M., T.J. Henstock, G.R. Keller, K.C. Miller and A. Levander 1998. Crustal and uppermost mantle structure along the Deep Probe seismic profile. *Rocky Mountain Geology*, **33** (2): 181-198.
- Steer, D.N., J.H. Knapp and L.D. Brown 1998. Super-deep reflection profiling: Exploring the continental mantle lid. *Tectonophysics*, **286**: 111-121.
- Su, W., R.L. Woodward and A.M. Dziewonski 1994. Degree 12 model of shear velocity heterogeneity in the mantle. *J. Geophys. Res.*, **99**: 6945-6980.
- Tapley, W.C. and J.E. Tull 1992. *SAC – Seismic Analysis Code: Command Reference Manual, Version 10.6e, March 20, 1992*. Regents of the University of California (Lawrence Livermore National Laboratory), 278 pp.
- Thybo, H. and E. Perchuć 1997. The seismic 8° discontinuity and partial melting in continental mantle. *Science*, **275**: 1626-1629.
- Tittgemeyer, M., F. Wenzel, K. Fuchs and T. Ryberg 1996. Wave propagation in a multiple-scattering upper mantle – observations and modelling. *Geophys. J. Internat.*, **127**: 492-502.
- Tittgemeyer, M., F. Wenzel and K. Fuchs 2000. On the nature of P_n . *J. Geophys. Res.*, **105**: 16,173-16,180.
- Ulrych, T.J., M.D. Sacchi and S.L.M. Freire 1999. Eigenimage processing of seismic sections. In Kirlin, R.L. and W.J. Done, eds., *Covariance Analysis for Seismic Signal Processing*, Society of Exploration Geophysicists, Tulsa: 241-274.
- VanDecar, J.C. 1991. *Upper-Mantle Structure of the Cascadia Subduction Zone from Non-linear Teleseismic Travel-time Inversion*. PhD Thesis, University of Washington, Seattle, 165 pp.
- van der Lee, S. and G. Nolet 1997. Upper mantle S velocity structure of North America, *J. Geophys. Res.*, **102**: 22,815-22,838.
- Vidale, J.E. and H.M. Benz 1992. Upper-mantle seismic discontinuities and the thermal structure of subduction zones. *Nature*, **356**: 678-683.
- Villeneuve, M.E., G.M. Ross, R.J. Thériault, W. Miles, R.R. Parrish and J. Broome 1993. Tectonic subdivision and U-Pb geochronology of the crystalline basement of the Alberta Basin, Western Canada. *Geological Survey of Canada Bulletin*, **447**, 86pp.
- Vinnik, L.P. 1977. Detection of waves converted from P to SV in the mantle. *Phys. Earth Planet. Int.*, **15**: 39-45.
- Walck, M. 1983. The P-wave upper mantle structure beneath an active spreading center: The Gulf of California, *Geophys. J. Roy. Astr. Soc.*, **76**: 697-723.
- Walck, M.C. and R.W. Clayton 1984. Analysis of upper mantle structures using wave field continuation of P waves, *Bull. Seis. Soc. Am.*, **74**: 1703-1719.
- Wessel, P. and W.H.F. Smith 1995. New version of the Generic Mapping Tools released. *Trans. AGU, Eos*, **76**: 329.
- Warner, M.R. and S.E. McGeary 1987. Seismic reflection coefficients from mantle fault zones. *Geophys. J. Roy. Astr. Soc.*, **89**: 223-230.

- Warner, M., J. Morgan, P. Barton, P. Morgan, C. Price and K. Jones 1996. Seismic reflections from the mantle represent relict subduction zones within the continental lithosphere. *Geology*, **24**: 39-42.
- Winardhi S. and R.F. Mereu 1997. Crustal velocity structure of the Superior and Grenville provinces of the southeastern Canadian Shield. *Can. J. Earth Sci.*, **34**: 1167-1184.
- Wood, B.J., A. Rawley and D.R. Frost 1996. Water and carbon in the Earth's mantle. *Phil. Trans. Roy. Soc.*, **354**: 1495-1511.
- Yilmaz, Ö. 1987. Chapter 7: Slant stack and application. In Doherty, S.M., ed., *Seismic Data Processing*, Investigations in Geophysics, Volume 2, Soc. Expl. Geophysicists, Tulsa: 428-453.
- Zelt, C. A. 1999. Modelling strategies and model assessment for wide-angle seismic traveltimes data. *Geophys. J. Internat.*, **139**: 183-204.
- Zelt, C. A. and D.A. Forsyth 1994. Modeling wide-angle seismic data for crustal structure: Southeastern Grenville Province. *J. Geophys. Res.*, **99**: 11,687-11,704.
- Zelt, C. A. and R. B. Smith 1992. Seismic traveltimes inversion for 2-D crustal velocity structure. *Geophys. J. Internat.*, **108**: 16-34.
- Zhou, H.-W. 1996. A high-resolution P wave model for the top 1200 km of the mantle. *J. Geophys. Res.*, **101**: 27,791-27,810.

Appendix A

Deep Probe Summary Data Plots

This appendix contains all data used in the RAYINVR interpretation of Chapter 5. Each figure contains three parts: (a) the data with interpreted picks indicated. (b) a raytrace diagram through the RAYINVR model, and (c) a plot of calculated travel times as compared to the interpreted travel times. The statistics for each shot are also indicated where N = number of travel times traced, $|\Delta t|$ = root-mean-squared travel-time residual, and χ^2 = the chi-squared misfit of the travel times.

From south to north the 12 shot locations included in this appendix are:

- 43 - Riverton, Wyoming (Fig. A.1, page 212)
- 49 - Montana / Alberta Border (combination of Deep Probe 149 and SAREX 1; Fig. A.2, page 213)
- 02 - Manyberries, Alberta (Fig. A.3, page 214)
- 03 - Medicine Hat, Alberta (Fig. A.4, page 215)
- 04 - CFB Suffield (South), Alberta (Fig. A.5, page 216)
- 05 - CFB Suffield (North), Alberta (Fig. A.6, page 217)
- 06 - Helmsdate, Alberta (Fig. A.7, page 218)
- 08 - Nose Hill, Alberta (Fig. A.8, page 219)
- 09 - Hughenden, Alberta (Fig. A.9, page 220)

- 10 - Jarrow, Alberta (Fig. A.10, page 221)
- 11 - Chailey, Alberta (Fig. A.11, page 222)
- 55 - CFB Cold Lake, Alberta (Fig. A.12, page 223)

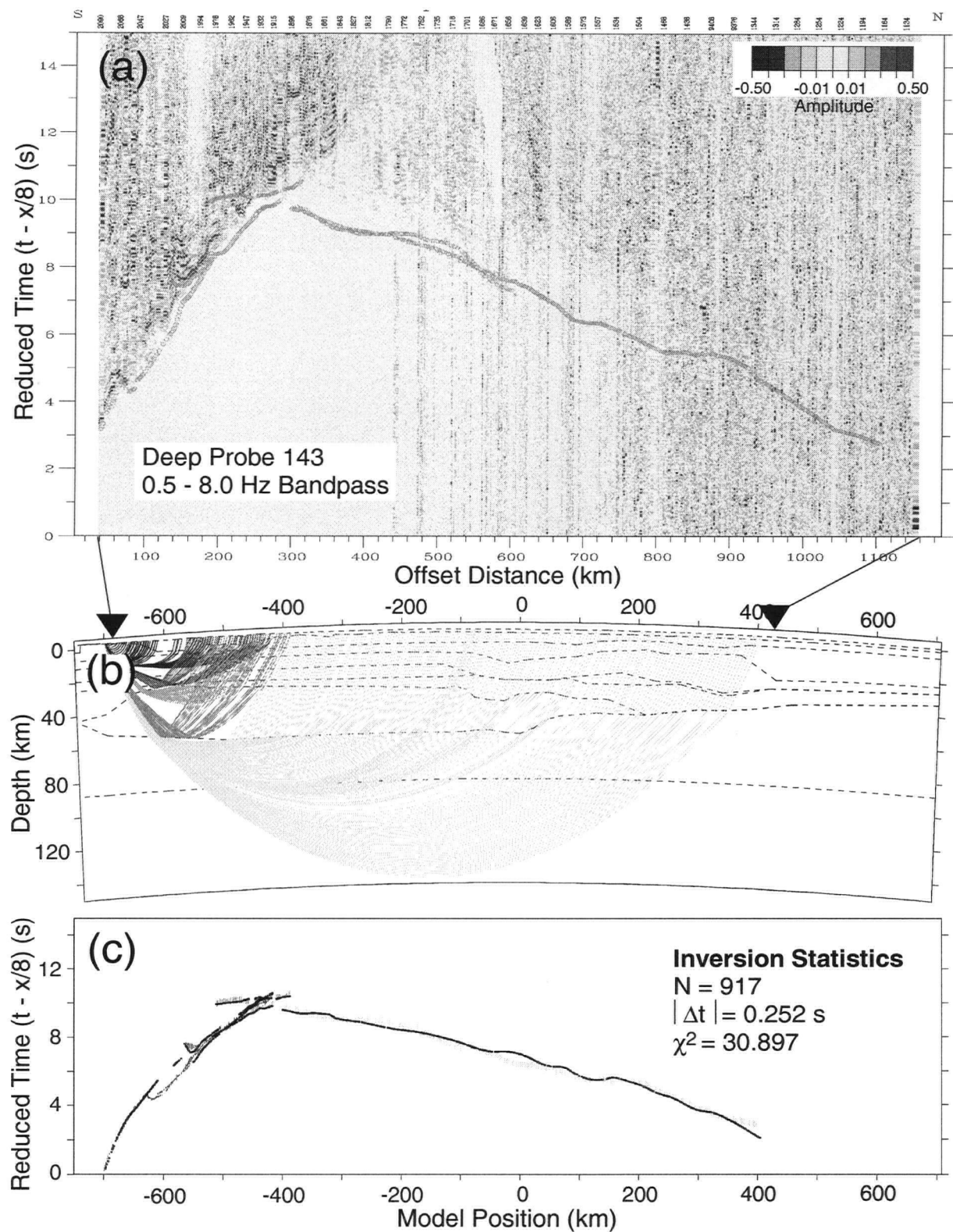


Figure A.1: Deep Probe 143: (a) Colour variable density plot with picks overlaid in green. (b) RAYINVR ray-trace diagram. Vertical exaggeration 4:1. Phases: P_g – dark blue, P_iP – magenta, P_i – light blue, P_mP – green, P_n – yellow. Location of recorded data indicated by triangles. (c) RAYINVR travel-time calculations (black dots) overlaid on picks. Colours for phases as above.

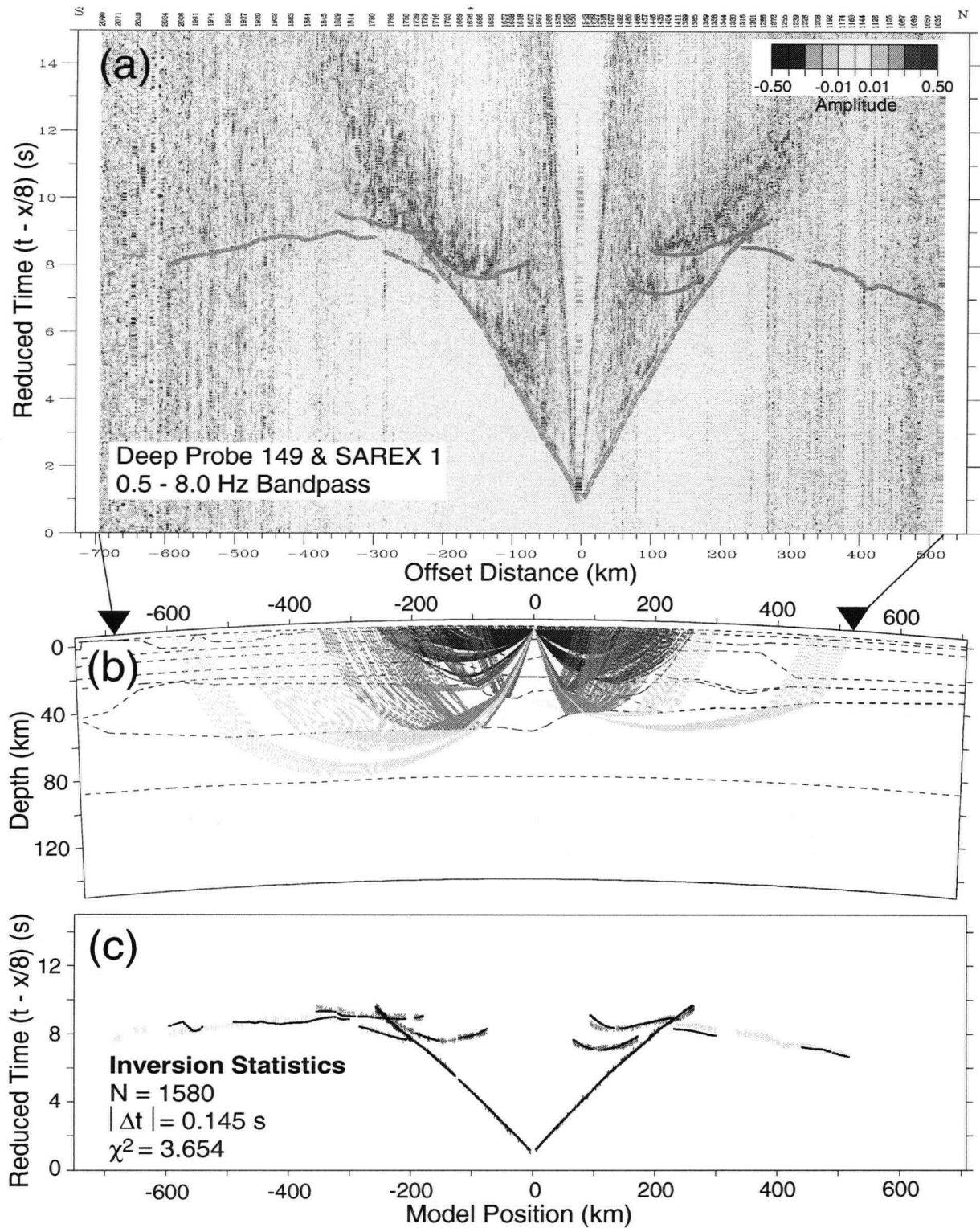


Figure A.2: Deep Probe 149 and SAREX 1: Colour variable density plot with picks overlaid in green. (b) RAYINVR ray-trace diagram. Vertical exaggeration 4:1. Phases: P_g – dark blue, P_iP – magenta, P_i – light blue, P_mP – green, P_n – yellow. Location of recorded data indicated by triangles. (c) RAYINVR travel-time calculations (black dots) overlaid on picks. Colours for phases as above.

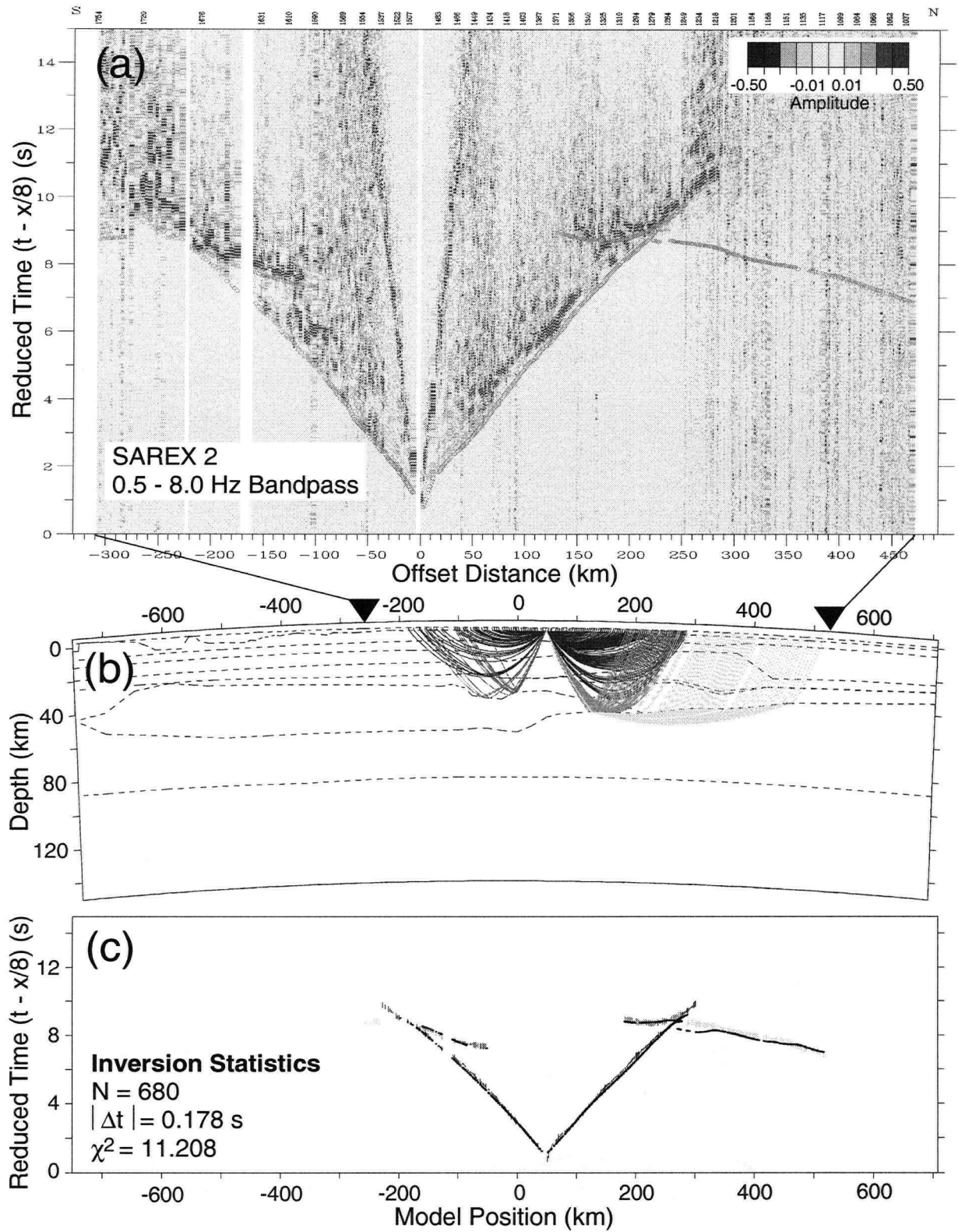


Figure A.3: SAREX 2: Colour variable density plot with picks overlaid in green. (b) RAYINVR ray-trace diagram. Vertical exaggeration 4:1. Phases: P_g – dark blue, P_iP – magenta, P_mP – green, P_n – yellow. Location of recorded data indicated by triangles. (c) RAYINVR travel-time calculations (black dots) overlaid on picks. Colours for phases as above.

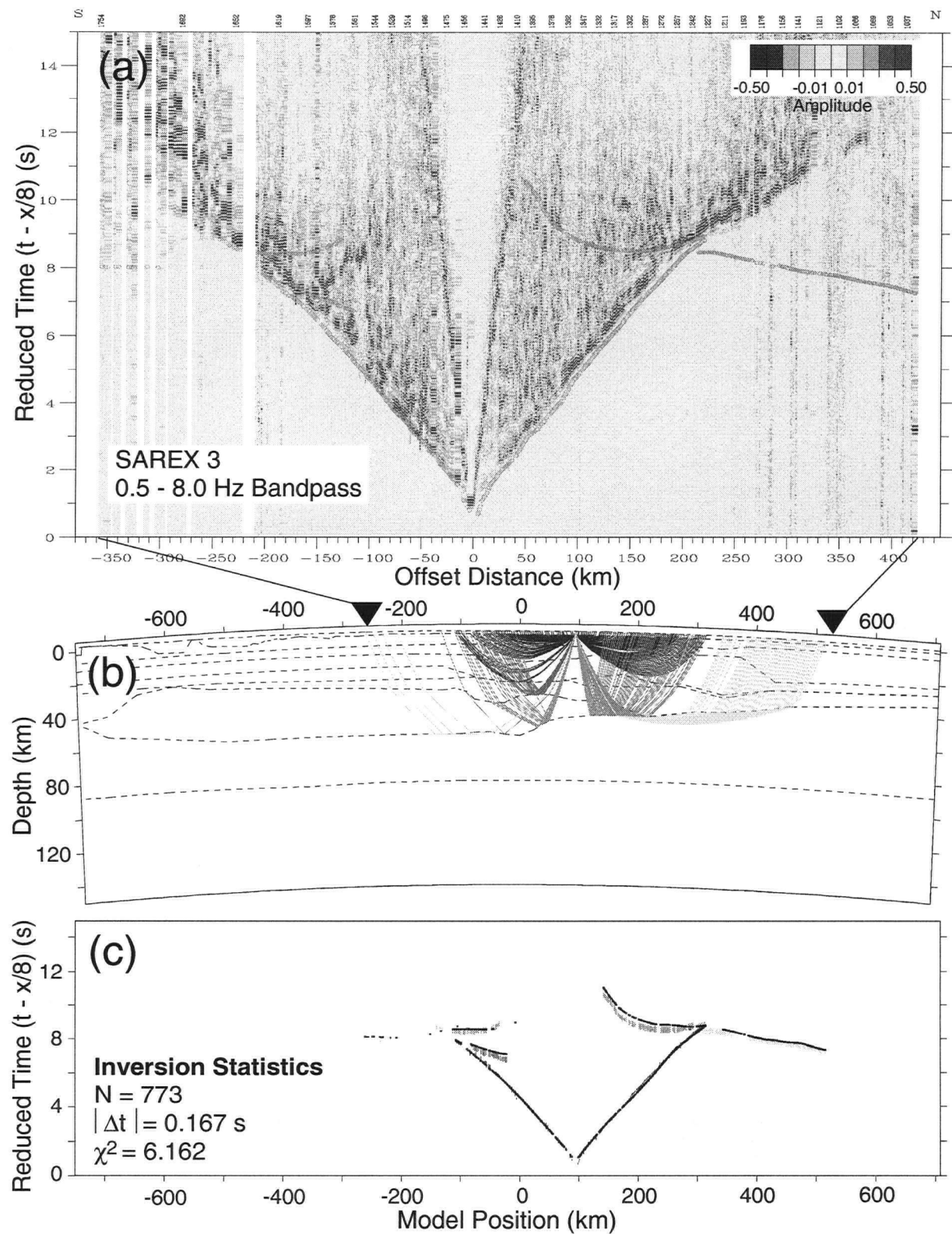


Figure A.4: SAREX 3: (a) Colour variable density plot with picks overlaid in green. (b) RAYINVR ray-trace diagram. Vertical exaggeration 4:1. Phases: P_g – dark blue, P_iP – magenta, P_mP – green, P_n – yellow. Location of recorded data indicated by triangles. (c) RAYINVR travel-time calculations (black dots) overlaid on picks. Colours for phases as above.

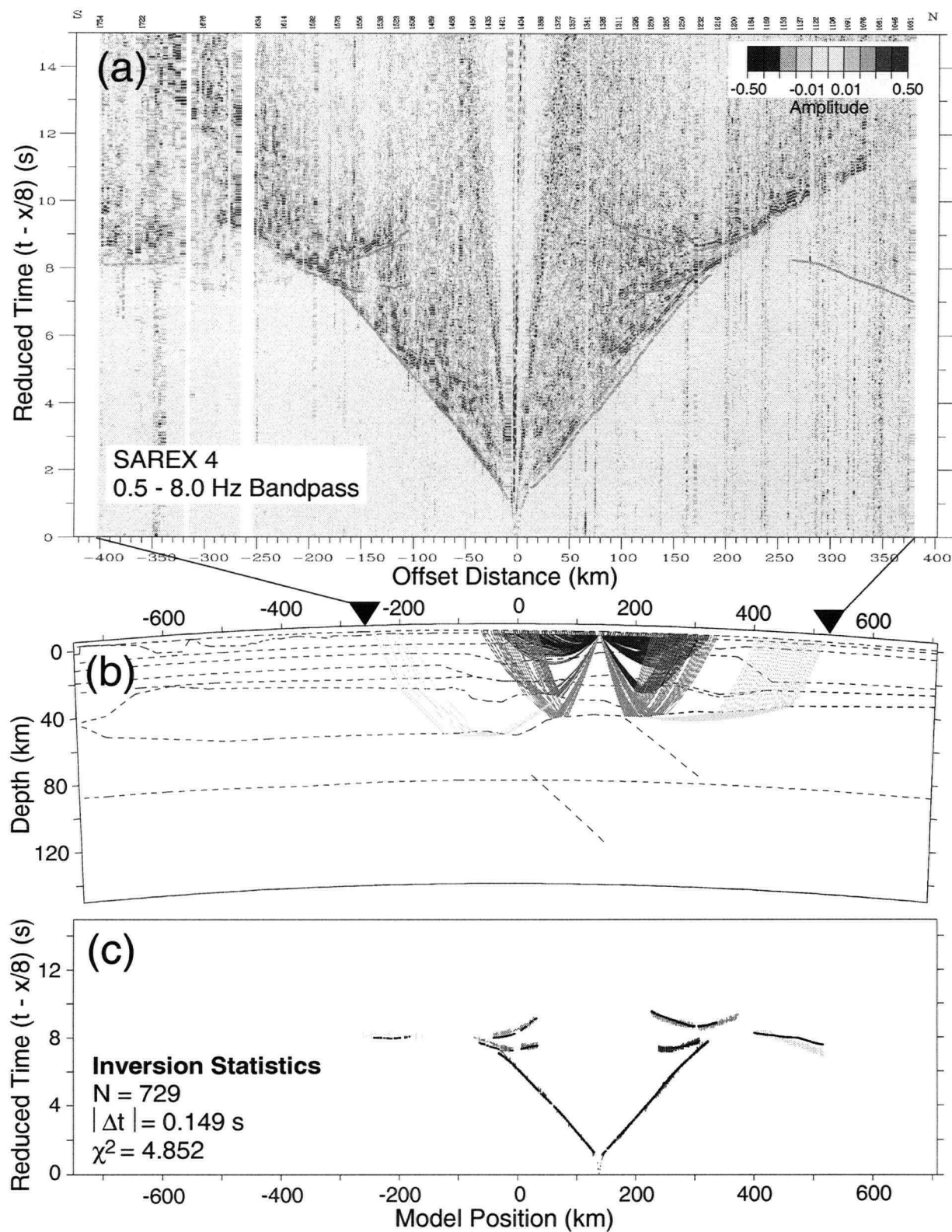


Figure A.5: SAREX 4: (a) Colour variable density plot with picks overlaid in green. (b) RAYINVR ray-trace diagram. Vertical exaggeration 4:1. Phases: P_g – dark blue, P_iP – magenta, P_mP – green, P_n – yellow. Location of recorded data indicated by triangles. (c) RAYINVR travel-time calculations (black dots) overlaid on picks. Colours for phases as above.

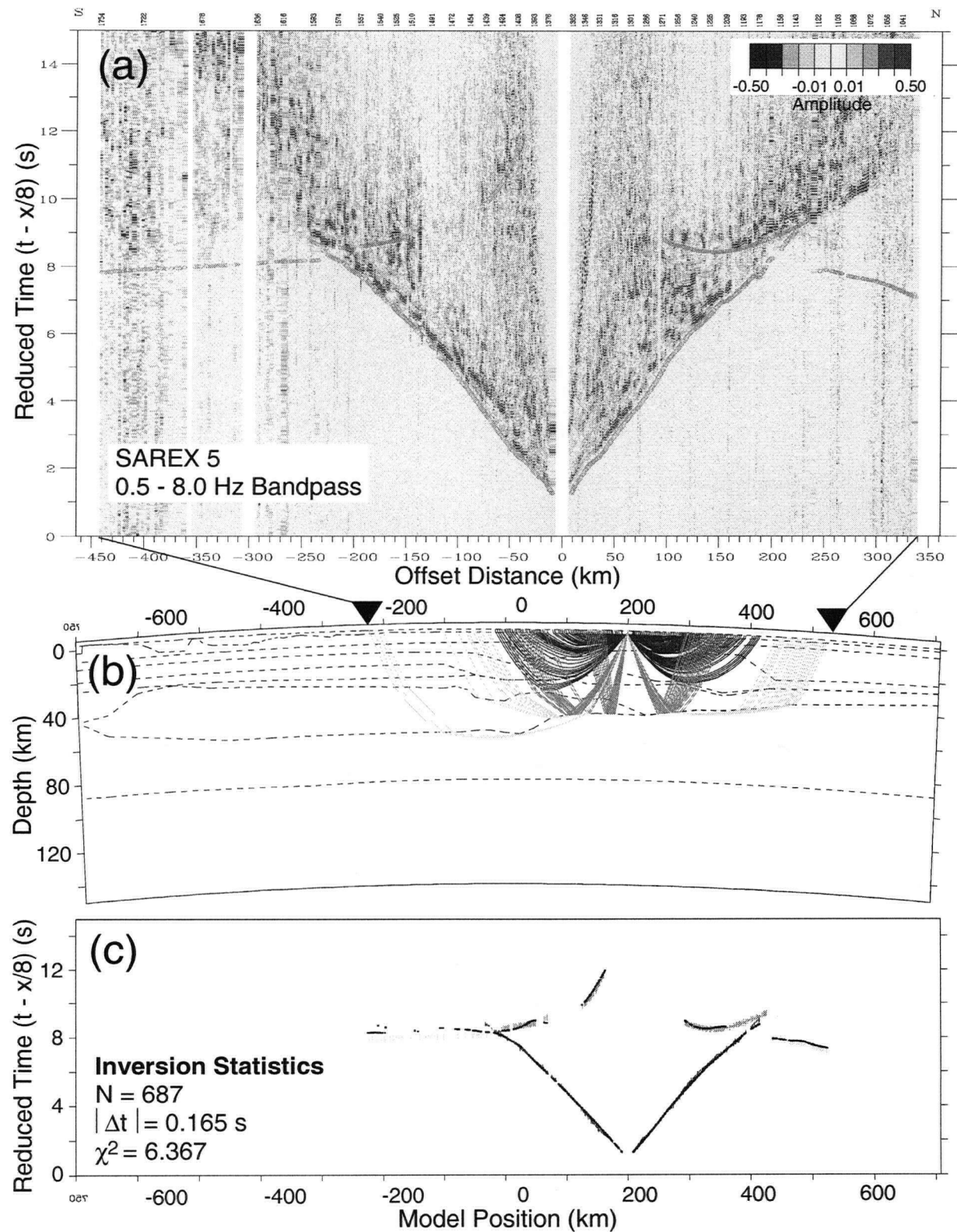


Figure A.6: SAREX 5: (a) Colour variable density plot with picks overlaid in green. (b) RAY-INVR ray-trace diagram. Vertical exaggeration 4:1. Phases: P_g - dark blue, P_mP - green, P_n - yellow. Location of recorded data indicated by triangles. (c) RAYINVR travel-time calculations (black dots) overlaid on picks. Colours for phases as above.

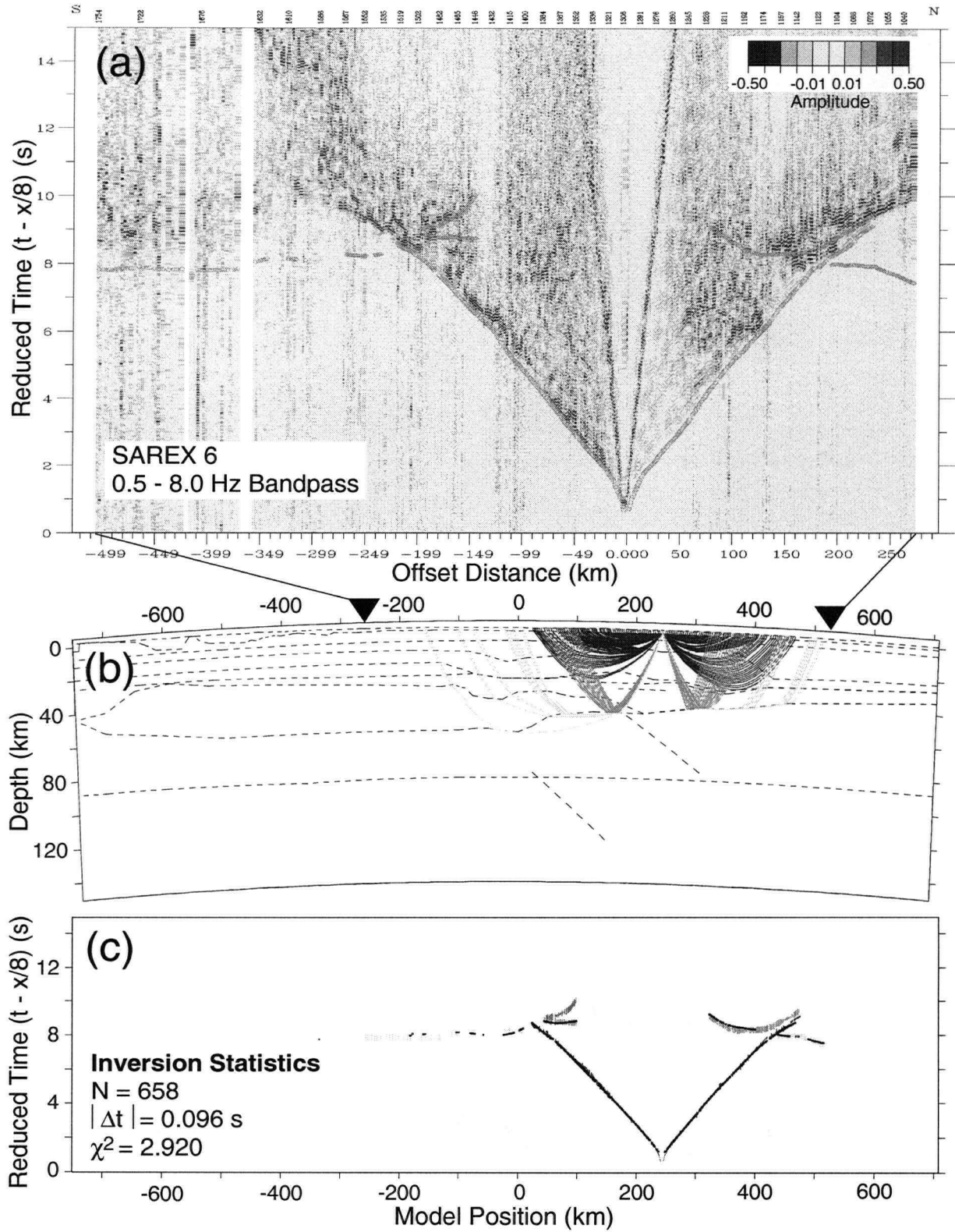


Figure A.7: SAREX 6: (a) Colour variable density plot with picks overlaid in green. (b) RAYINVR ray-trace diagram. Vertical exaggeration 4:1. Phases: P_g – dark blue, P_mP – green, P_n – yellow, $P_{f1}P$ – magenta. Location of recorded data indicated by triangles. (c) RAYINVR travel-time calculations (black dots) overlaid on picks. Colours for phases as above.

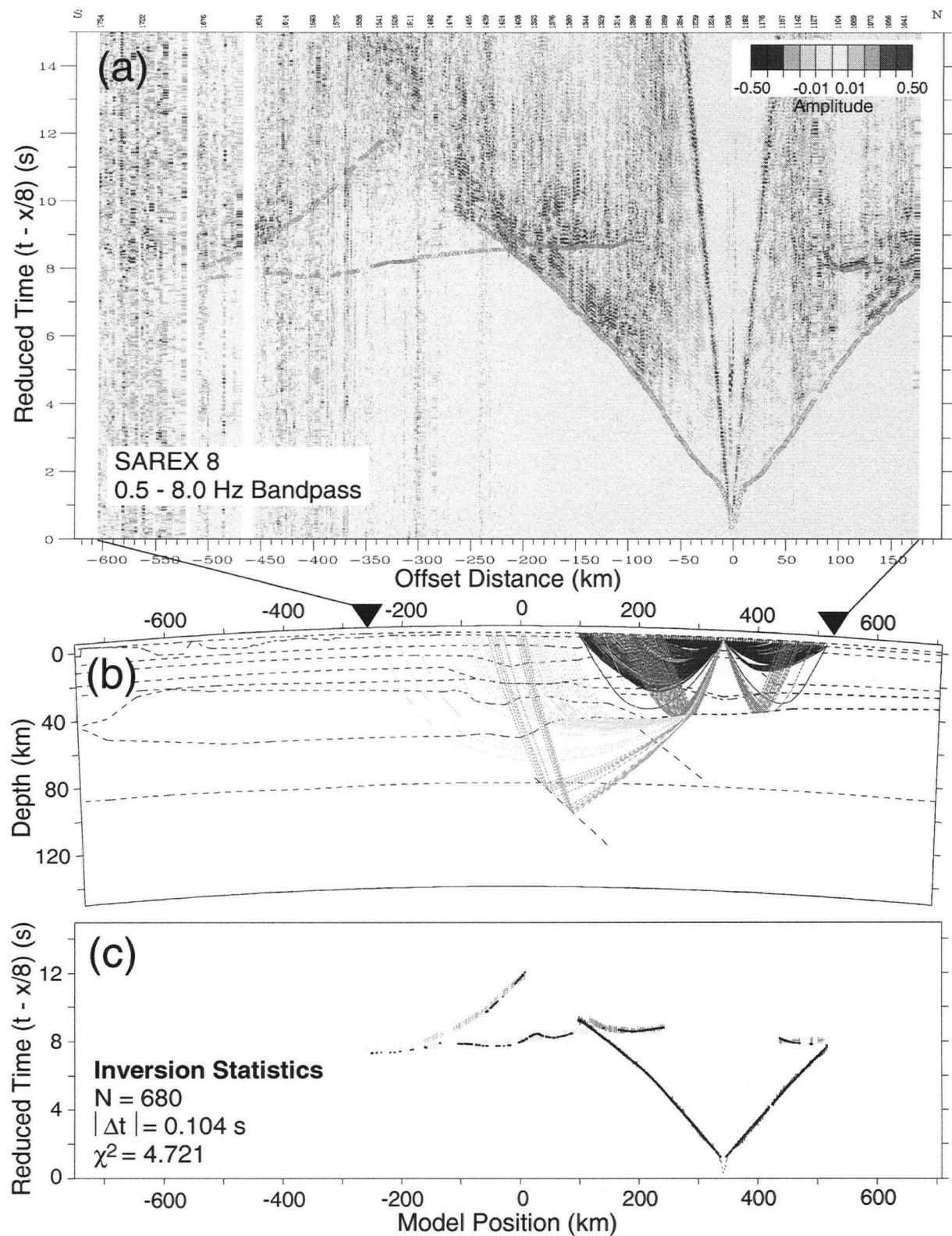


Figure A.8: SAREX 8: (a) Colour variable density plot with picks overlaid in green. (b) RAYINVR ray-trace diagram. Vertical exaggeration 4:1. Phases: P_g – dark blue, P_mP – green, P_n – yellow, $P_{f_2}P$ – light blue. Location of recorded data indicated by triangles. (c) RAYINVR travel-time calculations (black dots) overlaid on picks. Colours for phases as above.

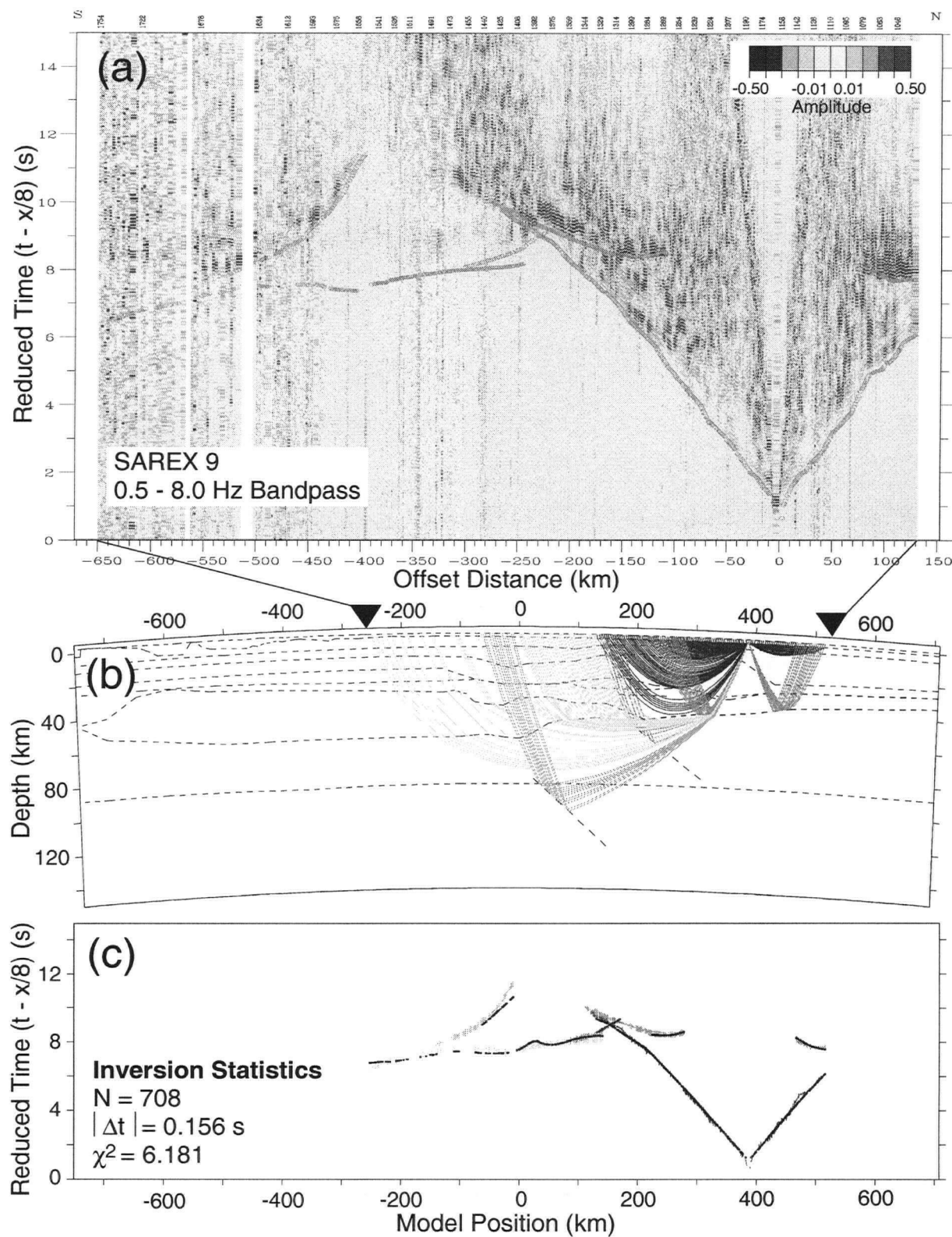


Figure A.9: SAREX 9: (a) Colour variable density plot with picks overlaid in green. (b) RAYINVR ray-trace diagram. Vertical exaggeration 4:1. Phases: P_g – dark blue, P_mP – green, P_n – yellow, $P_{f1}P$ – magenta, $P_{f2}P$ – light blue. Location of recorded data indicated by triangles. (c) RAYINVR travel-time calculations (black dots) overlaid on picks. Colours for phases as above.

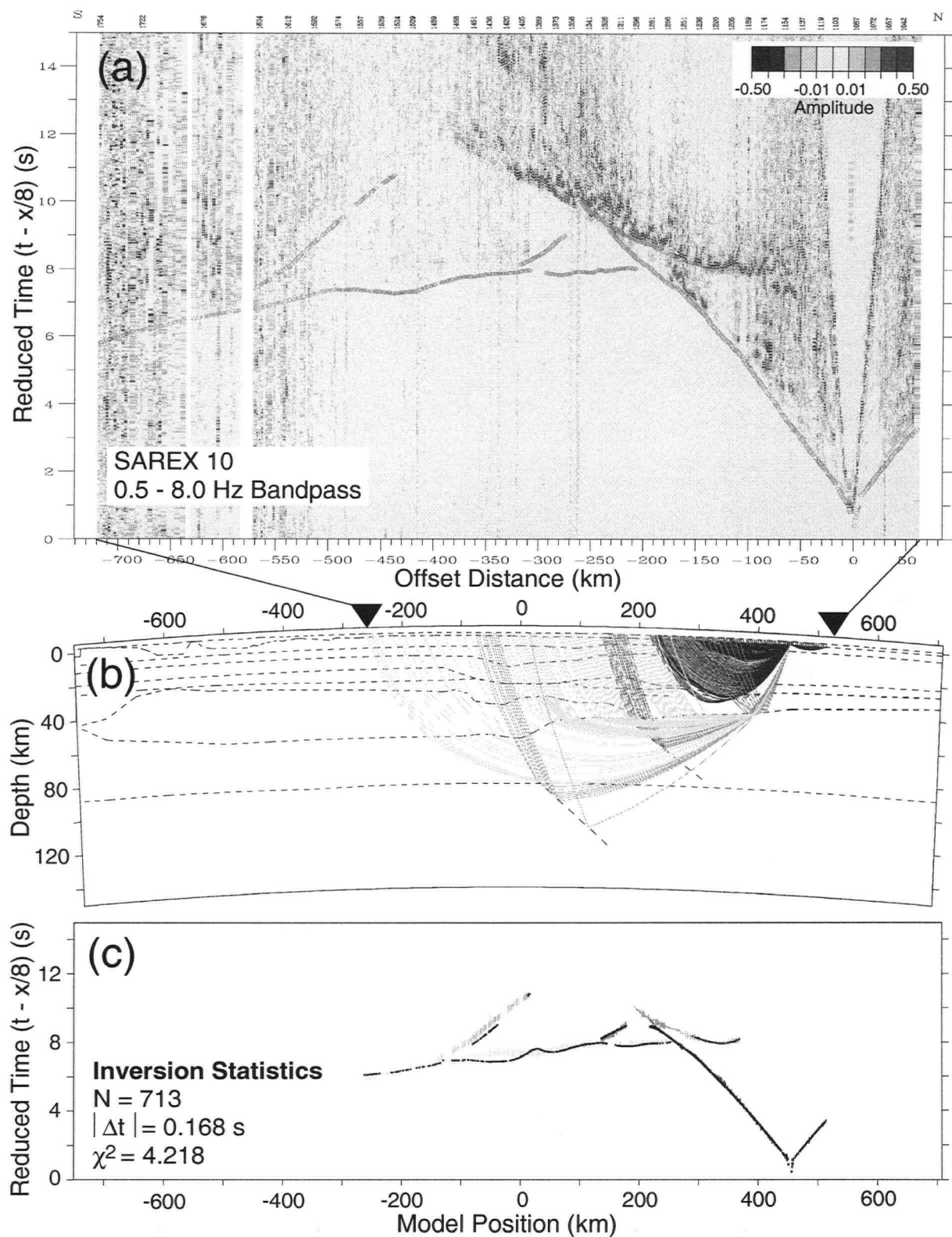


Figure A.10: SAREX 10: (a) Colour variable density plot with picks overlaid in green. (b) RAYINVR ray-trace diagram. Vertical exaggeration 4:1. Phases: P_g – dark blue, P_mP – green, P_n – yellow, $P_{f1}P$ – magenta, $P_{f2}P$ – light blue. Location of recorded data indicated by triangles. (c) RAYINVR travel-time calculations (black dots) overlaid on picks. Colours for phases as above.

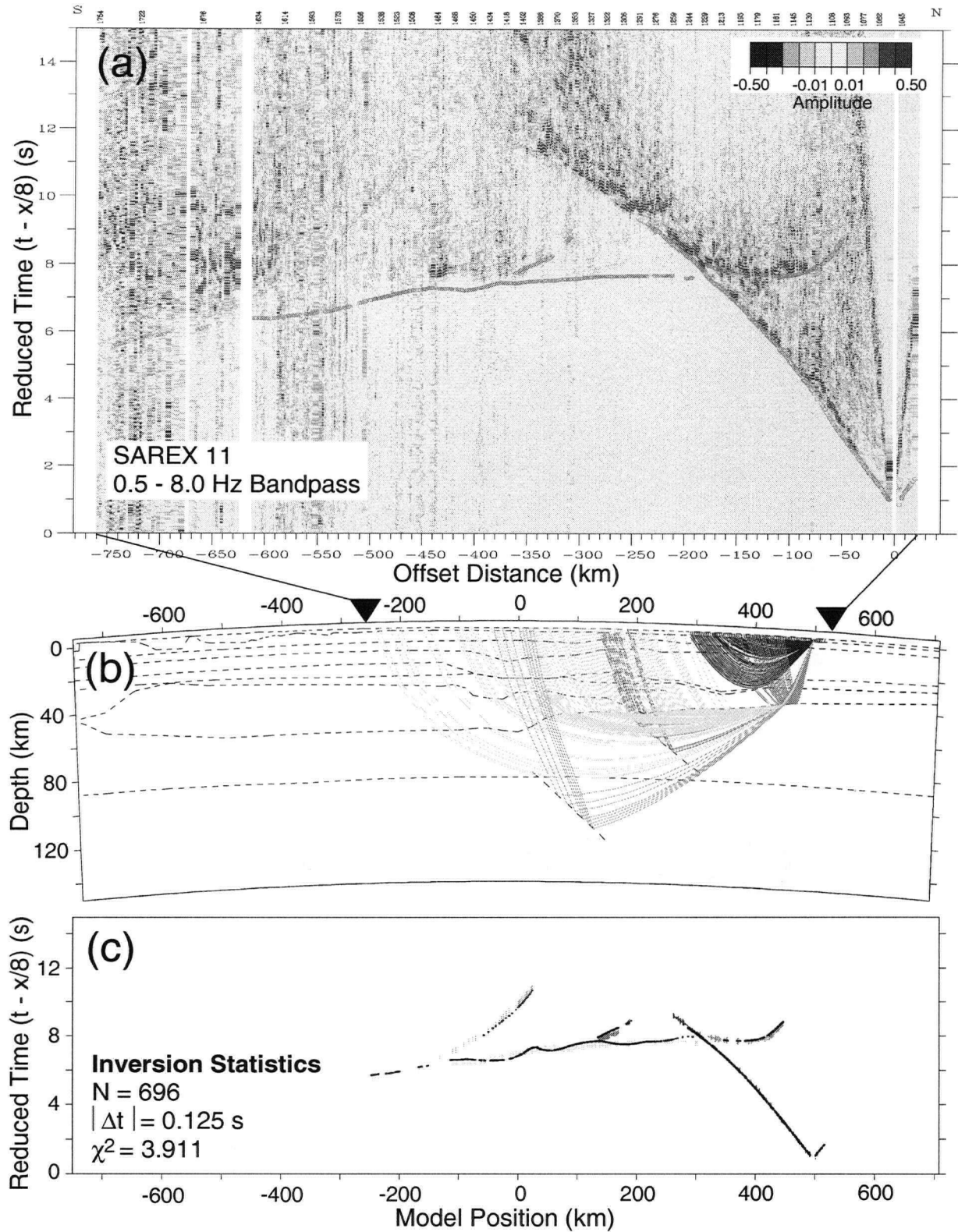


Figure A.11: SAREX 11: (a) Colour variable density plot with picks overlaid in green. (b) RAYINVR ray-trace diagram. Vertical exaggeration 4:1. Phases: P_g – dark blue, P_mP – green, P_n – yellow, $P_{f1}P$ – magenta, $P_{f2}P$ – light blue. Location of recorded data indicated by triangles. (c) RAYINVR travel-time calculations (black dots) overlaid on picks. Colours for phases as above.

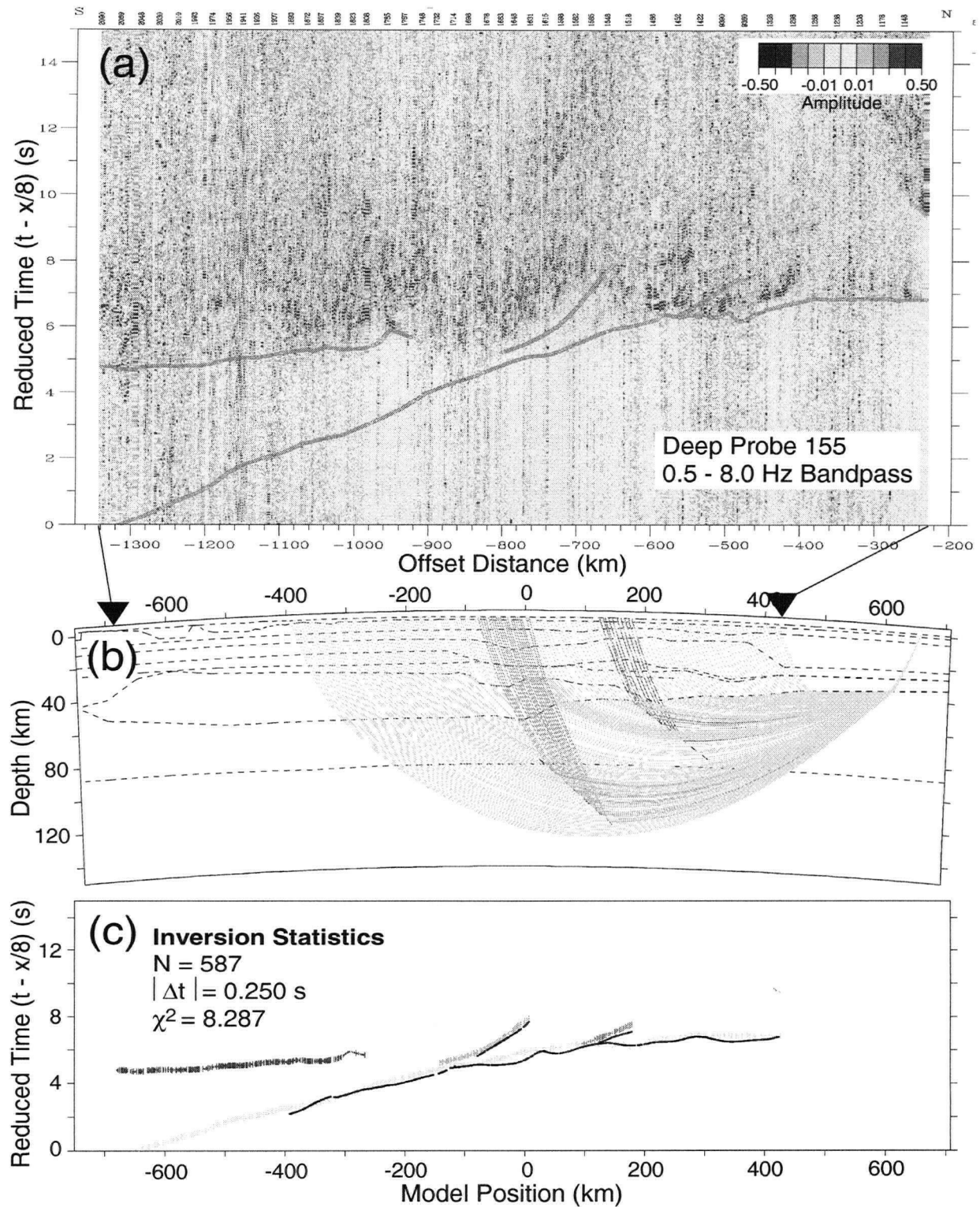


Figure A.12: Deep Probe 155: (a) Colour variable density plot with picks overlaid in green. (b) RAYINVR ray-trace diagram. Vertical exaggeration 4:1. Phases: P_mP – green, P_n – yellow, $P_{f1}P$ – magenta, $P_{f2}P$ – light blue, teleseismic P_n – dark blue. Location of recorded data indicated by triangles. (c) RAYINVR travel-time calculations (black dots) overlaid on picks. Colours for phases as above.

Appendix B

Summary of Modifications to the RAYINVR Code

B.1 General Modifications

The RAYINVR code [Zelt and Smith 1992] is free software made available by Dr. Colin Zelt of the Department of Geology and Geophysics at Rice University, Houston, Texas. A major goal of the revisions to this code, referred to here as RAYINVR v2.0, was to make as few changes as possible to the user interface. In fact, the original RAYINVR input files will run in RAYINVR v2.0 just as they did in earlier releases. This appendix details the changes made to the RAYINVR FORTRAN code, the theory of which is presented in Chapter 4. In this appendix, routine and variable names which correspond to those of the RAYINVR and RAYINVR v2.0 codes are denoted in italics.

One new switch, *ispher*, and one new parameter, *rearth*, have been added to the ray tracing parameters (*TRAPAR* namelist).

- *ispher* - radial earth geometry enabled (*ispher*=1). (default: 0; flat Earth geometry)
- *rearth* - radius of the Earth (default: 6371 km). This value could be modified for equatorial or polar regions where 6371 km is an unsatisfactory approximation for the radius of the Earth. It could also be modified for use on another planet.

In the command file *rayinvr.com*, a new commonblock */blksphere/* has been added to include *ispher* and *rearth*.

B.2 Ordinary Differential Equations for a Radial Earth

The RAYINVR subroutine, *TRACE*, located in file *trc.f* controls the tracing of a single ray through the velocity model given an initial set of conditions. This subroutine traces the ray in x, z space. In rewriting the code to accommodate radial Earth considerations, the parameterisation of the input model was left the same, *i.e.*, in x and z . However, the radial nature of the Earth means that units of x now get smaller with depth. This must be considered for all RAYINVR routines which use z and x to calculate length or time. The subroutine *TRACE* has been modified as follows.

TRACE uses one of two Runge-Kutta algorithms to solve the pairs of ordinary differential equations (ODE's) which make up the ray-tracing system (Eqs. 4.9 and 4.10). One of these algorithms has error control (subroutine *RNGKTA*) and the other does not (subroutine *RKDUMB*). Choice of routine is controlled by the user and is specified in the *TRAPAR* namelist with the switch *ifast*. Each Runge-Kutta routine calls an additional subroutine containing the ODE's that it solves numerically. New ODE subroutines have been added (as described above) for radial geometries.

Four new ODE subroutines were written.

- *ODED* and *ODER*
 - **Location:** *trc.f*
 - **New or revised routine?** New
 - **Description:** The radial Earth equivalents of subroutines *ODEX* and *ODEZ*. *term1*, *term2*, *vxv*, and *vzv* which determine the velocity components for the integration step are unchanged. The horizontal distance (km), depth (km) and initial angle (radians) which are passed to the subroutine are the same as for *ODEX* and *ODEZ*, but integration should occur over *dd* or *dr*.

- *ODEDFI* and *ODERFI*
 - **Location:** *rngkta.f*
 - **New or revised routine?** New
 - **Description:** The radial Earth equivalents of subroutines *ODEXFI* and *ODEZFI*. *term1*, *term2*, *vxv*, and *vzv* which determine the velocity components for the integration step are unchanged. The horizontal distance (km), depth (km) and initial angle (radians) which are passed to the subroutine are the same as for *ODEX* and *ODEZ*, but integration should occur over *dd* or *dr*.

B.3 Supplementary Routines

RAYINVR contains several supplementary subroutines which assist in ray tracing and in calculating travel times. As mentioned previously, the radial nature of the Earth means that units of x now get smaller with depth. Since the model parameterisation remains in units of x and z , then several RAYINVR subroutines which use x and z to calculate length or time must be modified. Most important among these subroutines is *TTIME* which calculates the travel time from source to receiver for each ray by integrating along the ray path, as described above.

- *TTIME*
 - **Location:** *misc.f*
 - **New or revised routine?** Revised
 - **Description:** This was the trickiest change made to the program. Using the law of cosines, the length of a ray step is calculated taking into consideration the Earth's curvature.
- *STRAIT*

- **Location:** *trc.f*
- **New or revised routine?** New
- **Description:** Change the method for propagating a straight line segment through a constant velocity layer for radial Earth cases. (A simple geometric problem.)

B.4 Plotting Routines

Plotting for the radial Earth case is complicated by the fact that we are dealing with a radial co-ordinate system, but the plotting routines used deal with Cartesian co-ordinates. Several subroutines were developed to transfer values back and forth between the original 'x' and 'z' parameterisation of radial co-ordinates, and the projection of this co-ordinate system into Cartesian co-ordinates for plotting to the screen or paper. The original parameterisation is generally in units of kilometres, but the transformed values are generally in pixel units.

- *PLTMOD*

- **Location:** *plt.f*
- **New or revised routine?** Revised
- **Description:** This is the main subroutine which is used to plot velocity models in RAYINVR. If the radial Earth option is being used, then the velocity model and any superimposed ray paths are plotted on a radial representation of the Earth.

PLTMOD calls numerous other subroutines to actually perform the plotting functions. Some of these subroutines had to be modified for the radial representation (including *SPHRPLT*, *CURVE*, *DASHCURVE*, and *AXISSPHERE*.)

- *SPHRPLT(xin, zin, xout, zout)*

- **Location:** *plt.f*
- **New or revised routine?** New
- **Variables:**
 - xin, zin* - input co-ordinates in units as defined in the input (km)
 - xout, zout* - output co-ordinates in same units
- **Description:** This subroutine converts an input pair of x, z co-ordinates to an equivalent pair of co-ordinates for plotting on a radial Earth.

The vertical exaggeration of radial co-ordinates takes some careful consideration. The routine is designed to accurately represent the 1:1 curvature of the Earth at any particular radius, using the scale shown for the horizontal axis. The "horizontal" shortening seen with depth is similarly correct.

- *CURVE(xplotin,zplotin,nsteps)*

- **Location:** *plt.f*
- **New or revised routine?** New
- **Variables:**
 - xplotin(2), zplotin(2)* - a pair of x, z co-ordinates (in km)
 - nsteps* - number of segments that the curve between the two points will be divided into for plotting
- **Description:** This subroutine plots a curve between two points on a radial plot that would have been a line on a Cartesian plot.

- *DASHCURVE(xplotin,zplotin,dash)*
 - **Location:** *plt.f*
 - **New or revised routine?** New
 - **Variables:**
 - xplotin(2), zplotin(2)* - a pair of x, z co-ordinates (in km)
 - dash* - length of the dashes (in km)
 - **Description:** This subroutine plots a dashed curve between two points on a radial plot that would have been a dashed line on a Cartesian plot.

- *AXISSPHERE*
 - **Location:** *plt.f*
 - **New or revised routine?** New
 - **Description:** This subroutine plots the axis, ticks, and tick labels for a radial representation. It calls the subroutines *REVERT* and *REVERT2* to convert co-ordinates previously calculated for a Cartesian system to their appropriate equivalents for the radial representation.

- *REVERT(xin,zin,xout,zout)*
 - **Location:** *plt.f*
 - **New or revised routine?** New
 - **Variables:**
 - xin, zin* - input co-ordinates in units defined by the plotting routines (pixels).
 - xout, zout* - converted output co-ordinates in these same units but shifted to the radial Earth representation.

- *REVERT2(xin,zin,xout,zout)*

- **Location:** *plt.f*

- **New or revised routine?** New

- **Variables:**

- xin, zin* - input co-ordinates in units defined by the plotting routines (pixels)

- xout, zout* - converted output co-ordinates (in km) shifted to the radial Earth representation.